OXYGEN REDUCTION REACTION ON DISPERSED AND CORE-SHELL METAL ALLOY CATALYSTS: DENSITY FUNCTIONAL THEORY STUDIES

A Dissertation

by

PUSSANA HIRUNSIT

Submitted to the Office of Graduate Studies of
Texas A&M University
in partial fulfillment of the requirements for the degree of

DOCTOR OF PHILOSOPHY

August 2010

Major Subject: Chemical Engineering

OXYGEN REDUCTION REACTION ON DISPERSED AND CORE-SHELL METAL ALLOY CATALYSTS: DENSITY FUNCTIONAL THEORY STUDIES

A Dissertation

by

PUSSANA HIRUNSIT

Submitted to the Office of Graduate Studies of
Texas A&M University
in partial fulfillment of the requirements for the degree of

DOCTOR OF PHILOSOPHY

Approved by:

Chair of Committee,	Perla B. Balbuena
Committee Members,	D. Wayne Goodman
	Victor Ugaz
	Hae-Kwon Jeong
Head of Department,	Michael Pishko

August 2010

Major Subject: Chemical Engineering

ABSTRACT

Oxygen Reduction Reaction on Dispersed and Core-Shell Metal Alloy Catalysts:
Density Functional Theory Studies. (August 2010)
Pussana Hirunsit, B.Eng., King Mongkut's Institute of Technology Ladkrabang,
Bangkok, Thailand;
M.Eng., King Mongkut's University of Technology Thonburi, Bangkok, Thailand;
M.S., Texas A&M University
Chair of Advisory Committee: Dr. Perla B. Balbuena

Pt-based alloy surfaces are used to catalyze the electrochemical oxygen reduction reaction (ORR), where molecular oxygen is converted into water on fuel cell electrodes. In this work, we address challenges due to the cost of high Pt loadings in the cathode electrocatalyst, as well as those arising from catalyst durability. We aim to develop an increased understanding of the factors that determine ORR activity together with stability against surface segregation and dissolution of Pt-based alloys. We firstly focus on the problem of determining surface atomic distribution resulting from surface segregation phenomena. We use first-principles density functional theory (DFT) calculations on PtCo and Pt_3Co overall compositions, as well as adsorption of water and atomic oxygen on PtCo(111) and Pt-skin structures. The bonding between water and surfaces of PtCo and Pt-skin monolayers are investigated in terms of orbital population. Also, on both surfaces, the surface reconstruction effect due to high oxygen coverage and water co-adsorption is investigated.

Although the PtCo structures show good activity, a large dissolution of Co atoms tends to occur in acid medium. To tackle this problem, we examine core-shell structures which showed improved stability and activity compared to Pt(111), in particular, one consisting of a surface Pt-skin monolayer over an IrCo or Ir_3Co core, with or without a Pd interlayer between the Pt surface and the Ir-Co core. DFT analysis of surface segregation, surface stability against dissolution, surface Pourbaix diagrams, and

reaction mechanisms provide useful predictions on catalyst durability, onset potential for water oxidation, surface atomic distribution, coverage of oxygenated species, and activity. The roles of the Pd interlayer in the core-shell structures that influence higher ORR activity are clarified. Furthermore, the stability and activity enhancement of new shell-anchor-core structures of Pt/Fe-C/core, Pt/Co-C/core and Pt/Ni-C/core are demonstrated with core materials of Ir, Pd_3Co, Ir_3Co, IrCo and IrNi. Based on the analysis, Pt/Fe-C/Ir, Pt/Co-C/Ir, Pt/Ni-C/Ir, Pt/Co-C/Pd_3Co, Pt/Fe-C/Pd_3Co, Pt/Co-C/Ir_3Co, Pt/Fe-C/Ir_3Co, Pt/Co-C/IrCo, Pt/Co-C/IrNi, and Pt/Fe-C/IrNi structures show promise in terms of both improved durability and relatively high ORR activity.

To love and patience

ACKNOWLEDGEMENTS

I am especially grateful to Prof. Perla B. Balbuena who gave me an opportunity to join her group and for the appreciable suggestions, counsel, and encouragement throughout the period of this work. My gratitude is also extended to the committee members, Dr. Wayne Goodman, Dr. Hae-Kwon Jeong and Dr. Victor Ugaz, for asking helpful questions, making helpful comments and for their time in serving on my committee.

Furthermore, I extend my gratitude to the National Nanotechnology Center in Bangkok, Thailand for providing me with support in the form of a scholarship. I would like to thank my fellow students in Dr. Balbuena's group during 2006-2010. They provided technical assistance with programs, as well as friendship and moral support. Also, special thanks to my partner, Robert Rose, for his editorial assistance, encouragement, patience and love. Finally, I wish especially to thank my mother, my father and my sister for their constant love and endless support from my home, so far away, in Bangkok, Thailand.

TABLE OF CONTENTS

CHAPTER Page

CHAPTER Page

LIST OF FIGURES

FIGURE Page

FIGURE Page

FIGURE Page

LIST OF TABLES

TABLE Page

TABLE Page

CHAPTER I

INTRODUCTION TO POLYMER ELECTROLYTE MEMBRANE FUEL CELL AND CATHODE CATALYSIS

In this chapter, how the fuel cell works is firstly introduced. Then, we focus on the surface science study on the cathode catalyst in which a review of some experimental works on the search for a better catalyst is presented.

1.1. Introduction

Fuel cells are expected to be one of a few key next generation resources for vehicles due to their low pollutant emission and the potential for reduced dependence on gasoline. A fuel cell uses electrochemistry fundamentals to produce energy in terms of electricity, with relatively benign water and heat as byproducts. Fuel cells applications are not only limited to vehicles; they can provide energy for large systems such as utility power stations and other devices as small as a light bulb.

A fuel cell uses a fuel (such as hydrogen) and oxygen to produce electricity. Hydrogen, or a hydrogen-rich fuel, is input for the anode where a catalyst separates hydrogen into electrons and protons while at the cathode, oxygen combines with electrons and protons producing water. There are many types of fuel cells which have different operating conditions and materials and offer different applications, advantages and disadvantages. Table 1.1 shows a comparison of different fuel cell types. In general, fuel cell research and development emphasizes achieving high efficiency, durability, and low manufacturing cost. However, the system requirements for each type of fuel cell to reach those objectives are specific for each type. In this work, we focus on the polymer electrolyte membrane (PEM) fuel cell type.

This dissertation follows the style of Surface Science.

Table 1.1
Comparison of fuel cell technologies [1].

Fuel Cell Type	Common Electrolyte	Operating Temperature	System Output	Applications	Advantages	Disadvantages
Polymer Electrolyte Membrane (PEM)	Solid organic polymer poly-perfluorosulfonic acid	50 - 100°C	<1kW – 250kW	•Backup power •Portable power •Small distributed generation •Transportation	•Low temperature •Quick start-up	•Requires expensive catalysts •High sensitivity to fuel impurities •Low temperature waste heat •Waste heat temperature not suitable for combined heat and power (CHP)
Alkaline (AFC)	Aqueous solution of potassium hydroxide soaked in a matrix	90 - 100°C	10kW – 100kW	•Military •Space	•Cathode reaction faster in alkaline electrolyte, higher performance	•Expensive removal of CO_2 from fuel and air streams required (CO_2 degrades the electrolyte)
Phosphoric Acid (PAFC)	Liquid phosphoric acid soaked in a matrix	150 - 200°C	50kW – 1MW (250kW module typical)	•Distributed generation	•Higher overall efficiency with CHP •Increased tolerance to impurities in hydrogen	•Requires expensive platinum catalysts •Low current and power •Large size/weight

Table 1.1 (cont'd)

Fuel Cell Type	Common Electrolyte	Operating Temperature	System Output	Applications	Advantages	Disadvantages
Molten Carbonate (MCFC)	Liquid solution of lithium, sodium, and/or potassium carbonates, soaked in a matrix	600 - 700°C	<1kW – 1MW (250kW module typical)	•Electric utility •Large distributed generation	•High efficiency •Fuel flexibility •Can use a variety of catalysts •Suitable for CHP	•High temperature speeds corrosion and breakdown of cell components •Complex electrolyte management •Slow start-up
Solid Oxide (SOFC)	Solid zirconium oxide to which a small amount of Yttria is added	650 - 1000°C	5kW – 3MW	•Auxiliary power •Electric utility •Large distributed generation	•High efficiency •Fuel flexibility •Can use a variety of catalysts •Solid electrolyte reduces electrolyte management problems •Suitable for CHP • Hybrid/GT cycle	•High temperature enhances corrosion and breakdown of cell components •Slow start-up •Brittleness of ceramic electrolyte with thermal cycling

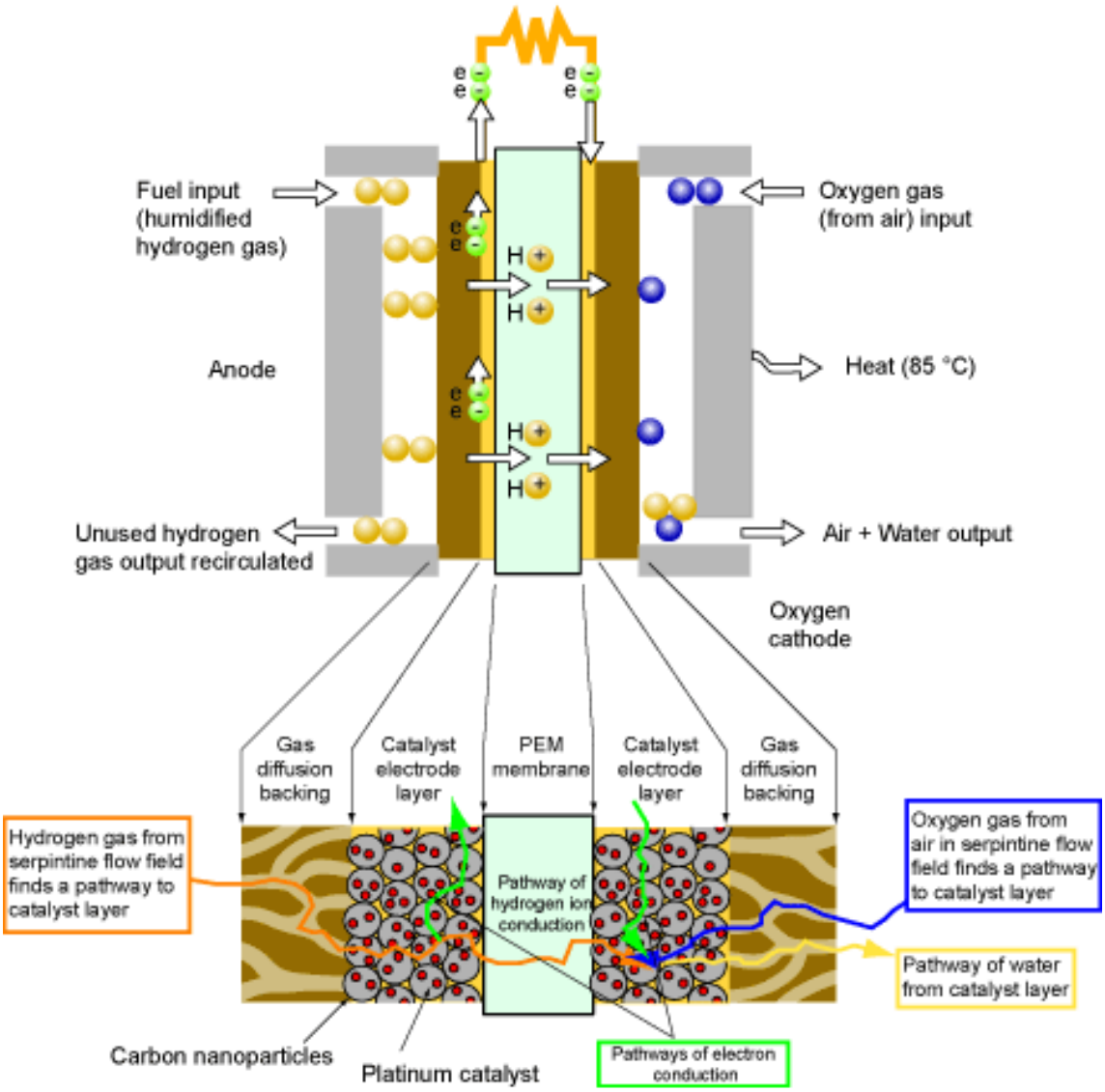

Fig. 1.1. Polymer electrolyte membrane fuel cell [1].

The PEM fuel cell illustrated in Fig. 1.1, uses hydrogen fuel which is fed to the anode on one side of the fuel cell, while oxygen from the air is channeled to the cathode on the other side of the cell. At the anode, a catalyst which commonly is platinum catalyzes the hydrogen dissociation into protons (H^+) and electrons (e^-): $H_2 \rightarrow 2H^+ + e^-$. The polymer electrolyte membrane located between the anode and the cathode allows only H^+ travel through it entering the cathode whereas the electrons must travel along an external

circuit to the cathode, providing an electrical current. At the cathode, electrons and protons react with oxygen to form water, which flows out of the cell: $1/2O_2 + 2H^+ + 2e^- \rightarrow H_2O$. Multiple fuel cells are assembled into fuel cell stack in order to produce enough electricity to power a vehicle. Therefore, the generated power depends on the number and size of the individual fuel cells in a fuel cell stack. According to the U.S. department of energy's fuel cell program's multi-year research in 2007, the primary focus is on fuel cells for transportation applications which has the primary objective which by 2010, develop a 60% peak-efficient and durable at a cost of $30 kW by 2015 [1].

The major challenges of PEM fuel cell are (i) the high cost dominated by membrane and Pt loading in catalysts (ii) the durability and reliability which are required to be at the same level with the current automotive engine i.e., 5,000-hour lifespan (150,000 miles) and be able to operate at vehicle operating conditions (40-80^{o}C) (iii) the requirement of a suitable air, thermal and water management for automotive fuel cell system (iv) the requirement of a suitable heat recovery system that allow the combined heat and power (CHP) efficiencies to exceed 80% [1]. In this work, we focus on the challenges of the high cost of PEM fuel cell due to Pt loading in the cathode electrode catalyst where ORR takes place and on the catalyst durability.

Although Pt is the key to fuel cells because of its unusual reactive catalytic properties, unwanted oxide formation reactions potentially occur. These oxides likely block the active site of the Pt atoms and eventually pull Pt atoms off the surface, consequently significantly reduce the reactivity and durability of the Pt cathode catalysts. There are extensively researches showing the progress on those problems that are exacerbated by alloying platinum with cheaper 3d metals such as Fe, Co, and Ni. More detailed investigations are discussed in the following sections.

1.2. Structures and chemistry of Pt surfaces

For understanding the reactivity and identifying mechanisms of reaction on the surface influencing the oxygen reduction reaction (ORR) thermodynamically and kinetically, the

determination of surface structure and the knowledge of chemistry at the interface of the catalyst with adsorbate species in the electrochemical environment are essential. We will start with the review of the investigation on the conventional pure Pt catalysts and then we will analyze more complicated alloy surfaces.

1.2.1. Surface experimental characterization techniques

The structure of surfaces can be quantified by experiments and ab initio calculations. The ab initio calculations are commonly used to identify the most favorable configuration showing the lowest energy and the favorable positions of the adsorbates to bond with the surfaces. There are also many advanced experimental methods used for surface structure and adsorbate surface bonding structure determination. Both methods are crucial to ensure that a complete picture is obtained from such investigations. Some key experimental methods [2-4] are summarized next.

1.2.1.1. Spectroscopic methods and scanning probe microscopy

Scanning tunneling microscopy (STM) is the most common method of a group of scanning probe microscopies. STM offers atomic-scale resolution both ex situ and in situ. It can be operated in ultra high vacuum (UHV), ambient pressure and in liquids. STM becomes a routine tool for the solid-liquid electrified surface characterizations. It is based on the concept of quantum tunneling occurring when a conducting tip is brought very near to the surface to be examined; a voltage difference applied between the two surfaces can allow electrons to tunnel through the vacuum between them without physical contact between two. The resulting tunneling current is a function of tip position, applied voltage, and the local density of states (LDOS) of the sample. Information is acquired by monitoring the current as the probe's position scans across the surface. Since STM provides information about the spatial variations of the surface electronic structure, not of the relative locations of the atomic centers on the surface, a more complex surface structural method, X-ray and electron scattering, mentioned in a later section, are required for a comprehensive analysis. STM can elucidate surface

structural phenomena such as low coverage of adsorbates on a surface and may distinguish atop, hollow and bridges sites. The technique plays the most valuable role in identifying inhomogeneity at surfaces such as step-site, island growth and coexistent surface structures. Also, STM can be a challenging technique, as it can require extremely clean and stable surfaces, sharp tips, and excellent vibration control.

X-ray photoelectron spectroscopy (XPS), for each and every element, there will be a characteristic binding energy associated with each core atomic orbital. XPS spectra are obtained by irradiating a material with a beam of X-rays while simultaneously measuring the kinetic energy (KE) and number of electrons that escape from the top 1 to 10 nm of the material being analyzed and then the electron binding energy (BE) of each of the emitted electrons can be determined. Each element will give rise to a characteristic set of peaks in the photoelectron spectrum at particular KEs and the respective BEs. The presence of peaks at particular energies therefore indicates the presence of a specific element in the sample and the intensity of the peaks is related to the concentration of the element within the sample. Thus, the technique provides a quantitative analysis of the surface composition and is sometimes known by the alternative name, Electron Spectroscopy for Chemical Analysis (ESCA). XPS is an ex situ technique and requires UHV conditions. Since the x-rays may penetrate to some depth, changing the angle between the surface and the x-rays electrons escaped from different depth from the surface can be collected, thus allowing the composition of the thin film can be determined as a function of depth.

1.2.1.2. Electron scattering

Low energy electron diffraction (LEED), an ex situ technique and a key feature of the technique is that it applies the long-range periodic order of the sample to concentrate the elastically scattered low energy electrons (~20-500 eV) into distinct diffracted beams. LEED can give the information on the symmetry of the surface structure and about the size and alignment of adsorbates on the surface. Yet, although LEED can probe several atomic layers near the surface, well-described adsorbate and substrate geometries models

are required for LEED to be able to gives the complete structures. LEED is usually applied to control the surface quality of a sample after preparation under UHV by establishing the exact surface structure, reconstruction, impurities, etc.

Surface Extended X-ray Absorption Fine Structure (SEXAFS), is an in situ technique that applies the same underlying phenomenon of elastically scattered low energy electrons as LEED but the key differences are (i) the source of electrons is not an electron beam form outside the surface, as in LEED, but photoelectrons emitted from a core level of an atom within the adsorbate (ii) SEXAFS is element specific and local. SEXAFS involve monitoring photo absorption by detecting in the intensity of Auger electrons (i.e., an electron emitted from an atom accompanying the filling of a vacancy in an inner electron shell) which data depends on surface sensitivity. Typically, SEXAFS provides accurate nearest-neighbor distances, coordination number and limited information on the direction of these neighbor and the distances to other near neighbors. The technique benefits from the fact that long range order is not required which sometimes becomes a limitation in LEED (about 10 nm) and also can probe different species in the sample.

1.2.1.3. X-ray scattering

X-rays are very weak scattered by atoms which is a property leading to the success of X-ray diffraction techniques. The techniques are based on the elastic scattering of X-rays from structures that have long range order. *Surface X-ray diffraction (SXS)* is an in situ technique and requires higher quality of the order than LEED in order to ensure that the weak surface diffraction beams are narrow and more easily detected than the diffuse scattering background. SXS is practical to investigate more complex surfaces with larger surface periodicity than LEED does and capable of structural precision of ~0.01Å, however, it is demanding in SXS to obtain precise structural information on the very weak scattering of adsorbates with low atomic number such as C and O and may face the error of 0.1 Å or more.

1.2.1.4. Ion scattering

This method is mainly used for low atomic number ions such as H^+, He^+ at low energies called *low energy ion scattering (LEIS)*. A surface is used as a target that scatters a noble gas ion beam (He+, Ne+, Ar+) with energies (0.5-3 keV). The energy of the scattered ions is in direct correlation with the mass of the target atoms, therefore, can be interpreted as a mass spectrum of the surface. LEIS provide the ability to define the atomic composition of the top most surface layer under UHV conditions. It formally exploits the well-defined crystallography of the surface but not explicitly the long-range order of an adsorbate. The main application is the investigation of a range of atomic adsorbate structures and a little contribution in quantitative structural information on the local adsorption geometry of molecular species.

1.2.2. Pt surface structures under ultrahigh vacuum (UHV)

Due to the development of advanced surface characterization techniques as mentioned above, the understanding of the atomic scale structures both in vacuum and at the solid-electrolytes become more extensive. In this part, Pt(111) surface structures changes on clean surfaces and surfaces with the presence of adsorbates are discussed.

1.2.2.1. Clean surfaces

On the atomic scale, most clean metals tend to arrange themselves in order to minimize their surface energy by two kinds of surface atom rearrangement; (i) relaxation in which small interlayer spacing changes relative to the ideal bulk lattice and (ii) reconstruction[5]. The low coordination of surface atoms is the main driving force of surface relaxation. In some cases, surface relaxation can affect the equilibrium position and bonding of adsorbates resulting in reconstruction of the outermost layers. Reconstruction is usually observed straightforwardly using LEED, LEIS, SXS and STM techniques while relaxation requires a more limited number of surface sensitivity probes, such as the so-called crystal truncation rod (CTR) data in SXS experiments[5].

On the clean fcc Pt (111) surface under UHV, there is no tendency for surface reconstruction and the interlayer spacing between the topmost and the second atomic layer, Δd_{12}, is expanded by ca. 2.5 ± 1.3% while fcc Pt(100) which is atomically less dense than Pt(111) surface, therefore shows stronger tendency for both reconstruction and relaxation resulting in higher surface Pt density[5]. Not only plane structure causes different behavior on relaxation and reconstruction of clean surfaces, but also temperature and impurities.

1.2.2.2. Adsorbate-induced change in surface structure

The presence of adsorbates generally alters the atomic interlayer spacing of the metal surfaces or induces the surface reconstruction. The driving force for those changes is the formation of strong bonds between metal surface atoms and the adsorbates which is comparable or sometimes stronger than the bonds between surface metal atoms themselves on the clean surface[5]. Here, we review some of adsorbates playing an important role in ORR.

1.2.2.2.1. Hydrogen adsorption

The most stable adsorption site for hydrogen on Pt(111) is the three-fold hollow site which may result from the tendency of hydrogen to occupy highly coordinated sites and reduce H-H repulsion when all three-fold next nearest neighbor sites are occupied[5]. Hydrogen adsorption energy on Pt(111) is linearly reduced when the hydrogen coverage, θ_H, increases as shown in Fig. 1.2. This variation is mainly from the H-H repulsion when hydrogen coverage reaches a certain value. The adsorption energy can be higher on defect sites e.g., step sites. Although DFT calculations showed top site as the most stable hydrogen adsorption site, the difference in the adsorption energies are insignificant among other various sites[6]. The Pt-H bond is relatively weak and the bond energies are approximately 240-270 kJ/mol depending on adsorption site and coverage[5]. Furthermore, a monolayer hydrogen adsorption on Pt(111) does not result in surface reconstruction and show negligible change in Δd_{12}[5]. This generally occurs in the

system with low heat of adsorption on the (111) surface of a metal with an appreciable cohesive energy[5].

1.2.2.2.2. Oxygen adsorption

Oxygen adsorption is more complicated than hydrogen adsorption because there are several states of oxygen involved. Gland et al.[7] characterized oxygen adsorption with three states at different temperatures under oxygen dosing of $< 10^{-6}$ torr: (i) molecular adsorption at temperatures below 120 K (ii) atomic oxygen adsorption at 150-500 K and (iii) oxide formation at 1000-1200 K. Gland et al.[7] also commented that O_2 dissociation proceeds by sequential population of chemisorbed O_2. Later, Campbell et al. [8] suggested that part of atomic oxygen adsorption may occur without passing the molecular state which dissociative adsorption can happen that O_2 molecule is not trapped in O_{2ad} state and then is dissociated and adsorbed as 2 O_{ad}. Like hydrogen adsorption, oxygen adsorption energy on Pt(111) is reduced with the oxygen coverage, θ_O, increases (Fig. 1.2) indicating the repulsive force between O-O adsorbed atoms. Under low pressure and temperature 300-500 K, the coverage of atomic oxygen is saturated at 0.25 ML with three-fold hollow site being the most favorable site and forming a well-ordered p(2x2) structure[9]. Higher coverage than 0.25 ML can be reached at higher pressure and temperature. The Pt-O bond energy is considerably higher than Pt-H bond energy. It can be close to 350 kJ/mol corresponding to the heat of O adsorption of 250 kJ/mol[5].

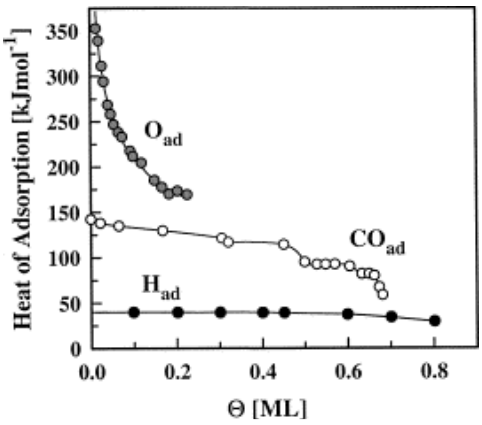

Fig. 1.2. The heat of adsorption of H_2, O, and CO on Pt(1 1 1)[5, 7, 10, 11]**.**

1.2.3. Pt surface structures in electrolyte

The voltammogram of Pt(111) in acidic and alkaline solution give distinctive curves. As illustrated in Fig. 1.3, hydrogen desorptiopn/adsorption region between ~0.05 < E < 0.375 V in both 0.05M H_2SO_4(Fig. 1.3a) and 0.1M KOH (Fig. 1.3b) shows a broad nearly flat curve suggesting hydrogen adsorption is not accompanied with anion adsorption. Depending on the solution pH , hydrogen can result from protons in the solution pH < 7 (reaction 1.1) and from water molecules in the solution pH > 7 (reaction 1.2) [5]. This state of adsorbed hydrogen will be referred to as underpotentially deposited hydrogen (H_{upd}).

$$Pt + H_3O^+ + e^- \rightarrow Pt\text{-}H_{upd} + H_2O \quad (pH < 7) \qquad (1.1)$$

$$Pt + H_2O + e^- \rightarrow Pt\text{-}H_{upd} + OH^- \quad (pH > 7) \qquad (1.2)$$

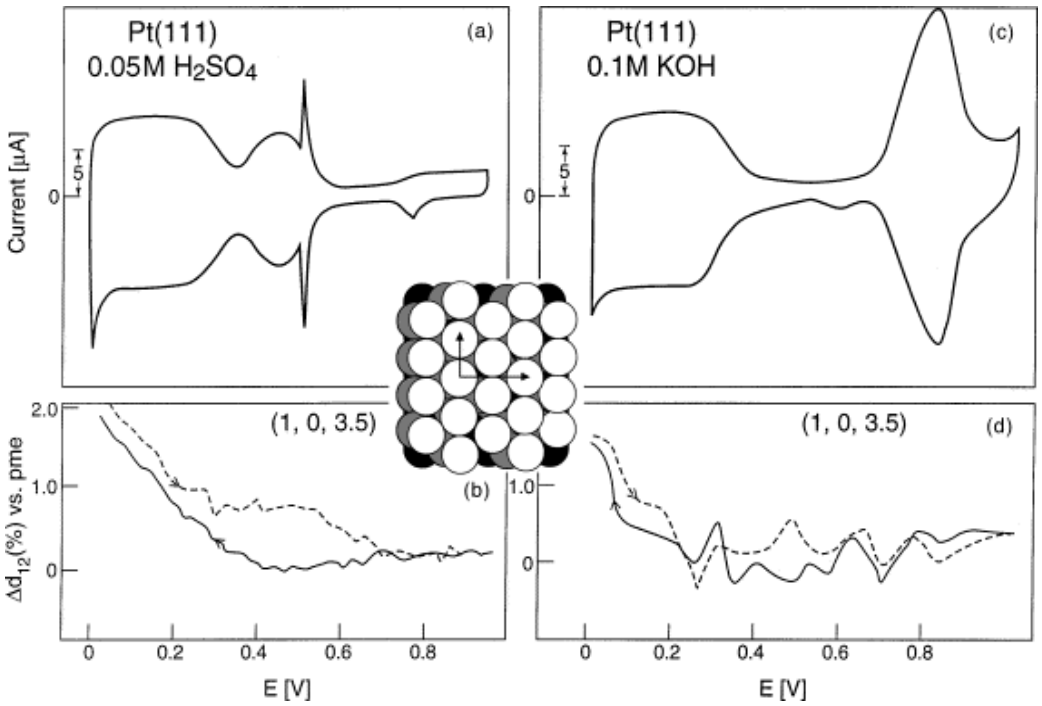

Fig. 1.3. Cyclic voltammetry of the Pt(1 1 1)-(1×1) surface in an electrochemical cell: (a) in H_2SO_4 and (c) in 0.1 M KOH. The potential was scanned at 50 mV/s. Changes in inter-layer spacing (Δd_{12}) measured from the potential of minimum expansion (PME) (e.g., the least coverage by any adsorbates) on scanning the potential at 2 mV/s (b) in H_2SO_4 and (d) in 0.1 M KOH. Insert: ideal model for the Pt(1 1 1)-(1 × 1) surface. Electrode potential E is given vs. the reversible hydrogen electrode (RHE)[5].

At higher positive potential ~0.4-0.6 V in H_2SO_4 and ~0.6-0.85 in KOH show peaks, the so-called anomalous peaks, indicating the reversible anion desorption/adsorption which is (bi)sulfate for H_2SO_4 solution and hydroxyl species for KOH solution. The adsorption of hydroxyl species, OH_{ad}, in alkaline solution may occur with charge transfer (reaction 1.3) while the OH_{ad} in acid solution proceeds according to reaction 1.4, yet these have not been proved[5].

$$OH^- + Pt \rightarrow Pt\text{-}OH_{ad} + e^- \quad (1.3)$$

$$2H_2O + Pt \rightarrow Pt\text{-}OH_{ad} + H_3O^+ + e^- \quad (1.4)$$

The well-ordered Pt(111) structure remains well-ordered between potential 0-0.8 V in which there is only reversible adsorption of hydrogen, anions and hydroxyl species. At

higher positive potential above ca. 1.0 V, oxide is formed in the first layer and the surface becomes irreversibly reconstructed and roughened[12].

1.2.3.1. Pt(111)-H_{upd}

The cyclic voltammogram in either acidic or alkaline solutions is affected by temperature, as illustrated in Fig. 1.4, due to the effects of temperature on adsorbates adsorption. In all electrolytes, the free energy of adsorption of Pt(111)-H_{upd} shows a similar trend with that in UHV in which the energy decreases with the increase of coverage (Fig. 1.5) indicating repulsive lateral interaction in the hydrogen adlayer causing the saturation coverage of H_{upd} to be much less than 1(~0.66H_{upd} per Pt)[13]. The bond energies of Pt-H in acidic and alkaline solutions are 240-250 kJ/mol which are independent of the solution pH and also close to that in UHV[14, 15].

1.2.3.2. Pt(111)-OH_{ad}

The temperature dependence of the current-potential characteristics for the OH adsorption is not as straightforward as that for the H adsorption[13]. For the coverage ~0.5 O/Pt, the OH heat adsorption is approximately 200 kJ/mol dependent of pH of the solution which is similar to the heat adsorption of H_{upd}[13]. The Pt-OH_{ad} bond energy is ~136 kJ/mol which is much less than that of Pt-O_{ad} at gas-solid interface which is ~350kJ/mol[5, 13]. DFT calculations showed that at low OH coverage (1/9 – 1/3 ML) OH binds preferentially at bridge and top sites with adsorption energy 225 kJ/mol and 15% higher when the coverage increases to be 0.5-1 ML[16].

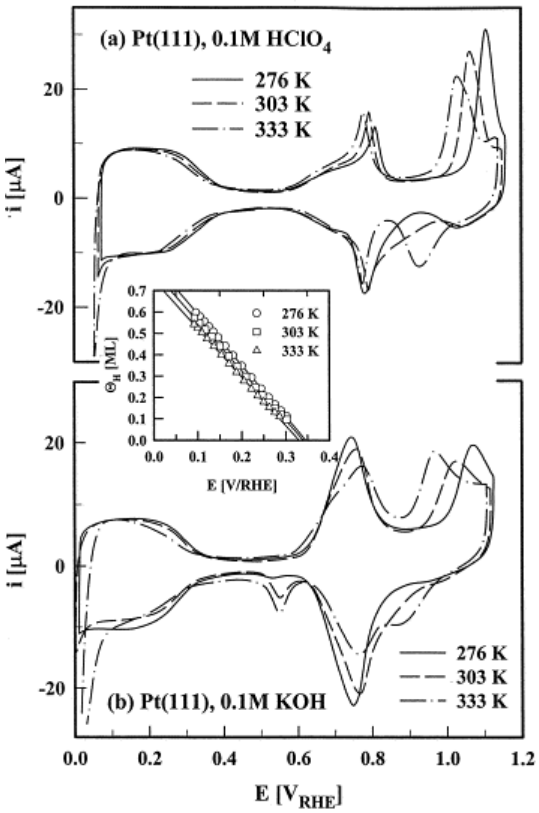

Fig. 1.4. Cyclic voltammograms of Pt(1 1 1) in (a) 0.1 M $HClO_4$ and (b) 0.1 M NaOH at various temperatures. Sweep rate 50 mV/s. Insert: potential dependent surface coverage by H_{upd} on Pt(1 1 1) in 0.1 M $HClO_4$ at 276, 303 and 333 K [13].

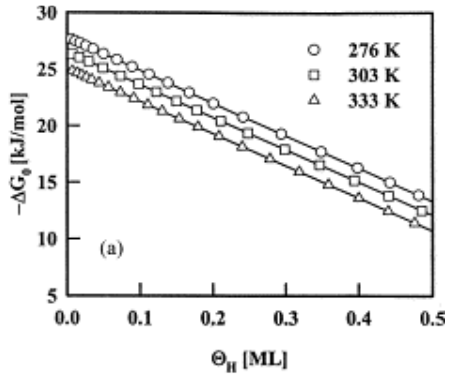

Fig. 1.5. Change of free energy of adsorption for H_{upd} on Pt(1 1 1) in 0.1 M $HClO_4$ with surface coverage of H_{upd}[13].

1.2.3.3. Pt(111) surface structure induced by H_{upd} and OH_{ad}

Surface relaxation induced by H_{upd} and OH_{ad} is measured using the interlayer spacing, Δd_{12}, and this can be performed experimentally in aqueous electrolytes using X-ray voltammetry (XRV). As seen in Fig. 1.3(b,d), the hydrogen adsorption on Pt(111) slightly expands Δd_{12} approximately by 1.5% in both H_2SO_4 and KOH and also is similar to what is observed under UHV showing small difference in the energetic between Pt-H bond in the gas-phase and in electrolyte[5]. Fig. 1.3(b,d) show no change in Δd_{12} upon adsorption/desorption of either (bi)sulfate or hydroxyl anions indicating reversible hydroxyl adsorption. Nevertheless, hydroxyl adsorption species can transform to the irreversible adsorption at high potential producing a surface roughening.

1.3. ORR on Pt(111)

Electrocatalysis involves the important phenomena occurring at the fuel cell electrode surfaces, where charge transfer reactions, and breaking or formation of chemical bonds occur. The kinetics of those processes is strongly dependent on the nature of the electrode materials and can be varied by many orders of magnitude for different electrode materials. Both the hydrogen evolution/oxidation reaction(HER/HOR) at the anode and the more complex ORR reaction at the cathode are electrochemical reactions governed by the same electrocatalytic law: while the reaction rate passes through a maximum for metals that moderately adsorb intermediates, the kinetics is very slow on metals which adsorb intermediates either strongly or weakly, i.e. the Sabatier principle [5]. Nevertheless, the establishment of comprehensive relationships between the energetic of intermediates and the kinetic rate of electrochemical reaction is difficult as a result of the complexity of surface-intermediate interactions, the presence of several different intermediate species on an electrode surface, and the effect of the modified surface by adsorption of those intermediate species.

The ORR is a very complex and important electrocatalytic reaction in fuel cell. The mechanism step reactions are still unclear. Under ORR, there is currently no electrode

material which produces a measurable current from ORR at the equilibrium potential, 1.23 V versus the normal hydrogen electrode (NHE) even for the most catalytically active materials: Pt group metals. The measurable currents are obtained only below 1 V_{NHE}, therefore, ORR kinetics study use the current density at a fixed potential e.g. 0.9 V_{NHE} as a measured of the reaction rate[5].

The ORR kinetics on Pt surfaces varies with the crystal plane and electrolyte types, illustrated in Fig. 1.6, which results from the sensitivity of the adsorption energy of the intermediate species to their site geometries [17, 18]. The order of activity for ORR in H_2SO_4 increases in the order Pt(111) < Pt(100) < Pt(110). A low activity of Pt(111) may come from strong adsorption of (bi)sulfate anion on (111) plane: (bi)sulfate anion is weakly solvated leading to direct chemical bonding with the metal surfaces[19]. Also, the ORR activity is significantly higher in H_2SO_4 than KOH electrolyte indicating that the adsorption of anion species also affects the kinetics of ORR on all three surfaces. The Pt surface in KOH electrolyte, Fig. 1.6b, is a good system to investigate the effect of OH_{ad} on ORR kinetics, since no other anions species co-adsorb with OH_{ad}. Fig. 1.6b shows that Pt(111) has the highest activity at E > 0.75, which is the potential range of dominant OH_{ad},. This may result from the structure-sensitive adsorption of OH_{ad}: the (111) surface has the lowest coverage by OH_{ad} and weakest Pt-OH_{ad} interaction among those surfaces.

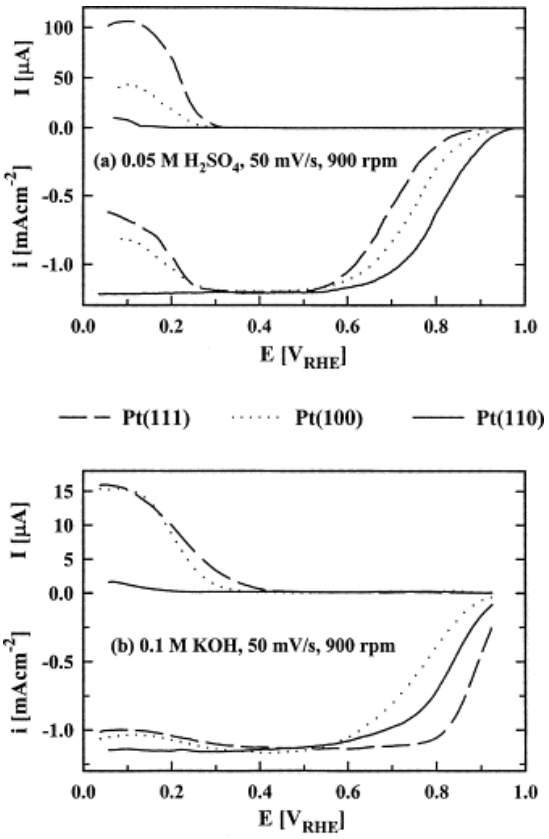

Fig. 1.6. Disk and ring (IR) currents during oxygen reduction on Pt(1 1 1) (a) in 0.05 M H_2SO_4 at a sweep rate of 50 mV/s[17]. (b) in 0.1 M KOH at a sweep rate of 50 mV/s [18].

1.4. ORR on Pt alloy surfaces

For single crystal surfaces, it is well-known that their reactivity is highly dependent on surface orientation and composition, which are affected by a number of factors such as alloy nature and preparation procedure, and environmental conditions such as electrochemical potential and pH. The relationship between bulk and surface composition of Pt-transition metal alloy catalysts has been discussed both in theoretical and experimental reports.

One of the strategies to modify the cathode catalyst toward more active, cheaper and more stable surfaces, is to alloy Pt with some cheaper 3-d metals such as Fe, Co, and Ni. These alloy surfaces have been found to have comparable and even better ORR catalytic

activity under PEM fuel cell operating conditions [20-36]. The enhancement of the ORR activity may be explained by the following effects: (i) modification of the electronic structure of 5d of Pt: changing in adsorption energy of oxygen containing species onto the Pt or alloying element (ii) change in Pt geometric properties such as Pt-Pt bond distance and coordination number (iii) leaching out of 3-d element, resulting in a rougher Pt surface and, thus higher number of active sites (iv) particle size effect (v) redox type processes involving the alloying elements [5, 31]. However, the experimental studies on activity of Pt alloy have to be analyzed very carefully, since a wide range of activity values can be obtained depending on supported catalyst due to its microstructure and/or method of preparation which affect both particle shape and size [5]. Thus, even specific activity normalized by Pt surface area may not be sufficient for comparison because catalysts particles may not have either the same size or shape as those they are compared with [5].

Recently, there are extensive researches on those Pt-alloys and in this section we review some of those works . Xiong et al. [37] investigated carbon supported PtM (M = Fe, Co, Ni and Cu) and found that PtFe and PtCo yield ordered structure whereas PtNi and PtCu have a disordered FCC structure. The ordered structure of PtFe and PtCo showed higher ORR activity compared to Pt and the disordered PtNi and PtCu in PEMFC (Fig. 1.7) and the activity increases with the extent of ordering where PtCo shows the highest activity and ordering. Pt alloys have been found to exhibit a volcano shape relationship between the catalytic activity and the Pt d-orbital vacancy, suggesting that at an optimum number of d-orbital vacancies the highest catalytic activity is obtained [20, 35, 36]. PtCo and PtFe has lower number of Pt nearest neighbors and shorter Pt-M distance than in the disordered PtNi, PtCu and Pt which may suggest a stronger d-d interaction between Pt and M atoms in the ordered PtCo and PtFe than in the disordered PtNi and PtCu. Also, the electronegativity difference in M where Fe < Co < Ni < Cu that affects the amount of charge transfer from Pt to M would be expected to increase in the order PtFe < PtCo < PtNi < PtCu. The differences in crystal structure and the electronegativity of M may

influence the Pt d-orbital vacancy resulting in favorable d-orbital vacancy in PtCo and PtFe for ORR.

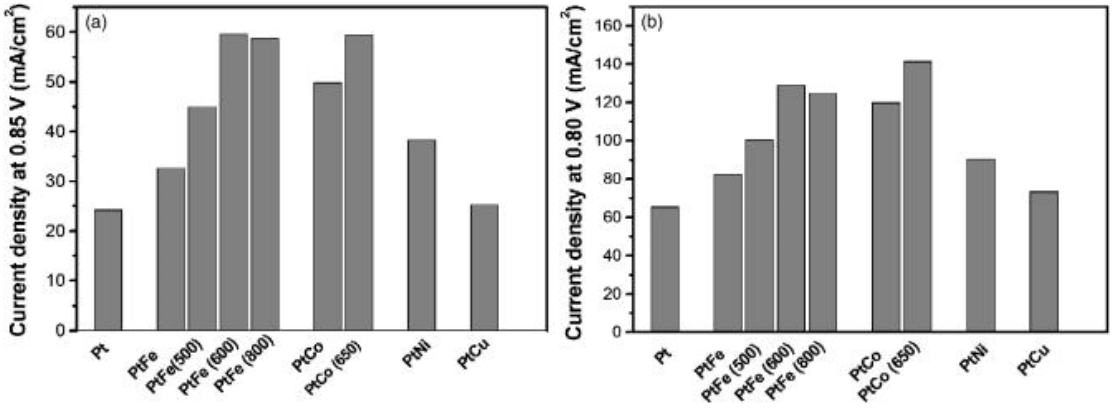

Fig. 1.7. Comparison of the current densities of the various catalysts at a given cell potential of (a) 0.85 and (b) 0.80 V in 1 M sulfuric acid at 75^{o}C. The numbers in parenthesis in the sample designations refer to the reheating temperatures [37].

There is now a consensus that Pt-Co alloys offer the enhancement in ORR activity based on both Pt mass and surface area [29]. Kho et al. [29] have investigated the correlation of structure, composition and electrochemical behavior of carbon supported Pt-Co alloy electrocatalysts for PEMFC cathode electrode (i) after catalyst preparation (ii) after preparation of Nafion-containing electrode layers and (iii) after an electrocatalyticallly stress application for ORR in 0.1 M $HClO_4$ at 25 ^{o}C. They found different structures and compositions of Pt-Co using low (600^{o}C) and high (950^{o}C) annealing temperature. The low-T catalyst exhibits one chemically ordered face-centered tetragonal (fct) phase with $Pt_{50}Co_{50}$ composition and two chemically disordered random alloys with one is face-centered cubic (fcc) Co-rich phase with $Pt_{38}Co_{62}$ composition and the other is fcc Pt-rich phase with $Pt_{85}Co_{15}$ composition. The fcc Co-rich phase suffers from severe chemical and electrochemical corrosion, but may play an important part for low-T catalysts to obtain the most ORR favorable up to 3x higher than Pt (Fig. 1.8). The high-T catalyst consists mainly of chemically ordered fct $Pt_{50}Co_{50}$ phase and with some of fcc Pt-rich

$Pt_{73}Co_{27}$ phase. Although high-T catalyst is less active than low-T catalyst (Fig. 1.8), it shows higher resistance to electrochemical corrosion. Thus, fcc Co-rich phase is desired for high activity while ordered fct phase is required for stability. Furthermore, low-T and high-T $Pt_{50}Co_{50}$ and $Pt_{75}Co_{25}$ catalysts show higher ORR activity than Pt may be caused by the delayed onset of water activation occurring at higher potential than Pt resulting in higher number of available sites.

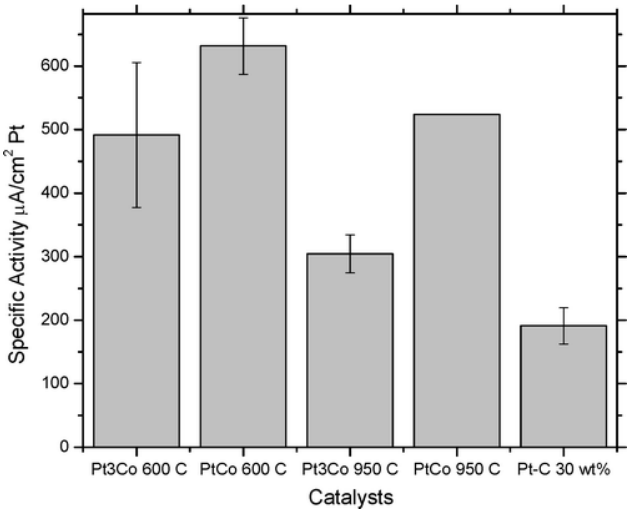

Fig. 1.8. Specific activities of the two $Pt_{75}Co_{25}$ (= Pt_3Co) alloys, the two $Pt_{50}Co_{50}$ (= PtCo) alloys, and the reference Pt electrocatalysts at 900 mV/RHE [29].

A more detailed study on Pt_3Ni has been performed by Stamenkovic et al. [26]. The study showed a remarkable higher ORR activity of Pt_3Ni which after a final annealing reveal the pure Pt surface atomic layer of Pt_3Ni (100), (110) and (111), the so-called Pt-skin structure. This surface is associated with the depletion of Pt in the next two to three atomic layers and these near-surface compositional changes results in distinctive electronic properties i.e. d-band center downshift compared to Pt. As a consequence, the chemisorption energies of oxygenated species are affected resulting in the reduction of H_{upd} and OH_{ad} coverage by 50% relative to Pt(111) leaving more active sites available, thus higher ORR activity. Fig. 1.9 shows the composition profile and cyclic

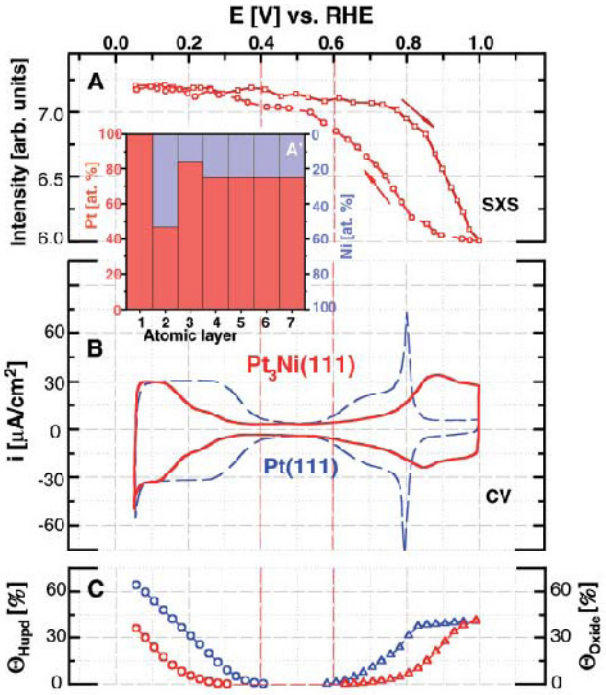

Fig. 1.9. In situ characterization of the $Pt_3Ni(111)$ surface in $HClO_4$ (0.1 M) at 333 K. (A) SXS data and (A') concentration profile revealed from SXS measurements. (B) Cyclic voltammetry in designated potential region (red curve) as compared to the voltammetry obtained from Pt(111) surface (blue curve). (C) Surface coverage calculated from cyclic voltammograms of $Pt_3Ni(111)$ (red curve) and Pt(111) (blue curve). The vertical red dot line represent potential region (from low E to high E) of H_{apd} adsorption/desorption processes, double-layer region, and region of OH_{ad} layer formation, respectively [26].

voltammmetry of $Pt_3Ni(111)$-skin and Pt(111) and corresponding H_{upd} and OH_{ad} coverage. The structure and electronic structure property sensitivity to activity is clearly shown in Fig. 1.10 in which the activity is in the order of $Pt_3Ni(100)$-skin < $Pt_3Ni(110)$-skin <<<< $Pt_3Ni(111)$-skin while Pt(100) << Pt(111) < Pt(110). In addition, the Pt-skin surfaces were also formed over Pt_3Fe and Pt_3Co after annealing at 1000 K[31]. Since 3-d metals are easier dissolved in acidic environment, Pt-skin is more stable: the topmost Pt layer protects the subsurface 3-d metal atoms from dissolution [26, 31]. Stamenkovic et al. [31] also found that the level of modification in electronic properties strongly depends on the presence of an alloying component in subsurface atomic layers (near-surface composition profile) and its nature; i.e. Pt_3Co show the highest catalytic activity

among Pt_3Fe, Pt_3Ni and Pt, thus it shows the highest value of d-band center shift from Fermi level.

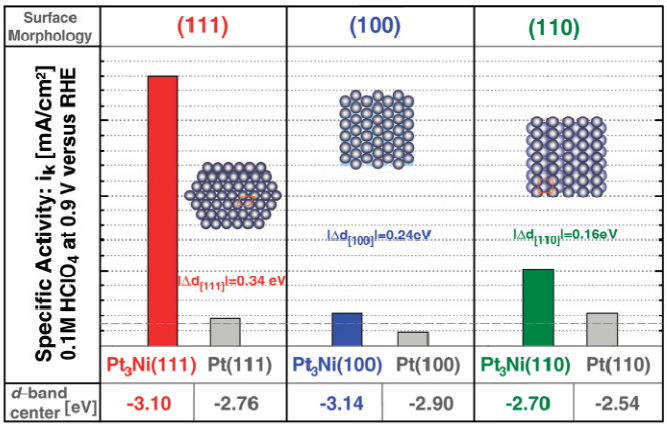

Fig. 1.10. Influence of the surface morphology and electronic surface properties on the kinetics of ORR. Rotating ring disk electrode (RRDE) measurements for ORR in $HClO_4$ (0.1 M) at 333 K (a horizontal dashed gray line marks specific activity of polycrystalline Pt) are shown [26].

Since monolayer of Pt on Pt_3Co, Pt_3Ni, Pt_3Fe alloys are evidenced to be a promising approach for a suitable cathode electrode, Vukmirovic et al.[38], Zhang et al.[39] and Nilekar et al.[27] have synthesized a new class of electrocatalyts for ORR, consisting of a monolayer of Pt or mixed monolayer of Pt and another late transition metal M (M= Ir, Ru, Rh, Au, Pd, Re and Os). They found an outstanding improvement of ORR activity (8x) on a monolayer of Pt on carbon-supported Pd nanoparticles, Pt/Pd/C, over Pt/C (Fig. 1.11) and suggested that the enhancement is caused by a decrease in the coverage of Pt-OH, consequently, a delayed oxidation of Pt in Pt/Pd/C. Because Pd is more easily oxidized than Pt, Pd-OH is formed easier then Pt-OH suppressing Pt-OH formation by Pt-OH and Pd-OH repulsion, thus a delayed oxidation on Pt. In order to broaden this Pt-OH repulsion perspective, they performed the experiment on $(M_{0.2}Pt_{0.8})$/Pd/C (M= Ir and Re). As shown in Fig. 1.12 and 1.13, both mixed metal monolayers have higher activity than that of Pt/C. In the case of Ir–Pt mixed monolayers a decrease in Pt–OH is achieved

in repulsion between Ir–OH and Pt–OH, while in Re–Pt case decrease in Pt–OH is achieved by repulsion between Re–O and Pt–OH because Re is covered with O rather than OH. They also indicated that the reduction of OH coverage on Pt is even greater by the presence of M-O than M-OH at lower potential than Pt-OH formation (E > 0.4 V), therefore, the second M metal used is important. Despite, a large improvement of ORR activity, the long-term durability of these new electrocatalysts still needs to be investigated.

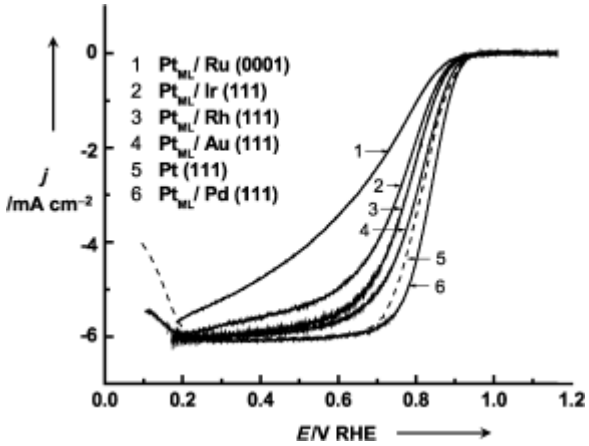

Fig. 1.11. Polarization curves for O_2 reduction on Pt monolayers supported on Ru(0001), Ir(111), Rh(111), Au(111), and Pd(111) in a 0.1 M $HClO_4$ solution on a disk electrode[39].

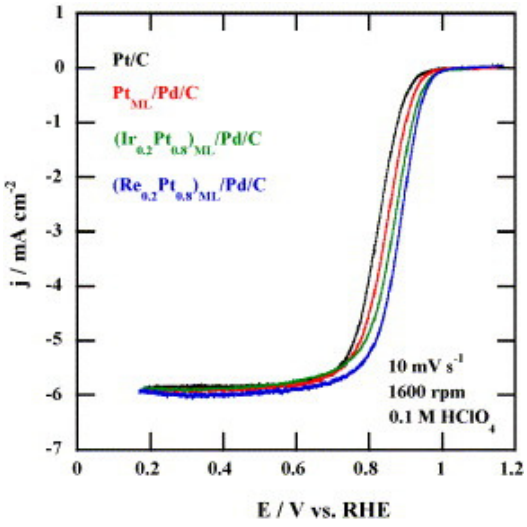

Fig. 1.12. Comparison of polarization curves for the ORR on Pt/C (10 nmol), PtML/Pd/C, $(Ir_{0.2}Pt_{0.8})$ML/Pd/C, and $(Re_{0.2}Pt_{0.8})$ML/Pd/C (20 nmol Pd) nanoparticles. The electrode geometric area is 0.164 cm^2 [38].

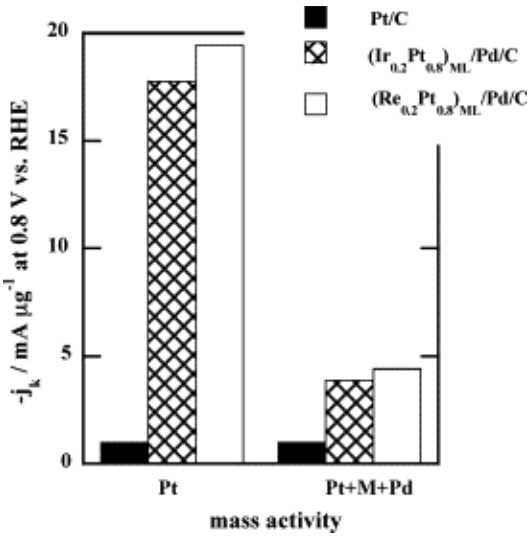

Fig. 1.13. The Pt and total noble metal mass activities of Pt/C (10 nmol), $(Ir_{0.2}Pt_{0.8})$ML/Pd/C, and $(Re_{0.2}Pt_{0.8})$ML/Pd/C (20 nmol Pd) nanoparticles for the ORR expressed as a current at 0.8 V [38].

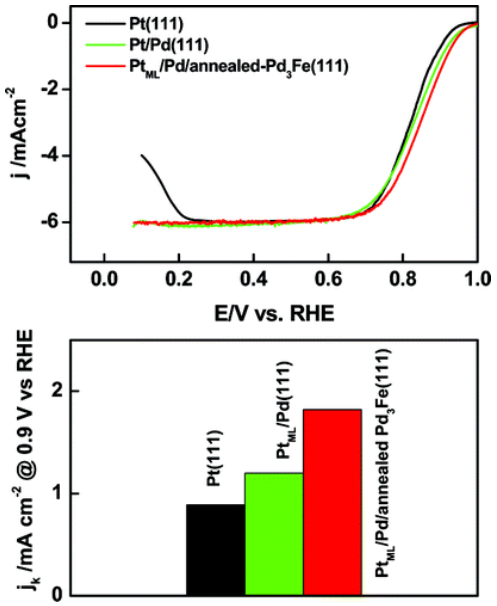

Fig. 1.14. Comparison of the ORR activity between Pt(111), Pt/Pd(111) and Pt/Pd/annealed Pd_3Fe. (a) Polarization curves for the ORR on a Pt monolayer covered annealed-Pd_3Fe(111) (red), annealed-Pd(111) (green), and Pt(111) surfaces (black) in oxygen-saturated 0.1 M $HClO_4$ at room temperature. Inset shows the bar plot for the comparison of ORR specific activities of the corresponding three surfaces at 0.9 V_{RHE} [40].

Another promising candidate to replace the use of conventional Pt catalysts for ORR is Pd-M (M= Co or Fe) [40, 41]. Zhou et al.[40] have demonstrated that the pure Pd formed on the high-temperature (800-1200 K) on Pd_3Fe(111), and annealed Pd_3Fe(111) provided a comparable ORR activity to Pt(111) as these surfaces show a downshift in the surface atoms d-band center causing weaker oxygen-containing species adsorption, thus decreasing the coverage of those species on the surface and facilitating O/OH removal process. It also showed a positive shift of the onset of the surface oxidation relative to Pd(111). However, the surface is unstable under acidic environment due to leaching out of the M metal and this may be caused the high ORR activity resulting from increased surface area enriched with noble metals. Therefore, the Pt monolayer was introduced on this structure to improve the stability and protect the unique surface property of Pd alloy materials. As seen in Fig. 1.14, the ORR activity is higher than Pt(111) and Pt/Pd(111). Zhou et al.[40] described the ORR acitivity enhancement is

caused by weakening OH binding energy (destabilization of OH) on Pt/Pd/annealed Pd_3Fe (OH binding energy on Pt(111), Pt/Pd(111) and Pt//Pd/annealed Pd_3Fe are -2.09, -2.07 and -1.93, respectively).

CHAPTER II

THEORETICAL STUDIES ON GEOMETRIC AND ELECTRONIC EFFECTS IN METAL/ALLOY CATALYSTS

A solid catalyst surface has three closely coupled functions under a chemical reaction: (i) it adsorbs the reactants and cleaves the required bonds (ii) it holds the reactants so that the reaction can proceed and (iii) it lets the products desorb back into the surroundings [42]. It is essential to develop and understanding of the differences in reactivity on one metal element and another and to be able to extend the understanding for alloy systems leading to a key to categorize good and bad catalysts for a specified reaction. In general, there are two main factors which determine the reactivity in heterogeneous catalysis: (i) geometrical effect and (ii) electronic effect [42]. In this chapter, we discuss these two effects.

2.1. Chemisorption

The electronic properties play a very important role on the trends in adsorption energies on transition metal surfaces. A simple model of d band can be used to describe interaction between adsorbate and metal surface [43]. A one-electron state for an adsorbate outside a metal surface will interact with all the valence states of the surface atoms and these states forming one or several bands of states [43]. The occupancy of the d bands varies along the transition metals as the shift through the Fermi level. Since the d bands are narrow, the interaction of an adsorbate state with the d states of a surface atom producing bonding and antibonding states for adsorbate state after interaction with narrow d bands [43]. As illustrated in Fig. 2.1, when the band is low and broad, the band is limited with a single resonance at the bottom of the band (often called weak chemisorptions) but as the d band center, ε_d, shifts up an antibonding state appears above the Fermi level (referred to strong chemisorptions) and the bond becomes increasingly stronger as the number of empty antibonding states increases [43].

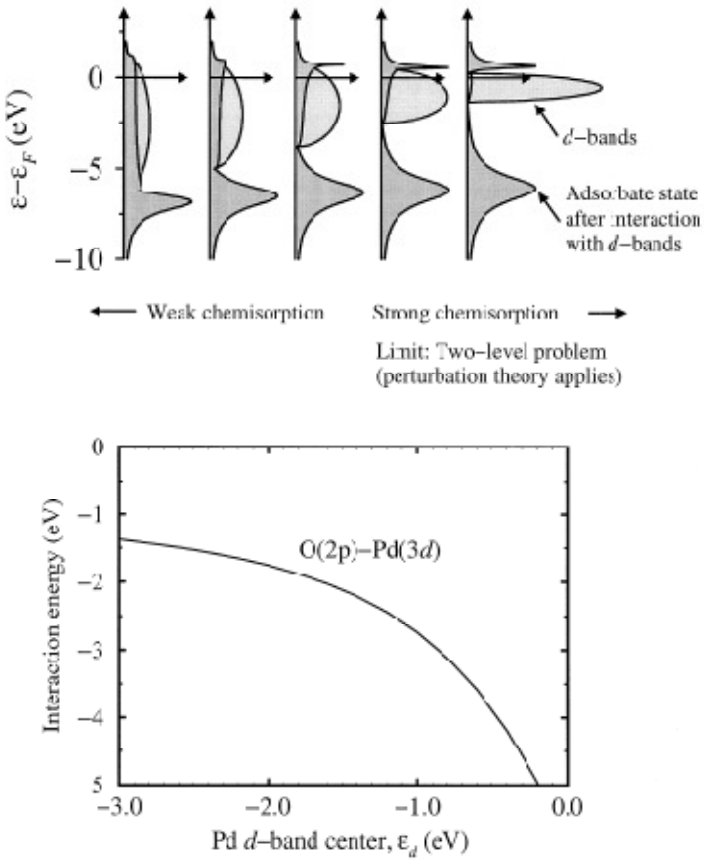

Fig. 2.1. The local density of states projected onto an adsorbate state interacting with the *d* bands at a surface. The strength of the adsorbate–surface increases as the center of the *d* bands ε_d is shifted up toward the Fermi energy ($\varepsilon_F = 0$) and the width *W* of the *d* bands is decreased to keep the number of electrons in the bands constant. As ε_d shifts up, the antibonding states are emptied above ε_F and the bond becomes stronger (bottom) [43].

DFT calculations have shown very good agreement on atomic adsorption energy with the experimental results considering Pt(111) for example. Fig. 2.2 shows the geometry of ordered p(2x2) oxygen adsorption on Pt(111) at 0.25 ML coverage. It clearly shows the agreement between calculated bond length and relaxation parameters and those obtained from the experiment and the deviation of calculated heat of adsorption from the experimental result is 0.28 eV [43]. The bond formation for atomic oxygen adsorption takes place in two steps: first, the oxygen valence 2p state interacts with the metals electrons giving rise to a single resonance completely filled and well below the Fermi

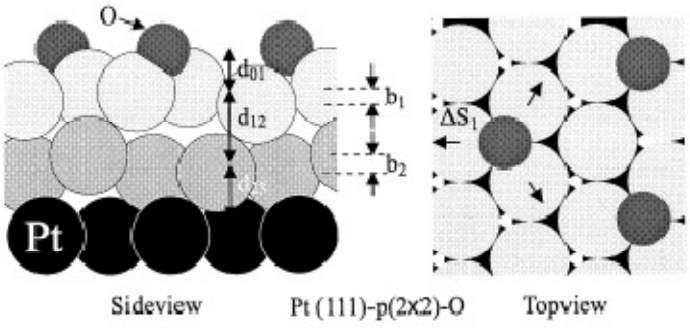

	Experiment	Theory
d_{01}	1.18 Å	1.21 Å
$(d_{12}- d)/d$	1.3 %	0.6 %
$(d_{23}- d)/d$	0.0 %	-0.1 %
b_1/d	3.1 %	3.5 %
b_2/d	4.0 %	3.9 %
$\Delta S_1/S_1$	1.6 %	2.9 %

Fig. 2.2. The experimental and theoretical (PW91) equilibrium structure of the Pt(111)– p(2x2)–O system [43, 44].

level and second, the coupling to the d electrons, giving rise to a splitting of the oxygen resonance into two states of d states bonding and antibonding [43]. Since the contribution from the coupling to metal s states is approximately the same for each of metals, the main trends in the chemisorptions should be given by the coupling to the d electrons characterized by the band center i.e. as the d band center is closer to the Fermi level, the adsorption energy to atomic adsorbates weakens [43, 45, 46]. Another analysis considers the contribution from the interaction between the metal, which have filled d band (such as Cu, Ag and Au) and the oxygen 2p states, they have to become orthogonal when they come into contact due to the Pauli principle. This raises the kinetic energy by an amount that is approximately proportional to the square of the adsorbate-metal d coupling matrix element V_{ad}^2: the stronger the overlap, the larger the repulsion and weaker adsorption energy [43]. The absolute magnitude of V_{ad}^2 depends on the metal, the adsorbate and adsorbate's position and can be considered as a property of a metal when the adsorbate and adsorbate's position are fixed [43]. The first model (d-band

center) should be expected of all simple atomic adsorbates with a filled valence level (after interaction with the metal s band) such as H, C, N, F, S and Cl and the latter model (adsorbate-metal d coupling matrix element) should hold for electronegative adsorbates, such as O, the halogens, H and S with deep-lying valence states after coupling with the metal sp states [43].

The adsorption of molecules is similar to the atomic adsorption but there is a slight complication arising from several adsorbate valence states which is important for the interaction with surface, however, the same electronic structure concept as explained above can be applied [43]. There may be a crossover between atomic adsorption and molecular adsorption somewhere (the dissociation occurs) in the group of transition metal depending on the transition metal row (i.e., the metal nobleness) and the adsorbed molecules [43].

Moreover, since the surface coverage of reactants, intermediates and products is varied along the reaction coordinate, reaction conditions and sometimes the coverage is large, the interactions between adsorbates are significant as well. Either attractive or repulsive interactions are possible and lead to different results. The attractive interaction causes the adsorbates prefer to cluster together and can lead to the island formation even at low coverage [43]. The repulsive interaction is more common and may result in adsorbate overlayer dispersion and generally induces surface reconstruction[43]. Dipole-dipole interaction is another adsorbate-adsorbate interaction that should be considered. Also, the metal surface electronic structure can be changed after the first adsorbate adsorption affecting the adsorption of the next adsorbate to be weaker or stronger than on the clean surface. All of those variations ultimately affect the reactivity of a surface.

2.2. Structure sensitivity to the reactivity

Although the electronic and geometric effects are not independent causing the change in reactivity, it is useful to consider them independently. Some factors of the geometric effect are discussed in the following subsections.

2.2.1. Strain

Surface strain can offer a mean of evaluating the magnitude of the electronic effect [43]. When a surface undergoes compressive or tensile strain, the overlap of metal d states at neighbor sites will either increase or decrease and so the d bandwidths and the d bands will change to maintain a constant filling. Thus, compressive or tensile strain leads to the downshift and upshifts of the d band centers, respectively, as illustrated in Fig. 2.3 [43]. The higher the energy of the d bands, the more likely antibonding of metal-adsorbate d states are to be moved further above the Fermi level and the more likely the metal-adsorbate d interaction is to become net attractive. Fig. 2.4, shows the effects of the variation in d band centers of Pd over Re(0001), Ru(0001) and Au(111) in which the substrate induced the change in the lattice constant. Pd/Au(111) is more reactive than Pd(111) because the Au lattice constant is bigger than that of Pd, however, while Pd and Re have similar lattice constant, the shift of Pd/Re(0001) is primarily caused by the interaction between the electrons of Pd and its substrate Re(0001)[47]. Nevertheless, the change in d band center still captures the reactivity trend.

For nanosized supported catalysts, two factors play a role: (i) the surface tension which tends to decrease the lattice constant and (ii) the interaction with the support which may either increase or decrease the lattice constant [43]. The effect of surface tension and strain caused by the oxide support is less pronounced with the increase of particle size[43].

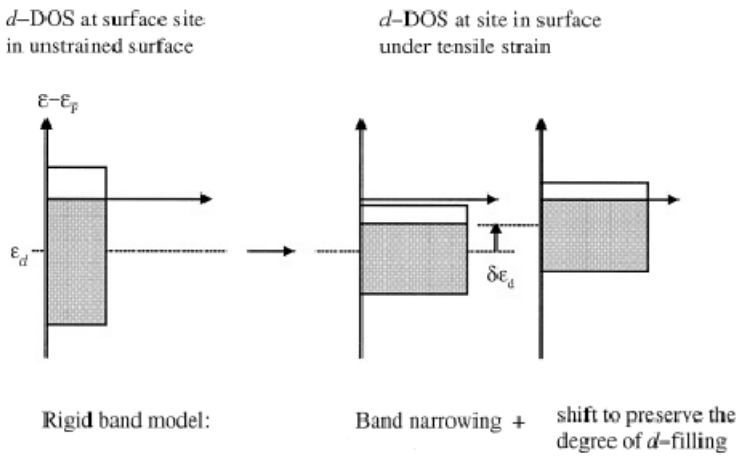

Fig. 2.3. The effect of tensile strain on the d band center. Increasing the lattice constant shrinks the band width, and, to keep the number of *d* electrons fixed, the *d* states have to move up in energy[43].

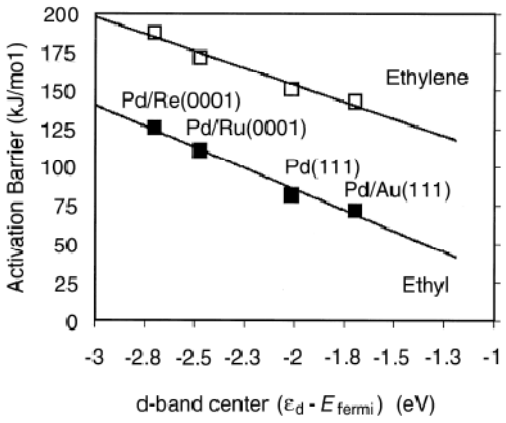

Fig. 2.4. Variations in the transition state energy for dehydrogenation of ethylene and of ethyl on Pd(111) and on palladium overlayers on various other metals. The variations in activation energy correlate well with the variations in the *d* band centers for the surface palladium atoms [47].

2.2.2. Surface facets

Although the local chemisorption configuration of adsorbates can be the same on different surface facets, the chemisorption energy can be varied due to primarily to the change in electronic structure (i.e. the d band centers) between the facets. Fig. 2.5 clearly

shows the correlation between chemisorption energy and activation energy versus the d band center on different surface facets.

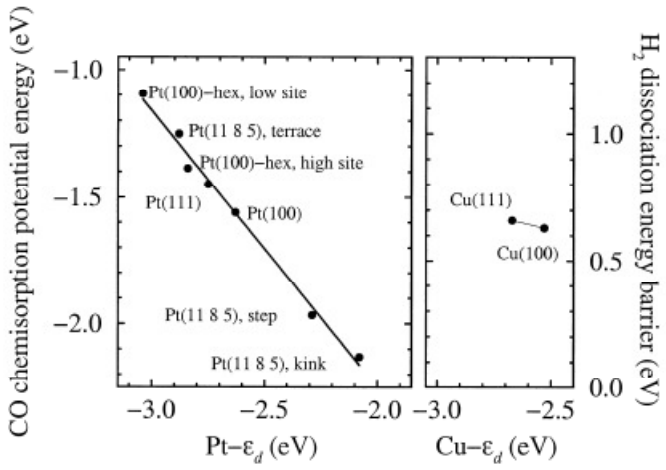

Fig. 2.5. Calculated variations in the chemisorption energy (PW91) for CO adsorbed atop platinum atoms in different surroundings. (Right) DFT energy barriers (PW91) for dissociative adsorption of H_2 atop copper atoms in two different copper surfaces. The correlation between chemisorption energy and the *d* band center for the relevant platinum atoms is evident [43, 48, 49].

2.2.3. Steps and defects

The high-Miller-index surfaces with defects such as steps, kinks, adatoms or vacancies induce higher variation in the electronic structure (i.e., the d band center). When the surface defects change the coordination number of the surface atoms to be smaller, the d band width is smaller and thus the d band center moves to higher energy [43]. The change in electronic structure due to defects may change the site preference of atomic adsorbates to be at the step (i.e., at the step edge, the lower coordination number of the surface atoms leads to energetically higher d band center and hence to higher reactivity) [43]. Fig. 2.5(left) also illustrates the influence of surface step and kink on the change of CO chemisorption energy on Pt. Furthermore, the barrier energy may be reduced when the reaction occurs at the step surface as the site helps to stabilize the transition state

complex [50, 51]. When the reactant molecules coordinate to more surface atoms, the total coupling matrix element between metal d states and adsorbate valence states increases, consequently, the indirect repulsion between the reaction products is reduced [43]. However, it should be noted that this may still lead to a higher barrier energy for certain elementary steps if the reactant species of this step are more stabilized than the transition state.

The smaller the particle size, the more pronounced the structure-sensitivity effects are because the ratio of the different facets and the density of steps and other defects will be strongly dependent on particle size [43]. Nevertheless, the strain effect plays a very important role as well.

2.3. Alloying

Alloying simultaneously changes the electronic structure (i.e., the d band center) of the alloy surface from that of the pure metallic surface alone. The effect of alloying may come from the segregation phenomena causing the difference in bulk lattice parameters of the alloy and the surface-induced strain effect in the surface. Many alloy and overlayer systems discussed in the previous chapter are examples of the influences of alloying on ORR reactivity and stability. Furthermore, the Pt-skin and Pt-skeleton surfaces may be the cases that allow alloying show the best benefit for ORR catalysis in which the Pt-skin or Pt-skeleton surfaces protects the subsurface transition metals atoms from further dissolution. Also, the segregation of Pt forming Pt-skin create a unique subsurface layer composition profiles directly influence the electronic and geometric structure of skin and skeleton which were found to be different. Stamekovic et al. [52] showed the relationship between the d-band center and ORR activity (Fig. 2.6) on (a) Pt-skin and (b) Pt-skeleton forms on different Pt_3M alloys. The volcano-type relation was displayed with Pt3Co at the maximum activity for both surfaces. When the d-band center is too close to the Fermi level (i.e. metals surfaces binds too strongly with oxygen and ORR intermediates), the catalytic activity is limited by the free surface active site availability while the ORR is difficult to proceed when the d-band center is too far from

the Fermi level (i.e. metals surfaces binds too weakly with oxygen and ORR intermediates). Therefore, the good catalyst should be well-balanced between those two opposing effects. However, it should be emphasized that the catalytic activity is not solely dependent on the d-band center; it also depends on the morphology of the alloy surface (i.e. geometrical effect).

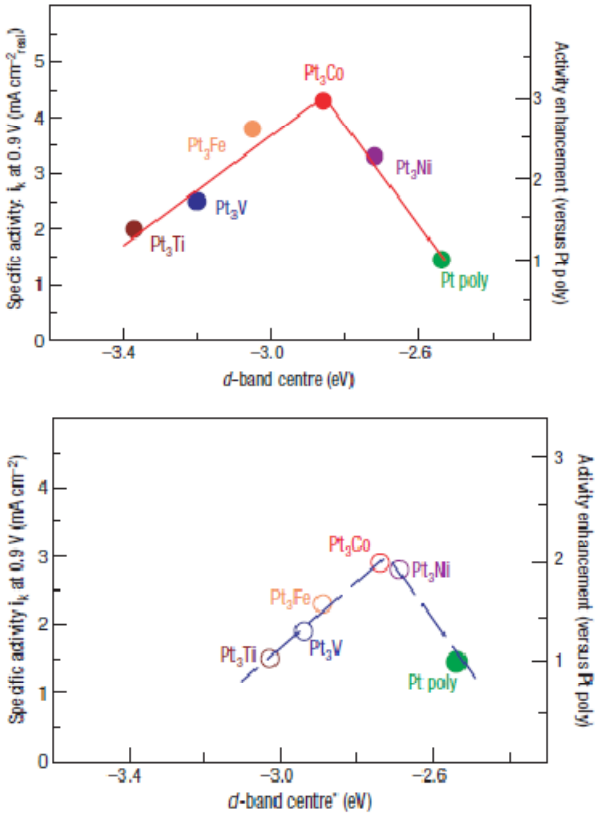

Fig. 2.6. Relationships between the experimentally measured specific activity for the ORR on Pt_3M surfaces in 0.1M $HClO_4$ at 333 K versus the *d*-band centre position for the (a) Pt-skin and (b) Pt-skeleton surfaces of Pt_3M alloys[52].

In addition, it is known that the variation in the center of d bands for metal overlayers is accompanied by a similar variation in the surface core level shifts [53-55]. The surface core level shifts can be viewed as a measure of the variation in the d band center [43].

Rodriguez and Goodman [56] showed an outstanding example of a strong correlation between the surface core level shift of metallic overlayers and the CO chemisorptions energy on these overlayers. Since the metallic overlayer can be caused by the preference of one metal to segregate to the surface over another metal, thus controlling the surface composition and influencing the electronic structure, segregation process does not only involve the reactivity but also the stability property as well.

CHAPTER III

INTRODUCTION TO DENSITY FUNCTIONAL THEORY

3.1. Fundamentals

Density Functional Theory (DFT) is a computational method that derives properties of the molecule based on a determination of the *electron density* of the molecule. DFT differs from the pure ab initio method, where the energy of the molecule and all of its derivative values depend on the determination of the wavefunction. The *wavefunction* is not a physical reality but a purely mathematical construct while the electron density is a physical characteristic of all molecules. Even though the wavefunction does not exist as a physical, observable property of an atom or molecule, the mathematical determination of the wavefunction (and with it, the atomic and molecular orbitals) has been a good predictor of energy and other actual properties of the molecule. Because of the remarkable work by Llewellyn Thomas and Enrico Fermi who were able to determine that there was a one-to-one correspondence between the electron density of a molecule and the wavefunction of a molecule with multiple electrons, thereby the density functional theory was formulated. Several major advantages of DFT is that first, it is based on a property that exists in real molecules, not purely mathematical terms, second the density depends only on the x-y-z coordinates of the individual electron while the wave function becomes more mathematically complicated as the number of electrons increases and as a result DFT calculations can be faster with better accuracy. However, some major approximations have to be made in DFT which affect the accuracy of molecular properties that are evaluated with DFT methods.

The fundamental underlying mathematics of this method is the *functional*. In mathematical terms, a function is denoted as $y = f(x)$. A functional is a function of a function denoted as $y = F[f(x)]$. It means the value of y is in and of itself dependent on another function. In the DFT method, the energy of the molecule is a *functional* of the electron density. The electron density is a function which depends on three variables: the

x-y-z coordinates corresponding to the electron positions. The *functional (F)* of the electron density gives the energy of the molecule. Regardless of the number of electrons, the electron density functional is always only dependent on those three variables, x-y-z.

$$\text{Electron density} = \rho(x,y,z) \quad (3.1)$$

$$\text{Energy} = F[\rho(x,y,z)] \quad (3.2)$$

In order to find the value of the functional F, some approximations are made. This is one of the reasons why there are so many different DFT methods which mean there are many ways of approximating the functional.

In the 1960s, Hohenberg and Kohn were able to use the Thomas-Fermi theorem to develop a more detailed version of the theory. The Kohn and Sham theory describes the mathematics of electron densities and their subsequent correlations to molecular energies can be shown in the simplest form following;

$$E_{DFT}[\rho] = T[\rho] + E_{ne}[\rho] + J[\rho] + E_{xc}[\rho] \quad (3.3)$$

where E is the energy, T is the kinetic energy of the electrons, E_{ne} is the nuclear-electron attraction(Columbic energy), J is the electron-electron repulsive (Columbic) energy, and E_{xc} is the electron-electron exchange-correlation energy. Each of these terms is a function of electron density, ρ, which is itself a function of x-y-z electron coordinate. Therefore, T, E_{ne}, J, and E_{xc} is a functional. The E_{xc} is the one that causes the most concern in DFT calculations. The E_{xc} functional addresses how an electron in an atom or molecule interacts with another electron. It is related to the Pauli Exclusion Principle, which states that no two electrons can occupy the same energy state.

Methods in DFT are complicated and diverse, but generally can be divided into three classes;

1. Methods that use *Local density approximation (LDA).* The LDA is determined solely based on the properties of the electron density. The most important assumption of LDA is that for a molecule with many electrons in a gaseous state, the density is uniform

throughout the molecule. The approximation, however, does not work well with electronic band structures of solids.

2. Methods that apply a gradient correction factor. The gradient accounts for the non-uniformity of the electron density and as such is known as *gradient-corrected*.

3. Methods that are a combination of a Hartree-Fock approximation to the exchange energy and a DFT approximation to the exchange energy, all combined with a functional that includes electron correlation. They are known as *hybrid* methods.

3.2. The Hohenberg-Kohn theorems[57, 58]

Theorem 1. The ground-state energy from Schrödinger's equation is a unique functional of the electron density. This theorem states that there exists a one-to-one mapping between the ground-state wave function and the ground-state electron density.

Theorem 2. The ground-state energy can be obtained variationally: the electron density that minimizes the total energy is the exact ground-state electron density corresponding to the full solution of the Schrödinger's equation.

The energy functional can be written as,

$$E[\{\psi_i\}] = E_{known}[\{\psi_i\}] + E_{xc}[\{\psi_i\}] \tag{3.4}$$

$$E_{known}[\{\psi_i\}] = -\frac{\bar{h}}{m}\sum_i \int \psi_i^* \nabla^2 \psi_i d^3r + \int V(r)n(r)\, d^3r + \frac{e^2}{2}\iint \frac{n(r)n(r')}{|e-r'|} d^3r\, d^3r + E_{ion} \tag{3.5}$$

The difficulty to solve the Schrödinger's equation was solved by Kohn and Sham who showed that the task of finding the right electron density can be expressed in a way that involves solving a set of equations in which equation only involves a single electron.

The Kohn-Sham equations have the form,

$$\left[-\frac{\bar{h}}{2m}\nabla^2 + V(r) + V_H(r) + V_{XC}(r)\right]\psi_i(r) = \varepsilon_i\psi_i(r) \qquad (3.6)$$

The solutions of the Kohn-Sham equations are single-electron wave functions that depend on only three spatial variables $\psi_i(r)$. The first potential term, V(r), defines the interaction between an electron and the collection of atomic nuclei. The second term, $V_H(r)$, is called the Hartree potential which described the Coulomb repulsion between the electron being considered in the equation and the total electron density defined by all electrons in the problem. The Hartree potential includes the self-interaction contribution because the electron being described in the equation is also a part of the total electron density. The self-interaction is unphysical and the correction for it is one that is included into the final potential, $V_{XC}(r)$. To solve the equation, it is usually an iterative way as outlined[58];

1. Define an initial guess of the trial electron density, n(r).
2. Solve the Kohn-Sham equations defined using the trial electron density to find the single-electron wave functions, $\psi_i(r)$.
3. Calculate the electron density defined by $\psi_i(r)$ given from step 2, $n_{KS}(r) = 2\sum_i \psi_i^*(r)\psi_i(r)$.
4. Compare the calculated, $n_{KS}(r)$, with the trial electron density, n(r). The ground-state electron density is obtained when both electron density are the same, then the total energy can be computed. If the two electron densities are different, then the trial electron density must be updated in some way and the procedure is repeated.

3.3. Exchange-Correlation functional

Local Density Approximation (LDA), the exchange-correlation potential is set at each position to be the known exchange-correlation potential from the uniform electron gas at the electron density observed at that position, $V_{XC}(r) = V_{XC}^{\text{electron gas}}[n(r)]$.

Generalized Gradient Approximation (GGA) uses the local gradient in the electron density. There are many GGA functionals. The most widely used functionals in calculations involving solids are the Perdew-Wang functional (PW91) and the Perdew-Burke-Ernzerhof functional (PBE)[58]. Different functionals can give different results, thus it is necessary to indicate the functional applied in a particular DFT calculation.

3.4. Well-converged DFT calculations[58]

In this part, the factors which are required to perform well-converged DFT calculations are discussed and emphasized in applying DFT calculations to solids which atoms periodically arrange in space. A well-converged DFT calculation is one in which the numerically derived solution accurately approximates the true solution of the mathematical problem posed by DFT with a specific exchange-correlation functional.

3.4.1 Plane Waves, the Brillouin Zone and k points

In a supercell, the shape of the cell that is repeated periodically in space, with lattice vectors; a_1, a_2 and a_3, the solution of the Schrödinger's equation for this periodic system must satisfy a fundamental property known as Bloch's theorem. The Bloch's theorem states that the solution can be expressed as a sum of terms with the form

$$\phi_k(r) = \exp(ik \cdot r)\, u_k(r) \qquad (3.7)$$

where $u_k(r)$ is periodic in space with the same periodicity as the supercell. That is, $u_k(r + n_1a_1 + n_2a_2 + n_3a_3) = u_k(r)$ for any integers n_1, n_2, n_3. It means that it is possible to solve the Schrödinger's equation for each value of k. Similarly, it also applies to electron density which is the quantity derived from solutions to the Schrödinger's equation. Many parts of the mathematical problems posed by DFT are more convenient to solve in terms of k rather than r. The functions, $\exp(ik \cdot r)$ is called plane waves and the space vector k is called reciprocal space (or k space) and the calculations refer to this idea call plane-wave calculations. The reciprocal lattice vectors can be defined in terms of lattice vectors in real space as,

$$b_1 = 2\pi \frac{a_2 \times a_3}{a_1 \cdot (a_2 \times a_3)} \quad (3.8)$$

$$b_2 = 2\pi \frac{a_3 \times a_1}{a_2 \cdot (a_3 \times a_1)} \quad (3.9)$$

$$b_3 = 2\pi \frac{a_1 \times a_2}{a_3 \cdot (a_1 \times a_2)} \quad (3.10)$$

A primitive cell as being the supercell must be determined. A supercell can be defined as that which contains the minimum number of atoms necessary to fully define a periodic material with infinite extent. In other words, a cell that is minimal in terms of volume but still contains all the information of the periodic system is called Wigner-Seitz cell. A primitive cell in k space has many special properties which is called the Brillouin Zone (BZ). The BZ is an important property in the band theory of solid state physics and also so important in plane-wave DFT calculations as a great deal of the work can be reduced to evaluating integrals of the form

$$\bar{g} = \frac{V_{cell}}{(2\pi)^3} \int_{BZ} g(k) dk \quad (3.11)$$

The key features of this integral are that it is defined in k space and that it integrates only over the possible values of k in the BZ. The accuracy of the integral evaluation significantly depends on the applied numerical methods, numbers of discrete points and appropriate weighting for each point. Because such integrals consume so much of the computational time, the balance between efficiently accuracy and computational time must be considered. Most DFT packages offer the option of choosing k points based on widely used method developed by Monkhorst and Pack in 1976. In general, the higher number of k points, a well-converged result is obtained but the higher total computational time is required. Thus, the appropriate k points number should be chosen.

3.4.2 Energy cutoffs

The Bloch's theorem tells that the solution of the Schrödinger's equation for a super cell has the form of equation (3.7). The periodicity of $u_k(r)$ means that it can be expanded in terms of a special set of plane waves as,

$$u_k(r) = \sum_G c_G \exp\,[iG \cdot r] \qquad (3.12)$$

where the summation is over all vectors defined by $G = m_1b_1 + m_2b_2 + m_3b_3$ with integer values for m_i. Combining equations (3.7) and (3.12) we get,

$$\phi_k(r) = \sum_G c_{k+G} \exp\,[i(k+G)r] \qquad (3.13)$$

This function appears to have a simple interpretation as solutions of the Schrödinger's equation: they are solutions with kinetic energy,

$$E = \frac{\bar{h}^2}{2m}|k+G|^2 \qquad (3.14)$$

The results with lower energies are more physically important than those at higher energies, therefore, the summation over an infinite number of possible values of G in equation (13) can be approximated including only solutions with kinetic energies less than some value called the cutoff energy, E_{cut}.

$$E_{cut} = \frac{\bar{h}^2}{2m} {G_{cut}}^2 \qquad (3.15)$$

One of the key points in DFT calculations is that in order to compare the DFT calculated energy differences, the same cutoff energy should be used in all calculations.

3.5. Pseudopotentials [57, 58]

Electrons in matter can be broadly categorized into two types - *core* electrons, which are strongly localized in the closed inner atomic shells, and *valence* electrons, which exist outside the core. Unfortunately, a plane-wave basis set is generally not suitable for describing core electron wavefunctions since a prohibitively large number would be required to accurately describe the oscillations in the core regions which maintain orthogonality between valence and core electrons. As a result, all-electron plane-wave calculations demand a huge computational expense that is simply not practical. However, by realizing that the electronic structure of the core-electrons remains largely

unchanged in different chemical environments, and is also of minimal interest generally, the problems relating to the core-electrons can be overcome by the use of the pseudopotential approximation. The approach concept is to replace the electron density from a chosen set of core electrons with a smoothed density chosen to match various important physical and mathematical properties of the true ion core. The properties of the core electrons are then fixed in this approximate fashion in all subsequent calculations; this is the frozen core approximation. The pseudopotential approximation replaces the strong ionic potential, $\nu_{ion}^{\text{all-elec}}(r)$, in the core region, by a weaker pseudopotential, $\nu_{ion}^{\text{pseudo}}(r)$. The corresponding set of pseudo-wavefunctions, $\psi^{\text{pseudo}}(r)$, and the all-electron wavefunctions, $\psi^{\text{all-elec}}(r)$, are identical outside a chosen cutoff radius, r_c, and so exhibit the same scattering properties, but $\psi^{\text{pseudo}}(r)$ does not possess the nodal structure that cause the oscillations inside r_c, which means they can now be described with a reasonable number of plane-waves. A schematic illustration of the pseudopotential concept is shown in Fig. 3.1.

The details of a particular pseudopotential define a minimum energy cutoff that should be used in calculations including atoms associated with that pseudopotential. Pseudopotentials requiring high cutoff energy is said to be hard and soft for the opposite. The most widely used pseudopotential is based on work by Vanderbilt called ultrasoft pseudopotentials. One disadvantages of using ultrasoft pseudopotentials is that the construction of the pseudopotential for each atom requires a number of empirical parameters to be specified. Another frozen core approach that avoids some of the ultrasoft pseudopotentials disadvantages is the projector augmented-wave (PAW) method introduced by Blöchl and later adapted for plane-wave calculations by Kresse and Joubert. The PAW method has shown to give more reliable results for small molecules and extended solids than the ultrasoft pseudopotentials method.

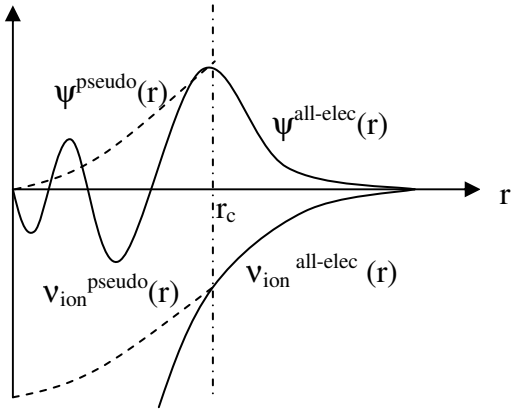

Fig. 3.1. A schematic illustration of the pseudopotential concept. The solid lines show the all-electron wavefunction, $\psi^{\text{all-elec}}(r)$, and ionic potential, $\nu_{\text{ion}}{}^{\text{all-elec}}(r)$. The dashed lines show the corresponding pseudo-wavefunction, $\psi^{\text{pseudo}}(r)$, given by the pseudopotential, $\nu_{\text{ion}}{}^{\text{pseudo}}(r)$. All quantities are shown as a function of distance, r, from the atomic nucleus. The cutoff radius, r_c, indicates the point beyond which the all-electron and pseudo quantities become identical.

CHAPTER IV

SURFACE ATOMIC DISTRIBUTION AND WATER/ATOMIC OXYGEN ADSORPTION ON Pt-Co ALLOYS*

In this chapter, we present the results and discussion in our investigation on surface atomic distribution and adsorption of water and atomic oxygen on Pt-Co alloys.

4.1. Introduction

In Chapter I we described several challenges of the PEM fuel cells on cathode catalysis. Alloying Pt with cheaper 3d metals such as Fe, Co, and Ni has shown comparable and even better ORR catalytic activity under PEM fuel cell operating conditions[21, 22, 26, 30, 31]. In Chapter I, we also briefly reviewed the experimental results regarding several potential metal catalysts for the ORR. Pt-Co alloy is one of them showing promising reactivity and stability results. For the single crystal surfaces, it is well-known that their reactivity is highly dependent on surface orientation and composition, which are affected by a number of factors such as alloy nature, preparation procedure, and environmental conditions such as electrochemical potential and pH. The relationship between bulk and surface composition of Pt-transition metal alloy catalysts has been discussed both in theoretical and experimental reports[21, 29, 31, 59-61]. It has been found experimentally that at a bulk ratio of 75 % Pt and 25% Co in an ultra high vacuum environment it is possible to form a topmost surface layer consisting of only of Pt atoms (so-called Pt-skin) after annealing at 1000 K[31]. Also, the Pt-skin was found to be stable in acidic environment while other surface compositions show significant changes

---

*Reprinted with permission from "Surface Atomic Distribution and Water Adsorption on Pt-Co Alloys" by P. Hirunsit and P.B.Balbuena, 2009, Surface Science, 603, 911-919, Copyright 2009 by Elsevier.
*Part of this chapter is reprinted with permission from "Effects of Water and Electric Field on Atomic Oxygen Adsorption on Pt-Co Alloys" by P. Hirunsit and P.B.Balbuena, 2009, Surface Science, 603, 3239-3248, Copyright 2009 by Elsevier.

over time[31]. The ORR catalytic activity of at 333 K has been found to be in the order: Pt-skin on Pt_3Co > Pt_3Co > Pt[21]. Thus, the depletion of Pt and enrichment of Co in the near-surface layer and the interaction between the topmost layer of pure Pt with this kind of near-surface atomic distribution has a profound influence on the catalytic activity of alloys at these conditions[21, 31, 61, 62].

Metal surfaces in contact with aqueous solutions create a unique reaction environment that can markedly influence the ORR reactivity[63]. However, the structure and chemistry of water-metal interfaces require further understanding. Water may form a partially dissociated layer on some metal surfaces such as Ru(0001)[64-69] and Cu(110) [70, 71]. However, on most hexagonally close-packed surfaces and on other metal surfaces such as Ni(111), Cu(111), Rh(111) and Pt(111) water does not dissociate[72, 73]. Ogasawara et al's [72] X-ray adsorption, X-ray emission and X-ray photoelectron spectroscopy studies revealed that water adsorbed on Pt(111) does not dissociate and forms a non-tetrahedral arrangement of flat ice with both Pt-O and Pt-HO surface/water bonding. Several DFT studies indicate that the interaction between water and metal surfaces is dominated by chemical bonding formed between the oxygen lone pair from water molecules and the surface electronic states[64, 66, 69, 71, 72, 74, 75]. It has been suggested that the bond is localized mostly in the contact region and the adsorption energy is mainly affected by the topmost layer of the substrate surface[74, 76]. Furthermore, it has been found that for water adsorbed on Pt-Co the rate of Pt-OH and Pt-O formation on Pt-Co is slower than those on Pt(111), thus the potential exists to reduce the oxygen-containing intermediates which are thought to accumulate on and poison the surface[77, 78]. Experimental results have supported this concept showing that Pt-Co alloy catalysts give a higher overall ORR rate than Pt(111) surfaces[32, 33]. Water adsorbed on alloys such as Pt-skin over Pt–Co and Pt3Cr surfaces has also been studied by Roques and Anderson [79, 80]. The study on Pt_3Cr alloy catalyst showed that water favors the Cr site on Pt3Cr(111), and water adsorption energies on Pt sites of Pt-skin monolayers on Pt3Cr(111), Pt3Cr and Pt(111) are comparable, and they were found slightly weaker relative to Pt(111) [79]. On Pt-skin of Pt–Co alloys the authors found

that water adsorption energy is somehow dependent on the Co concentration in the sub-surface however less than that of OH adsorption energy [80]. The results of some of these Pt-skin models [79, 80] are discussed in a later section in this paper.

4.2. Objective

In this chapter, we use density functional theory (DFT) to characterize surface atomic distribution of PtCo and Pt_3Co bulk compositions, and the interactions between a water molecule on PtCo(111) and Pt-skin surfaces and atomic oxygen atom on those surfaces. We then compare the results to previous findings on pure Pt to obtain further insights into the role of Co in the Pt–Co alloy catalysts enhancing ORR reactivity.

4.3. Computational details

The calculations were performed using the Vienna ab initio simulation package, VASP[81-84]. The metal slab models were simulated using a 2×2 unit cell containing 4 to 6 layers of metal atoms and a vacuum region of more than 6 layers (>13 Å). The first two layers from the bottom of the slab, or the bottom layer only, were fixed for 6- and 4-layer slabs respectively, while the other layers were relaxed to their lowest energy configurations. The fixed layers were set to their bulk bond distances according to their optimized lattice constants which were determined from bulk calculations. Experimental structures for PtCo synthesized using low temperature (~600 °C) annealing were found to be coexisting chemically as disordered face-centered cubic (fcc) phases with different stoichiometries, and a chemically ordered face-centered tetragonal (fct) structure was obtained using high (~950 °C) temperature annealing[29, 34, 37]. In this work, the simulated structures are ordered fcc and fct (Fig.4.1) for PtCo and ordered fcc for Pt_3Co. The close-packed plane (111) of the fcc structure was used to determine initial atomic positions for PtCo and Pt_3Co fcc structures. The various ordered atomic planes (001), (100) or (010), and (111) in fct PtCo structure (Fig. 4.1) were considered. The calculated lattice constants are 3.89 Å for fcc Pt_3Co in good agreement with the experimental value of 3.85 Å[85] and 3.78 Å for fcc PtCo bulk compositions. To the best of our knowledge,

the experimental lattice parameter of ordered fcc PtCo has not been reported, but it was found that the experimental lattice parameter for PtCo bulk alloy transforming from fcc to hcp is 3.77 Å[86]. The calculated a and c lattice parameters of fct PtCo are 3.81 and 3.72 Å, respectively. They are also in good agreement with the experimental a and c lattice parameters which are 3.78 and 3.71 Å[37], respectively.

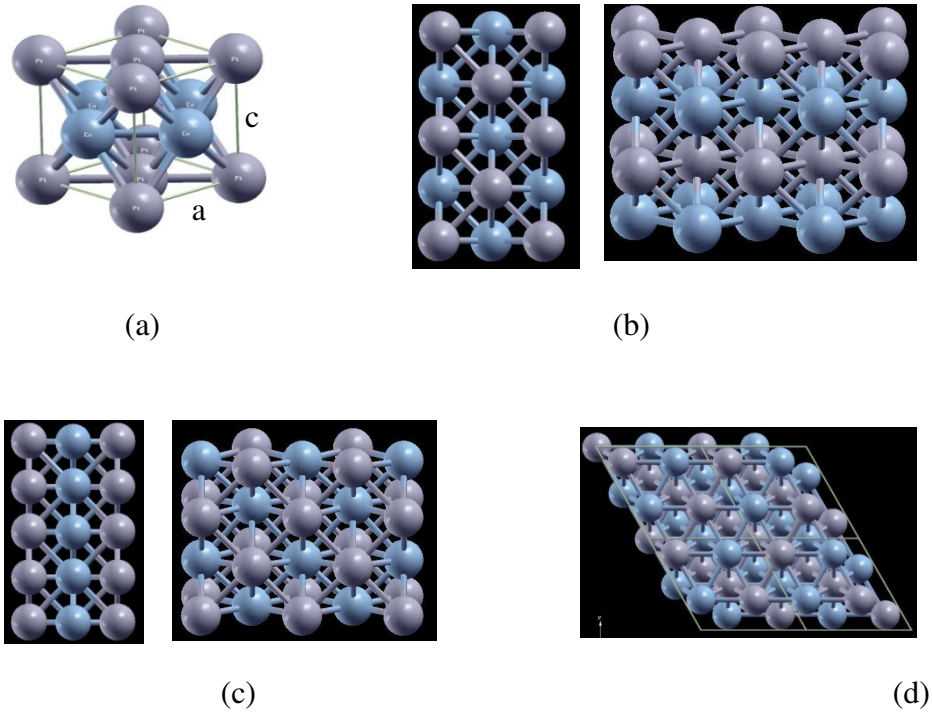

Fig. 4.1. Atomic configuration of (a) fct PtCo crystal structure (b) (001) plane top and side view (c) (100) and (010) plane top and side view (d) (111) plane top view. Blue atoms are Co and grey atoms are Pt.

The slab model (Fig. 4.2) is used to represent the surface. Each layer in the simulated slab model contained four atoms. In the study of surface composition, atoms in the first three layers were changed to the specified compositions of Pt and Co at each layer while maintaining the total number of atoms of each element to be the same in the slab. In the investigation of the interactions of the surface with water and atomic oxygen, the

adsorbates were located on one side of the slab to simulate the adsorbed system. The adsorbates and the slab surface layers were allowed to relax simultaneously, while as mentioned above some slab layers were fixed to their bulk optimized lattice constants.

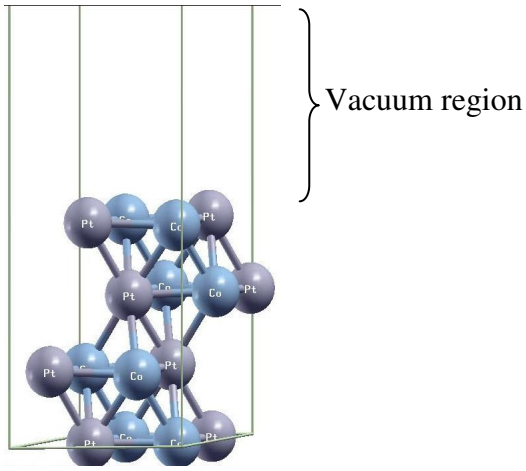

Fig. 4.2. Slab model.

DFT calculations were performed with the exchange-correlation functional Perdew-Burke-Ernzerhof (PBE) [87] described within the generalized gradient approximation, with 9 × 9 × 1 k-points Monkhorst-Pack [88] mesh sampling in the surface Brillouin zone. The plane-wave cutoff energy was optimized at 400 eV. The results were checked for convergence with respect to the energy cutoff and the number of k-points. Spin polarization was taken into account and the Methfessel-Paxton smearing [89] of order 2 with a value of smearing parameter σ of 0.2 eV was applied. The convergence criterion for ionic relaxation loop was set to 10^{-5} eV/Å. Electronic density of states (DOS) were obtained for individual atoms (partial DOS) using a much bigger k-point mesh (16 × 16 × 1) and the values are referenced to the Fermi level. Bader charge analysis [90, 91] were performed using the software provided at http://theory.cm.utexas.edu/vtsttools/bader/. The simulation graphics in this work were generated using XCrySDen[92].

4.4. Results and discussion

4.4.1. Surface and subsurface atomic distribution and electronic structure

One of the main problems in alloy catalysis is the assessment of surface composition. For a given bulk composition, different atomic distributions on the surface and first subsurface layers may result depending on the sample preparation and pretreatment[21, 29, 31]. We emphasize the importance of the subsurface because it plays a role in surface segregation and surface reactivity[93]. In this section we report the energetically most stable configurations of fcc and fct PtCo and fcc Pt_3Co slabs under vacuum conditions. Note that the results of this study do not address the alloy surface stability which can be determined using surface free energy and surface segregation energy as recently reported[94]. Table 4.1 shows that the most stable plane of fct PtCo is the (111). Therefore, the subsequent calculations on the fct PtCo system were done only using the fct PtCo(111) bulk structure.

Table 4.1.
Total slab energies (eV) of ordered fct PtCo planes.

Structure	Total Energy (eV)	Relative energies (eV)
plane (001)	-98.90	2.32
plane (100)	-99.14	2.08
plane (111)	-101.22	0.0

Tables 4.2-4.4 display layer-by-layer atomic distributions and the corresponding calculated total slab energies for fcc PtCo(111), fct PtCo(111), and Pt_3Co(111) bulk compositions. For fcc PtCo, the total simulated slab layers are six, whereas for Pt_3Co and fct PtCo bulk compositions, four slab layers were used. Cases of pure Co on the topmost layer were not considered since under vacuum, Pt has been shown in both theoretical[61] and experimental studies[95, 96] to have a strong surface segregation tendency.

Table 4.2.
Compositions (atomic percent) of Pt and Co in each layer for fcc PtCo bulk composition and corresponding total slab energies (in eV). The total energy of the fcc PtCo slab uniformly distributed is -153.15 eV.

	A-1	A-2	A-3	A-4	A-5	A-6
layer 1 (surface)	$Pt_{75}Co_{25}$	$Pt_{75}Co_{25}$	Pt_{100}	Pt_{100}	$Pt_{25}Co_{75}$	$Pt_{25}Co_{75}$
layer 2	$Pt_{50}Co_{50}$	$Pt_{25}Co_{75}$	$Pt_{25}Co_{75}$	Co_{100}	$Pt_{50}Co_{50}$	$Pt_{75}Co_{25}$
layer 3	$Pt_{25}Co_{75}$	$Pt_{50}Co_{50}$	$Pt_{25}Co_{75}$	$Pt_{50}Co_{50}$	$Pt_{75}Co_{25}$	$Pt_{50}Co_{50}$
layers 4, 5, and 6	$Pt_{50}Co_{50}$	$Pt_{50}Co_{50}$	$Pt_{50}Co_{50}$	$Pt_{50}Co_{50}$	$Pt_{50}Co_{50}$	$Pt_{50}Co_{50}$
Total energy (eV)	-153.75	-153.71	-153.89	**-154.26**	-152.45	-152.39
Relative energies to $Pt_{50}Co_{50}$ slab (eV)	-0.61	-0.56	-0.74	**-1.11**	0.70	0.76

The Pt-rich surfaces (A1–A4) are more favorable than the PtCo surface (uniform distribution) and those with higher Co ratio on the surface (A5 and A6) are the least favorable. The energetically most stable fcc PtCo surface is the Pt-skin A-4 system having a subsurface layer of pure Co, and $Pt_{50}Co_{50}$ bulk composition underneath. The Pt-skin A-3 system shows higher energy than the A-4; these two systems differ only in the composition in the second and third layers. Thus, under vacuum, the absence of Pt in the second layer under the Pt-skin topmost layer is energetically more favorable. This may be due to a strong binding energy between the Pt top monolayer and the pure Co subsurface layer. However, a comparison of the energies between cases A-1 and A-2 indicates that the system with a higher concentration of Co in the second layer (A-2) does not become more favorable than the lowest of the two (A-1) when the surface composition contains 25% Co.

Similarly, for fct PtCo(111), Table 4.3 shows that a pure Pt monolayer over pure Co (case B-2 Table 4.3) is energetically more favorable than the B-1 and B-3 cases where there is some Co present on the surface. Thus, fct PtCo systems show the same trend as those of fcc PtCo where the Pt-rich surfaces are the most stable under vacuum. The

interlayer separations d_{12} and d_{23} indicate that in the most stable Pt-skin structure (B2) there is a small expansion between the top and 2nd layer, and a strong contraction of the separation between the 2nd and 3rd layers. In the next more stable surface (B-1) we detect a large expansion between the first two layers and a contraction of equivalent magnitude between the 2nd and 3rd layers. The least stable surface (B-3) is also the least affected by geometric changes. A similar trend of structure relaxation has been shown by Roques and Anderson[97] for Pt-skin surfaces, and the greater the overall Co concentration in the alloy, the greater the relaxation amplitude is.

Table 4.3.
Compositions (atomic percent) of Pt and Co in each layer for fct PtCo(111) bulk composition and corresponding total slab energies (in eV). The total energy of the fct PtCo slab uniformly distributed is -101.22 eV. d_{12} and d_{23} are the distances between atoms in the first and 2nd layer and the 2nd and 3rd layer compare to those of PtCo slab uniformly distributed, respectively.

	B-1	B-2	B-3
layer 1 (surface)	$Pt_{75}Co_{25}$	Pt_{100}	$Pt_{25}Co_{75}$
layer 2	$Pt_{25}Co_{75}$	Co_{100}	$Pt_{75}Co_{25}$
layers 3 and 4	$Pt_{50}Co_{50}$	$Pt_{50}Co_{50}$	$Pt_{50}Co_{50}$
Total energy (eV)	-101.60	**-101.91**	-100.35
Relative energies to $Pt_{50}Co_{50}$ slab (eV)	-0.38	**-0.70**	0.87
d_{12}	+4.3%	+0.8%	+0.5%
d_{23}	-4.9%	-9.8%	+1.3%

Table 4.4 shows energetic information for slabs of Pt_3Co overall composition. Like in the cases of fcc and fct PtCo, the system with the Pt-skin (case C-1) is the most stable and the total energies increase as more Co is exposed to the surface, following the order: Pt-skin < $Pt_{75}Co_{25}$ < $Pt_{50}Co_{50}$.

Table 4.4.
Compositions (atomic percent) of Pt and Co in each layer for Pt_3Co bulk composition and corresponding total slab energies (in eV). The total energy of the Pt_3Co slab uniformly distributed is -96.94 eV.

	C-1	C-2
layer 1 (surface)	Pt_{100}	$Pt_{50}Co_{50}$
layer 2	$Pt_{50}Co_{50}$	Pt_{100}
layers 3and 4	$Pt_{75}Co_{25}$	$Pt_{75}Co_{25}$
Total energy (eV)	**-97.60**	-96.15
Relative energies to $Pt_{70}Co_{50}$ slab (eV)	**-0.66**	0.79

However, this order was not found in recent experimental studies by Axnanda and Goodman[98], who utilized ion scattering spectroscopy (ISS) of Pt-Co supported on Mo(110) under ultra high vacuum (UHV) conditions to characterize the surface composition and to obtain surface phase diagrams. The experimental results showed that for Pt_3Co bulk composition the surface composition of the stable structure had ~15% of Co, and ~25% of Co was found on the surface with PtCo bulk composition. In order to test if our slab model size is not a factor which causes the disagreement with the experimental result, the simulated slabs were expanded to contain 16 atoms in each slab layer. Three surface compositions with Pt_3Co bulk compositions were calculated: i) Pt_3Co, ii) Pt-skin having the same layer-by-layer distribution as C-1 (Table 4.4), iii) a slab where the surface composition is Co12.5%Pt87.5%, the second layer Co37.5%Pt62.5% and the third and fourth layers Co25%Pt75%. Case (iii) has a surface composition close to the experimental result. We have not performed the calculations for all possible surface compositions but only for those three cases because the purpose of these calculations on the expanded surfaces were only to check if the most stable 100% Pt-skin surface was an artifact of the small cell size. However, the DFT results again predicted that the Pt-skin (case ii) is the most energetically stable structure with lower total system energy (by 1.51 eV) than (iii). This discrepancy regarding the stable surface

composition on Pt_3Co may be caused by various factors, including the finite temperature effect, since the calculations correspond to 0 K while the experimental surface composition was obtained after annealing at 1000 K, and the presence of a Mo substrate underneath the experimental thin film Pt-Co system.

The electronic structure of the surface atoms is analyzed through the local DOS, shown in Fig. 4.3 for fct PtCo, B-1, B-2, B-3, Pt_3Co, C-1, C-2 and Pt(111) surfaces. Their d-band centers (corresponding to all the surface atoms) are predicted at 1.82, 2.09, 2.51, 1.54, 1.97, 2.23, 1.71 and 2.11 below the Fermi level respectively. We have calculated atomic oxygen adsorption energies on all distinct sites of fct PtCo and Pt-skin structure B-2: the strongest energies found are -5.04 eV and -3.31 eV, respectively; We have also recently reported O adsorption energies on Pt_3Co and Pt-skin over Pt_3Co, the strongest adsorption sites in each case yielded -4.82 and -4.07 eV, and -4.48 eV was the adsorption energy found on Pt(111)[93]. Thus, the order of calculated adsorption energies follows the increase of Co on the surfaces: fct PtCo > Pt_3Co> Pt > Pt-skin/Pt_3Co > Pt-skin/PtCo, indicate that adsorption becomes stronger as the d band center is shifted up in energy towards the Fermi level, as predicted by the d band model [43, 99] which it can be used to predict and explain the trend of the chemisorptions energy of several adsorbates on surfaces (discussed in Chapter II). As expected, the decrease of Co composition on the surface (B-3 > PtCo > B-1 > B-2) is also reflected on changes in spin polarization: the difference between the contributions of the spin down and up systems becomes negligible when all the Co atoms are substituted by Pt on the surface, where the small spin polarization is induced by the subsurface atoms (Fig. 4.3d). Similar observations hold for the Pt_3Co structure (Fig. 4.3(e-g)). The results of Pt_3Co (Fig. 4.3(f)) are in agreement with the results from Iwashita et al.,[100] and Shirai et al.,[101] who also found that the minority-spin down DOS of Co located in a narrow range at about -0.5 to 1 eV from the Fermi level and the majority-spin up 3-d states of Co hybridize well with Pt 5-d states. Also, Fig. 4.3 illustrates that Co-rich surfaces have a high density of electrons at the Fermi level and large densities of unoccupied states

near the Fermi level coming from the Co atoms, thus offering reactive sites for adsorption of nucleophilic or electrophilic species.

(a) B3-$Pt_{25}Co_{75}/Pt_{75}Co_{25}$ (d-band center = -1.54 eV)

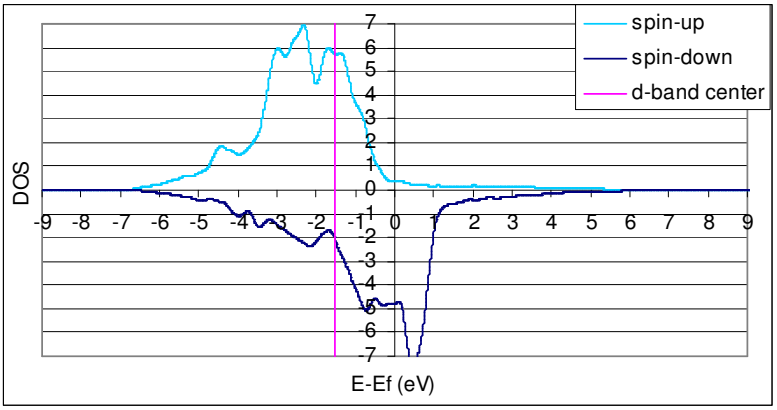

(b) PtCo fct (d-band center = -1.82 eV)

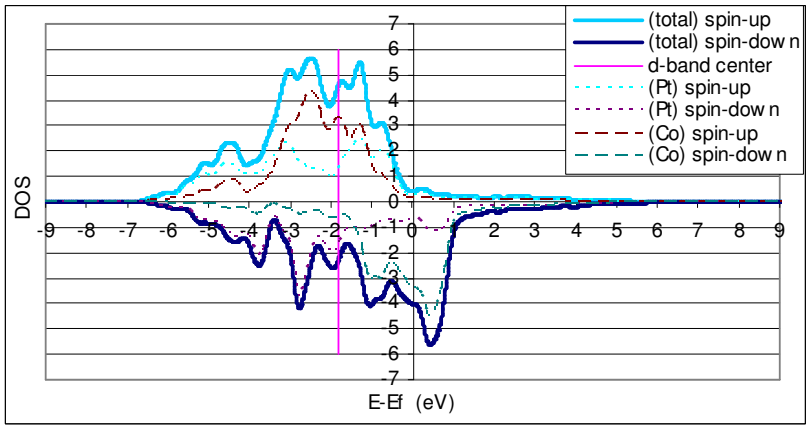

Fig. 4.3. d-Band density of states of surface atoms in structure (a) B-1 (b) fct PtCo (c) B-3 (d) B-2 (e) C-2 (f) Pt3Co (g) C-1. Structures B-1, B-2,B-3,C-1 and C-2 refer to Table 4.3-4.4. The d-band center calculated on the basis of all surface atoms of each structure is also shown in the figure (vertical pink line). The Fermi level is at zero.

(c) B1-$Pt_{75}Co_{25}/Pt_{25}Co_{25}$ (d-band center = -2.09 eV)

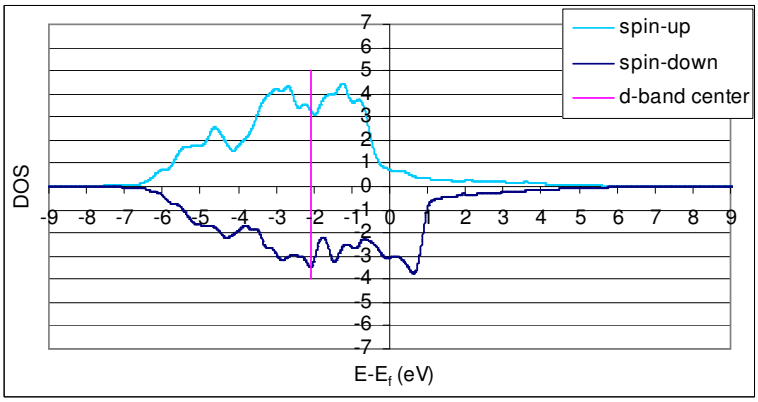

(d) B2 Pt-skin (d-band center = -2.51 eV)

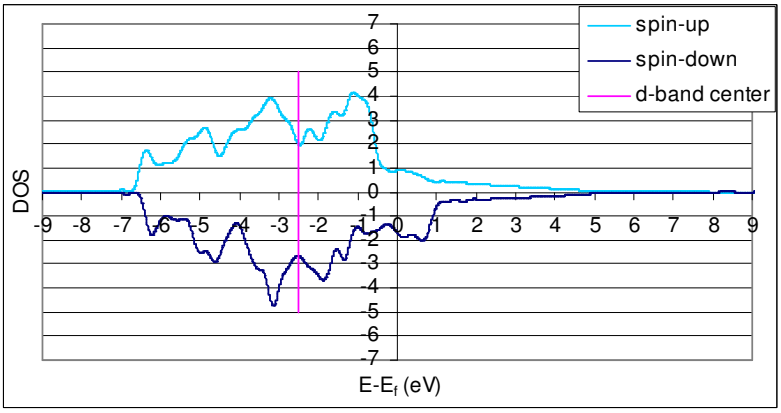

(e) C2 $Pt_{50}Co_{50}/Pt_{100}$ (d-band center = -1.71 eV)

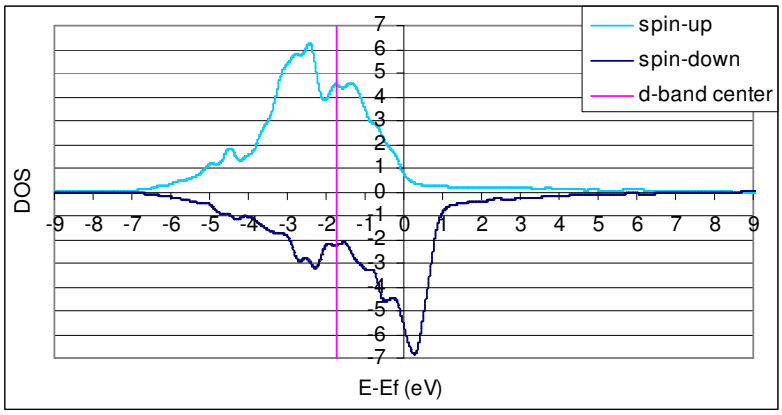

Fig. 4.3. (cont'd)

(f) Pt_3Co (d-band center = -1.97 eV)

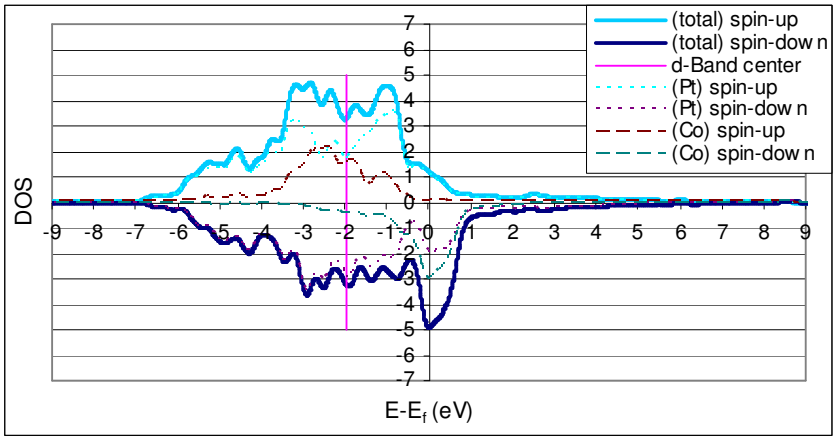

(g) C1 Pt-skin/ $Pt_{50}Co_{50}$ (d-band center = -2.23 eV)

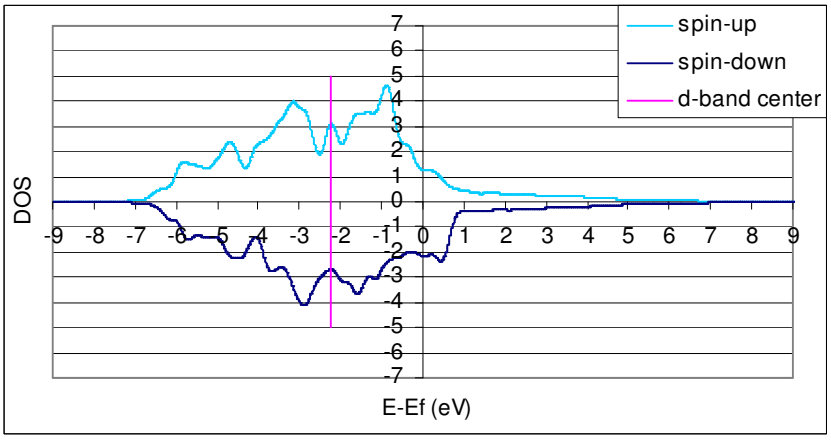

Fig. 4.3. (cont'd)

4.4.2. PtCo(111) and Pt_{100}/Co_{100}/$Pt_{50}Co_{50}$ interactions with a water molecule

In this section we analyze interactions of a water molecule located on fcc and fct PtCo and on the most stable structure $Pt_{100}/Co_{100}/Pt_{50}Co_{50}$ (structure A-4, Table 4.2). The initial orientations of the water molecule were i) both O-Hs are parallel to the surface and ii) one O-H points towards the surface and the other is parallel to the surface, on the sites illustrated in Fig. 4.4; the optimized configurations are shown in Fig. 4.5.

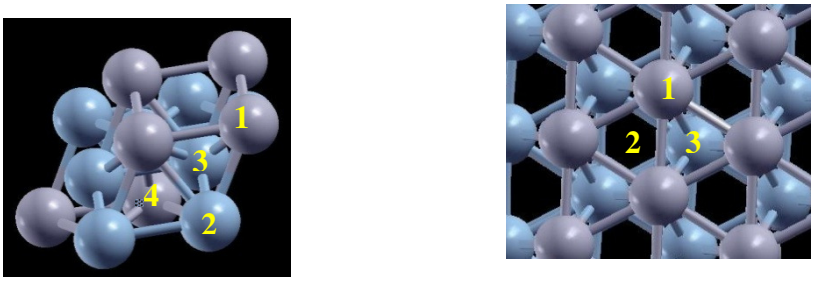

(a) (b)

Fig. 4.4. Water adsorption sites (a) Top view of fcc and fct PtCo(111). Four sites of water oxygen locations: 1) top of Pt, 2) top of Co, 3) 3-fold site top with Co in the 2nd layer underneath, and 4) 3-fold site top with Pt underneath in the 3rd layer. (b) Top view of the structure $Pt_{100}/Co_{100}/Pt_{50}Co_{50}$ with fcc bulk structure. Three sites of water oxygen locations 1) top of Pt 2) 3-fold hollow site and 3) 3-fold site with Co underneath in the 2nd layer. Grey-Pt, Blue-Co.

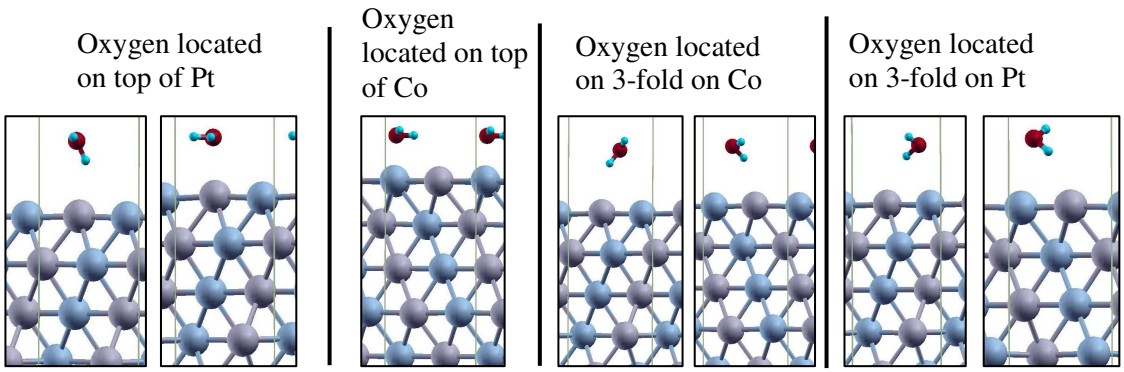

Fig. 4.5. Optimized water molecule orientations (i-vii) on fcc PtCo(111) surface and calculated energies at different water oxygen locations are shown in Fig. 4.4(a). There are two configurations for each water oxygen location corresponding to two different initial water molecule configurations except the case of the water oxygen location on top of Co where both initial configurations led to the same results. Note that the water molecules does not interact (forming hydrogen bonds) to water molecules in the adjacent cells as the distances between them in x and y directions are in the range 4.4-5.4 Å.

Table 4.5.
Water molecule binding energies ($E_{binding}$) on fcc PtCo(111) surface and optimized structural parameters for a water molecule at different O_{water} locations as illustrated in Fig. 4.4(a) and 4.5.

O location	Configuration [a]	$E_{binding}$ (eV)	$d_{O\ldots surface}$ (Å)	$d_{H\ldots surface}$ (Å)	$d_{O\text{-}H1}$ (Å)	$d_{O\text{-}H2}$ (Å)	∠HOH (^{o})
Top of Pt	(i)	-0.10	3.40	2.51	0.98	0.98	103.9
	(ii)	-0.12	2.71	2.66	0.98	0.98	104.6
Top of Co	(iii)	**-0.34**	2.20	2.32	0.98	0.98	105.7
3-fold on Co	(iv)	-0.14	3.20	2.58	0.98	0.98	103.6
	(v)	-0.12	3.41	2.68	0.98	0.98	104.7
3-fold on Pt	(vi)	-0.14	3.06	2.50	0.98	0.98	104.0
	(vii)	-0.12	3.21	2.59	0.98	0.98	104.5

[a]: referred to Fig. 4.5.

The optimized structural parameters and water binding energies are given in Table 4.5. The binding energy is calculated by subtracting the total energy of the system of a water molecule on the PtCo slab from the sum of the total energies of the PtCo slab and that of the water molecule, $E_{(slab/water)}$-$E_{(slab)}$-$E_{(water)}$. The top of Co (configuration iii) is the most stable site for water adsorption on fcc PtCo, where the binding energy is 59% higher than the next stable site which is the 3-fold on Pt (configuration (vi)). The strong interaction of water with the Co site is also supported by the shortest distance between water oxygen and the surface ($d_{O\ldots surface}$). Water orients almost parallel to the surface as denoted by the difference of the distance between O…surface and H…surface being very small (0.11 Å). The HOH angle is wider than that calculated for the free water molecule, $d_{O\text{-}H}$ = 0.97 Å and ∠HOH = 104.5^o which are in good agreement with the corresponding experimental values ($d_{O\text{-}H}$ = 0.96 Å and ∠HOH = 104.5^o)[102]. In all cases, the O-H bonds of the adsorbed molecule are 0.2 Å longer than those of the free water molecule. Same lengths for O-H bonds[66, 74] and wide ∠HOH angles (105.6^o[74] and 106^o[66]) were also found for the water molecule on Pt(111) with the dipole vector parallel to the surface. The longer O-H bonds reflect their weakening due

to bonding with the surface, in agreement with Ogasawara et al,[72] who observed an enhancement of the electron density between the H and Pt atoms and a depleted electron density region on the H atom along the O-H bond for water on Pt(111). In addition, the Pt top site becomes the least stable location for water molecule adsorption on PtCo, with one O-H pointing towards the surface (configuration i). DFT calculations on Pt(111) surfaces have reported water molecule adsorption energies of -0.30 eV[74] and -0.35 eV[66] at the most stable site (top) with the water dipole oriented parallel to the surface. In the presence of Co, the water molecule with the same orientation (configuration ii) binds to the Pt atom on the surface approximately 0.18 eV weaker than that on the pure Pt(111) surface. On the other hand, the H_2O binding energy at the most stable site on Pt(111) (-0.35 eV[66]) is very close to that on top of Co, the most stable site on PtCo (-0.34 eV). The preference of water to bind with Co rather than with Pt on PtCo agrees with our earlier discussion of the DOS showing reactivity of the Co sites.

Adsorption of a water molecule on fct PtCo are reported in Table 4.6, where O is located on top of Pt and on top of Co with two different initial water orientations as inidcated for fcc PtCo. According to Table 6, as in fcc PtCo, a water molecule located on top of the Co atom with two OH bonds parallel to the surface is the most stable configuration, having the strongest water binding energy and the shortest $d_{O...surface}$ distance, with the two initial water orientations leading to the same result. In summary, the results reported in Tables 4.5 and 4.6 show similar trends regarding favorable water location, structure, and orientations and do not reveal significant differences of water binding energies (< 0.03 eV).

On the Pt-skin ($Pt_4/Co_4/PtCo$) structure (A4) both initial configurations of water molecules at the locations shown in Fig. 4.4b were tested. The H_2O binding energies and optimized structural parameters are reported in Table 4.7. The most favorable location of a water molecule on this surface is on top of Pt with the water dipole oriented parallel to the surface (configuration ix in Fig. 4.6). This adsorption site and water orientation were also found to be the most stable one for a water molecule on Pt(111)[66, 74]. The fct Pt-

skin structure does not change much from the fct PtCo structure but the fcc Pt-skin structure significantly differs from the fcc PtCo structure and this gives rise to a 3-fold site with no atom underneath (Fig. 4.4(a) site 2) which is mainly caused by the 1st subsurface layer being completely occupied by smaller Co atoms. Despite the structure reconstruction, the water binding energy on the Pt-skin fcc structure (-0.12 eV) is similar to that on the Pt-skin surface of the fct structure, -0.15 eV (Table 7), which is essentially as strong as the O-Pt bond on PtCo (-0.17 eV) but it is much weaker than that on a pure Pt(111) surface (-0.3 eV)[66, 74]. Also, the H-Pt bond at the top Pt site of the A4 structure (configuration viii, Fig. 4.6) on the Pt-skin surface is as strong as that on PtCo(111) (configuration i, Fig. 4.5); the binding energy difference is ~0.03 eV and the $d_{H\ldots surface}$ distance difference is ~0.17 Å. The calculated water binding on the Pt-skin on 4 layers of Co(001) was reported to be -0.12 eV[97], in perfect agreement with that found on the fcc Pt-skin A4 structure. Thus, only the atoms on the surface and on the 2nd layer mainly influence water adsorption energy. At the 3-fold site locations and at the top of Pt with H bonding to surface, the binding energies are very low (~ -0.08 eV), and they are smaller than the weakest H_2O binding energies on the PtCo(111) surface. As shown in Table 4.7, the water molecule characteristics are similar to those at the same site on the PtCo(111) surface (Tables 4.5 and 4.6).

Table 4.6.
Water binding energies (Ebinding) on fct PtCo(111) surface and optimized structural parameters for the water molecule at different O_{water} locations and water orientations on the fct PtCo(111) surface.

O location	Water orientation	$E_{binding}$ (eV)	$d_{O\ldots surface}$ (Å)	$d_{H\ldots surface}$ (Å)	$d_{O\text{-}H1}$ (Å)	$d_{O\text{-}H2}$ (Å)	∠HOH (°)
Top of Pt	1 O-H pointing to the surface	-0.07	3.47	2.49	0.98	0.98	104.5
	2 O-Hs parallel to the surface	-0.17	2.63	2.60	0.98	0.98	104.3
Top of Co	2 O-Hs parallel to the surface	**-0.33**	2.27	2.37	0.98	0.98	104.8

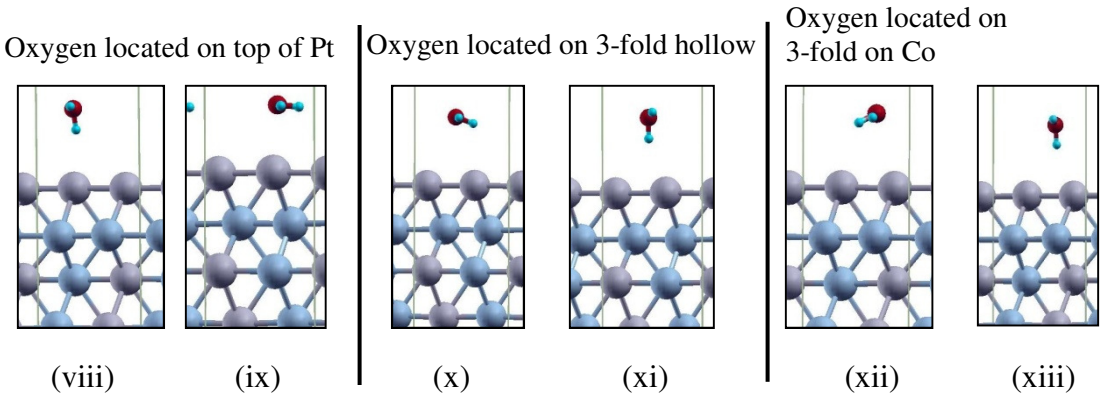

Fig. 4.6. Water molecule orientations (viii-xiii) on Pt-skin (A4). There are two configurations for each oxygen location shown in Fig. 4.4(b) corresponding to two different initial water molecule configurations. Grey-Pt, Blue-Co. Note that the water molecules does not interact (forming hydrogen bonds) to water molecules in the adjacent cells as the distances between them in x and y directions are in the range 4.4-5.4 Å.

Table 4.7.
Water molecule binding energies ($E_{binding}$) on Pt-skin (A4) and optimized structural parameters for a water molecule at different O locations as illustrated in Fig. 4.4(b) and 4.6.

O location	Water Configuration [a]	$E_{binding}$ (eV)	$d_{O\ldots surface}$ (Å)	$d_{H\ldots surface}$ (Å)	$d_{O\text{-}H1}$ (Å)	$d_{O\text{-}H2}$ (Å)	∠HOH (°)
Bulk structure is fcc PtCo(111)							
Top of Pt	(viii)	-0.07	3.64	2.68	0.98	0.97	104.5
	(ix)	**-0.12**	2.87	2.82	0.98	0.98	104.2
3-fold hollow	(x)	-0.08	3.30	3.27	0.98	0.97	103.7
	(xi)	-0.08	3.49	2.51	0.98	0.97	104.1
3-fold Co	(xii)	-0.08	3.25	3.08	0.97	0.98	103.7
	(xiii)	-0.09	3.51	2.53	0.98	0.98	103.9
Bulk structure is fct PtCo(111)							
Top of Pt	2 O-Hs parallel to the surface	-0.15	2.76	2.71	0.98	0.98	104.1

[a]: referred to Fig. 4.6.

In order to further understand the nature of the water/surface interactions, in the following discussion we examine the electronic structure of the occupied molecular

orbitals of an isolated gas-phase H_2O along with those of the adsorbed water at the most stable sites on Pt(111), fct PtCo(111) and Pt-skin (A4) structures using the partial DOS projected onto the d orbital of surface atoms (Fig. 4.7). The green peaks in Fig. 4.7 correspond to the occupied molecular orbitals $2a_1$, $1b_2$, $3a_1$, and $1b_1$ in order of increasing energy in the DOS of the p orbital of oxygen in free H_2O[64]. Upon adsorption, states in the two lowest energy peaks in the O p DOS remain localized on H_2O and do not show any obvious interaction with the surfaces. To estimate how the energies of states change due to the adsorption, we have shifted the energy of the free water at $2a_1$ to the energy of this $2a_1$ orbital of the adsorbed H_2O on each surface. This procedure has been previously performed to characterize water on Ru(0001)[64]. With these energy references, the energies in $2a_1$ and $1b_2$ of p O adsorbed on every surface are the same as with a gas-phase water. Energies in $3a_1$ and $1b_1$ of adsorbed water shift to lower energies with respect to those of free water. The $3a_1$ peaks are shifted to lower energies by 0.25, 0.39 and 0.19 eV and the $1b_1$ peaks by 1.0, 0.82 and 0.5 eV for water adsorbed on Pt(111), PtCo(111) and Pt-skin (A4). The $3a_1$ and $1b_1$ peaks broaden upon adsorption and the $1b_1$ peak of water adsorbed on Pt-skin is broader than on the other surfaces. This clearly shows an orbital bonding state mixed with the d orbital of the surface atoms. Similar results were found for water on Ru(0001)[64].

Additional insights are provided by Bader charge analysis and calculated charge density differences for the most stable water adsorption cases on the PtCo(111) and Pt-skin (A4) structures.

(a)

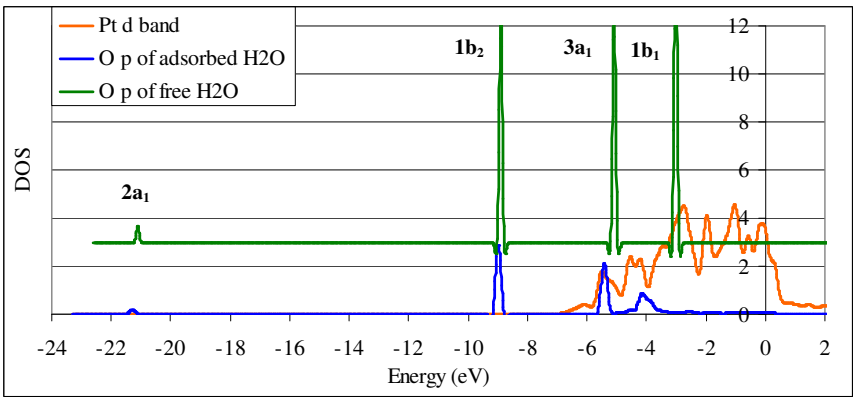

(b)

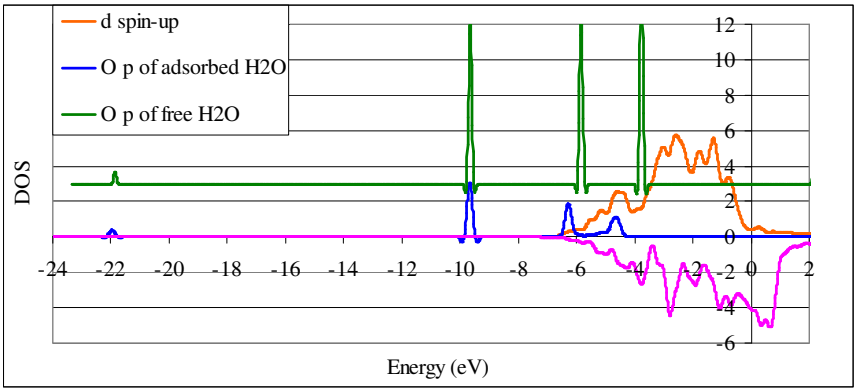

(c)

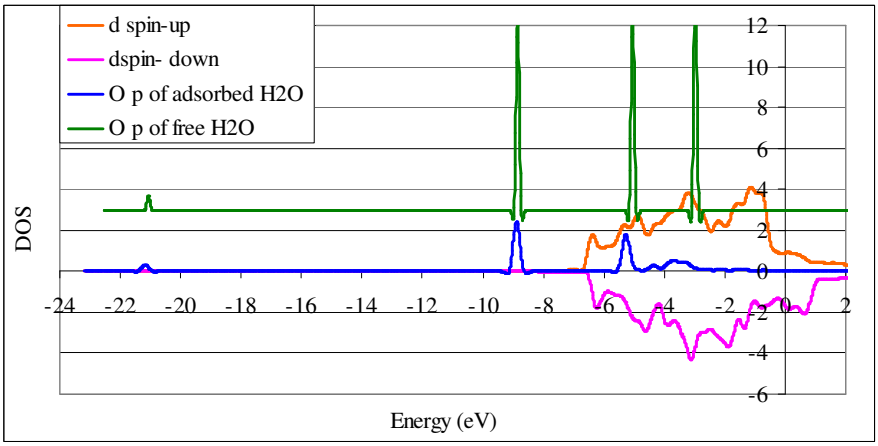

Fig. 4.7. Partial DOS projected onto the oxygen of H_2O adsorbed on the surfaces. The green lines are partial DOS projected onto the oxygen p orbital of a gas phase free water molecule. The blue lines are DOS projected onto the oxygen p orbital of a water molecule adsorbed on the surface and the orange and pink lines are DOS projected on the d states of atoms on the surface of (a) Pt(111) (b) fct PtCo(111) and (c) Pt-skin (A4). The Fermi level is zero and the oxygen p levels of gas phase free water have been shifted so that the 2a1 peaks coincide in each graph.

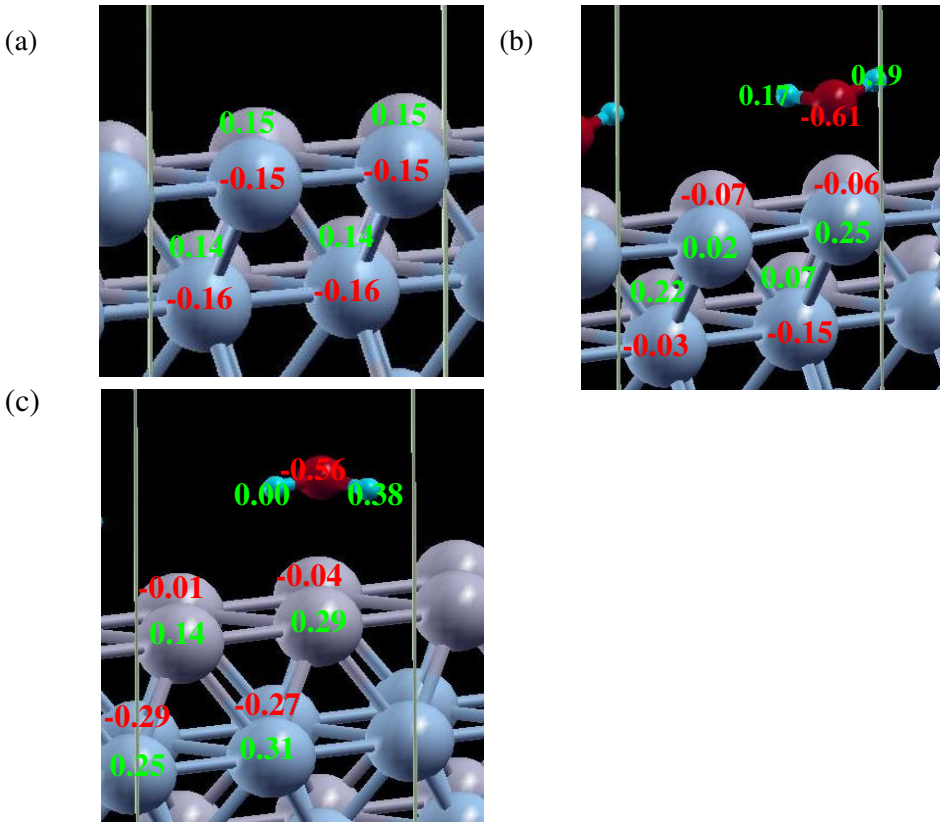

Fig. 4.8. Partial charges obtained from Bader charge analysis: (a) fcc PtCo(111) clean surface (b) configuration iii, water located on top of Co on PtCo (c) configuration ix, water located on top of Pt on Pt-skin (A4) (configurations iii and ix refer to Fig. 4.5 and 4.6, respectively). Grey: Pt, Blue: Co. The unit cell is outlined with vertical solid lines.

We have tested our computation of Bader charges using a water molecule. The calculated partial charges of the oxygen atom and each of the hydrogen atoms of an isolated water molecule are -1.264 and +0.632 respectively, showing a small difference from those based on the charge density generated from an MP2 calculation with the aug-cc-pVDZ basis set using Gaussian 98 which are -1.157 and +0.576 for oxygen and hydrogen atoms, respectively[90, 91]. We are interested in a preliminary estimation of how surface atomic charges may change with the presence of a water molecule. As seen in Fig. 4.8(a-b), for the clean surface of a PtCo structure, Pt atoms show positive charges while Co atoms show negative charges but the opposite trend occurs when water binds to the surface. The oxygen charge upon adsorption becomes much less negative than that

of an isolated water molecule and the interacting Co surface atom shows the highest positive charge number compared with other surface atoms. Thus, Bader charge analysis suggests a partial oxidation of Co under water and a certain degree of charge transfer from the water molecule.

Further understanding can be obtained from the charge density difference defined as the difference between the charge density of the total system and those of a clean slab and a water molecule. The charge difference contour (Fig. 4.9(a)) reveals a charge density increase (yellow and pink contours) in the bonding region; such enhanced density may be originated from electron transfer both from water and from the Co atom. The charge of oxygen on the Pt-skin structure is also much less negative than that of an isolated water molecule and the Pt atom which bonds with water shows the highest positive charge (+0.3) compared with other Pt surface atoms (Fig. 4.8(c)). In contrast, the charge density difference contour plot of the Pt-skin (Fig. 4.9(b)) illustrates the loss of electron density (blue and green contours) along the bonding. This behavior, which was also found for a water molecule bonded to Pt(111)[72], indicates charge transfer to the surroundings in order to minimize the Pauli repulsion between the p orbital of the water oxygen and the Pt d orbital[72]. The enhanced density found in the bonding region for the PtCo surface (Fig. 4.9a) may result from a lower repulsion that can be explained from the much smaller overlap between the water $3a_1$ and the Pt d orbitals in the DOS of PtCo surfaces (Fig. 4.7b) compared to Pt(111) and Pt-skin (A-4) surfaces (Fig. 4.7a and c).

(a)

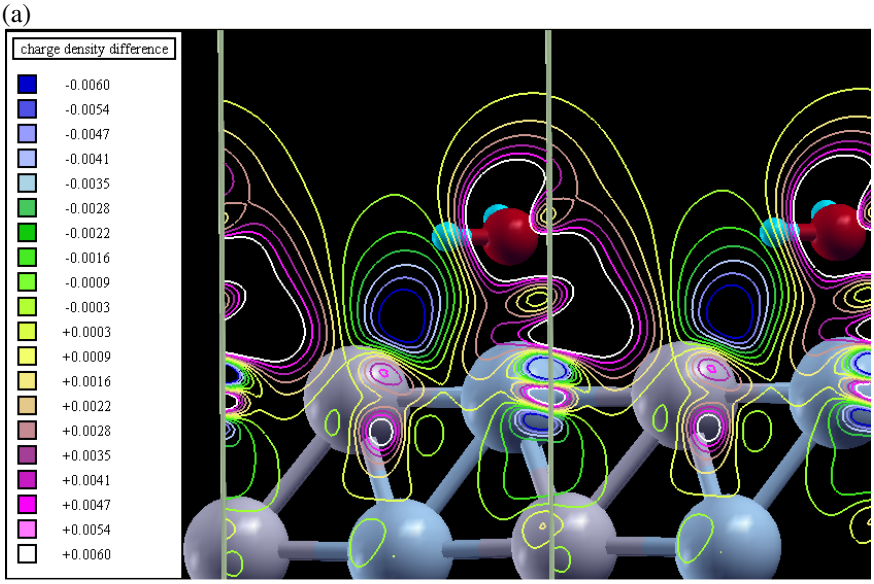

(b)

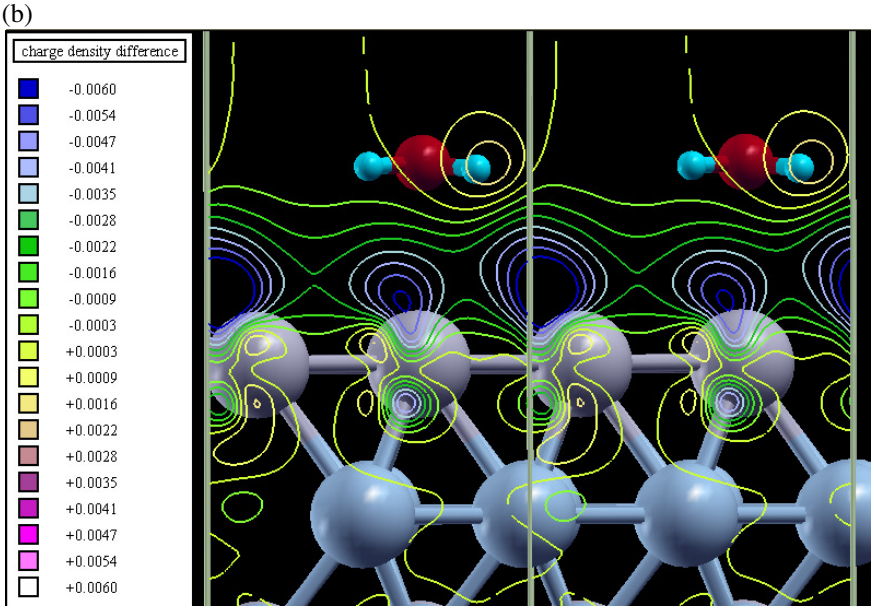

Fig. 4.9. Contour plot of the charge density difference projected on yz plane (in units of e/Å^3) of (a) configuration iii, water located on top of Co on PtCo (b) configuration ix, water located on top of Pt on A4 Pt-skin (configurations iii and ix refer to Fig. 4.5 and 4.6, respectively). Grey: Pt, Blue: Co. The unit cell is outlined with vertical solid lines.

4.4.3. O adsorption at 0.25 ML coverage on PtCo(111) and Pt/Co/PtCo structures

In this section we report results using a 2x2 unit cell. Two atop and four 3-fold O adsorption sites on fcc and fct PtCo are shown in Fig. 4.10. The calculated binding energies and the optimized distances between O and the surface are reported in Table 4.8. The binding energy is calculated by equation (4.1).

$$BE_O = E_{(slab/oxygen)} - E_{(slab)} - E_{(atomic\ oxygen)} \quad (4.1)$$

where BE_O is the atomic oxygen binding energy, $E_{(slab/oxygen)}$ is the total energy of the system with an O atom adsorbed on the surface, $E_{(slab)}$ is the energy of the clean slab and $E_{(atomic\ oxygen)}$ is the energy of O.

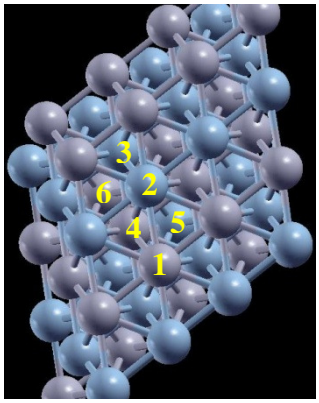

Fig. 4.10. Top view of fcc and fct PtCo(111) adsorption sites: 1) top of Pt, 2) top of Co, 3) 3-fold site top with Co underneath in the 2nd layer –hcp(Co), 4) 3-fold site top with Pt underneath in the 2nd layer –hcp(Pt), 5) 3-fold site top with Co underneath in the 3rd layer –fcc(Co), and 6) 3-fold site top with Pt underneath in the 3rd layer –fcc(Pt). Grey-Pt, Blue-Co.

Table 4.8.
Calculated binding energies, BEO, (in eV) of atomic oxygen on fcc and fct PtCo surfaces at different studied adsorption sites and optimized distances (in Å). Element names in parenthesis after fcc or hcp sites indicate the type of atom underneath that hollow site.

Adsorption site[a]	fcc PtCo				fct PtCo			
	BE_O	$d_{O...surf.}$[b]	$d_{O...Pt\ surface}$[b]	$d_{O...Co\ surface}$[b]	BE_O	$d_{O...surf.}$	$d_{O...Pt\ surface}$[b]	$d_{O...Co\ surface}$[b]
1. top of Pt	No stable state is found				-2.96	1.83	1.85	-
2. top of Co	-3.89	1.64	-	1.64	-3.64	1.63	-	1.63
3. hcp(Co)	-4.48	1.27	2.09	1.85	-4.47	1.21	2.10	1.85
4. hcp(Pt)	-4.83	1.08	2.10	1.87	-4.93	1.03	2.11	1.87
5. fcc(Co)	-4.35	1.21	2.09	1.84	-4.47	1.12	2.09	1.83
6. fcc(Pt)	**-5.06**	1.13	2.07	1.87	**-5.04**	1.07	2.09	1.87

[a] See Fig. 4.10 for site.
[b] $d_{O...surface}$ is the distance between O and the surface in vertical z direction, $d_{O...Pt\ surface}$ is the distance between O and the bound Pt atom, and $d_{O...Co\ surface}$ is the distance between O and the bound Co atom.

Table 4.8 illustrates the similarity of binding energies for fcc and fct structures. The most stable adsorption site for atomic oxygen is fcc(Pt) followed by hcp(Pt). Adsorption in top sites is significantly weaker and the top of Co is the least stable site showing ~1.17 eV less adsorption energy than the fcc(Pt) site. The trends of strong and weak adsorption energies are also correlated with the distance between O and the surface. At the 3-fold sites where $d_{O...surface}$ is in the range of 1.1-1.3 Å, O atoms tend to be closer to the higher oxyphilic Co than to Pt. The experimental heat of O desorption from Pt(111) at 200-300 K at very low coverage is approximately in the range of -3.6 to -4.8 eV[7]. Previous DFT results at the same O coverage on Pt(111) yielded energies at the fcc site of -4.61 eV/O[103], -4.48 eV/O[93] and on $Pt_3Co(111)$ -4.82 eV/O at the fcc(Co) site[93]. As expected, the Co-rich surface as in PtCo is more reactive towards O adsorption and this can be explained by a higher density of electrons at the Fermi level,

as well as to a large density of unoccupied states near the Fermi level mostly contributed from the Co atoms[104].

The O adsorption sites on the fcc and fct Pt-skin (Pt/Co/PtCo) structures are shown in Fig. 4.11. Despite the structure reconstruction of fcc Pt-skin, both fcc and fct Pt-skin structures show comparable adsorption energies at the most stable site. The distances between the surface and the 2nd layer of each structure are in the same range of 2.1-2.2 Å. We have calculated the d-band center relative to the Fermi energy (ε_d - ε_f) for both structures and found only 0.1 eV difference, which indicates that the surface atoms are electronically similar. The O binding energies on the Pt-skin structures are much lower than those on ordered PtCo (Table 4.9) and on Pt(111). This trend has also been observed for O on Pt-skin of Pt_3Co(111)[93, 105]. The weakened O binding on Pt-skin is caused by the reduced number of unoccupied states near the Fermi level[104], as well as to the involvement of the subsurface 3d metals which may yield a strong binding between the 1st and 2nd layers while the electronic structure of the surface Pt atoms is considerably modified with respect to pure Pt[93].

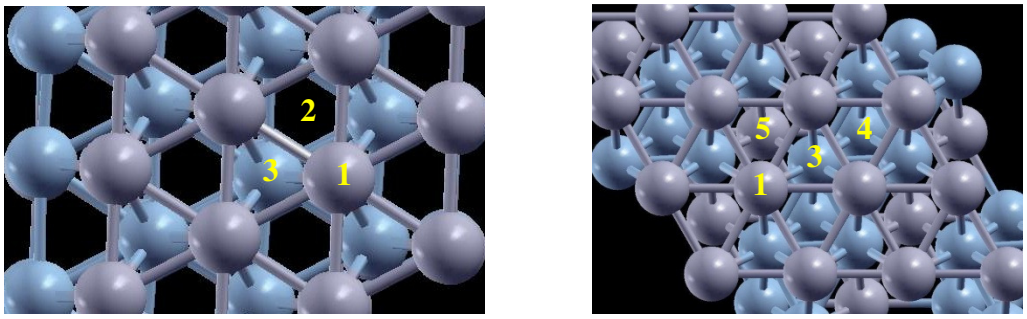

(a) (b)

Fig. 4.11. The structure of fcc and fct Pt-skin. (a) Top view of the fcc Pt/Co/PtCo(111) sites: 1) top of Pt, 2) 3-fold site top with no atom underneath in the 2nd layer –empty, 3) 3-fold site top with Co underneath in the 2nd layer –hcp(Co). (b) Top view of fct Pt/Co/PtCo(111) sites: 1) top of Pt, 3) 3-fold site top with Co underneath in the 2nd layer –hcp(Co), 4) 3-fold site top with Co underneath in the 3rd layer –fcc(Co), and 5) 3-fold site top with Pt underneath in the 3rd layer –fcc(Pt). Grey-Pt, Blue-Co.

Table 4.9.
Calculated binding energies (in eV) of O on fcc and fct Pt-skin surfaces at different studied adsorption sites and optimized distances (in Å).

Adsorption site[a]	fcc Pt/Co/PtCo(111) structure			fct Pt/Co/PtCo(111) structure		
	BE_O	$d_{O...surface}$[b]	$d_{O...Pt\ surface}$[b]	BE_O	$d_{O...surface}$[b]	$d_{O...Pt\ surface}$[b]
1. top of Pt	No stable state is found			-2.44	1.87	1.87
2. empty	**-3.15**	1.39	2.10	-	-	-
3. hcp(Co)	-2.94	1.39	2.10	-2.31	1.37	2.09
4. fcc(Co)	-	-	-	**-3.31**	1.37	2.10
5. fcc(Pt)	-	-	-	-3.27	1.38	2.09

[a] See Fig. 4.11 for site.
[b] $d_{O...surface}$ is the distance between an oxygen atom and the surface in vertical z direction, and $d_{O...Pt\ surface}$ is the distance between an oxygen atom and the Pt atom on the surface binding with the oxygen atom.

4.5. Conclusion

DFT calculations of atomic surface distributions of fcc and fct PtCo(111) and fcc Pt_3Co(111) overall compositions indicate that structures with Pt-skin surfaces ($Pt_{100}/Co_{100}/Pt_{50}Co_{50}$ and $Pt_{100}/Pt_{50}Co_{50}/Pt_{75}Co_{25}$) are the most favorable configurations. The Pt-skin surface having 100% Co in the second layer underneath the surface (A-4) is the most stable structure for fcc and fct PtCo bulk compositions. Water adsorption energies become stronger with the increase of Co on the surface, and this analysis suggests that both the surface and the first sub-surface layer are the main factors determining water adsorption energies. On the PtCo(111) surface the strongest binding energy was found when water was located on top of Co with its dipole parallel to the surface and the weakest when water is on top of Pt with one OH pointing toward the surface. The O_{H2O}-metal binding energy at Co atop site on PtCo(111) is as strong as that on top of Pt on the Pt(111) surface. The higher reactivity of the Co surface sites is explained by the density of states of surface d atoms which indicates that as Co composition on the surface increases there is a larger contribution of the minority-spin

states at the Fermi level and in the neighbor unoccupied states. The d-band of Pt-skin surfaces shows some spin polarization induced by Co atoms in the sub-surface.

As reported previously, adsorption on Pt-skin surfaces is found weaker than on pure Pt(111) and dependent on the Co concentration on the sub-surface. Water adsorbed on Pt top site of $Pt_{100}/Co_{100}/Pt_{50}Co_{50}$ shows the strongest water binding energy on this structure; the interaction is close to that on Pt top site of PtCo(111) but is weaker than on top sites of Pt(111) surfaces. Both the fcc and fct PtCo bulk structures yield similar trends with respect to the favorable water molecule adsorption location, orientation and water binding energies. The H_2O bonding interactions with Pt(111), PtCo(111) and $Pt_{100}/Co_{100}/Pt_{50}Co_{50}$ are mainly through the 1b1 and 3a1 orbitals interacting with d orbitals of the surface atoms. Furthermore, Bader charge analysis shows that the interaction with water determines surface Co to become oxidized due to charge transfer to Pt atoms. A depletion of the electron density along the O–Pt bond on the Pt-skin surface is attributed to charge transfer to the surroundings in order to minimize the Pauli repulsion between the p and d orbitals of water and the surface respectively. In contrast, the electron density along the O–Co on the PtCo surface increases because of less repulsion due to smaller overlap between the water 3a1 and the d orbitals of Co compared to that found in Pt(111) and Pt-skin surfaces.

The fcc and fct PtCo structures show similar O binding energy strengths, both being stronger than those reported on Pt(1 1 1) and Pt_3Co. Under vacuum, the fcc(Pt) site is the strongest whereas the atop sites are the least favorable sites on PtCo. On Pt-skin structures (Pt/Co/PtCo) O binding energies are significantly weaker than on PtCo and Pt(1 1 1). The stronger O binding energy of Co-rich surface can be explained with the electronic structure (d band) similar to what described in water adsorption and the Co-rich subsurface alternate the electronic structure of Pt-skin structure resulting in weaker O binding energy on Pt-skin than on Pt(111).

CHAPTER V

EFFECTS OF WATER AND ELECTRIC FIELD ON ATOMIC OXYGEN ADSORPTION ON Pt-Co ALLOYS*

Here, we present our results of the extent study on the effects of a water layer adsorption and co-adsorption of water and atomic oxygen on PtCo and Pt-skin (Pt/Co/PtCo). In the last part of this chapter, we show the investigation on the effects of the electric field on water and atomic oxygen adsorption on the particular surfaces.

5.1. Introduction

The ORR is a very complex reaction in which the detailed mechanism is still uncertain[106]. The number of possible elementary steps and mechanistic routes in the reduction of O_2 to H_2O is vast, since it involves four electron transfers, four proton transfers, and O-O bond cleavage[107]. One of proposed pathways (the so-called "direct route") to the four electrons reduction involves an initial dissociative chemisorption of O_2, involving the splitting of the O-O bond to form adsorbed oxygen atoms, that are then electroreduced to water in a series of reaction steps[106]. The need to understand the surface electrochemistry and catalytic properties of the alloys on those elementary steps is essential[107, 108]. In each elementary step, the surface is covered with several adsorbate types at different coverages and those can affect the surface reactivity. The alloy surfaces and the aqueous solution create a unique reaction environment that can markedly influence the ORR reactivity[63, 109]. Also, as described in Chapter II, adsorbates types, their coverage and their interaction among them induce changes in surface structure affecting reactivity. Surface reconstruction effects due to the adsorption of atomic oxygen and co-adsorption with water are presented here.

---

*Reprinted with permission from "Effects of Water and Electric Field on Atomic Oxygen Adsorption on Pt-Co Alloys" by P. Hirunsit and P.B.Balbuena, 2009, Surface Science, 603, 3239-3248, Copyright 2009 by Elsevier.

Furthermore, electric fields present in electrochemical cells influence the orientation of adsorbed species and may modify ORR pathways[109]. The formation of OH(ads) via the water dissociation reaction: $H_2O(ads) \rightarrow OH(ads) + H^+(aq) + e^-$ (U) on Pt was studied using B3LYP DFT and MP2 approaches[109]. In this reaction, the adsorbed water molecule is oxidized and as the oxidation takes place an electron is transferred to the electrode at a given potential U[110]. Moreover, water was experimentally found to react with O(ads) on Pt(111) at 100 K generating OH(ads)[111, 112]. Roques and Anderson reported calculated adsorption energies of OH, H_2O and reversible potential shifts for OH(ads) formation from H_2O(ads) on Pt_3Cr and Pt-skin on Pt_3Cr[113]. A positive potential shift means that the OH formation by $H_2O(ads) \rightarrow OH(ads) + H^+(aq) + e^-$ (U) reaction on the particular alloy has a tendency to occur at higher potential than on Pt(111) surface and the opposite trend holds for the negative shift. Their results showed negative shift at overall 0.25 and 0.5 ML coverage and positive shift at overall 0.75 ML on Pt_3Cr surfaces. The electric field dependence of O_2, O, OH and OOH adsorption properties on Pt(111) clusters has also been studied by means of an ab initio DFT-based approach by Panchenko et al[114].

An important question regarding the electrochemical surface is how the active sites evolve under high concentration of the oxygenated compounds and water. In the previous chapter, we reported the results of DFT calculations using a slab model of the interactions between an adsorbed water molecule and adsorbed atomic oxygen with PtCo(1 11) and Pt-skin over PtCo surfaces and an analysis of their electronic properties. We showed adsorption trends of water and atomic oxygen on these surfaces and obtained some insights about how adsorbed water behaves on a PtCo surface compared with a pure Pt surface. In this chapter, we focus on the co-adsorption of atomic oxygen with water; both species play an important role in surface oxidation and ORR reactivity.

5.2. Objective

We investigate the adsorption energetics and surface reconstruction due to atomic oxygen adsorption at high coverage on PtCo(1 11) and Pt-skin surfaces with and without

the presence of water. Since water dissociation may arise at electrochemical potentials characteristic of fuel cell operation, we examine the effect of an electric field applied in a direction perpendicular to the metal surface on water adsorption and co-adsorption with atomic oxygen on PtCo(1 11) and Pt-skin surfaces. This analysis may lead to further insights into the role of Co in the Pt-skin and dispersed Pt–Co alloy catalysts especially in ORR processes.

5.3. Computational details

The calculations were performed using the same DFT calculations details described in the previous chapter. Here, we show the calculation details which are additional and/or different from those in the previous chapter.

According to our the DFT calculations shown in the previous chapter, the Pt4/Co4/PtCo structure was found to be the most stable structure for both fcc and fct PtCo[104]. Therefore, this Pt-skin structure has been included in this study. At 0.5 ML and higher O coverage, and for surfaces with both O and water adsorbed, the unit cell was expanded to be 4×4 and the slab model contained 3-4 layers. The oxygen atoms and water molecules were located on one side of the slab to simulate the adsorbed system. The $3 \times 3 \times 1$ k-points Monkhorst-Pack [115] mesh sampling in the surface Brillouin zone was used with the 4×4 unit cell. The plane-wave cutoff energy was optimized at 400 eV. For Pt(111) with water layer and atomic oxygen adsorption are simulated using 3x3 unit cells contained 4 layers. We also investigated the effect of an electric field on adsorbed water and oxygen on Pt(111), Pt-skin and fct PtCo surfaces using slab models and Pt and PtCo using cluster models to represent the surface. Both approaches provide some interesting perspectives, because they represent extended surfaces and low-coordination sites, respectively. The slab models used under electric field are similar to those described in the previous chapter for a 2×2 unit cell, using $4 \times 4 \times 1$ k-points. For the cluster models, the geometries of the cluster were taken from the DFT optimized geometries of the surface. The cluster was frozen during the simulation and only the adsorbed species

were allowed to relax. We tested models with different cluster size and found that for PtCo, a cluster with 16 atoms produced similar geometries of an adsorbed water molecule with those obtained by DFT calculations in extended surfaces. Previous reports have shown that the binding energy of atomic oxygen on Pt(111) does not change significantly with cluster sizes larger than 10 Pt atoms for pure Pt[116]. Therefore, a cluster with 16 atoms was used in this work. The cluster calculations were carried out in the framework of the B3LYP density functional theory method with spin unrestricted orbitals using Gaussian 03[117], witha cc-pVDZ basis set for the O and H atoms and a LANL2DZ basis set for Pt and Co atoms. The B3LYP method is known to provide very good results for transition metal including surface cluster models[118, 119]. In both slab and cluster models, electric field intensities of -0.51, -0.39, -0.26, -0.13, 0.00, 0.13, 0.26, 0.39, 0.51 V/Å were applied in a direction perpendicular to the surfaces.

5.4. Results and discussion

5.4.1. Effects of water on O adsorption on fct PtCo(111) and Pt-skin surfaces

In this section, we first report results from simulations of O adsorbed on Pt/Co/PtCo and PtCo structures in the presence of water molecules. To avoid artificial interactions of water molecules from neighboring cells, here we used a larger 4x4 cell. In addition, as we have seen in the previous chapter that fcc and fct structures show a similar trend in the calculated results, the simulations in this section are only for the fct structure. The surfaces expanded in a 4x4 unit cell are exposed to 8 water molecules equivalent to 0.5 ML coverage. Two oxygen molecules (0.125 ML coverage) were added to adsorb at two adjacent hcp(Pt) sites on PtCo and fcc(Co) sites on Pt/Co/PtCo structures. These two O adsorption sites are very stable on the corresponding structures shown in Tables 4.8 and 4.9 in the previous chapter.

It is found that water molecules arrange in two different configurations: either with their dipole vector parallel to the surface or with one OH bond pointing to the surface and the other OH bond parallel to the surface, in order to maximize hydrogen bonds among them

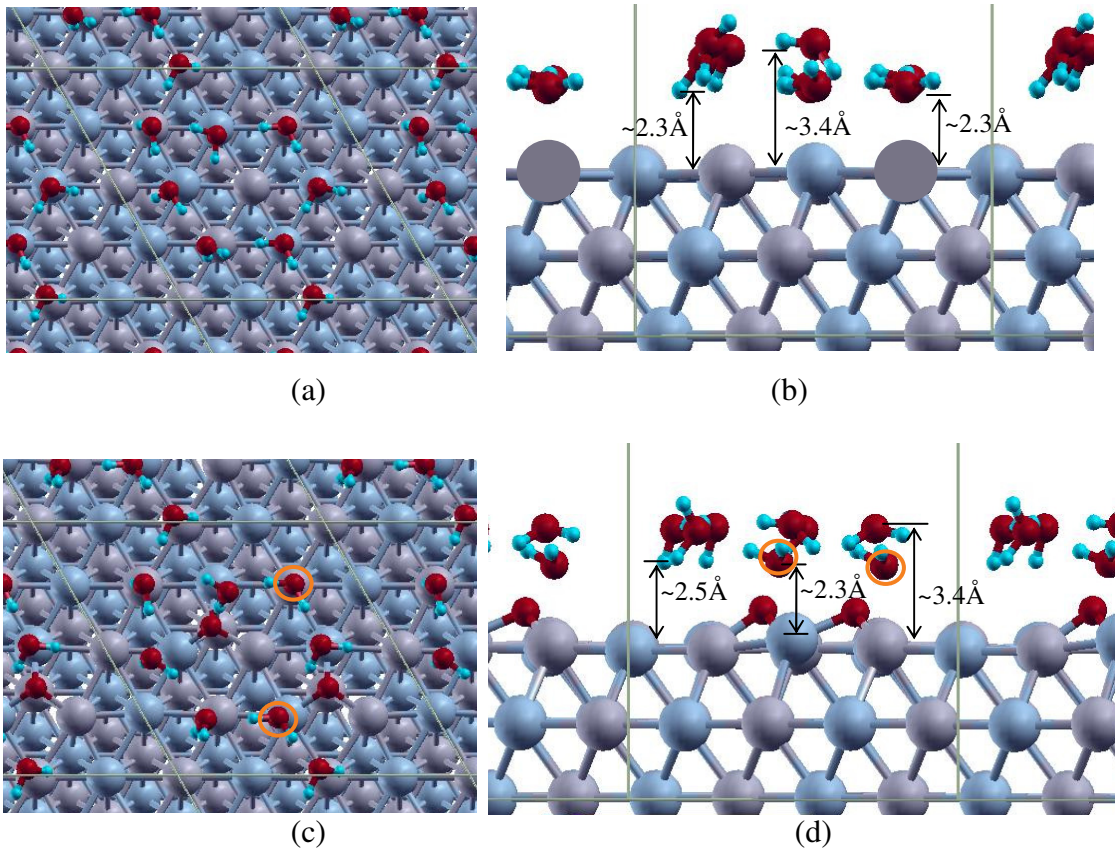

Fig. 5.1. Water molecules/atomic oxygen adsorbed on PtCo. Top: Water molecules adsorbed on PtCo (a) top view (b) side view. Bottom: 0.125 ML O coverage at hcp(Pt) site and 0.5 ML of water. (c) top view (d) side view. Grey: Pt, Blue: Co. The unit cell is outlined with a solid line.

enhancing the stability of the system. Also water molecules tend to stay on atop sites and form a cyclic hexamer on both surfaces, in agreement with previous DFT calculations[74]. Also, the hexamer configuration was observed by STM experiments on Ag(111)[120], Cu(111)[121] and Pd(111)[122] surfaces. Fig. 5.1(a,b) and 5.2(a,b) show that water bonds either through H or O with the surfaces and locate approximately at the same distances above the surfaces. Binding of water with PtCo is slightly stronger than with Pt-skin as water-surface distances are ~2.3Å for PtCo and ~2.4 Å for Pt-skin. Ab initio MD simulations of water on Pt(111)[123] found that the Pt-O distance is3.25Åand approximately 2.3 Å for the Pt-H distance in the water layer with H-down configuration, and DFT calculations reported that the O-Pt bond length for water forming a hexamer on

Pt(111) is 2.3-2.8 Å. These surface-water distances on Pt(111) are very close to the ones we found on Pt-skin surfaces (~2.4 Å).

When O atoms are adsorbed (Fig. 5.1(c,d) and 5.2(c,d)), the water layer is further away from the surface for both structures. The H-bonds among water molecules are weaker than those in bulk water, especially where the particular water molecules form H-bond with an adsorbed O atom.

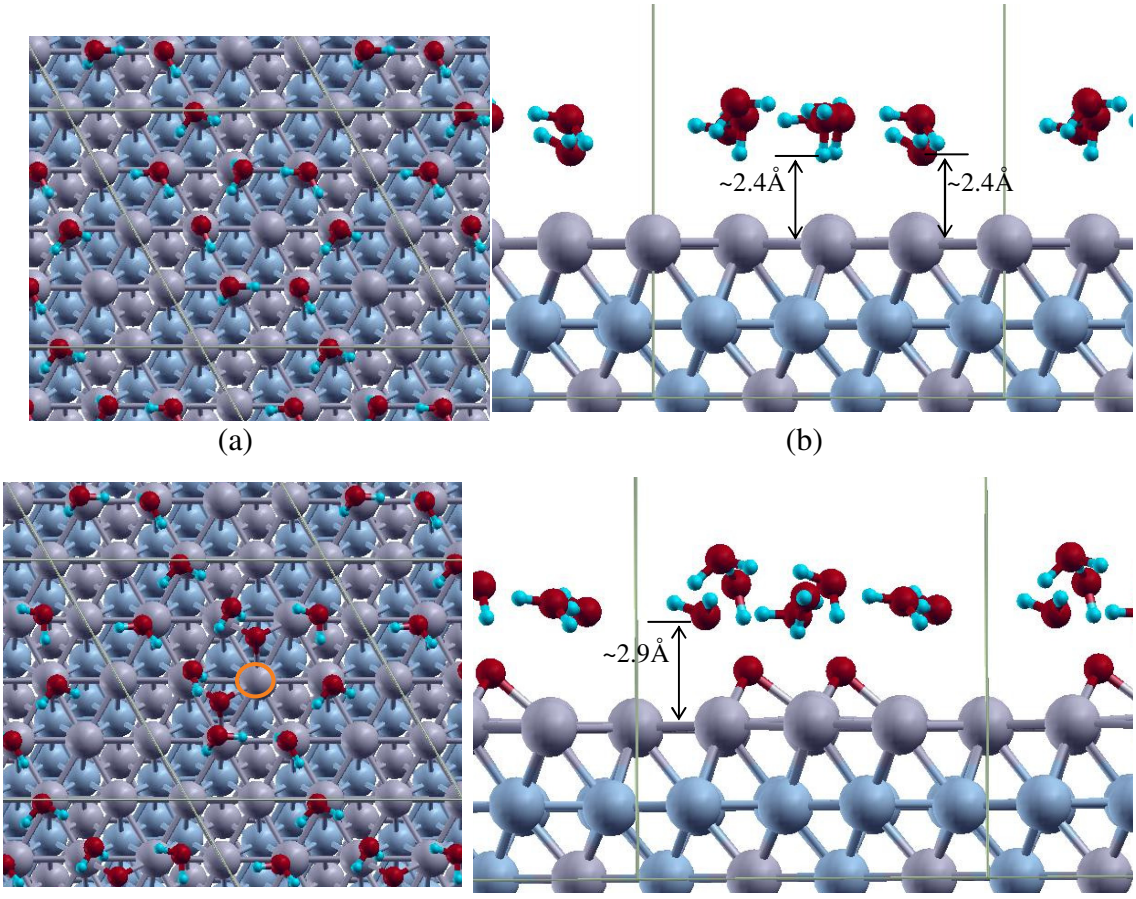

Fig. 5.2. Water molecules/atomic oxygen adsorbed on Pt-skin. Top: Water molecules adsorbed on Pt-skin (Pt/Co/PtCo) (a) top view (b) side view. Bottom: 0.125 ML coverage of O atoms adsorbed at fcc(Co) site on Pt/Co/PtCo and 0.5 ML of water(c) top view (d) side view. Grey: Pt, Blue: Co. The unit cell is outlined with a solid line.

On the *PtCo surface* (Fig. 5.1(c,d)), water molecules form H-bonds of 2.2 and 1.7 Å with the adsorbed O atoms and of 2.3 Å length with the nearby water molecules whereas the other H-bonds among water molecules which do not form H-bond with O are shorter (1.7-1.8 Å). Interestingly, we found that the water-oxygen adsorption induces surface reconstruction: two surface atoms (orange circles in Fig. 5.1c), one Pt and one Co, that are located higher than the others in z direction. The Pt atom is ~0.10 Å upward and the Co atom is ~0.3 Å upward from the average surface atom positions. The water molecules adsorb through their O atoms whereas their H atoms form H-bonds with the nearby water molecules. Such surface reconstruction is related to the strong interaction of the adsorbates with the surface atoms, especially with Co, resulting in some water molecules staying closer to the surface (the shortest O-surface distance is 2.3 Å, (Fig. 5.1c)) and others locating further away. The water molecules rearrange to maximize H-bonds among them and with the adsorbed O resulting in some weaker water-water H-bonds compared to those in absence of O.

In contrast, surface reconstruction is much less pronounced on the *Pt-skin surface* (Fig. 5.2(c,d)) where Pt surface atoms bonding with O or water are only ~0.05-0.08 Å above the surface plane, except for a Pt atom twofold coordinated with O atoms on the Pt-skin surface (orange circle in Fig. 5.2c) that is located 0.2 Å above the average surface plane; this is another indicator of the enhanced stability of this surface. This upward position of Pt may result from the attempt to screen the interaction between the two adsorbed oxygen atoms[124].

The oxygen binding energies in presence of water molecules, $BE_{O/W}$, are calculated using equation (5.1):

$$BE_{O/W} = [E_{(slab/water/oxygen)} - E_{(slab/water)} - E_{(oxygen)}]/2 \qquad (5.1)$$

where $E_{(slab/water/oxygen)}$ is the total energy of the system with water molecules and two oxygen atoms adsorbed on the surface (1/8 ML oxygen coverage), $E_{(slab/water)}$ is the energy of the system which only water molecules adsorbed on the surface and $E_{(oxygen)}$is

the energy of two oxygen atoms in gas phase. It should be emphasized that these oxygen binding energies, $BE_{O/W,}$ (Table 5.1) are different than those reported in Tables 4.8 and 4.9 in the previous chapter because $BE_{O/W}$ include interactions of oxygen both with the water layer *and* with the surface. In both surfaces the water layer interacts with each adsorbed O atom via an H-bond. Therefore, we reasonably assume that the interaction between the water layer and adsorbed oxygen on both surfaces are similar, thus the presence of the water layer on the Pt-skin structure induces a larger effect on the O binding energy with the metal surface as shown by the higher percentage of change (Table 5.1) than that without water. However, the distances $d_{O...surface}$, $d_{O...Pt\ surface}$ and $d_{O...Co\ surface}$show very slight elongation compared to those of O adsorbed on the clean surface (Tables 4.8 and 4.9 in the previous chapter), with the largest differences (0.04 and 0.09 Å for $d_{O...surface}$ and$d_{O...Pt\ surface}$,respectively) given in the Pt-skin surface.

Table 5.1.
Oxygen binding energy in presence of water, BEO/W, and optimized distances (in Å) on PtCo and Pt-skin (the systems of Fig. 5.1 c-d and 5.2 c-d).

Structure	$BE_{O/W}$(eV/O)	% differencebetween BE_O and $BE_{O/W}$	$d_{O...surface}$[a]	$d_{O...Ptsurface}$[a]	$d_{O...Cosurface}$[a]
PtCo	-4.85	1.62%	1.08	2.11	1.89
Pt/Co/PtCo	-3.08	6.95%	1.47	2.13	-

[a]$d_{O...surface}$ is the distance between O and the surface in vertical z direction, $d_{O...Pt\ surface}$ is the distance between O and the bound Pt atom, and $d_{O...Co\ surface}$ is the distance between O and the bound Co atom. The reported values are the average values of the two adsorbed O atoms.

5.4.2 Surface reconstruction at higher O coverage

New simulations of O adsorption without water were performed on the same surfacesat0.5 ML coverage with all O atoms located at fcc(Pt) on PtCo surface and at fcc(Co) on Pt-skin surface. After that, an additional O atom was added -increasing the coverage to 0.5625 ML- and it was found that adsorption is most stable at fcc(Co) on

PtCo and at fcc(Pt) on Pt-skin surface. Optimized geometries for PtCo surfaces are shown in Fig. 5.3.

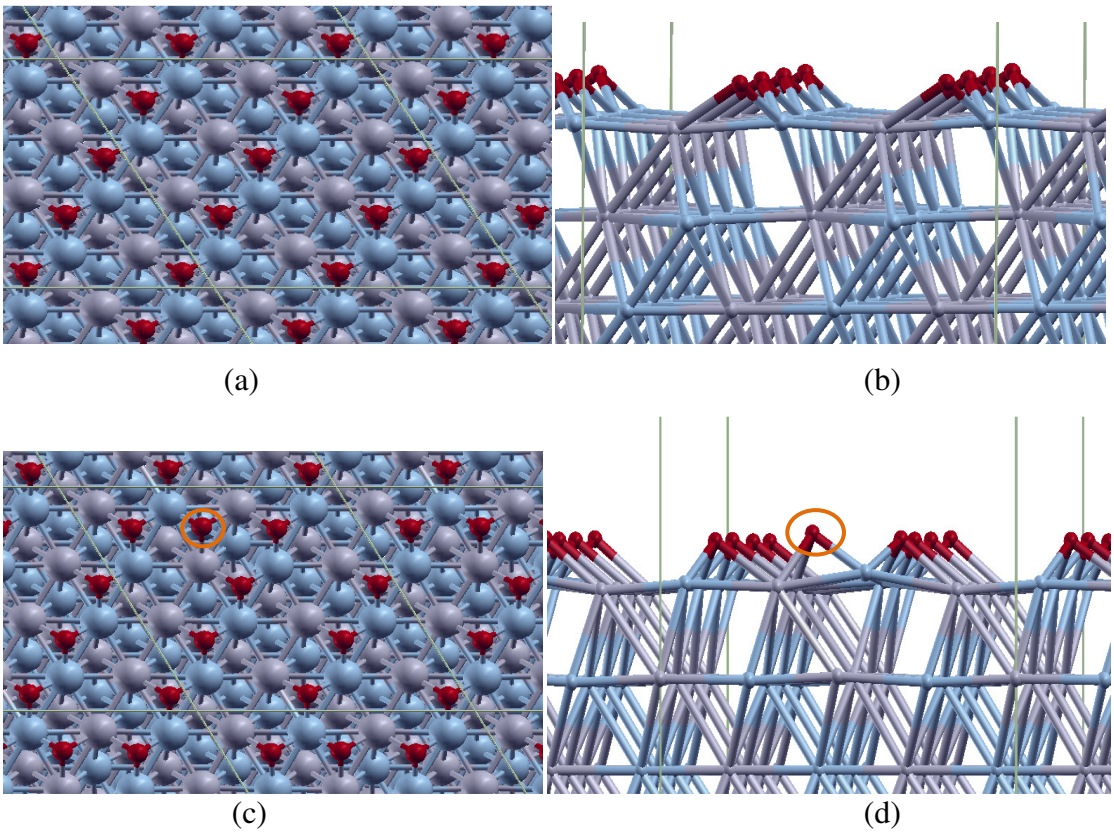

Fig. 5.3. 0.5ML and 0.5625 ML of atomic oxygen adsorbed on PtCo. Top: 0.5 ML of atomic oxygen adsorbed on PtCo at fcc(Pt) site (a) top view (b) side view. Bottom: 0.5625 ML of atomic oxygen adsorbed on PtCo with the additional oxygen atom (orange circle) adsorbed at fcc(Co) site (c) top view (d) side view. Grey: Pt, Blue: Co. The unit cell is outlined with a solid line.

On the *PtCo surface* (Table 5.2), the Co surface atoms *shift upward* while the Pt surface atoms *slightly shift downward* and the opposite trend is found for the subsurface atoms. Comparing with the clean surface, the displacements of surface and subsurface atoms are mostly in the Co atoms and they increase with the increase of O coverage. These may

result from higher affinity of O toward Co than Pt and to the attempt to reduce O…O interactions. However, the atomic displacements on the PtCo surface are *significantly smaller* than those reported for Pt(111) at the same O coverage which was shown to be 1.44 Å upward compared with clean Pt(111)[124]. Furthermore, the O-$Pt_{surface}$ and O-$Co_{surface}$ bond lengths show negligible change (<0.05 Å) with increasing O coverage. Similarly, the Pt-Pt and Co-Co surface bond lengths show <0.03 Å changes and small elongations ~0.1-0.2 Å of the Pt-Co bond lengths on the surface.

Table 5.2.
Binding energy of the additional O , $BE_{O/add}$, adsorbed on PtCo and surface atoms displacement. Pt/Co surface atoms and subsurface atoms maximum displacements[a] in the direction perpendicular to the surface (z direction) and the O-$Pt_{surface}$ and O-$Co_{surface}$ atoms bond lengths for PtCo surface at different coverage of adsorbates (Å).

Adsorbates	$BE_{O/add}$ (eV)	Pt surface atom displace-ment	Co surface atom displace-ment	Pt subsurface atom displace-ment	Co subsurface atom displace-ment	$d_{O…Ptsurface}$	$d_{O…Cosurface}$
Clean surface		0.0	0.0	0.0	0.0		
O at 0.5 ML (Fig. 5.3 a,b)	0.00	-0.04	+0.23	+0.06	-0.12	2.05	1.83
O at 0.5625 ML (Fig. 5.3 c,d)	-3.66	-0.08	+0.45	+0.09	-0.14	2.03-2.10	1.79-1.84
8 water molecules (Fig. 5.1 a,b)		(-0.05) – (+0.04)	(-0.02) – (+0.11)	(-0.02) – (+0.04)	(-0.03) – (+0.01)		
8 water molecules and O at 0.125 ML (Fig. 5.1 c,d)		(-0.05) – (+0.09)	(-0.02) – (+0.32)	(-0.02) – (+0.02)	(-0.02) – (+0.04)	2.11	1.89

[a]The displacement is compared with the clean surface. The minus sign shows the downward shift and plus sign show the upward shift of atom.

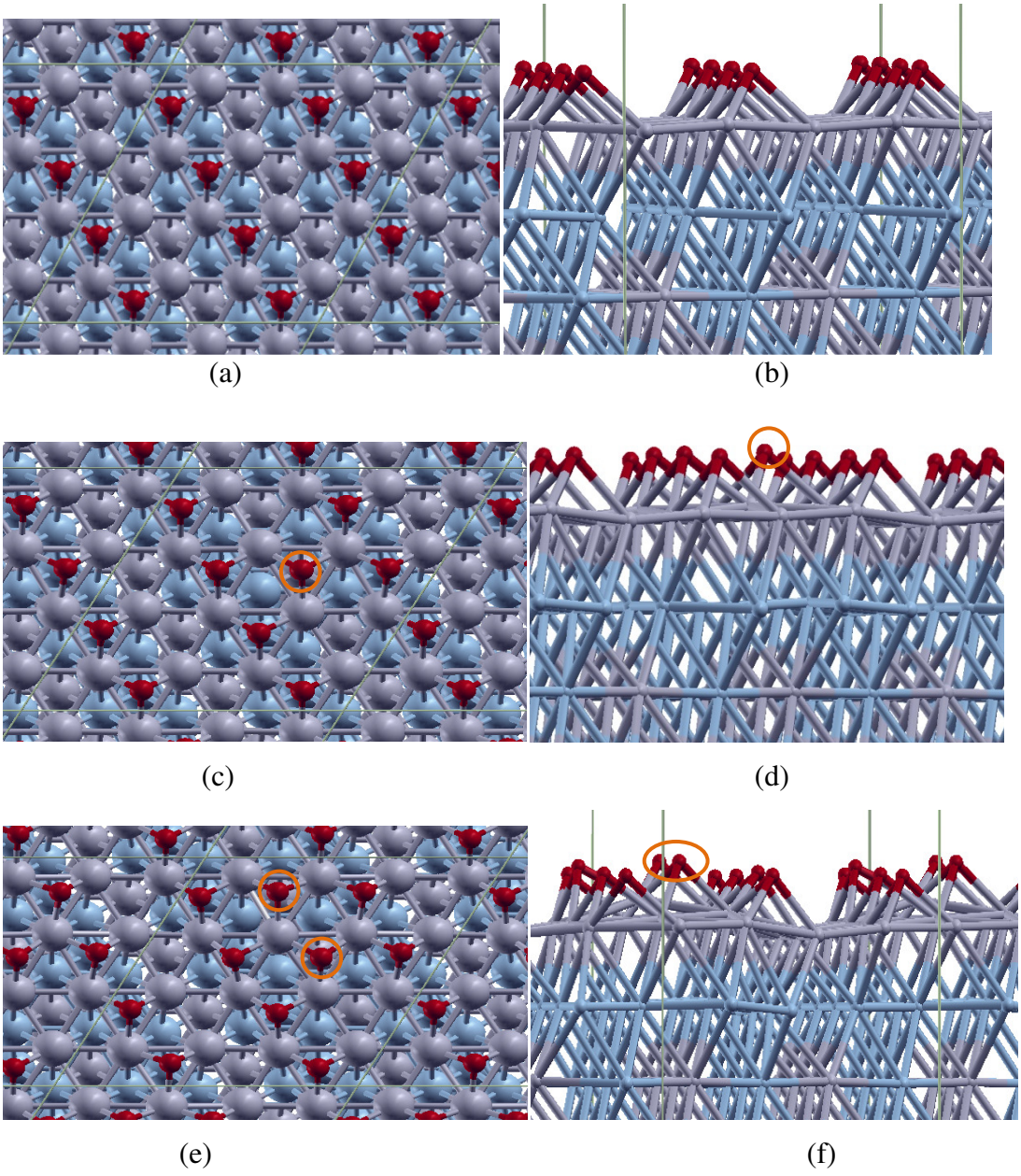

Fig. 5.4. 0.5ML and 0.5625 ML of atomic oxygen adsorbed on Pt-skin. Top: 0.5 ML of atomic oxygen adsorbed on Pt-skin (Pt/Co/PtCo) at fcc(Co) site (a) top view (b) side view. Middle: 0.5625 ML of atomic oxygen adsorbed on Pt-skin (Pt/Co/PtCo) with the additional oxygen atom (orange circle) adsorbed at fcc(Pt) site (c) top view (d) side view. Bottom: 0.6250ML of atomic oxygen adsorbed on Pt-skin (Pt/Co/PtCo) with the two additional oxygen atoms (orange circles) adsorbed at fcc(Pt) site (e) top view (f) side view. Grey: Pt, Blue: Co. The unit cell is outlined with a solid line.

Table 5.3.
Binding energy of the additional O , $BE_{O/add}$, adsorbed on Pt-skin (Pt/Co/PtCo) and surface atoms displacement. Pt surface atoms and Co subsurface atoms' maximum displacements[a] in the direction perpendicular to the surface (Z direction) and the O-$Pt_{surface}$ and Pt-Pt surface atoms bond lengths for Pt-skin (Pt/Co/PtCo) surface at different coverage of adsorbates (Å).

Adsorbates	$BE_{O/add}$(eV)	Pt surface atom displacement	Co subsurface atom displacement	$d_{O\ldots Ptsurface}$	$d_{Pt\text{-}Pt\ surface}$
Clean surface		0.0	0.0		2.70
O at 0.5 ML	0.00	+0.03	(-0.08) (+0.08)	2.07	2.65-2.77
O at 0.5625 ML	-2.26	(-0.13) (+0.17)	(-0.03) (+0.13)	2.05-2.08	2.64-2.83
O at 0.6250 ML	-2.19	(-0.25) (+0.74)	(-0.16) (+0.12)	2.02-2.12	2.65-2.83
8 water molecules (Fig. 5.2a,b)		(-0.09) – (+0.07)	(-0.02) – (+0.02)		
8 water molecules and O at 0.125 ML (Fig. 5.2c,d)		(-0.12) – (+0.14)	(-0.02) – (+0.03)	2.13	

[a]The displacement is compared with the clean surface. The minus sign shows the downward shift and plus sign show the upward shift of atom.

The *Pt-skin* surface (Fig. 5.4) also shows significantly lower displacements (Table 5.3) than those reported on Pt(111) at 0.5625 and 0.625 ML, respectively. However, Pt-skin surface atoms show slightly *larger displacements than Pt* on PtCo and *much smaller than those of Co* on PtCo surface at the same coverage. The displacements are either upward or downward for both Pt surface atoms and induce the displacements of Co subsurface atoms but at a lower extent. Such displacements of surface and subsurface atoms increase at higher O coverage, as shown in Table 5.3 for 0.625 ML. Similarly to the behavior on thePtCo surface, Pt-O bond lengths show small change (<0.07 Å) and there is a slight increase in the magnitude of the compression and stretching of Pt-Pt surface bonds lengths with the increase of O coverage. Furthermore, Tables 5.2 and 5.3show that water adsorption insignificantly affects surface reconstruction for both surfaces (the displacement of surface and subsurface atoms < 0.1 Å). However, when

both *water and O are adsorbed* on the surface, surface displacements are found at low oxygen coverage and their magnitude are comparable with that at high O coverage in absence of water. On the other hand, subsurface atom displacements are very subtle in the case of water and 0.125 ML of O adsorption. Therefore, subsurface atom displacements require higher coverage of O adsorption.

Charges of O and surface atoms using Bader charge analysis are displayed in Table 5.4. On the PtCo surface, Co atoms bear high positive charges whereas the charges of Pt surface atoms show negligible negative charges, the only exception is the Pt atom bonded to the additional O atom at 0.5625 ML. In comparison, the Pt atoms on Pt(111) are much more oxidized, bearing positive charges from 0.24 to 0.90e.Interestingly, the charge distribution on Pt-skin surface at 0.5ML and 0.5625ML shows significant changes, where those Pt atoms involved with 2 to 3 O atoms become oxidized, whereas those involved with only one O becomes much less oxidized. The lower degree of oxidation of the surface atoms explains the higher stability of Pt-skin compared to Pt(111)[125, 126].

The binding energies due to the additional oxygen, $BE_{O/add}$, shown in Tables 5.2 and 5.3 are calculated using equation (5.2) for 0.5625 ML O coverage and equation (5.3) for 0.625 MLO coverage:

$$BE_{O/add} = E_{(slab/\ oxygen\ 0.5625\ ML)} - E_{(slab/\ oxygen\ 0.5\ ML)} - E_{(atomic\ oxygen)} \quad (5.2)$$

$$BE_{O/add} = E_{(slab/\ oxygen\ 0.6250\ ML)} - E_{(slab/\ oxygen\ 0.5625\ ML)} - E_{(atomic\ oxygen)} \quad (5.3)$$

where $E_{(slab/\ oxygen\ x\ ML)}$ is the total energy of the system with O atoms adsorbed on the surface at x ML coverage, and $E_{(atomic\ oxygen)}$ is the energy of O. Note that $BE_{O/W}$ and $BE_{O/add}$cannot be compared because $BE_{O/W}$ includes interactions of O… surface and O…water whereas $BE_{O/add}$ includes interactions of O… surface and O…O. From the $BE_{O/add}$values it can be concluded that they follow similar trends that low coverage adsorption regarding the differences between PtCo and Pt-skin surfaces, although the adsorption energy decreases as the coverage increases.

Table 5.4.
Atomic charge (in unit of electrons) of surface O and surface atoms on PtCo, Pt/Co/PtCo and Pt(111) at 0.5ML and 0.5625ML O coverage.

O coverage	PtCo			
	O	$Pt_{surface}$	$Co_{surface}$	
0.5 ML	-0.74	-0.09	0.80	
0.5625 ML	-0.73	(-0.05) – (-0.13)	0.80	
	-0.68 (additional O)	0.11 (Pt bonding with 2 O)	0.97 (Co bonding with 3 O)	
O coverage	Pt/Co/PtCo			
	O	$Pt_{surface}$ bonding with 3 O	$Pt_{surface}$ bonding with 2 O	$Pt_{surface}$ bonding with 1 O
0.5 ML	-0.65		0.00	0.25
0.5625 ML	(-0.61)-(-0.64)	0.44	0.19-0.27	(-0.03)-(0.03)
	-0.67 (additional O)			
		Pt(111)[a]		
	O	$Pt_{surface}$ bonding with 3 O	$Pt_{surface}$ bonding with 2 O	$Pt_{surface}$ bonding with 1 O
0.5 ML	-0.76		0.54	0.24
0.5625 ML	-0.77 (additional O)	0.90	0.53	0.24

[a] The charge values of Pt(111) are from ref [124]

The Pt(111) surface reconstruction due to water and oxygen adsorption are studied by incorporating atomic oxygen at 0.11-1.00 ML coverage located at 3-fold fcc adsorption site in a layer of water with hexagonal hydrogen bonded network (Fig. 5.5). The surface and subsurface atoms displacements shown in Table 5.5 indicate that the displacement of those atoms due to atomic oxygen solely or with water layer is very subtle at all varied oxygen coverage and much less than those on PtCo and Pt-skin at the same oxygen coverage. Water layer rearrange hydrogen bond to interact with the adsorbed oxygen and among them resulting in water molecules moving away from the surface and the distance of water molecule to the surface increase approximately less than 1 Å (The change of distances between the water molecule to the surface at different oxygen coverage are shown in Appendix A). Therefore, the presence of Co on surface and subsurface plays a

role on surface reconstruction on PtCo and Pt/Co/PtCo due to oxygen adsorption and co-adsorption with water.

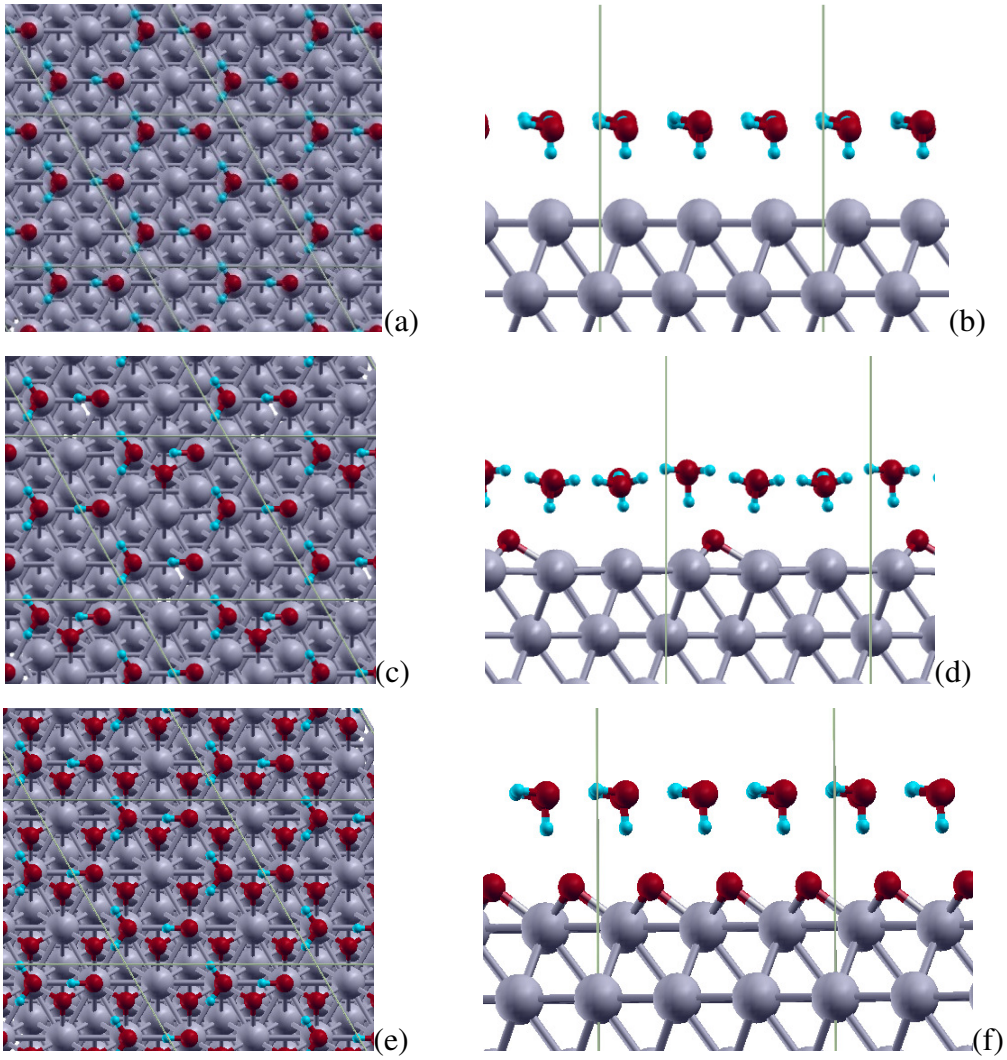

Fig. 5.5.Atomic oxygen co-adsorption with water layer on Pt(111). (a) top view of water layer with hexagonal hydrogen bond network, (b) side view of (a), (c) top view of 0.11 ML of O located at 3-fold fcc site co-adsorbed with water layer with hexagonal hydrogen bond network, (d) side view of (c), (e) top view of 1.00 ML of O located at 3-fold fcc site co-adsorbed with water layer with hexagonal hydrogen bond network, (f) side view of (e). The unit cell is outlined with a solid line.

Table 5.5.
Surface atoms displacement (Å) at varied O coverage both with and without water adsorption on Pt(111). Pt surface atoms and Pt subsurface atoms' maximum displacements[a] in the direction perpendicular to the surface (Z direction).

	Pt surface atom displacement		Pt subsurface atom displacement	
O coverage	without water	with water	without water	with water
0.11	(-0.03) – (0.06)	(-0.06) – (0.06)	(-0.02) – (0.03)	(-0.02) – (0.02)
0.22	(-0.08) – (0.17)	(-0.09) – (0.12)	(-0.05) – (0.06)	(-0.04) – (0.05)
0.33	(-0.05) – (0.17)	(-0.08) – (0.26)	(-0.02) – (0.05)	(-0.04) – (0.09)
0.44	(-0.07) – (0.07)	(-0.09) – (0.07)	(-0.03) – (0.07)	(-0.05) – (0.04)
0.56	(-0.08) – (0.13)	(-0.09) – (0.06)	(-0.07) – (0.09)	(-0.08) – (0.07)
0.67	(-0.09) – (0.11)	(-0.11) – (0.21)	(-0.06) – (0.09)	(-0.07) – (0.08)
0.78	(-0.06) – (0.08)	(-0.09) – (0.11)	(-0.01) – (0.08)	(-0.04) – (0.05)
0.89	(-0.06) – (0.06)	(-0.12) – (0.12)	(0.01) – (0.07)	(-0.05) – (0.05)
1.00	(-0.05)	(-0.20) – (0.00)	(0.05)	(-0.03) – (0.05)

[a]The displacement is compared with the clean surface. The minus sign shows the downward shift and plus sign show the upward shift of atom.

5.4.3. Electric field effects

In this section, we first analyze the effect of an applied electric field on the structure (Fig. 5.6) of water adsorbed on pure Pt, the alloys and Pt-monolayer over the alloy core surfaces, and then the corresponding effect on water co-adsorbed with oxygen on the same surfaces.

5.4.3.1 A water molecule adsorbed on Pt, PtCo, and Pt/Co/PtCo surfaces.

We have performed the calculations using cluster models and slab models. The water molecules is located at the Pt atop site, most stable site, on Pt(111) and Pt-skin slab at the Co atop site on PtCo. Tables 5.6 and 5.7 show the effect of an applied field on the geometry of the adsorbed water and on the charges calculated on slab models of Pt(111), PtCo(111) and Pt/PtCo (111) surfaces. For pure Pt, at positive fields, the water molecule

gets closer to the surface via O-Pt interaction yielding slightly higher binding energies; the same is observed on the Pt-skin surface (although the O-Pt distances are slightly longer) and on the PtCo surface through stronger O-Co interactions. When the field becomes negative, the repulsive force between O and the surface induces water reorientation that is revealed by the elongation of the O-Pt and O-Co distances and the weaker binding energies, while the H atoms become closer to the surface, but it is only at higher electric field -in the order of -0.8 V/Å for Pt(111)and probably at less negative fields for the Pt-skin- when the change of orientation of water on the surface is evident. However, the effect is much more pronounced in small clusters, where the water orientation change on Pt(111) is found at -0.13 V/Å, and larger effects of the electric fields are observed on water binding energies.(Tables and Figures of the cluster calculations are included as Appendix A). On the PtCo surface the change of orientation is not clearly observed, not even in the cluster models up to -0.51 V/Å due to the much stronger character of O-Co interaction.

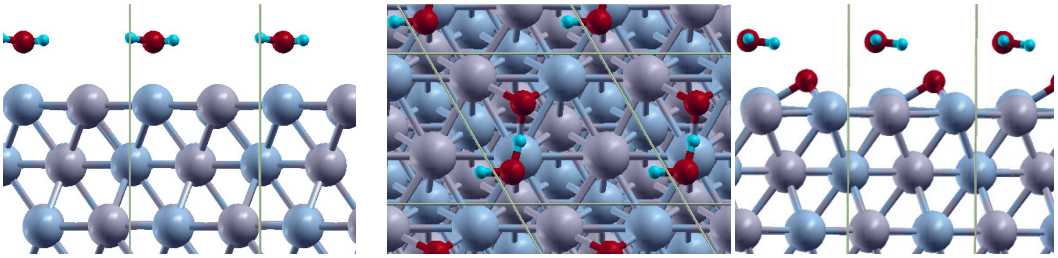

(a) (b) (c)

Fig. 5.6. The structure for the study on electric field effect. (a) water adsorbed at Co atop site on PtCo, (b) top view of water co-adsorbed with oxygen at fcc(Pt) site on PtCo (c) side view of (b). Water is adsorbed at the atop site on Pt(111) and Pt/Co/PtCo and oxygen is adsorbed at fcc(Co) site. The electric field is applied in a direction perpendicular to the surfaces. Grey: Pt, Blue: Co. The unit cell is outlined with a solid line.

Table 5.6.
Water binding energies and metal-O distances of a water molecule bonding with Pt(111), PtCo(111) and Pt/Co/PtCo (111) surfaces using slab models.

	Pt(111)		PtCo		Pt-skin	
E field (V/Å)	BE water (eV)	Pt-O (Å)	BE water (eV)	Co-O (Å)	BE water (eV)	Pt-O (Å)
0.51	-0.30	2.41	0.96	2.11	-0.22	2.64
0.39	-0.27	2.46	-0.40	2.46	-0.20	2.68
0.26	-0.25	2.51	-0.38	2.30	-0.18	2.70
0.13	-0.22	2.53	-0.35	2.26	-0.17	2.74
0.00	-0.21	2.54	-0.34	2.26	-0.16	2.76
-0.13	-0.19	2.55	-0.31	2.28	-0.15	2.77
-0.26	-0.18	2.66	-0.30	2.30	-0.15	2.81
-0.39	-0.17	2.64	-0.28	2.29	-0.15	2.88
-0.51	-0.17	2.61	-0.04	2.30	-0.14	2.86

Table 5.7 illustrates the charge distribution on each of the surfaces, which do not change significantly under the applied field. On Pt(111) the charge on the Pt atom bonded to water and on the water molecule are only slightly positive, whereas average charge on the rest of the surface is slightly negative. Much higher polarization is observed on the Pt-Co surface, with a clear oxidation of the Co atoms and reduction of the Pt atoms, and on the Pt-skin where all the surface atoms are negatively charged, thus reducing the interaction with the oxygenated compounds. The 1st layer underneath the Pt-Co alloy surface also shows an interesting polarization, which keeps the same pattern of the surface with Pt negatively charged and Co atoms positively charged, whereas on the Pt-skin (Pt/Co/PtCo) all the subsurface Co atoms are positively charged with an average value of 0.35 e (Tables for subsurface atoms' charges included in Appendix A). More pronounced changes in charge distribution are found in the cluster models, where the overall water charges become negative under negative fields.

Table 5.7.
Charges (in e) on Pt and water during bonding of a water molecule with Pt(111), PtCo(111) and Pt/Co/PtCo (111) surfaces using slab models.

	Pt(111)			PtCo(111)				Pt/Co/PtCo (111)		
E field (V/Å)	<Pt>	[a]Pt2	H_2O	<Pt>	[a]Co15	Co16	H_2O	[a]Pt1	<Pt>	H_2O
0.51	-0.10	0.07	0.08	-0.48	0.58	0.28	0.00	-0.13	-0.25	0.05
0.39	-0.08	0.07	0.08	-0.50	0.54	0.37	0.01	-0.15	-0.25	0.03
0.26	-0.08	0.07	0.07	-0.50	0.51	0.37	0.03	-0.16	-0.26	0.04
0.13	-0.08	0.06	0.06	-0.50	0.51	0.37	0.02	-0.16	-0.26	0.03
0.00	-0.09	0.06	0.05	-0.50	0.51	0.37	0.02	-0.16	-0.26	0.02
-0.13	-0.09	0.05	0.04	-0.51	0.51	0.37	0.00	-0.16	-0.26	0.01
-0.26	-0.08	0.01	0.04	-0.51	0.51	0.37	-0.01	-0.17	-0.26	0.01
-0.39	-0.09	0.02	0.03	-0.51	0.51	0.37	-0.02	-0.20	-0.26	0.01
-0.51	-0.09	0.03	0.14	-0.51	0.52	0.38	-0.04	-0.16	-0.23	0.00

[a]bonded with O

5.4.3.2 Atomic oxygen adsorption on Pt, PtCo, and Pt/Co/PtCo surfaces in presence of a water molecule.

In presence of adsorbed oxygen located at the three-fold hollow site, a water molecule also changes orientation on the surface under strong negative electric fields on slab models; as discussed in the previous section, the effect is detected on Pt(111) and Pt-skin surfaces, but less evident on the Pt-Co surface. This can be observed in Table 5.8, by the elongation of the O-Pt and O-Co distances under negative fields. Note that at the same time, the O-H_2O distance becomes shorter (H-bond stronger) in the three surfaces. The opposite effect: shortening of the O-Pt and O-Co distances and elongation of the O-H_2O distances is found for positive fields, denoting the increase of the water-metal interaction through oxygen and the weakening of H-bond between water and adsorbed oxygen.

Table 5.8.
Binding energies and metal-O distances of a water molecule bonding with Pt(111), PtCo(111) and Pt/Co/PtCo (111) surfaces covered with 0.25 ML of O using slab models. Pt-O bond is 2.03 Å in Pt(111), 2.09 Å in PtCo (111), and 2.08 Å in Pt-skin; Co-O is 1.84 Å in PtCo (111). These are average values that do not change significantly under the applied fields.

	Pt(111)		PtCo(111)		Pt/Co/PtCo (111)	
E field (V/ Å)	Pt-O(H_2O) (Å)	O-H_2O (Å) (H-bond)	Co-O(H_2O) (Å)	O-H_2O (Å) (H-bond)	Pt-O(H_2O)	O-H_2O (H-bond)
0.51	[a]	[a]	2.34	2.02	3.07	2.30
0.39	3.01	2.28	2.32	1.89	3.11	2.29
0.26	3.05	2.27	2.36	1.87	3.15	2.26
0.13	3.13	2.23	2.39	1.85	3.20	2.24
0.00	3.18	2.19	2.41	1.85	3.23	2.24
-0.13	3.19	2.18	2.43	1.83	3.24	2.23
-0.26	3.23	2.17	2.47	1.82	3.26	2.21
-0.39	3.30	2.15	2.51	1.80	3.34	2.18
-0.51	3.35	2.13	[a]	[a]	3.37	2.15

[a] Converged simulations of Pt(111) at 0.51 V/ Å and PtCo at -0.51 V/ Å could not be found.

The charge distribution on the surfaces in presence of water and adsorbed oxygen using slab models is shown in Table 5.9. Note that since O adsorbs in a hollow site the average charge of the three Pt atoms on the pure Pt surfaces are positive, much higher on Pt(111) than on the skin surface; the Co atoms on PtCo bear high positive charges and the Pt2 atom forming part of the fcc site is less negative. The PtCo alloy has a highly polarized subsurface, and the Pt-skin has all Co atoms bearing positive charges in the subsurface (Tables for subsurface atoms' charges included in Appendix A). When the results in this section are compared with those from cluster models (Tables and Figures of the cluster calculations are included as Appendix A), it is found that the lower coordination sites on the metal surface induce larger water orientation effects and changes in water-surface bond lengths and charge distributions but, as found with the slab models, no significant effect is detected on metal–O bond lengths. Current computational resources make impossible to evaluate nanoparticles of 500–1000 atoms for example within a DFT approach. For this reason, packed surfaces of slab models are used to provide one type of sites found in these nanoparticles, whereas low-coordination sites (steps, corners, edges) may be represented by stepped surfaces or by cluster models.

Table 5.9.
Charges (in e^-) on Pt, O, and water during bonding of a water molecule with Pt(111), PtCo(111) and Pt/Co/PtCo (111) surfaces covered with 0.25 ML of O using slab models. <Pt> is the average charge of the Pt atoms surrounding O in the fcc site of Pt(111) and Pt/Co/PtCo, while the fcc site on the PtCo surface is formed by two Co atoms (average charge indicated by <Co>) and the Pt2 atom.

E field (V/ Å)	Pt(111)				PtCo(111)					Pt/Co/PtCo(111)			
	<Pt>	[a]Pt4	O	H_2O	[a]Pt1	Pt2	<Co>	O	H_2O	<Pt>	[a]Pt3	O	H_2O
0.51	*	*	*	*	-0.43	-0.14	0.68	-0.88	0.04	0.04	-0.22	-0.68	0.04
0.39	0.23	-0.06	-0.67	0.04	-0.41	-0.11	0.62	-0.87	0.09	0.03	-0.23	-0.69	0.04
0.26	0.22	-0.06	-0.68	0.03	-0.43	-0.13	0.67	-0.91	0.05	0.03	-0.23	-0.69	0.04
0.13	0.22	-0.06	-0.77	0.03	-0.43	-0.13	0.67	-0.91	0.05	0.02	-0.23	-0.69	0.03
0	0.21	-0.06	-0.74	0.05	-0.43	-0.14	0.67	-0.91	0.04	0.02	-0.23	-0.71	0.03
-0.13	0.22	-0.06	-0.68	0.02	-0.43	-0.14	0.68	-0.91	0.04	0.02	-0.23	-0.71	0.02
-0.26	0.22	-0.06	-0.69	0.01	-0.43	-0.14	0.65	-0.91	0.03	0.02	-0.24	-0.70	0.02
-0.39	0.21	-0.06	-0.69	0.01	-0.44	-0.14	0.66	-0.91	0.02	0.02	-0.23	-0.72	0.01
-0.51	0.21	-0.06	-0.69	0.00	*	*	*	*		0.01	-0.23	-0.72	0.01

[a]Pt surface atom not bonded to the atomic oxygen.
*Converged simulations of Pt(111) at 0.51 V/ Å and PtCo at -0.51 V/ Å could not be found

5.5. Conclusion

On Pt-skin structures (Pt/Co/PtCo) O binding energies are significantly weaker than on PtCo and Pt(1 1 1), and they are further reduced by water co-adsorption thus favoring the subsequent oxygen reduction on the surface. Water molecules on the surfaces arrange maximizing H-bonds among themselves in order to enhance the system stability. At 0.25 ML of O coverage, strong interactions of water and oxygen with surface atoms, especially with Co, induce a small buckling of Co atoms that are shifted ~0.3 Å upward from the surface plane, but the buckling effect is negligible on Pt/Co/PtCo. At higher O coverage, further surface reconstruction effects are found where surface and subsurface

atoms shift upward or downward with respect to the bare surface due to screening of O-O interactions. Buckling increases with the increase of O coverage, and at a given coverage, the Co surface atoms displacement on PtCo is much larger than those of Pt surface atoms on PtCo and Pt-skin surfaces. However, especially on Pt-skin surfaces, buckling effects are negligible compared to those found on Pt(111) surfaces at the same O coverage. This finding is another indication of the stabilization effect of the alloy subsurface on the Pt-skin atoms [125, 126]. On the other hand, at relatively low O coverage, co-adsorption of O with water induces surface atom displacements of a magnitude comparable to that found at higher O coverage in absence of water. However, buckling of subsurface atoms mainly is affected by O adsorption rather than by water adsorption.

Spontaneous water dissociation is not found on the ordered and segregated alloy surfaces within the entire applied electric field range (-0.51 to 0.51 V/Å). Under a negative electric field, water tends to change orientation switching from a metal–O to a metal–H interaction. In extended surfaces, the change barely starts to be detected on Pt(111) and Pt-skin surfaces, but is not observed on Pt–Co due to the strongest O–Co interaction. In cluster models, where the surface atoms have much lower coordination, the changes are more pronounced. The electric fields induce very small in the binding energies and geometries of water adsorption for all the surfaces, but significant polarization of the surface and subsurface is found on the PtCo surface.

CHAPTER VI

SURFACE POURBAIX DIAGRAMS, STABILITY, AND OXYGEN REDUCTION ACTIVITY OF Pt/Ir-Co AND Pt/Pd/Ir-Co*

6.1. Introduction

As discussed in Chapters I, IV and V, Pt-skins from alloy catalysts show many good characteristics including lower Pt loading, and enhanced ORR activity and stability under acidic environment. The reduction of Pt loading can be improved even more, if Pt is only present on the shell while the core is composed of non-Pt elements. Pt/Pd is a very good candidate showing high ORR activity [27, 38, 127, 128]. Pd becomes an interesting metal contributing in a comparable or slightly better ORR activity in Pd-M (M=Co, Fe or Ti) than that of the commercial Pt catalyst [129-133]. Pd-skin surface can be formed in $Pd_3Fe(111)$ which the atomic fraction of Pd at the surface increases as a function of the annealing temperature and once the alloy is in contact with acid solution a small amount of Fe on the surface is immediately dissolved leaving Pd-skin on the surface[40]. This structure showed ORR activity comparable to that of Pt(111) surface which may result from such as the electronic property modification (the downshift in d band) by the Pd segregated surface layer[134], the atomic distribution in near-surface region and the effects from the interaction between Pd and the second metal. However, Pd-M or Pt-M (M = 3d transition metals) are not stable under an acidic environment; the M element is easily leached out causing a high surface area enriched with noble metals which may also dominate to high activity of this structure [40, 135]. When Pt-skin monolayers were deposited on structures such as $Pt/Pd/Pd_3Fe$, they showed even higher

*Part of this chapter is reprinted with permission from "Platinum Monolayer Electrocatalysts: Improving the Activity for the Oxygen Reduction Reaction with Palladium Interlayer on IrCo Alloy Core." By K. Gong, W. F. Chen, K. Sasaki, D. Su, M. B. Vukmirovic, W. Zhu, E. Izzo, V. Srinivasamurthi, L. Protsailo, P. Hirunsit, P. B. Balbuena, and R. R. Adzic, 2010, In press, Journal of Electroanalytical Chemistry,

ORR activity than Pt(111) and Pt/Pd(111)[40]. The OH species is destabilized on Pt/Pd/Pd_3Fe structure comparing to Pt/Pd(111) and Pt(111) showing weaker OH binding energy which may enhance the OH removal step in ORR [40]. Furthermore, Ir is one of the most stable core in acidic medium [136] and have high cohesive energy which can reduce the segregation tendency[136]. It also showed relatively high activity toward ORR after alloying with Co, yet lower than Pt(111) [137, 138]. However, the presence of Co causes large contraction of the Pt monolayer surface lattice resulting in unfavorable surface properties for ORR i.e. very weak adsorption of O_2 lowering the reactivity of Pt [39, 40, 127]. Thus, the new inexpensive hierarchical core-shell structure consisting of an inexpensive inner core, a palladium interlayer and Ir-Co alloyed core, and a surface platinum monolayer was experimentally developed and able to achieve relatively high ORR mass activity [139].

The atomic distribution in the nanostructure plays an important role which is influenced by the nature of the alloy, potential, and pH of electrolyte and should be determined in order to understand ORR catalysis at the atomic level. In addition, the importance of the atomic surface distribution should be emphasized because it is a substantial feature governing the ORR catalytic activity. A surface Pourbaix diagram shows the most stable surface structure as a function of potential and pH. In this chapter, we report the surface Pourbaix diagrams of core-shell structures comprising an IrCo and Ir_3Co core and a surface Pt monolayer with an interlayer of a Pd monolayer between the Pt surface monolayer and Ir-Co core. The diagrams can help to explain part of the reasons for the high-performance of the particular catalysts under ORR conditions.

Although the ORR at the cathode seems to be a simple combination of four protons and four electrons reacting with molecular oxygen to form two water molecules, the fundamental mechanisms are not yet fully understood due to its complexity which involve a number of different adsorbate intermediates and the electrode potential that causes oxidative corrosive processes which alter the initial surface properties. There are

two major proposed ORR pathways; “dissociative”[140] and “associative”[140-142] pathways. The associative pathways can be separated into two mechanisms: with and without hydrogen peroxide forming. The limiting steps on different electrode materials can be different partially resulting from how strong the intermediate species bind with the electrode. Norskøv et al. [109] examined those ORR pathways on several pure metal electrodes and found the ORR activity is low on metals such as Mo, Fe which bind oxygen too strongly and protonation/electron transfer is the limiting step on these metals. In contrast, metals that bind oxygen too weakly show low barrier for protonation/electron transfer but the oxygen dissociation step become limited. The effect of high O/OH coverage can even change the preferred pathways[109]. In this chapter, three possible ORR mechanisms will be investigated.

6.2. Objectives

1. Investigate segregation and dissolution trends of Pt/Pd/IrCo, Pt/Pd/Ir_3Co and those without Pd interlayer relative to Pt(111).
2. Examine the electronic properties of the surface structures and their interactions with ORR intermediates.
3. Study the influence of the electrochemical potential on the stability of surface structures.
4. Investigate possible ORR pathways and activity on the surfaces.

6.3. Methodology and computational details

6.3.1. Calculation method for surface segregation and Pt surface dissolution potential

In the surface segregation study, we used the method described in the work by Ma and Balbuena[61], where the segregating atom switches positions with one atom of the surface layer (or to the next top layer if segregation inside the core is investigated) as shown in Fig. 6.1, and the segregation energy is calculated as the difference of energies of the segregated and non segregated systems. The negative segregation energy indicates

the segregation is thermodynamically favorable and the opposite for the positive segregation energy.

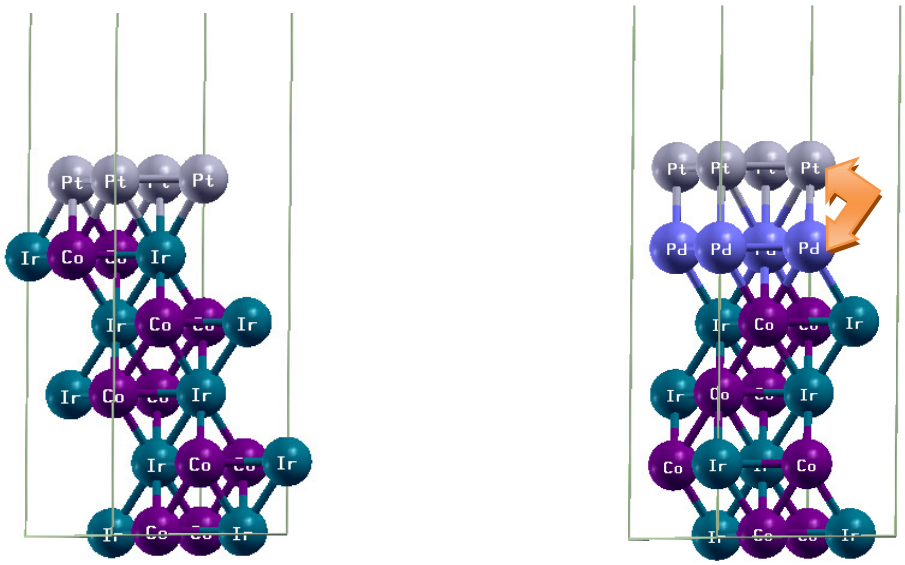

Fig. 6.1. Slab models of (a) Pt/IrCo and (b) Pt/Pd/IrCo. For example, the Pd segregated structure is constructed by exchanging a Pd atom in the 2nd layer with a Pt atom in the surface as shown by the arrow.

In order to analyze the dissolution of the Pt surface atoms on the alloy surface, the potential shift of the Pt dissolution reaction $Pt \rightarrow Pt^{2+} + 2e^-$ relative to that on Pt(111) was obtained as in ref [126]. The potential shift is denoted as ΔU.

$$\Delta U = \frac{\mu^{surf}_{Pt,alloy} - \mu^{surf}_{Pt,pure}}{ne} \qquad (6.1)$$

where $\mu^{surf}_{Pt,alloy}$ is the chemical potential of Pt in the alloy, $\mu^{surf}_{Pt,pure}$ is the chemical potential of Pt in Pt(111) and n an number of electron. The chemical potential is evaluated as

$$\mu_{Pt} = \frac{\Delta A}{\Delta N_{Pt}} \approx \frac{\Delta E}{\Delta N_{Pt}} \quad (6.2)$$

where A is the total free energy, E is the total energy and N_{Pt} is the number of Pt atoms.

The entropy contribution is not considered because we are interested in the difference value which those contribution may be canceled each other. Since the Pt dissolution tends to take place on the surface, the slab model is also used to calculate the chemical potential values and apply the eq.(6.3). A Pt atom is removed from the original optimized slab system and this new slab missing a Pt atom is optimized and obtain E'_{slab}.

$$\mu_{Pt} \approx \frac{E_{slab} - E'_{slab}}{\Delta N_{Pt}} \quad (6.3)$$

where E_{slab} is the energy of the original slab, E'_{slab} is the energy of the new slab missing a Pt surface atom, and ΔN_{Pt} is the different in the number of Pt atoms between the two slab systems.

6.3.2. Calculation method for surface Pourbaix diagram and ORR activity

It is a challenge to apply first-principles simulation to model an electrode system because in the simulation the number of electrons in the simulation box is fixed, rather than the electrochemical potential of system. The method we apply here to construct the surface Pourbaix diagrams and calculate free energy of the ORR step is based on Norskøv et al's work [109]. The method involves the thermochemistry of the reaction step regardless additional barrier from the protons and electron transfer. Also, recent calculations has shown proton transfer barrier to the metal surface may be small [143]. The barrier for each reaction step simply comes from the difference of the free energies of the intermediates in those steps. The method is explained as follows;

1) The reference potential is set to be that of the standard hydrogen electrode (SHE). This mean that at pH = 0 in the electrolyte and 1 bar of H_2 in the gas phase at 298

K the reaction free energy of $½H_2(g) \rightarrow H^+(aq) + e^-$ is zero at zero electrode potential (U = 0). Therefore, at the standard conditions, the free energy of the reaction $HA^* \rightarrow A + H^+ + e^-$ can be calculated as the free energy of $^*AH \rightarrow A + ½H_2$.

2) The zero point energy (ZPE) and entropic effect (TS) are included. The values shown in Table 6.1 are taken from those presented in ref [109] where ZPE and TS are calculated using DFT calculations for adsorbed species and using the standard tables for gas phase molecules[144]. The reference state is assigned to be gas phase H_2O at 0.035 bar because at this pressure at 300 K gas phase and liquid phase of water are in equilibrium.

Table 6.1.
Zero point energies and entropies of species in the reaction steps (eV).

	TS	ZPE	TΔS	ΔZPE
H_2O	0.67	0.56	0	0
H_2	0.41	0.27	-	-
$1/2O_2$	0.32	0.05	-	-
O*	0	0.07	-	-
OH*	0	0.30	-	-
OOH*	0	0.47	-	-
H*	0	0.17	-	-
$^*O + H_2$	0.41	0.34	-0.27	-0.22
$^*OH + 1/2H_2$	0.20	0.44	-0.47	-0.12

(*) means absorbed species

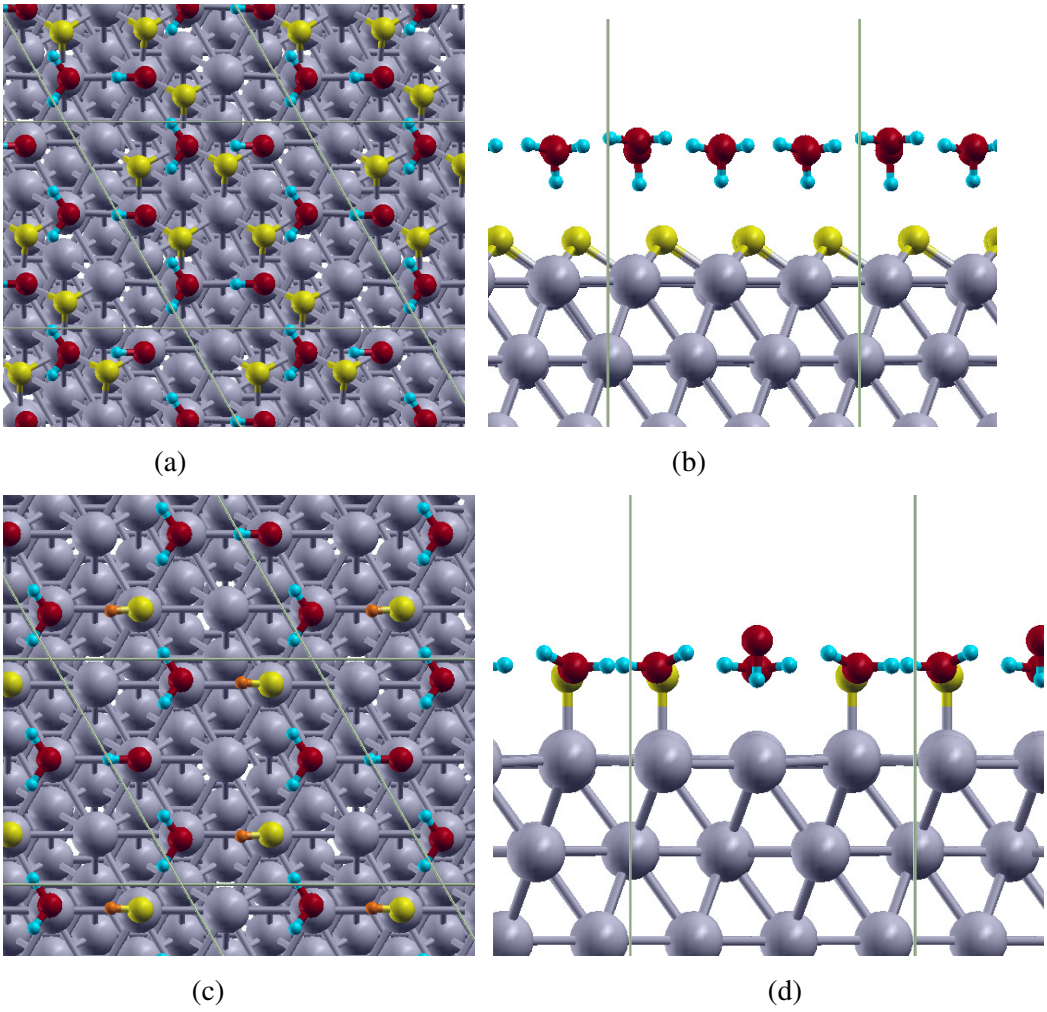

Fig. 6.2. Water layer co-adsorption with O and OH on Pt(111). (a) top view of a water layer co-adsorbed with 0.56 ML O, (b) side view of (a, (c) top view of water co-adsorbed with 0.22 ML OH, and (d) side view of (c). Grey-Pt, Yellow-O belonging to OH, Red-O belonging to H_2O, Orange-H belonging to OH and Blue-H belonging to H_2O. The unit cell is outlined with a solid line.

3) Since the interaction with water stabilizes adsorbates, the adsorption energies are affected by water environment. The model has included this effect in term of ΔG_W which is a shift in adsorption energy due to interaction with water. For the case of O adsorption a complete monolayer of water is included in the model for all varied O coverage, i.e. the number of water molecules are the same at all O coverage. We have included the

structure of a water layer with hexagonal hydrogen bond network studied by Ogasawara et al[145]. For OH, OOH and HOOH, the water molecules are added to form hexagonal hydrogen-bonded network, which is a structure, found to be very stable [146-149] i.e. the number of water molecules is varied with OH/OOH/HOOH coverage. Fig. 6.2 illustrates the structure of a water layer on Pt(111) with O adsorption and OH co-adsorption with water. The binding energies, BE_O and BE_{OH}, and their shift associated with water adsorption, ΔG_W, are shown in Table 6.2. The ΔG_W are calculated by subtracting BE_O/BE_{OH} with H_2O co-adsorbed from those without H_2O co-adsorbed. The same values of ΔG_W are also applied for the other structures.

4) The effect of a bias involving an electron in the electrode is treated by shifting the energy by –eU (ΔG_U) where U is the electrode potential relative to SHE.

Table 6.2.
Binding energies of O and OH at different coverage both with and without water presence and the shift of binding energies denoted as ΔG_W (eV/O, eV/OH).

O coverage (ML)	BE_O (w/o water)	BE_O (w/water)	ΔG_W of O
0.11	-4.52	-4.60	-0.08
0.22	-4.29	-4.28	0.01
0.33	-3.94	-4.14	-0.20
0.44	-3.76	-3.87	-0.11
0.56	-3.62	-3.69	-0.07
0.67	-3.45	-3.54	-0.09
OH coverage (ML)	BE_{OH} (w/o water)	BE_{OH} (w/water)	ΔG_W of OH
0.11	-2.34	-3.42	-1.08
0.22	-2.34	-3.44	-1.10
0.33	-2.21	-3.39	-1.18
0.44	-2.17	-2.90	-0.73

5) The local electric field in the double layer, which is a layer consisting of surface charges and counter ions formed at the interface, is taken account in a term ΔG_{field}. This term can be expressed as a term accounts for the change in reaction free energy caused by electric field and is obtained by varying the external electric field in the DFT calculation. The thickness of double layer is assumed to be 3 Å. Hence, the interesting electric field interval is between -0.4 V/Å and 0.4 V/Å. In Fig. 6.3, the change of adsorption energies, ΔG_{field}, for O, OH and OOH adsorbates at 0.25 ML coverage on Pt(111), Pt/IrCo, Pt/Ir_3Co, Pt/Pd/IrCo and Pt/Pd/Ir_3Co both with and without Pd segregation on Pd interlayer structures are shown as a function of the electric field strength. The electric field slightly affects on O, OH and OOH adsorption energies on all the surfaces where the maximum change is approximately 0.13 eV. The maximum change appears on a wide range of electric field on Pt/Ir_3Co and at high electric field (±0.4 V/Å). Other than that, the change is very small (less than ±0.05 eV) and show similar trend for all structures. Although the change in adsorption energy on Pt/Ir_3Co fluctuates with the change in electric field strength, we do not believe it is caused by the calculations were not well converged since we have carefully checked the convergence. The fluctuation may cause by interaction between Pt surface and rich Ir core. Furthermore, the term ΔG_{field} is also not strongly dependent on O/OH coverage. As shown in Fig. 6. 4, the coverage of O and OH on Pt(111) are varied at 0.11, 0.25 and 0.75 ML; however, the changes in adsorption energies are insignificant (less than 0.02 eV). Thus, ΔG_{field} in this study will not be included in the calculation model. In addition, Karlberg et al.[150] showed that the impact of ΔG_{field} term on the output of the model studied on pure metals is very small and the conclusion obtained from the model does not change without ΔG_{field} included.

(a)

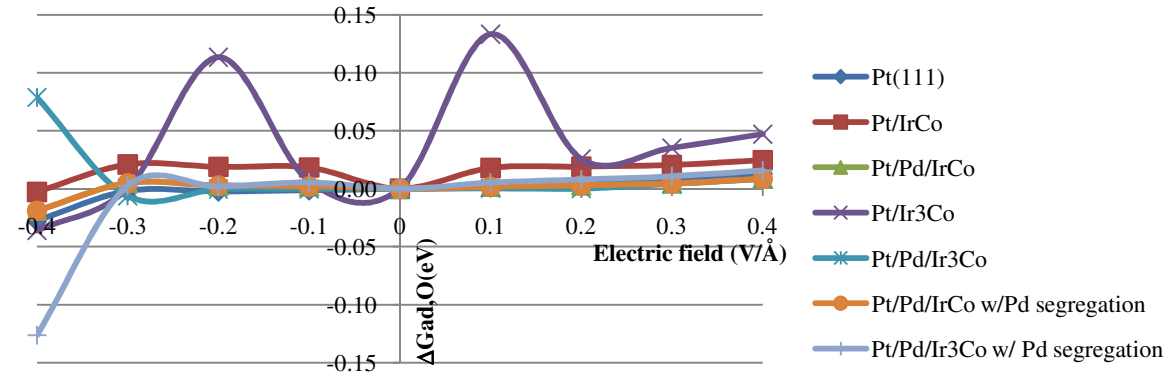

(b)

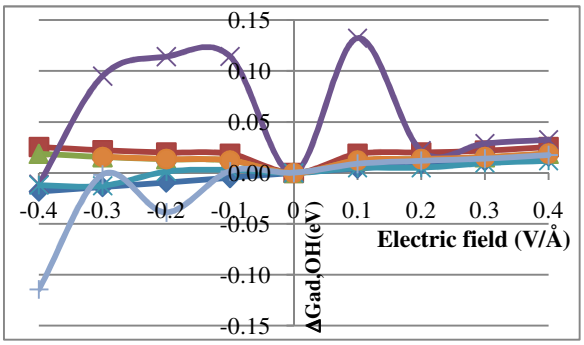

(c)

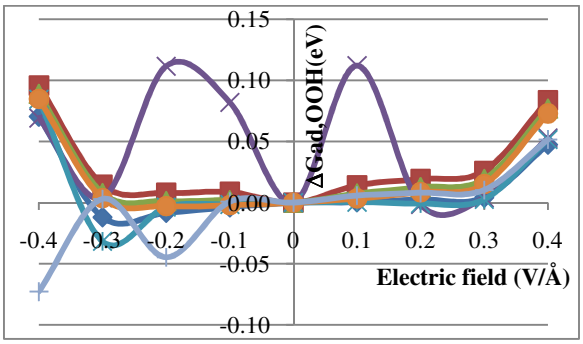

Fig. 6.3. The change of (a) O, (b) OH and (c) OOH adsorption energy at 0.25 ML as a function of electric field strength.

(a)

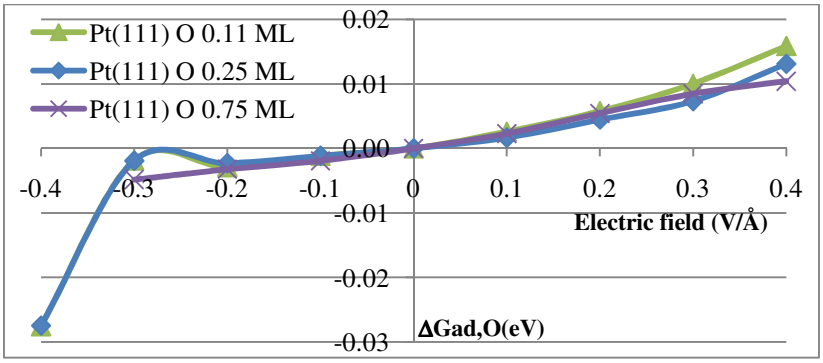

(b)

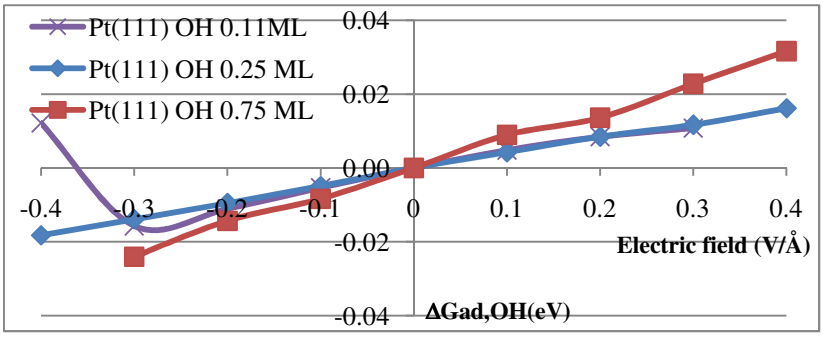

Fig. 6.4. The change of (a) O, and (b) OH adsorption energy at different O/OH coverage as a function of electric field strength.

6) The pH effect is included by correcting the free energy of H^+ by the concentration dependence of the entropy

$$\Delta G_{pH} = -kT \cdot \ln[H^+] = kT \cdot \ln 10 \cdot pH \qquad (6.4)$$

7) The reaction free energy is then calculated as;

$$\Delta G(U, pH, P_{H_2} = 1bar, T = 300K) = \Delta E + ZPE - TS + \Delta G_W + \Delta G_U + \Delta G_{pH} \quad (6.5)$$

where ΔE is reaction energy calculated using DFT.

6.3.3. DFT calculation details

A 2×2 unit cell is used to study the segregation energy and potential shift calculations which do not involve adsorbate coverage variation. For the calculations of the reaction free energies which involve with water adsorption and adsorbates coverage variation, the unit cell is expanded to be 3×3 for Pt(111) while 4×4 is used for Pt/Ir-Co and Pt/Pd/Ir-Co. The slab model contained 4 layers and 6 layers for 2×2 unit cells. The oxygenated adsorbate species and water molecules were located on one side of the slab to simulate the adsorbed system. The last two bottom layers and the bottom layer was fixed for the slab with 6 and 4 layers, respectively, while the other layers were relaxed to their lowest energy configurations. The fixed layers were set to their bulk bond distances according to their optimized lattice constants which were determined from bulk calculations. The calculated lattice constants are 3.81 Å for fcc Ir_3Co and 3.74 Å for fcc IrCo bulk compositions and they are in good agreement with the experimental values [137] of 3.81 Å for $Ir_{0.7}Co_{0.3}$ and 3.77 Å for $Ir_{0.5}Co_{0.5}$. The calculated Ir-Ir distances in Ir_3Co and IrCo bulk composition: 2.67 Å and 2.63 Å, respectively are also in fair agreement with the experimental values [137] of 2.70 for $Ir_{0.7}Co_{0.3}$ and 2.67 Å for $Ir_{0.5}Co_{0.5}$. The lattice constants of Pt/Pd/Ir_3Co and Pt/Pd/IrCo structures were also fixed according to those of Ir_3Co and IrCo core compositions. Spin-polarized DFT calculations were performed with the exchange-correlation functional Perdew-Burke-Ernzerhof (PBE) [87] described within the generalized gradient approximation, with $3 \times 3 \times 1$ k-points Monkhorst-Pack [88] mesh sampling in the surface Brillouin zone for 3×3 and 4×4 unit cells and with 8×8×1 for 2×2 unit cell. The plane-wave cutoff energy was optimized at 350 eV. The results were checked for convergence with respect to energy cutoff and number of k-points. Spin polarization was taken into account and the Methfessel-Paxton smearing [89] of order 2 with a value of smearing parameter σ of 0.2 eV was applied. The convergence criteria for ionic relaxation loop and electronic self-consistent iteration were set to 10^{-4} eV/Å and 10^{-5} eV, respectively.

6.4. Results and discussion

6.4.1. Segregation trends of Pt/IrCo, Pt/Ir$_3$Co, Pt/Pd/IrCo and Pt/Pd/Ir$_3$Co in vacuum and under O adsorption

The segregation trend is studied both under vacuum and 0.25 ML O coverage adsorption. Firstly, the investigation of O adsorption on the surfaces is reported. The atomic oxygen adsorption energies on Pt/Pd/IrCo and Pt/Pd/Ir$_3$Co are calculated at different possible sites shown in Fig. 6.5 and are reported in Table 6.3. The fcc(Ir) is the most stable site for O adsorption on Pt/Pd/IrCo and Pt/Pd/Ir$_3$Co and fcc(Co) is the next most stable site with BE_O difference less than 0.06 eV. The top Pt sites are the least stable site, then bridge sites and hcp sites. The trend for BE_O on those sites on Pt/IrCo and Pt/Ir$_3$Co are expected to be similar. The fcc(Ir) site is the most stable on with BE_O of -3.50 and -3.79 eV on Pt/IrCo and Pt/Ir$_3$Co, respectively.

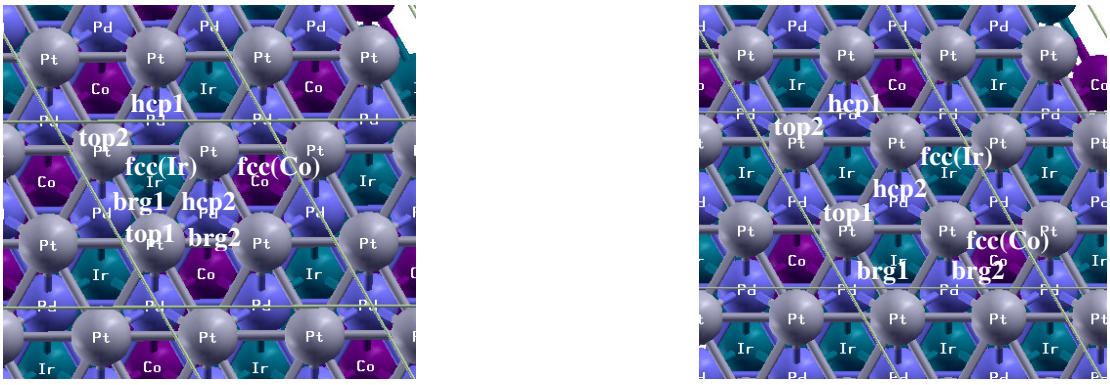

Fig. 6.5. Atomic oxygen adsorption sites on (a) Pt/Pd/IrCo and (b) Pt/Pd/Ir$_3$Co.

Table 6.3.
The binding energies of O, BE_O, on Pt/Pd/IrCo and Pt/Pd/Ir_3Co (eV/O). The location of the site is referred to Fig.6.5. The O binding energies of Pt/IrCo and Pt/Ir_3Co at fcc(Ir) site is -3.50 and -3.79 eV, respectively.

Pt/Pd/IrCo		Pt/Pd/Ir_3Co	
O adsorption site	BE_O	O adsorption site	BE_O
top1	[a]	top1	-2.56
top2	[a]	top2	[a]
hcp2	-3.37	hcp1	-3.56
hcp1	-3.33	hcp2	-3.54
fcc(Co)	-3.56	fcc(Co)	-3.74
fcc(Ir)	**-3.57**	fcc(Ir)	**-3.80**
Bridge1	-3.12	Bridge1	-3.25
Bridge2	-3.13	Bridge2	-3.23

[a] converged structures were not found.

Negative segregation energies (E_{seg}) indicate that segregation of the specified element is energetically favorable and the opposite for positive E_{seg}. Table 6.4 shows the segregation energies in vacuum and under oxygen adsorption. Atomic oxygen is located at the most stable fcc three-folded hollow site where Ir is located underneath for all structures.

For both cores, atoms from the Pd interlayer do not tend to segregate in vacuum, but they do under O, whereas both Co and Ir are stable inside the core. Without the Pd interlayer, both core elements are also stable, however Co may form subsurface alloys. The most energetic stable structure of the structure without Pd interlayer under vacuum is identified by varying the composition in each atomic layer while the overall composition is fixed. The results are shown in Table 6.5 in which the thermodynamically stable structure is Pt-skin surface with segregation of Co from layer the deepen layers forming rich-Co in the second layer for both IrCo and Ir_3Co cores. The segregation of Co is favorable only inside the core but not to the surface where the Pt-skin is still preserved. The change of the composition in each atomic layer due to the segregation of Co may influence the change in the segregation trend we observed in Table 6.4. The further segregation of the segregated structures under oxygen adsorption has been

Table 6.4.
Segregation energies of Pt/Pd/Ir-Co and Pt/Ir-Co structures in vacuum and under 0.25 ML of O adsorption.

	E_{seg} in vacuum (eV)		E_{seg} (eV) under 0.25 ML of O	
	$Pt/Pd/Ir_3Co$	**Pt/Pd/IrCo**	**$Pt/Pd/Ir_3Co$**	**Pt/Pd/IrCo**
Pd (subsurface) → surface	0.02	0.07	**-0.16 $Pt_{75}Pd_{25}/Pt_{25}Pd_{75}/Ir_{75}Co_{25}$**	**-0.12 $Pt_{75}Pd_{25}/Pt_{25}Pd_{75}/Ir_{50}Co_{50}$**
Ir (core in layer 3) → subsurface	0.37	0.64	0.46	0.54
Co (core in layer 3) → subsurface	0.19	0.11	0.26	0.16
Ir (core in layer 4) → layer3	**-0.07**	0.10	0.66	0.08
Co (core in layer 4) → layer3	**-0.22**	**-0.06**	0.19	0.06
	Pt/Ir_3Co	**Pt/IrCo**	**Pt/Ir_3Co**	**Pt/IrCo**
Co (subsurface) → surface	0.57	0.43	0.30	0.17
Ir (subsurface) → surface	0.46	0.37	0.60	0.52
Co (core in layer 3) → subsurface	**-0.48**	**-0.36**	**-0.40 $Pt_{100}/Ir_{50}Co_{50}/Ir_{100}/Ir_{75}Co_{25}$**	**-0.33 $Pt_{100}/Ir_{25}Co_{75}/Ir_{75}Co_{25}/Ir_{50}Co_{50}$**
Ir (core in layer 3) → subsurface	0.03	0.33	0.05	0.28

Table 6.5.
Relative energies of structures with varied atomic composition (atomic percent) in each layer for $IrCo(Ir_{50}Co_{50})$ and $Ir_3Co(Ir_{75}Co_{25})$ bulk compositions (without Pd interlayer) in vacuum.

Overall composition of $Pt_{100}/Ir_{50}Co_{50}$		Overall composition of $Pt_{100}/Ir_{75}Co_{25}$	
	Relative energy (eV)		Relative energy (eV)
$Pt_{100}/Ir_{50}Co_{50}$	0.000	$Pt_{100}/Ir_{75}Co_{25}$	0.000
$Pt_{100}/Ir_{25}Co_{75}/Ir_{75}Co_{25}/Ir_{50}Co_{50}/Ir_{50}Co_{50}$	-0.367	$Pt_{100}/Ir_{50}Co_{50}/Ir_{100}/Ir_{75}Co_{25}/Ir_{75}Co_{25}$	-0.486
$Pt_{100}/Ir_{25}Co_{75}/Ir_{50}Co_{50}/Ir_{75}Co_{25}/Ir_{50}Co_{50}$	-0.371	$Pt_{100}/Ir_{50}Co_{50}/Ir_{75}Co_{25}/Ir_{100}/Ir_{75}Co_{25}$	-0.703
$Pt_{100}/Co_{100}/Ir_{100}/Ir_{50}Co_{50}/Ir_{50}Co_{50}$	**-0.701**	**$Pt_{100}/Ir_{25}Co_{75}/Ir_{100}/Ir_{100}/Ir_{75}Co_{25}$**	**-0.982**

investigated and their segregation energies are shown in Table 6.6 and 6.7. It is clearly that under oxygen adsorption Co and Ir tend to segregate to the surface for the structure without Pd interlayer while the presence of Pd interlayer can prevent Co or Ir presenting on the surface. Both IrCo and Ir_3Co core agree on the same segregation trend conclusion. Since Ir and Co are easily oxidized at lower potential than Pt and they do not tolerate well in acidic environment especially Co, the segregation of Co and Ir to the surface can be problematic in term of the catalyst stability for ORR. Therefore, the Pd interlayer can induce better ORR activity compared to those without Pd interlayer which were observed in the experiment[139].

Table 6.6.
Segregation energies (eV) of the segregated structures of Co to the subsurface with Pt/IrCo and Pt/Ir_3Co overall compositions under 0.25 ML O adsorption.

Pt/IrCo overall composition		
	$Pt_{100}/Ir_{25}Co_{75}/Ir_{75}Co_{25}/Ir_{50}Co_{50}$	**$Pt_{100}/Co_{100}/Ir_{100}/Ir_{50}Co_{50}/Ir_{50}Co_{50}$**
Co layer 2 → 1 (O bond w/ Co)	**-0.361**	**-0.483**
Co layer 2 → 1 (O not bond w/ Co)	0.417	**-0.003**
Co layer 3 → 2	**-0.002**	-
Co layer 4 → 3	0.016	**-0.018**
Ir layer 2 → 1 (O bond w/ Ir)	**-0.299**	-
Ir layer 2 → 1 (O not bond w/ Ir)	0.744	-
Ir layer 4 → 3	0.177	-

Table 6.6. (cont'd)

Pt/Ir_3Co overall composition		
	$Pt_{100}/Ir_{50}Co_{50}/Ir_{100}/Ir_{75}Co_{25}/Ir_{75}Co_{25}$	**$Pt_{100}/Ir_{25}Co_{75}/Ir_{100}/Ir_{100}/Ir_{75}Co_{25}$**
Co layer 2 → 1 (O bond w/ Co)	**-0.122**	**-0.318**
Co layer 2 → 1 (O not bond w/ Co)	0.282	0.151
Co layer 4 → 3	**-0.111**	-
Ir layer 2 → 1 (O bond w/ Ir)	**-0.219**	**-0.219**
Ir layer 2 → 1 (O not bond w/ Ir)	0.802	0.423
Ir layer 4 → 3	0.435	-

Table 6.7.
Segregation energies of the segregated structures of Pd segregate to the surface with Pt/Pd/IrCo and $Pt/Pd/Ir_3Co$ overall compositions under 0.25 ML O adsorption.

	Pt/Pd/IrCo overall composition	$Pt/Pd/Ir_3Co$ overall composition
	$Pt_{75}Pd_{25}/Pt_{25}Pd_{75}/Ir_{50}Co_{50}$	$Pt_{75}Pd_{25}/Pt_{25}Pd_{75}/Ir_{75}Co_{25}$
Co layer 3 → 2	0.141	0.220
Ir layer 3 → 2	0.440	0.389

6.4.2. Electrochemical potential shift and Bader charge analysis in vacuum and under atomic oxygen adsorption

Here we investigate the relative potential shift, ΔU, which corresponds to the $Pt \rightarrow Pt^{2+} + 2e^-$ electrode reaction compared to that on pure Pt(111) surface. A positive shift indicates a delay on the dissolution of Pt atoms with respect to that occurring on a Pt(111) surface; the opposite holds for a negative shift. Table 6.8 shows that in vacuum and under 0.25 ML O adsorption, there is no significant stability improvement for Pt atoms on Pt-skin structures compared to Pt(111) in term of Pt surface atom dissolution.

In addition, the Bader charges analysis of Pt/Ir-Co and Pt/Pd/Ir-Co atoms in the 1st, 2nd and 3rd layers under vacuum and with 0.25 ML O adsorption at -0.2, -0.1, 0.0, and 0.2 eV/Å of the applied electric field strength are shown in Table 6.9-6.12. The atomic charges slightly change (< 0.01 e^-) with the electric field strength on all structures. The Co atoms in the core are oxidized and Ir atoms are reduced. Considering the clean surface, when the Pd interlayer presence, Co in the first core layer is slightly more oxidized, Ir is less reduced and the Pt-skin show slightly less negative charge than those without the Pd interlayer, while the Pd layer is slightly oxidized showing small positive charges (almost neutral). Upon atomic oxygen adsorption, the change in Ir and Co atoms' charge is subtle, the Pt atoms bonding with O are oxidized and those are free from O remain negative charges whereas the Pd shows less degree of oxidation than those in the clean slab. Since the presence of Pd interlayer does not reduce the oxidation degree of Pt-skin, the similar potential shift of the structures both with and without Pd interlayer were shown.

Table 6.8.
Calculated electrode potential shift, ΔU, in V, in vacuum and under 0.25 ML O.

		ΔU in vacuum (V)	ΔU with 0.25ML of O adsorbed (V)
$Pt/Pd/Ir_3Co$		0.09	0.07
	Pd segregates	N/A	-0.08**
Pt/Ir_3Co		-0.02	-0.08
Pt/Pd/IrCo		0.09	-0.01
	Pd segregates	N/A	-0.01**
Pt/IrCo		-0.02	-0.03

**The calculation is performed on a 2x4 supercell with 0.25 ML O coverage.

Table 6.9.
Partial charges obtained from Bader charge analysis on **Pt/IrCo** under vacuum and 0.25 ML O adsorption.

Pt/IrCo		1st layer				2nd layer				3rd layer			
Electric field (eV/Å)	O	Pt1	Pt2	Pt3	Pt4	Co5	Co6	Ir15	Ir16	Co7	Co8	Ir17	Ir18
Clean slab	N/A	-0.116	-0.152	-0.152	-0.116	0.433	0.433	-0.190	-0.190	0.331	0.331	-0.300	-0.300
-0.2 (w/O)	-0.656	0.118	-0.135	0.106	0.136	0.430	0.434	-0.252	-0.205	0.333	0.329	-0.343	-0.295
-0.1 (w/O)	-0.656	0.118	-0.135	0.106	0.136	0.430	0.434	-0.252	-0.205	0.333	0.329	-0.343	-0.295
0.0 (w/O)	-0.654	0.117	-0.134	0.105	0.136	0.430	0.434	-0.252	-0.204	0.332	0.329	-0.341	-0.297
0.2 (w/O)	-0.656	0.118	-0.135	0.106	0.136	0.430	0.434	-0.252	-0.205	0.333	0.329	-0.343	-0.295

Table 6.10.
Partial charges obtained from Bader charge analysis on **Pt/Pd/IrCo** under vacuum and 0.25 ML O adsorption.

Pt/Pd/IrCo		1st layer				2nd layer				3rd layer			
Electric field (eV/Å)	O	Pt1	Pt2	Pt3	Pt4	Pd5	Pd6	Pd7	Pd8	Co9	Co10	Ir17	Ir18
Clean slab	N/A	-0.098	-0.095	-0.095	-0.095	0.016	0.053	0.053	0.016	0.370	0.370	-0.266	-0.266
-0.2 (w/O)	-0.653	0.187	-0.108	0.160	0.164	-0.031	0.028	0.030	-0.009	0.372	0.371	-0.298	-0.267
-0.1 (w/O)	-0.653	0.187	-0.108	0.160	0.164	-0.031	0.028	0.030	-0.009	0.372	0.371	-0.298	-0.267
0.0 (w/O)	-0.654	0.187	-0.108	0.159	0.165	-0.030	0.028	0.030	-0.010	0.372	0.371	-0.295	-0.268
0.2 (w/O)	-0.653	0.187	-0.108	0.160	0.164	-0.031	0.028	0.030	-0.009	0.372	0.371	-0.298	-0.267

Table 6.11.
Partial charges obtained from Bader charge analysis on **Pt/Ir$_3$Co** under vacuum and 0.25 ML O adsorption.

Pt/Ir$_3$Co		1st layer				2nd layer				3rd layer			
Electric field (eV/Å)	O	Pt1	Pt2	Pt3	Pt4	Co5	Ir10	Ir11	Ir12	Co6	Ir13	Ir14	Ir15
Clean slab	N/A	-0.097	-0.126	-0.082	-0.143	0.513	-0.052	-0.039	-0.043	0.432	-0.150	-0.117	-0.081
-0.2 (w/O)	-0.664	0.140	-0.110	0.186	0.156	0.503	-0.112	-0.053	-0.056	0.435	-0.180	-0.117	-0.091
-0.1 (w/O)	-0.671	0.138	-0.113	0.184	0.156	0.505	-0.115	-0.052	-0.054	0.434	-0.170	-0.117	-0.100
0.0 (w/O)	-0.675	0.132	-0.118	0.179	0.150	0.505	-0.111	-0.053	-0.056	0.435	-0.176	-0.117	-0.100
0.2 (w/O)	-0.681	0.130	-0.121	0.178	0.147	0.504	-0.113	-0.052	-0.056	0.434	-0.181	-0.116	-0.092

Table 6.12.
Partial charges obtained from Bader charge analysis on **Pt/Pd/Ir$_3$Co** under vacuum and 0.25 ML O adsorption.

Pt/Pd/Ir$_3$Co		1st layer				2nd layer				3rd layer			
Electric field (eV/Å)	O	Pt1	Pt2	Pt3	Pt4	Pd5	Pd6	Pd7	Pd8	Co9	Ir13	Ir14	Ir15
Clean slab	N/A	-0.111	-0.115	-0.058	-0.110	0.066	0.060	0.059	0.059	0.480	-0.158	-0.125	-0.082
-0.2 (w/O)	-0.661	0.169	-0.102	0.170	0.194	0.007	0.038	0.036	0.066	0.459	-0.163	-0.137	-0.096
-0.1 (w/O)	-0.665	0.168	-0.106	0.167	0.192	0.006	0.036	0.034	0.066	0.469	-0.165	-0.139	-0.099
0.0 (w/O)	-0.671	0.163	-0.108	0.163	0.189	0.005	0.037	0.034	0.066	0.463	-0.165	-0.137	-0.098
0.2 (w/O)	-0.681	0.163	-0.112	0.161	0.187	0.008	0.036	0.034	0.066	0.458	-0.164	-0.137	-0.097

6.4.3. Surface Pourbaix diagrams

The diagram is constructed by assuming the surface is in equilibrium with protons and liquid water at 300 K without the presence of molecular oxygen, so that oxygen and hydroxyl may be exchanged between the surface and a reference electrolyte through the following reaction steps [151];

$$H_2O\ (l) + * \leftrightarrow HO* + H^+\ (aq) + e^- \quad (6.6)$$

$$\text{and,} \quad HO* \leftrightarrow O* + H^+(aq) + e^- \quad (6.7)$$

where * is a site on the catalyst surface, O* and HO* denote adsorbed species on a site. The oxidation of water to O* and HO* depends on potential (U) and pH and as explained in section 3.2 the reference potential is set to be that of the standard hydrogen electrode (SHE), thus the free energy, ΔG in eq(6.5), of the reactions are calculated directly from reactions;

$$H_2O\ (l) + * \leftrightarrow HO* + 1/2H_2(g) \quad (6.8)$$

$$HO* \leftrightarrow O* + 1/2H_2(g) \quad (6.9)$$

The free energy, ΔG, of a given surface structure with different O* and HO* coverage formed by reaction (6.6) and (6.7) is calculated as a function of potential U_{SHE} and pH. Since the metal dissolution may occur in acid solution, the free energy of dissolution of the surface atoms are estimated from standard reduction potentials as uniform dissolution corresponding to the bulk dissolution [151]. The dissolution of Pt in acidic solution;

$$Pt(s) \leftrightarrow Pt^{2+}(aq) + 2e^- \quad (6.10)$$

In order to calculate ΔE in eq(6.5), the binding energies of O* and HO* on the surfaces at the desired coverage are required. Table 6.13 shows the binding energy values on the Pt/Ir-Co and Pt/Pd/Ir-Co surfaces. The energy shifts due to the interaction with water are assumed to be the same with those calculated on Pt(111). At a specific pH, the plot

between ΔG and U_{SHE} is constructed as shown for an example in Fig. 6.6, where the plot shows surface structure of Pt/Pd/IrCo at pH=0. The similar plots at higher pH and of the other structures are shown as the supplement data in Appendix B. Then, the surface Pourbaix diagram in Fig. 6.6 is constructed by plotting the most stable surface as a function of pH and U_{SHE}. The most stable surface at a specific pH and U_{SHE} is designated as the one showing negative and the lowest free energy. The surface structures can be co-existing when the free energy difference is less than 0.05 eV/surface atom.

Table 6.13.
Binding energies of O and OH on Pt/Ir-Co and Pt/Pd/Ir-Co at different coverages, eV/(O/OH).

O coverage (ML) on Pt	Pt	O coverage (ML)	Pt/IrCo	Pt/Pd/IrCo	Pt/Pd/IrCo w/Pd segregated	Pt/Ir3Co	Pt/Pd/Ir3Co	Pt/Pd/Ir3Co w/Pd segregated
0.111	-4.52	0.125	-3.89	-3.92	-4.09	-3.95	-3.96	-4.14
0.222	-4.29	0.250	-3.89	-3.90	-4.09	-3.96	-3.98	-4.17
0.333	-3.94	0.375	-3.35	-3.39	-3.41	-3.37	-3.50	-3.50
0.444	-3.76	0.500	-3.03	-3.13	-3.19	-3.15	-3.30	-3.29
OH coverage (ML) on Pt		OH coverage (ML)						
0.111	-2.34	0.125	-2.13	-2.17	-2.10	-2.23	-2.16	-2.10
0.222	-2.34	0.250	-1.98	-1.96	-2.02	-2.03	-1.91	-2.06
0.333	-2.21	0.375	-1.89	-1.84	-2.00	-2.03	-1.93	-2.00

[a] The structures are shown in Appendix B.

The O and OH binding energies of the Pt-skin alloys are significantly weaker than pure Pt and the binding energies on all surfaces tend to decrease with the increase of coverage due to the repulsion between adsorbates. The Pd interlayer slightly affects O and OH binding energy.

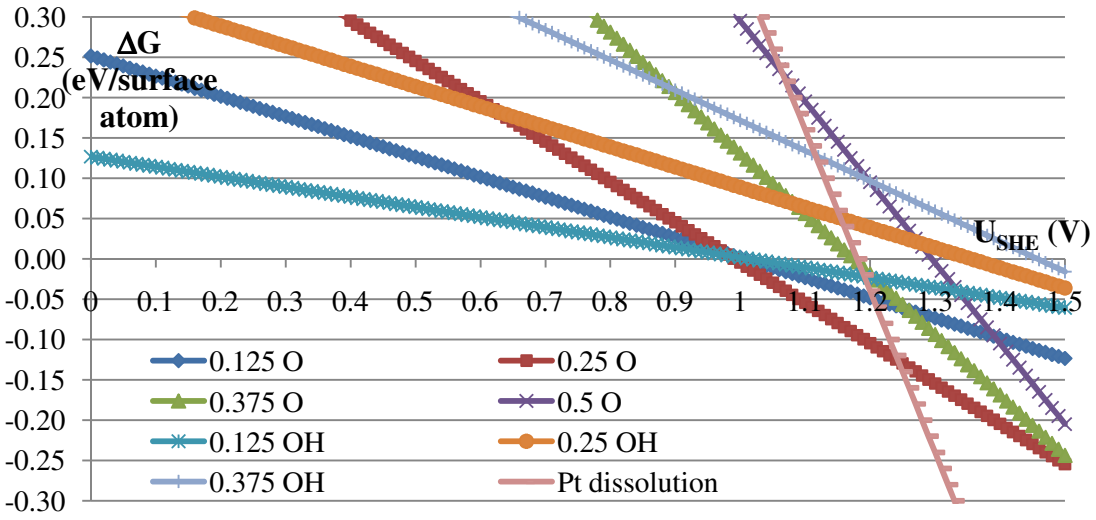

Fig. 6.6. Stability of O* and *OH on Pt/Pd/IrCo at pH = 0. A structure with 0.25 ML O* by water oxidation forms at 1.0 V_{SHE} and this structure is still stabilized even at high potential of 1.5 V_{SHE}.

The surface Pourbaix diagram of Pt(111) (Fig. 6.7a) shows that at pH = 0 and the potential below 0.70 V, the clean surface is the most stable and water starts to be oxidized forming 0.11 ML of O* and 0.11 ML of *OH between 0.70 and 0.88 V. At higher potential the coverage is increasing to be 0.22 ML, 0.33 ML and 0.44 ML of O* at 1.2 V. The diagram of Pt(111) has been investigated previously by Norskøv et al.[151] and their results showed the clean surface is stable up to 0.73 V agree with our results, then above 0.73 V the surface is covered with 0.33 ML of *OH and 0.25 ML of O* and the O* coverage increased to be 0.33 ML, 0.5 ML and 0.67 ML at 1.5 V. The smaller of stable O* coverage at higher potential than those reported by Norskøv et al.[151] may result from the difference in the exchange-correlation functional; nevertheless, the same trend of the rapid increase O* coverage with the potential increase is shown. The surface Pourbaix diagrams of Pt/IrCo (Fig. 6.7b), Pt/Ir_3Co (Appendix B), Pt/Pd/IrCo (Fig. 6.7c), Pt/Pd/IrCo with Pd segregation (Fig. 6.7d) and Pt/Pd/Ir_3Co both with and without Pd segregation (Appendix B) were constructed and they showed that water is oxidized at higher potential than Pt(111). The clean surface is stable up to 0.99 V at pH = 0 for Pt/IrCo and Pt/Pd/IrCo, 0.95 V for Pt/Ir_3Co and Pt/Pd/Ir_3Co, 0.89 V for Pt/Pd/IrCo with

Pd segregated and 0.85 V for Pt/Pd/Ir_3Co with Pd segregated. Furthermore, the lower O* coverage of 0.25 ML is the stable one for all surfaces up to 1.2 V. The segregated Pd atoms on the surface result in a lower potential at the onset of water oxidation compared to surfaces without Pd segregation. The delayed onset of water oxidation and lower coverage of O*/HO* on the Pt-skin surfaces relative to the Pt(111) surface may contribute to the higher ORR activity on those structures than on Pt(111). The higher activity may be occurring because the surfaces contain more free active sites even at higher potential while on the pure Pt surface water are oxidized at lower potential and the surface is covered with a higher concentration of oxygenated species. The calculated potentials at which Pt dissolution occurs at pH = 0 are shown to be ~1.25-1.30 V on all surfaces indicating that the main obstacle to ORR activity on these surfaces is activity not Pt dissolution. However, the stability of the Pt/IrCo and Pt/Ir_3Co structures are challenged by the segregation of the core components, Ir and Co, consequently, these metals would subsequently dissolve while introducing significant changes in surface composition and morphology.

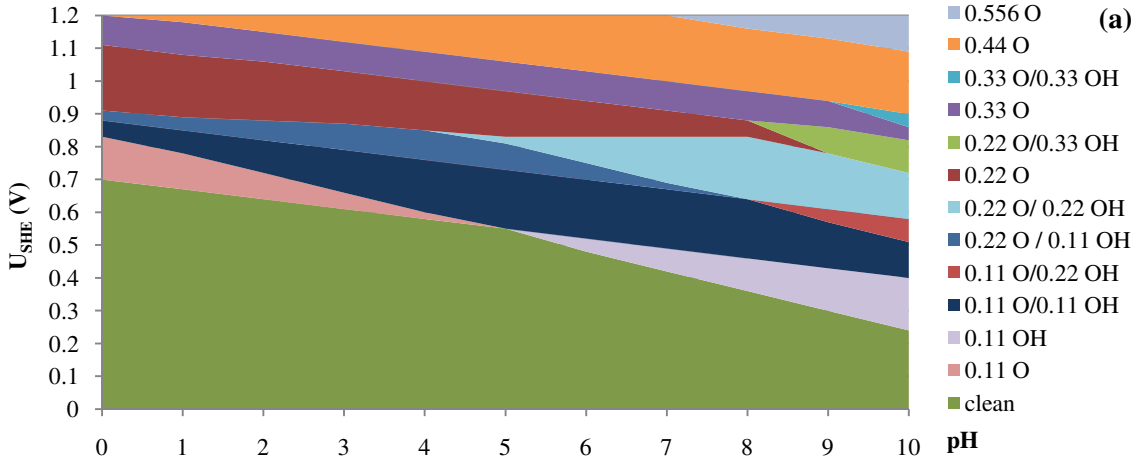

Fig. 6.7. Surface Pourbaix diagram of (a) Pt(111), (b) Pt/IrCo, (c) Pt/Pd/IrCo and (d) Pt/Pd/IrCo with Pd segregated .

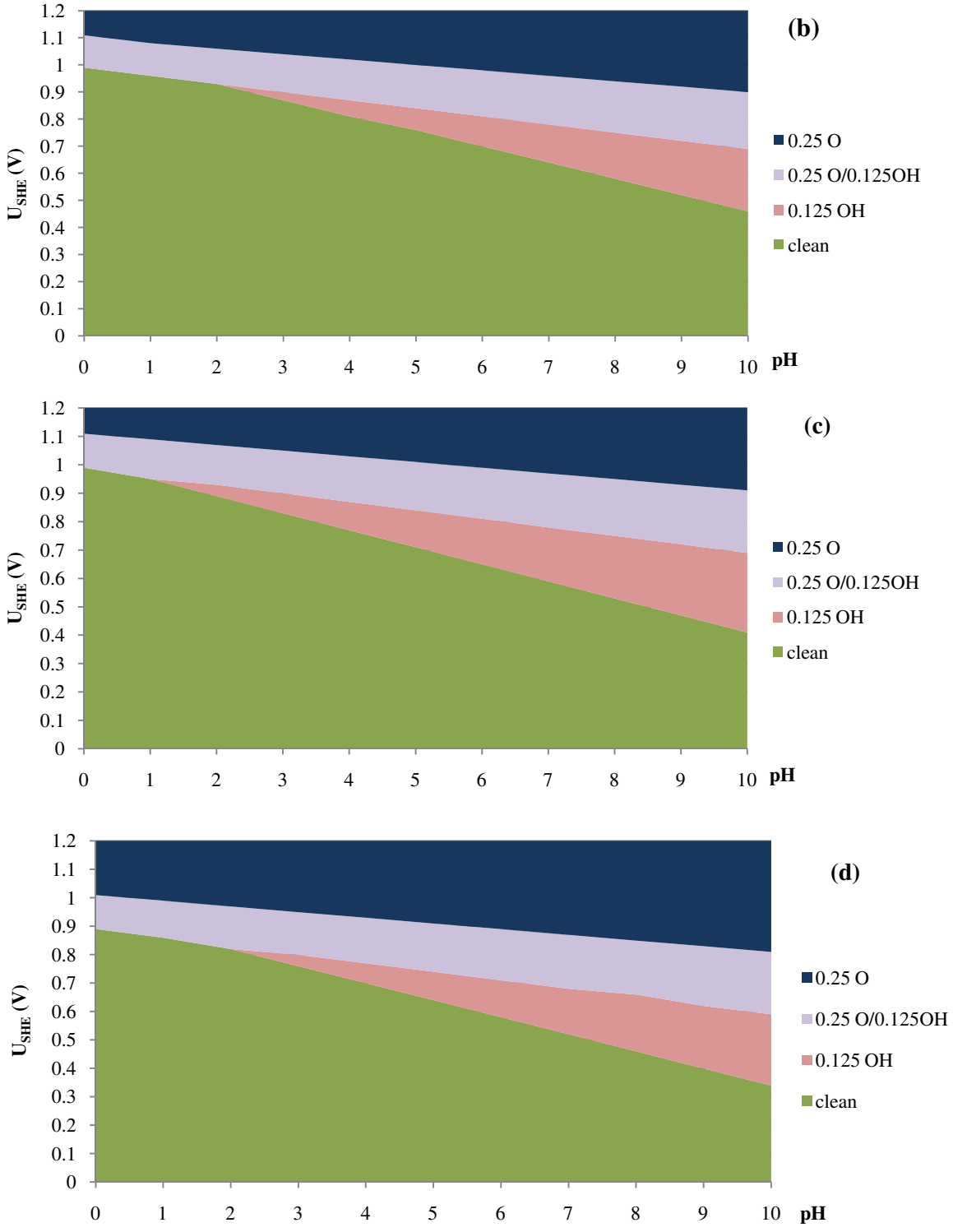
(b)
(c)
(d)
U_{SHE} (V)
pH
0.25 O
0.25 O/0.125OH
0.125 OH
clean
0
0.1
0.2
0.3
0.4
0.5
0.6
0.7
0.8
0.9
1
1.1
1.2
0
1
2
3
4
5
6
7
8
9
10

Fig. 6.7. (cont'd)

6.4.4. Reaction barrier energies and activity

The following three possible ORR mechanisms are investigated in this section. The first mechanism is called the dissociative mechanism in which O_2 dissociate to be O then, form OH and H_2O whereas O_2 does not dissociate but coupled with a proton and an electron transfer forming OOH in the second (Associative I) and the third (Associative II) mechanism. The OOH coupled with a proton and an electron transfer produce HOOH (hydrogen peroxide) in the associative II mechanism. All three mechanisms share the same last step of OH removal forming water. In addition, the dissociative and associative I mechanisms share the step of $O^* + H^+ + e^- \leftrightarrow HO^*$ and the associative I and II mechanisms share the step of OOH formation, $^*O_2 + H^+ + e^- \leftrightarrow HOO^*$.

Dissociative mechanism	**Associative I mechanism**	**Associative II mechanism** (forming hydrogen peroxide)
$1/2O_2 \leftrightarrow O^*$	$O_2 \leftrightarrow {}^*O_2$	$O_2 \leftrightarrow {}^*O_2$
$O^* + H^+ + e^- \leftrightarrow HO^*$	$^*O_2 + H^+ + e^- \leftrightarrow HOO^*$	$^*O_2 + H^+ + e^- \leftrightarrow HOO^*$
$HO^* + H^+ + e^- \leftrightarrow H_2O$	$HOO^* \leftrightarrow HO^* + O^*$	$HOO^* + H^+ + e^- \leftrightarrow HOOH^*$
	$O^* + H^+ + e^- \leftrightarrow HO^*$	$HOOH^* + H^+ + e^- \leftrightarrow 2HO^*$
	$HO^* + H^+ + e^- \leftrightarrow H_2O$	$HO^* + H^+ + e^- \leftrightarrow H_2O$

* denote adsorbed species

The reaction barrier free energies are calculated at 0.9 V and pH = 0. The clean surface of Pt(111), Pt/IrCo, Pt/Ir_3Co, Pt/Pd/IrCo, Pt/Pd/Ir_3Co with and without Pd segregation, and the surfaces that show to be the most stable one at 0.9 V, pH = 0 according to the surface Pourbaix diagrams on each structure; 0.22 ML O and 0.11 ML OH on Pt(111), 0.25 ML O and 0.125 ML OH on Pt/Pd/IrCo and Pt/Pd/Ir_3Co with Pd segregated, are considered. The calculated barrier free-energy of each reaction step on Pt(111), Pt/(Pd)/IrCo and Pt/(Pd)/Ir_3Co are shown in Fig. 6.8, 6.9 and 6.10, respectively. The presence of O and OH on the surface and their concentration can affect the binding energy of ORR intermediate species which can be caused by attractive or repulsive interactions among themselves and by changes in surface electronic properties (i.e.

surface charges and d-band). The intermediate binding energies are the key parameters in reaction barrier energy determination, thus the presence of O and OH on the surface and their concentrations significantly affect the reaction barrier magnitude and consequently the ORR activity.

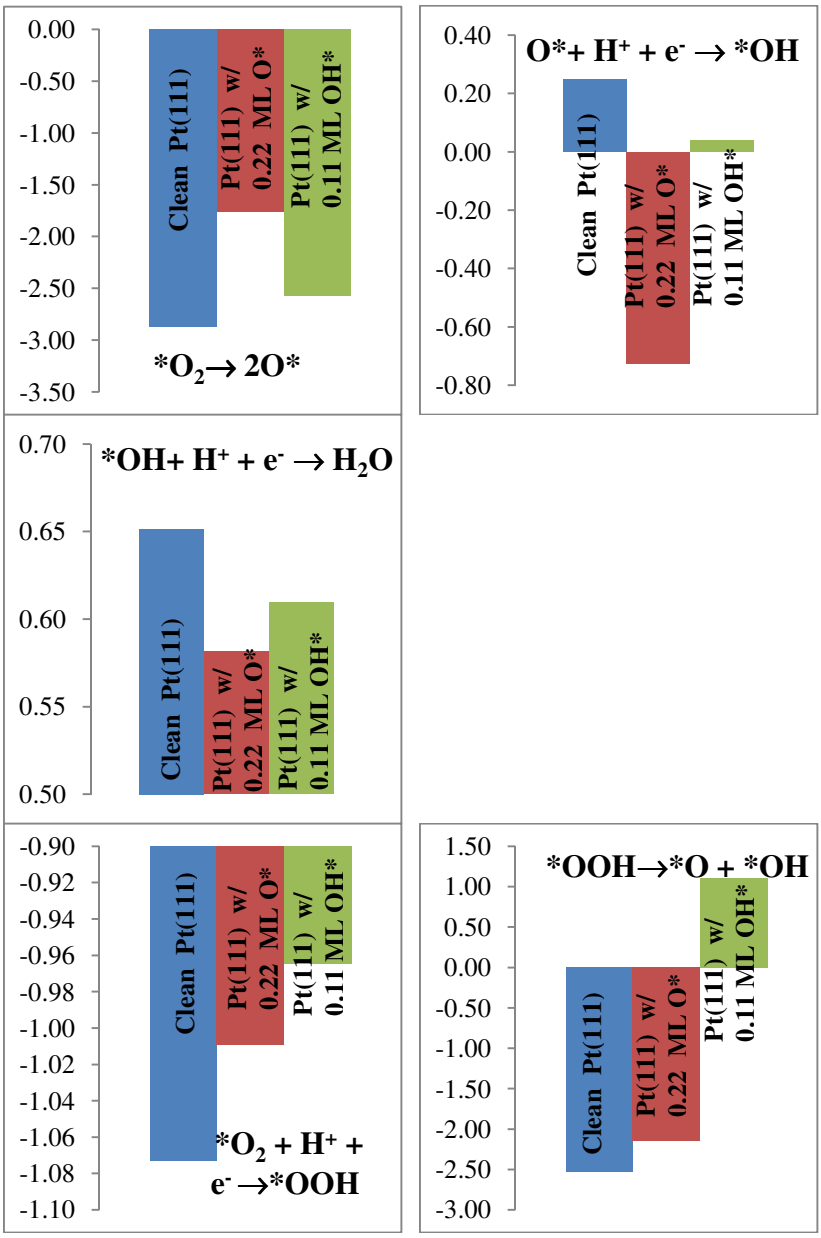

Fig. 6.8. Reaction barrier free-energy of all reaction steps at 0.9 V, pH = 0 on Pt(111), Pt(111) with 0.22 ML O* and Pt(111) with 0.125 ML *OH surfaces.

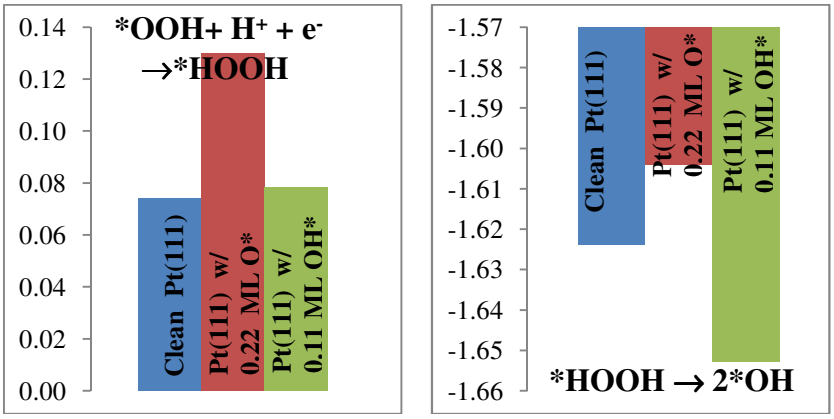

Fig. 6.8. (cont'd)

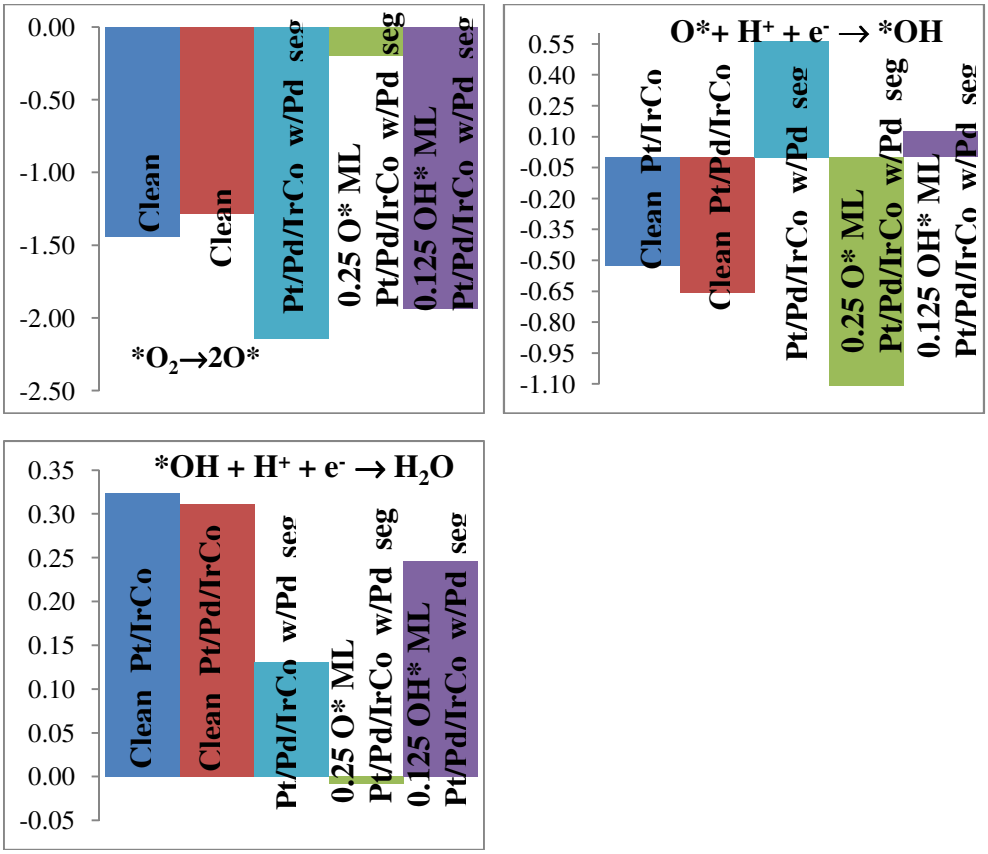

Fig. 6.9. Reaction barrier free-energy of all reaction steps at 0.9 V, pH = 0 on Pt/IrCo, Pt/Pd/IrCo, Pt/Pd/IrCo with Pd segregated, 0.22 ML O* and 0.125 ML *OH on Pt/Pd/IrCo with Pd segregated surfaces.

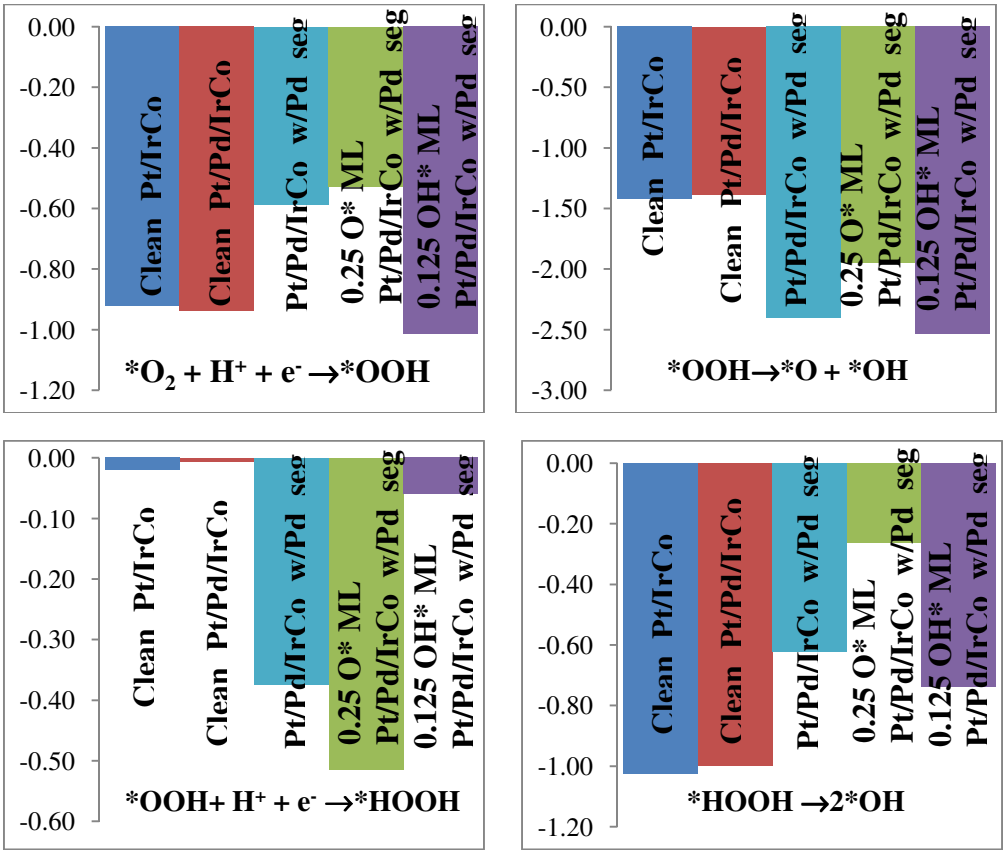

Fig. 6.9. (cont'd)

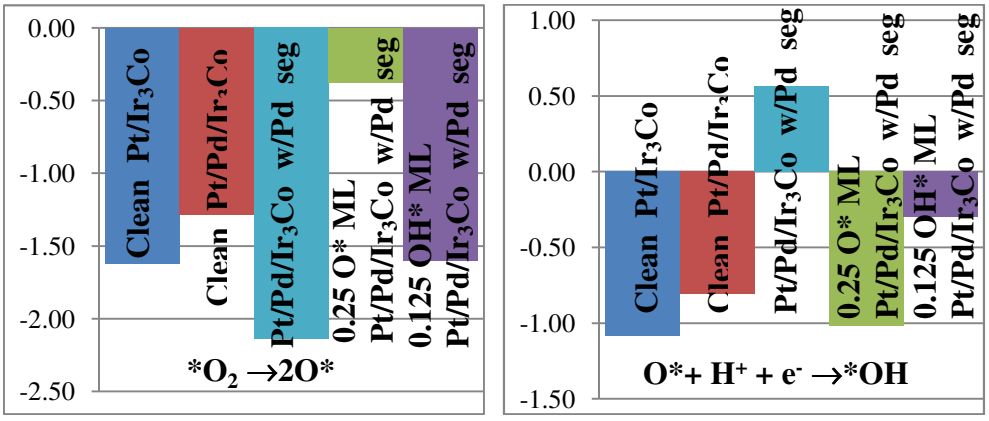

Fig. 6.10. Reaction barrier free-energy of all reaction steps at 0.9 V, pH = 0 on Pt/Ir_3Co, $Pt/Pd/Ir_3Co$, $Pt/Pd/Ir_3Co$ with Pd segregated, 0.22 ML O and 0.125 ML OH on $Pt/Pd/Ir_3Co$ with Pd segregated surfaces.

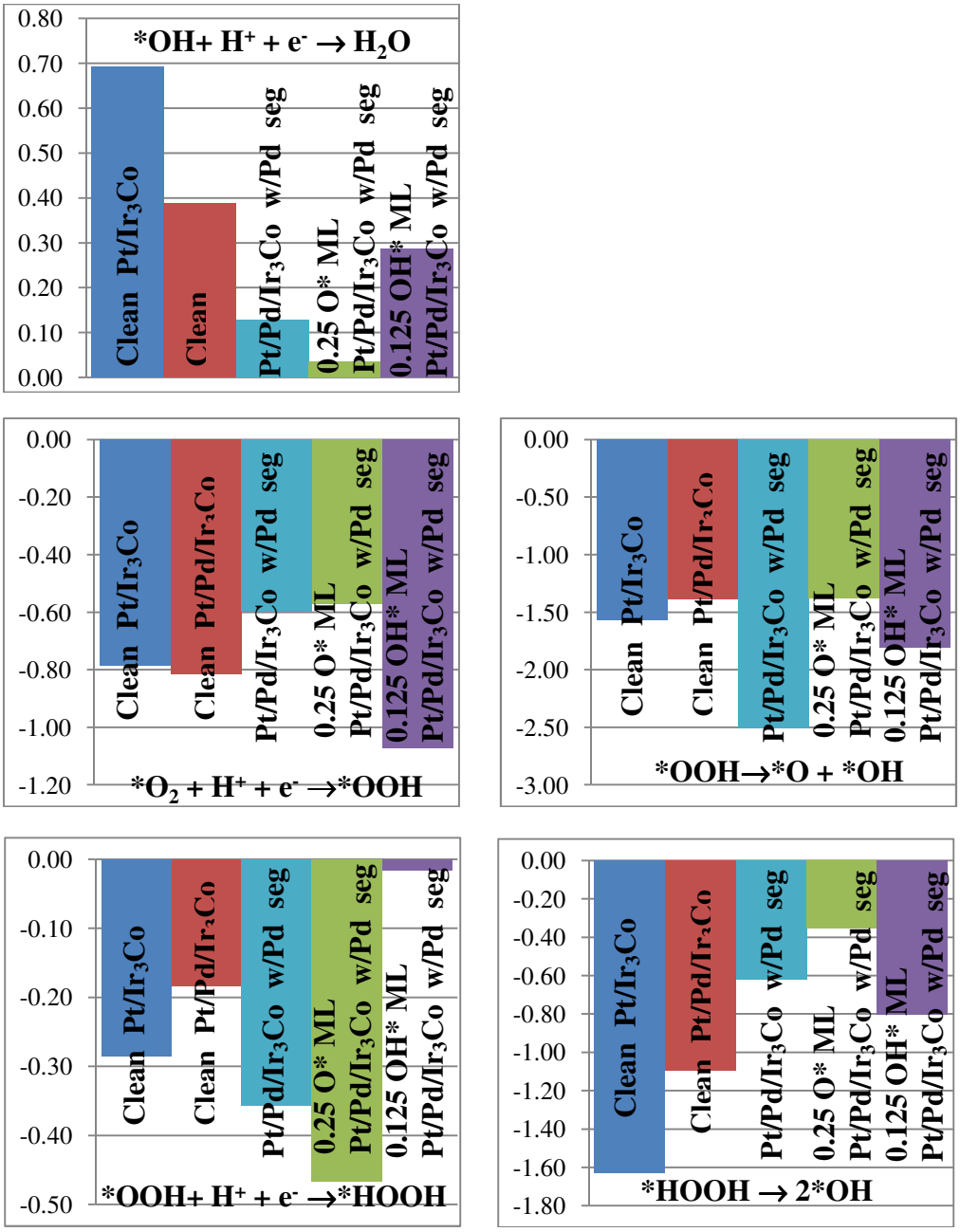

Fig. 6.10. (cont'd)

Considering Pt surfaces (Fig. 6.8), the dissociation of O_2 forming either O* or *OOH show negative barrier energies but tend to increase when the surface is covered with O* and *OH coverage, hence these steps may show positive barrier with large O* and *OH

coverage on the surface. H_2O formation which is the common step in all three mechanisms shows the highest free-energy barrier on the clean and with 0.22 ML O* surfaces indicating that it is the rate-limiting step. However, with the presence of 0.11 ML OH*, the OOH dissociation step shows the highest barrier resulting in disfavored of the associative I mechanism on this surface. Therefore, all three mechanisms can be activated on Pt(1111) and Pt(111) with 0.22 ML O* surfaces whereas the dissociative and associative II mechanisms are favorable on Pt(111) with 0.11 ML *OH surface. All have the same limiting step of water formation. With the presence of OH on the surface, the step of OOH dissociation becomes more difficult than water formation due to the significant weakening of O and OH adsorption.

Fig. 6.9 and 6.10 show that Pt/IrCo, Pt/Ir_3Co, Pt/Pd/IrCo, Pt/Pd/Ir_3Co, 0.125 ML *OH on Pt/Pd/IrCo and Ir_3Co with Pd segregated, and 0.25 ML O* on Pt/Pd/Ir_3Co with Pd segregated structures have the same limiting step which is the water formation step. Thus, all three mechanisms are possible to be activated on those surfaces. The step of $O^* + H^+ + e^- \rightarrow {}^*OH$ shows the highest barrier on Pt/Pd/IrCo and Ir_3Co with Pd segregated, therefore the dissociative and associative I mechanisms are disfavored for these surfaces and the associative II becomes the activated mechanism with water formation as the limiting step. The presence of Pd interlayer results in slightly lower free-energy barrier on the limiting step of water formation. Interestingly, the surface with 0.25 ML O* on Pt/Pd/IrCo with Pd segregated shows negative barrier free energy for all steps, with the highest barrier of -0.01 eV on the water formation step. Similarly, the surface with 0.25 ML O* on Pt/Pd/Ir_3Co with Pd segregated shows barriers as small as 0.04 eV. This indicates all steps are thermodynamically favorable on the surfaces with moderate O coverage. The presence of O induces a significant decrease in O and OH binding energies due to the repulsion between adsorbates resulting in lower energy barriers especially in the $^*OH + H^+ + e^- \rightarrow H_2O$ step. However, like Pt(111), the presence of O on the surface with Pd segregated increases the free-energy barrier in $O_2 \rightarrow 2O$ step which may turn out to be a positive barrier or even activated at higher O coverage, since O_2 adsorption may be hindered and significantly weakened due to the site blocking

effect. In addition, the presence of OH on the surface with Pd segregated causes the barrier energy in water formation step (the limiting step) to be increased indicating that this step becomes more difficult to overcome. The steps involving HOOH and OOH species are thermodynamically favorable as they show negative barrier on these Pt-skin surfaces. However, quite an increase of the energy barrier in *OOH+ $H^+ + e^- \rightarrow$*HOOH step is shown when 0.125 ML *OH covered the Pd segregated surface compared to that without *OH adsorption because the presence of OH substantially stabilizes OOH adsorption and the step may show positive barrier at higher OH coverage.

For further analysis and comparison of the relative reactivity of all surfaces at 0.9 V, pH = 0, we constructed an activity measure based on a microkinetic model [25].

The measure of maximal activity, $A = kTmin_i\left(log\left(\frac{k_i}{k_0}\right)\right)$ (6.11)

where k is Boltzmann's constant, T is temperature in Kelvin, $k_i = \nu_i e^{-\frac{E_a^i}{kT}}$; if step i is activated and k_0 normalizes the activity of nonactivated electron/proton transfer to zero. It is assumed that all species involving the rate-limiting step can react with the surface.

The DFT-based activities at 1 bar, 300 K, and 0.9 V following the associative II mechanism which is favorable for all surfaces are shown in Fig. 6.11. As discussed above, the ORR activity on all surfaces is limited by the step of OH removal to form water. The activity values in Fig. 6.11 arrange nicely following the OH adsorption trend; therefore, OH adsorption energy is an indicator of ORR activity of these surfaces. In agreement with the experimental results [139], the highest activity among the clean surfaces at a potential of 0.9 V is observed for Pt/Pd/IrCo (w/Pd seg) surface, followed by Pt/Pd/Ir_3Co (w/Pd seg) surface and Pt/Pd/IrCo; Pt/Ir_3Co and Pt(111) both show much lower activity. The calculated activity show that with the segregation of Pd to the surface associated with small coverage of O and OH on the surface can bring the higher activity of Pt/Pd/Ir-Co. The strong repulsive interaction between O and OH benefit the decrease of OH adsorption resulting in lower barrier in the limiting step of water formation, thus higher activity when the surfaces contain small O and OH coverage. Although, high

concentration of O and OH may help to reduce the barrier in the water formation step, it may raise the energy barrier in the other steps or even worse it may activate them because of the limited number of active free sites on the surface. It should be noted that the calculation model does not account for active site availability which is definitely a crucial factor when the surface is covered with high concentration of intermediate species. Furthermore, the significant challenge may turn to be Pd dissolution ($Pd \rightarrow Pd^{2+} + 2e^-$; $U^0 = 0.915$ V) resulting in the significant change of the surface composition and morphology and eventually the reduction in ORR activity.

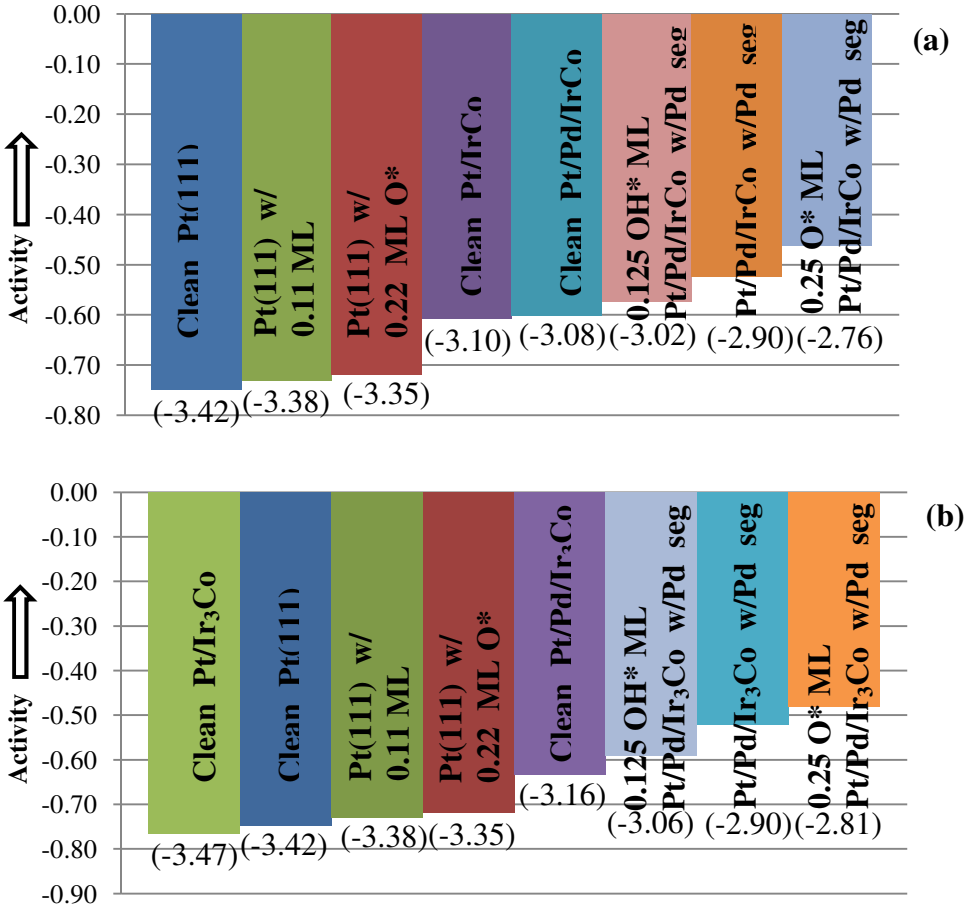

Fig. 6.11. Oxygen reduction activity following associative II mechanism at 0.9 V plotted in the order of strongest to weakest OH binding energy (with water), shown in parenthesis in eV. (a): IrCo, (b): Ir_3Co cores.

6.5. Conclusion

DFT has been applied to study stability and activity of Pt-skin core-shell structure on IrCo and Ir_3Co core both with and without Pd interlayer between Pt-skin and core elements. The segregation under vacuum of core elements especially Co for the structures without Pd interlayer is thermodynamically favorable which lead to the formation of Co-rich subsurfaces. With the presence of atomic oxygen adsorption, Co and Ir are likely to segregate to the surface which can be easily dissolve and oxidized under ORR environment. The Pd interlayer plays a considerable role to prevent the segregation of core elements to the surface and maintain Pt-skin on the surface inducing higher ORR activity illustrated in the experiment[139] compared to those without Pd interlayer. However, oxygen adsorption on the surface might draw the segregation of Pd to the surface weakens the long-term stability of the structure because Pd can be oxidized at lower potential than Pt consequently, changing surface composition, structure and eventually may lead to substantial reduction of ORR activity.

In vacuum and under 0.25 ML O adsorption, there is no significant stability improvement in term of Pt surface atom dissolution for the Pt-skin with Pd interlayer structures compared to Pt(111) as the Pd interlayer is not found to reduce the oxidation degree on Pt-skin. The atomic charges on all structures are not sensitive to the applied electric field in which the charges change less than 0.01 e^- with the electric field strength varied between -0.2 eV/Å and 0.2 eV/Å.

The calculated surface Pourbaix diagrams show that in the strong acid region the clean surface is stable up to ~0.9-1.0 V then, the small coverage of 0.25 ML O/0.125 ML OH are stable up to 1.2 V and not sensitive with the increase of potential. However, Pt(111) show the clean surface is stable up to ~0.7 V then, O/OH adsorption are stable and the coverage rapidly increases with the increase of potential. The delayed onset of water oxidation lead to more surface free site available consequently, the relative ORR activity increase on Pt/(Pd)/Ir-Co. The diagrams of the structure with and without Pd interlayer are not significantly different but when Pd segregates to the surface the onset of water

oxidation potential is lower due to strong O adsorption. The calculations show that activity is the main challenge rather than Pt dissolution.

At 0.9 V and pH = 0, the calculation indicate that all three mechanisms can be activated on Pt(111) and Pt(111) with 0.22 ML O surfaces whereas the dissociative and associative II mechanisms are favorable on Pt(111) with 0.11 ML OH surface. Similarly, all three mechanisms are possible to be activated on Pt/IrCo, Pt/Ir_3Co, Pt/Pd/IrCo, Pt/Pd/Ir_3Co, 0.125 ML *OH and 0.25 ML O* on Pt/Pd/IrCo and Ir_3Co with Pd segregated surfaces while only the associative II mechanism is activated on Pt/Pd/IrCo and Ir_3Co with Pd segregated. The step of water formation is determined to be the limiting one for all surfaces. Interestingly, all steps are thermodynamically favorable on the surfaces with Pd segregated associated with moderate O coverage in which the presence of O induce the substantial destabilization on O and OH adsorption due to the repulsion between adsorbates. Also, the presence of OH on the surface with Pd segregated influences the water formation step (the limiting step) to become more difficult to overcome. The steps involve HOOH and OOH species are thermodynamically favorable.

The activity trend is in agreement with the experimental results [139], the highest activity among the clean surfaces at a potential of 0.9 V is observed for Pt/Pd/IrCo (w/Pd seg) surface, followed by Pt/Pd/Ir_3Co (w/Pd seg) surface and Pt/Pd/IrCo; Pt/Ir_3Co and Pt(111) both show much lower activity. OH adsorption energy is an indicator of ORR activity of these surfaces. The presence of Pd interlayer results in slightly higher activity. The segregation of Pd to the surface associated with small coverage of O on the surface can bring the higher activity of Pt/Pd/Ir-Co. Although the strong repulsive interaction between O and OH decrease the OH stabilization, high concentration of O and OH considerably reduce the active site availability which is an important factor on catalysis activity. Furthermore, the segregation of Pd to the surface may be a crucial effect which leads to considerable changes of the surface composition and morphology caused by Pd dissolution.

CHAPTER VII

STABILITY AND OXYGEN REDUCTION REACTION ACTIVITY OF SHELL-ANCHOR-CORE MATERIALS

7.1. Introduction

A number of experimental and theoretical studies have shown enhanced activities of Pt-based alloy electrocatalysts, in many cases arranged in core-shell structures that expose pure platinum on the surface and cheaper transition metals as core material[25, 28, 35, 38, 39, 41, 152]. The Pt-based dispersed alloys and Pt-skin surface core-shell structure minimize the amount of platinum loading in the catalyst and favorably modify the electronic and geometric properties of the surface toward higher ORR activity, a remaining problem is that the accompanying transition metals are prone to easy dissolution in an acid medium. Thus, a better catalytic formulation is needed to mitigate this effect. A new class of core-shell materials composed of a platinum monolayer over a composite core where an extra element has been added to the transition metals in order to anchor them to the core was proposed by Ramirez-Caballero and Balbuena [153]. The concept is to retain their beneficial properties toward the surface atoms for ORR and enhancing the stability of the catalyst against dissolution in acidic medium which prevent the catalytic activity depletion. Based on DFT calculations in their study [153], the proposed structure (Fig. 7.1) is composed of a pure Pt-skin surface over transition metal (Fe, Co and Ni) layers where extra carbon atoms are added to interstitial sites of the transition metal in order to stabilize them to the Ir core (Pt/Fe-C/Ir, Pt/Ni-C/Ir and Pt/Co-C/Ir). The previous study [153, 154] has demonstrated a positive electrochemical potential shift for the dissolution of Pt atoms and unfavorable segregation of the core metal elements suggesting improved durability of the new shell-anchor-core material. The enhanced durability arises from the use of carbon in the interstitial sites of the subsurface that anchors the Fe/Ni/Co atomic layers in their positions, impeding their segregation to the surface while keeping their beneficial properties that favor ORR activity on the top platinum monolayer. The elements Fe/Ni/Co were selected based on

their anti-segregation property under atomic oxygen adsorption upon the preliminary screening of transition metals.

In this chapter, only the structures with a X:C ratio of 2:1 where X is Fe, Co or Ni and C is carbon (4 interstitial carbon atoms in Fig. 7.1) which yielded the best durability and activity properties for all the systems are considered [153, 154]. DFT calculations are employed to further explore ORR activity on Pt/Fe-C/Ir, Pt/Ni-C/Ir by constructing their surface Pourbaix diagrams and calculating ORR barrier energies. We also examine the structure in which we substituted the Pt monolayer surface with the Pd surface since studies [129, 133] have reported good ORR catalytic properties for Pd surface structures. In addition, stability and activity of the structure including other core materials (Pd_3Co, Ir_3Co, IrCo and IrNi) are investigated in order to examine the possibility to reduce the cost of catalyst by replacing relative expensive metal such as Ir, Pd with cheaper metals such as Co, Ni.

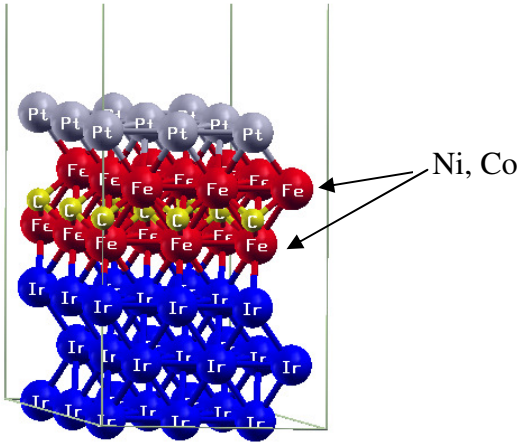

Fig. 7.1. Slab model of Pt/Fe-C/Ir with 3 × 3 unit cell.

7.2. Objectives

We analyze properties which indicate whether ORR activity on the structures of Pt/Fe-C/Ir, Pt/Ni-C/Ir, Pt/Co-C/Ir and Pd/Fe-C/Ir is enhanced comparing to pure Pt. The performed tasks are: 1. Study the influence of the electrochemical potential on the stability of intermediates at various coverages by constructing surface Pourbaix diagrams and 2. Investigate possible ORR pathways and activity on the surfaces.

We investigate durability and activity of Pt/Fe-C/core, Pt/Co-C/core and Pt/Ni-C/core with core materials of Pd_3Co, Ir_3Co, IrCo and IrNi. The performed tasks are: 1. Investigation of the segregation trends of elements; 2. Examination of the relative potential shift for Pt surface dissolution; and 3. Analysis of activity descriptor.

7.3. Methodology and computational details

The DFT calculations were performed using the Vienna ab initio simulation package, VASP[81-84]. To construct surface Pourbaix diagrams and calculate activity (section 7.4.1 and 7.4.2), metal slab models (Fig. 7.1) of fcc(111) structure are composed of a Pt monolayer surface, two layers of Fe, Ni or Co in which C atoms are inserted into the interstitial sites, and three layers of Ir. Simulations were done using a 3×3 unit cell containing 6 layers of metal atoms and a vacuum region of more than 6 layers (>13 Å). The bottom two layers of the slab were fixed, while the other layers were relaxed to their lowest energy configurations. The fixed layers were set to Iridium bulk bond distances according to its optimized lattice constants which were determined from bulk calculations. The calculated lattice constant is 3.838 Å and it is in good agreement with the experimental value[137] of 3.871 Å. For segregation energies and electrode potential shift calculation (section 7.4.3), the metal slab details are similar to those described above except that a 2×2 unit cell is used. The fixed layers were set to bulk bond distances of core material of a particular structure that was determined from bulk calculations. The studied core materials are Pd_3Co, Ir_3Co, IrCo and IrNi. The calculated lattice constants of Pd_3Co, Ir_3Co, IrCo and IrNi are 3.83, 3.81, 3.74 and 3.75 Å,

respectively. The experimental lattice constants values for Pt/Pd_3Co is 3.87 Å [155], for $Ir_{0.7}Co_{0.3}$ is 3.81 Å [137], for $Ir_{0.5}Co_{0.5}$ is 3.77 Å [137] and for IrNi is approximately 3.72 Å [156]. The calculated values are in good agreement with the experimental values. The details for surface Pourbaix diagrams construction and ORR activity calculation methods are discussed in Chapter VI section 6.3.2. However, the shift of energy due to water interaction is calculated for specific structure and not assumed to be the same with Pt(111) surface. Also, the details for segregation energy and electrode potential shift calculation are shown in Chapter VI section 6.3.1.

Spin-polarized DFT calculations were performed with the exchange-correlation functional Perdew-Burke-Ernzerhof (PBE) [87] described within the generalized gradient approximation, with $3 \times 3 \times 1$ k-points Monkhorst-Pack [88] mesh sampling in the surface Brillouin zone. The plane-wave cutoff energy was optimized at 350 eV. The results were checked for convergence with respect to energy cutoff and number of k-points. Spin polarization was taken into account and the Methfessel-Paxton smearing [89] of order 2 with a value of smearing parameter σ of 0.2 eV was applied. The convergence criteria for ionic relaxation loop and electronic self-consistent iteration were set to 10^{-4} eV/Å and 10^{-5} eV, respectively.

7. 4. Results and discussion

7.4.1. Surface Pourbaix diagrams of Pt/Fe-C/Ir, Pt/Ni-C/Ir, Pt/Co-C/Ir and Pd/Fe-C/Ir

The diagram is constructed by assuming that the surface is in equilibrium with protons and liquid water at 300 K without the presence of molecular oxygen, so that oxygen and hydroxyl may be exchanged between the surface and a reference electrolyte without the limitation of active free site availability through the following reaction steps[151];

$$H_2O\ (l) + * \leftrightarrow HO* + H^+\ (aq) + e^- \qquad (7.1)$$

$$\text{and,} \quad HO* \leftrightarrow O* + H^+(aq) + e^- \qquad (7.2)$$

where * is a site on the catalyst surface, O* and HO* denote adsorbed species on a site.

The free energy, ΔG, of a given surface structure with different O* and HO* coverage formed by reaction (1) and (2) is calculated as a function of potential U_{SHE} and pH where the reference potential is set to be that of the standard hydrogen electrode (SHE).

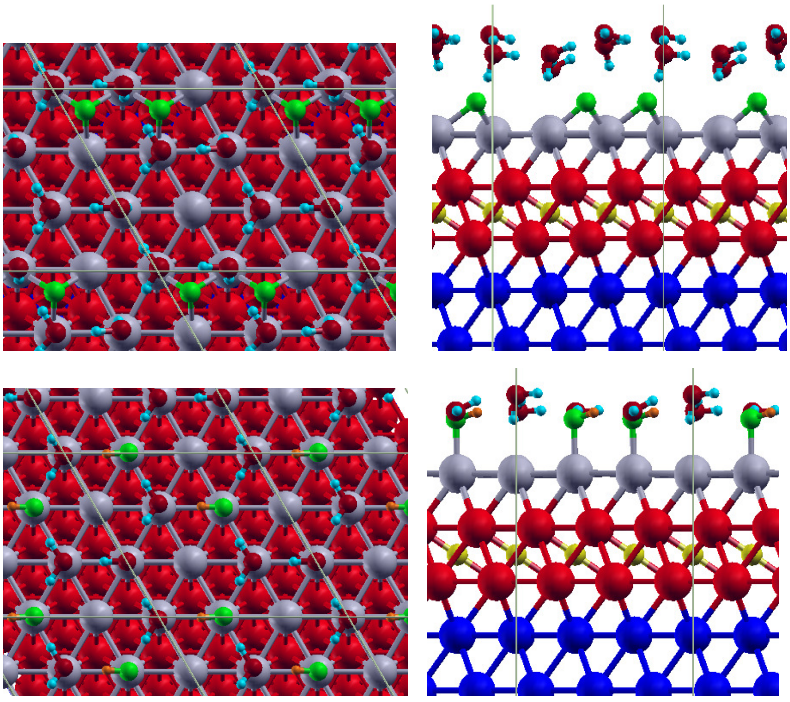

Fig. 7.2. Upper: top view and side view of 0.22 ML O co-adsorbed with water on Pt/Fe-C/Ir structure. Lower: top view and side view of 0.22 ML OH co-adsorbed with water on Pt/Fe-C/Ir structure.

Firstly, the binding energies of O* and HO* on the surfaces at varied coverage are calculated. The example of the structures of 0.22 ML O and OH co-adsorbed with water on Pt/Fe-C/Ir are illustrated in Fig. 7.2. The oxygen atoms adsorbed on fcc site and OH adsorbed on atop site. When atomic oxygen adsorb on the surface, a water layer with hexagonal hydrogen bond network studied by Ogasawara et al[145] is added. Whereas when OH adsorbed on the surface, the water molecules are added to form hexagonal hydrogen-bonded network with OH, which is a structure found to be very stable on

Pt(111) [146-149] i.e. the number of water are varied with OH coverage. The similar water structures are also included on the other alloy structures.

Table 7.1 shows O and OH binding energies at different coverage with and without water. The O and OH binding energies of the Pt monolayer surface structures are significantly weaker than pure Pt and the binding energies tend to decrease with the increase of coverage due to the repulsion between adsorbates and the change of surface electronic properties. The O adsorption is weaker on the shell-anchor-core surfaces than on Pt(111). Although the order from strongest to weakest O adsorption among the shell-anchor-core structures changes slightly when the O coverage is varied, always Pt(111) yields the strongest and Pt/Fe-C the weakest adsorption. Similar trend is followed by OH adsorption.

Table 7.1 shows that solvation significantly stabilizes OH adsorption on all surfaces yielding binding energies ~1-1.5 eV/OH higher due to hydrogen bonds among water and OH molecules. However, the effect on O adsorption is much reduced, with an average less than 0.05 eV/O, indicating that water and adsorbed O are not likely to form hydrogen bonds. The strongest OH binding energies are those with Pt(111), and on the other surfaces they follow similar trend as the O adsorption.

At a specific pH, the plot between ΔG and U_{SHE} is constructed. The same plots are also constructed at pH = 1-10 for all surfaces. Then, the surface Pourbaix diagram in Fig. 7.3 is constructed by plotting the most stable surface as a function of pH and U_{SHE}. The most stable surface at a specific pH and U_{SHE} is designated as the one showing negative and the lowest free energy. More than one surface structure can be co-existing when the free energy difference is less than 0.05 eV/surface atom.

Table 7.1.
O and OH adsorption energies at different coverage on Pt, Pt/Fe-C/Ir, Pt/Ni-C/Ir, Pt/Co-C/Ir and Pd/Fe-C/Ir with and without water.(eV/O, eV/OH)

Without water					
O coverage (ML)	Pt	Pt/Fe-C/Ir	Pt/Ni-C/Ir	Pt/Co-C/Ir	Pd/Fe-C/Ir
0.111	-4.52	-3.72	-4.39	-4.20	-4.11
0.222	-4.29	-3.60	-3.94	-3.96	-3.82
0.333	-3.94	-3.25	-3.64	-3.50	-3.55
0.444	-3.76	-3.11	-3.43	-3.30	-3.44
OH coverage (ML)					
0.111	-2.34	-2.09	-2.16	-2.21	-2.22
0.222	-2.34	-2.10	-2.10	-2.17	-2.22
0.333	-2.21	-2.03	-2.02	-2.08	-2.06
With water					
O coverage (ML)	Pt	Pt/Fe-C/Ir	Pt/Ni-C/Ir	Pt/Co-C/Ir	Pd/Fe-C/Ir
0.111	-4.60	-3.75	-4.28	-4.14	-4.27
0.222	-4.29	-3.55	-3.97	-3.73	-3.92
0.333	-4.14	-3.24	-3.58	-3.47	-3.59
0.444	-3.87	-3.09	-3.37	-3.28	-3.48
OH coverage (ML)					
0.111	-3.42	-3.19	-3.15	-3.17	-3.66
0.222	-3.44	-3.32	-3.23	-3.23	-3.48
0.333	-3.39	-3.22	-3.07	-3.15	-3.41

Since the metal dissolution may occur in acid solution, the free energy of dissolution of the surface atoms are estimated from standard reduction potentials as uniform dissolution corresponding to the bulk dissolution [151]. The dissolution of Pt and Pd in acidic solution;

$$Pt(s) \leftrightarrow Pt^{2+}(aq) + 2e^- \qquad U^0 = 1.18\ V \qquad (7.3)$$

$$Pd(s) \leftrightarrow Pd^{2+}(aq) + 2e^- \qquad U^0 = 0.915\ V \qquad (7.4)$$

The calculations show that at pH = 0 the Pt dissolution occurs at 1.22 V, 1.28 and 1.25 V for Pt/Fe-C/Ir, Pt/Ni-C/Ir and Pt/Co-C/Ir, respectively. Graphs with the reaction free energies as a function of potential are provided as Appendix C at three different values of pH. The Pt dissolution potential tends to increase linearly with the pH, for example the onset potential for dissolution of each system increases in 0.04 V when the pH rises from 0 to 4. On the other hand, the Pd dissolution on Pd/Fe-C/Ir structure may take place at lower potential of 0.95 V at pH = 0. Therefore, the Pd/Fe-C/Ir structure may not be appealing for the reaction under harsh acidic environment due to the low stability of Pd on the surface at high potentials.

The surface Pourbaix diagrams show that at pH = 0 water oxidation (reaction 7.1) takes place at 0.94 V, 0.67 V and 0.74 V on Pt/Fe-C/Ir, Pt/Ni-C/Ir and Pt/Co-C/Ir, respectively (indicated by the arrows in Fig. 7.3). The diagram of Pt(111) has been investigated previously by Norskøv et al.[151] and their results showed at pH = 0 the clean surface is stable up to 0.73 V, then above 0.73 V the surface is covered with 0.33 ML of *OH and 0.25 ML of O* and the O* coverage increased to be 0.33 ML, 0.5 ML and 0.67 ML at 1.5 V. Thus, a clear advantage is found for the much higher water oxidation potential on the Pt/Fe-C/Ir surface. On the other hand, water oxidation on Pt/Ni-C/Ir and Pt/Co-C/Ir surfaces happen at a similar potential (~0.7 V) to that on Pt(111). However, the O* coverage above the water oxidation potential is much lower on these Pt-skin structures compared to Pt(111). For example, at pH =0, a low coverage of 0.22 ML O* is found up to 1.0 V for Pt/Ni-C/Ir and up to 1.15 V for Pt/Co-C/Ir. In addition, a high coverage of OH is not found on these Pt-skin surfaces in the acidic region. Therefore, the site

blocking effect on these Pt-skin surfaces is less important and the surface structures may not be substantially affected due to high adsorbates coverage.

Also, the positive potential shift of Pt/Ni-C/Ir and Pt/Co-C/Ir relative to Pt(111) [154] may result from the lower O coverage above the water oxidation potential that can assist in the delay of Pt dissolution from Pt/Ni-C/Ir and Pt/Co-C/Ir compared to Pt(111). These important properties can result in higher Pt oxidation potentials and lower site blocking effect which may lead to better ORR activity on these Pt-skin surfaces relative to the Pt(111) surface.

In Chapter VI we have analyzed surface Pourbaix diagrams for core-shell structures without the anchor layer (Fig. 6.7). In those cases, we find a shift towards higher potentials for the onset of water oxidation. However, those surfaces exhibit higher coverage of O and OH that the shell-anchor-core structures.

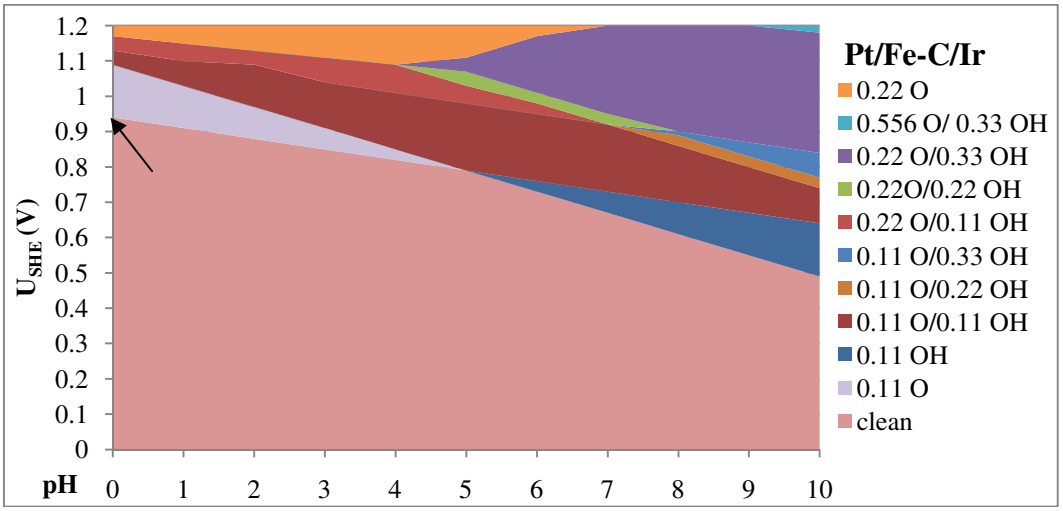

Fig. 7.3. Surface Pourbaix diagrams of Pt/Fe-C/Ir, Pt/Ni-C/Ir, Pt/Co-C/Ir, and Pd/Fe-C/Ir. The arrows indicate the onset water oxidation potential at pH = 0.

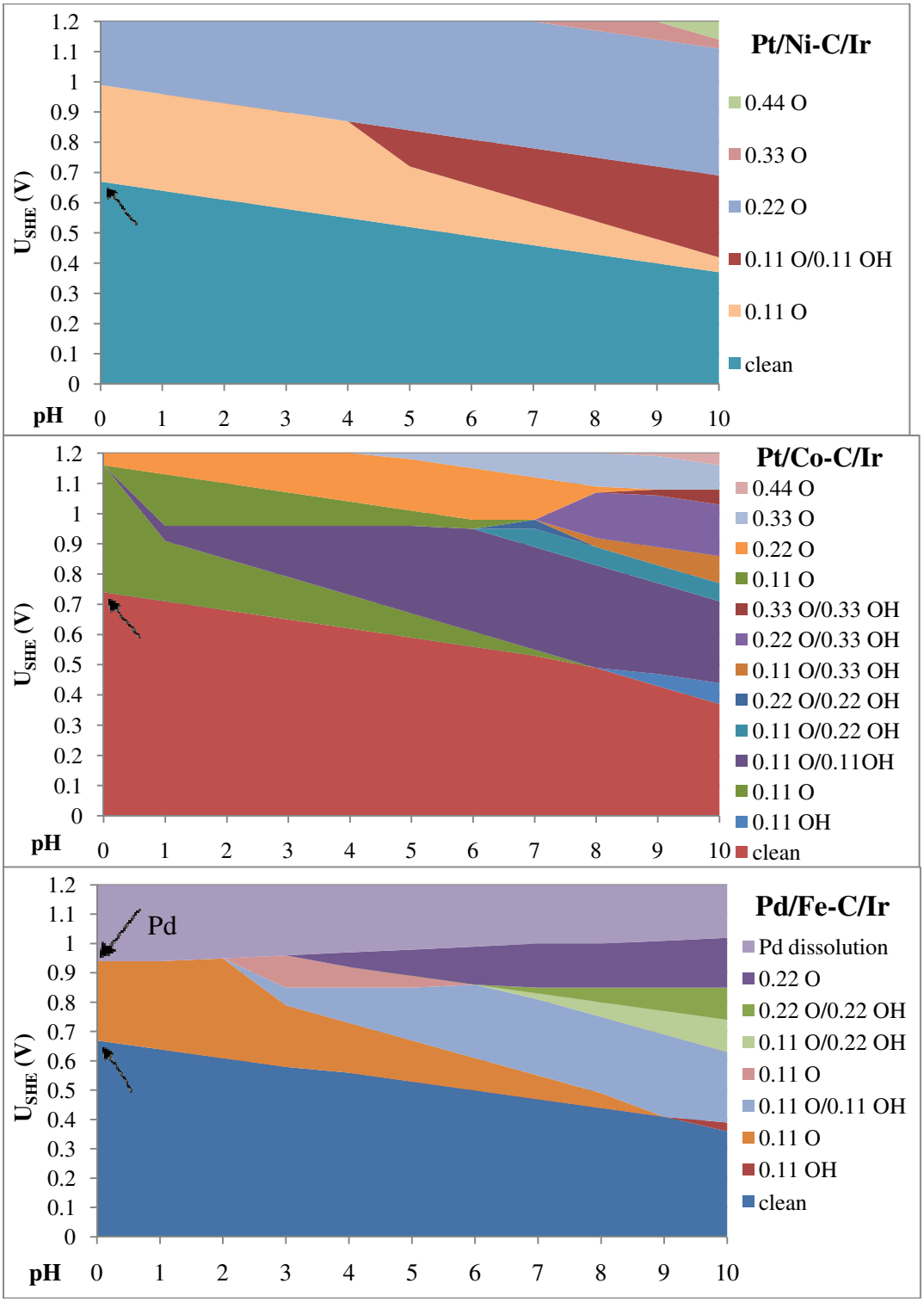
Pt/Ni-C/Ir
0.44 O
0.33 O
0.22 O
0.11 O/0.11 OH
0.11 O
clean
Pt/Co-C/Ir
0.44 O
0.33 O
0.22 O
0.11 O
0.33 O/0.33 OH
0.22 O/0.33 OH
0.11 O/0.33 OH
0.22 O/0.22 OH
0.11 O/0.22 OH
0.11 O/0.11OH
0.11 O
0.11 OH
clean
Pd/Fe-C/Ir
Pd
Pd dissolution
0.22 O
0.22 O/0.22 OH
0.11 O/0.22 OH
0.11 O
0.11 O/0.11 OH
0.11 O
0.11 OH
clean
U_SHE (V)
pH

Fig. 7.3. (cont'd)

7.4.2. Reaction barrier energies and activity of Pt/Fe-C/Ir, Pt/Ni-C/Ir and Pt/Co-C/Ir

Three possible ORR mechanisms are investigated similar to Chapter VI.

Dissociative mechanism	Associative I mechanism	Associative II mechanism (forming hydrogen peroxide)
$1/2O_2 \leftrightarrow O^*$	$O_2 \leftrightarrow {}^*O_2$	$O_2 \leftrightarrow {}^*O_2$
$O^* + H^+ + e^- \leftrightarrow HO^*$	${}^*O_2 + H^+ + e^- \leftrightarrow HOO^*$	${}^*O_2 + H^+ + e^- \leftrightarrow HOO^*$
$HO^* + H^+ + e^- \leftrightarrow H_2O$	$HOO^* \leftrightarrow HO^* + O^*$	$HOO^* + H^+ + e^- \leftrightarrow HOOH^*$
	$O^* + H^+ + e^- \leftrightarrow HO^*$	$HOOH^* + H^+ + e^- \leftrightarrow 2HO^*$
	$HO^* + H^+ + e^- \leftrightarrow H_2O$	$HO^* + H^+ + e^- \leftrightarrow H_2O$

* denote adsorbed species

The reaction barrier free energy of each step is calculated at 0.9 V and pH = 0 and shown in Fig. 7.4. The step of OH removal to form water indicate the highest barrier energy on all surfaces in which Pt(111) shows the highest barrier while the other surfaces are comparable and much lower than Pt(111). The other steps on these shell-anchor-core structures show negative free energy barriers except the step of OH formation, $O^* + H^+ + e^- \rightarrow {}^*OH$, shows positive barrier on Pt/Ni-C/Ir. All three proposed mechanisms have the same limiting step of water formation, thus all three mechanisms are possible on the surfaces with the same highest energetic barrier. The high barrier for OH removal suggests that OH may be a significant intermediate poison the surfaces by the accumulation of OH on the surface resulting in site blocking effect.

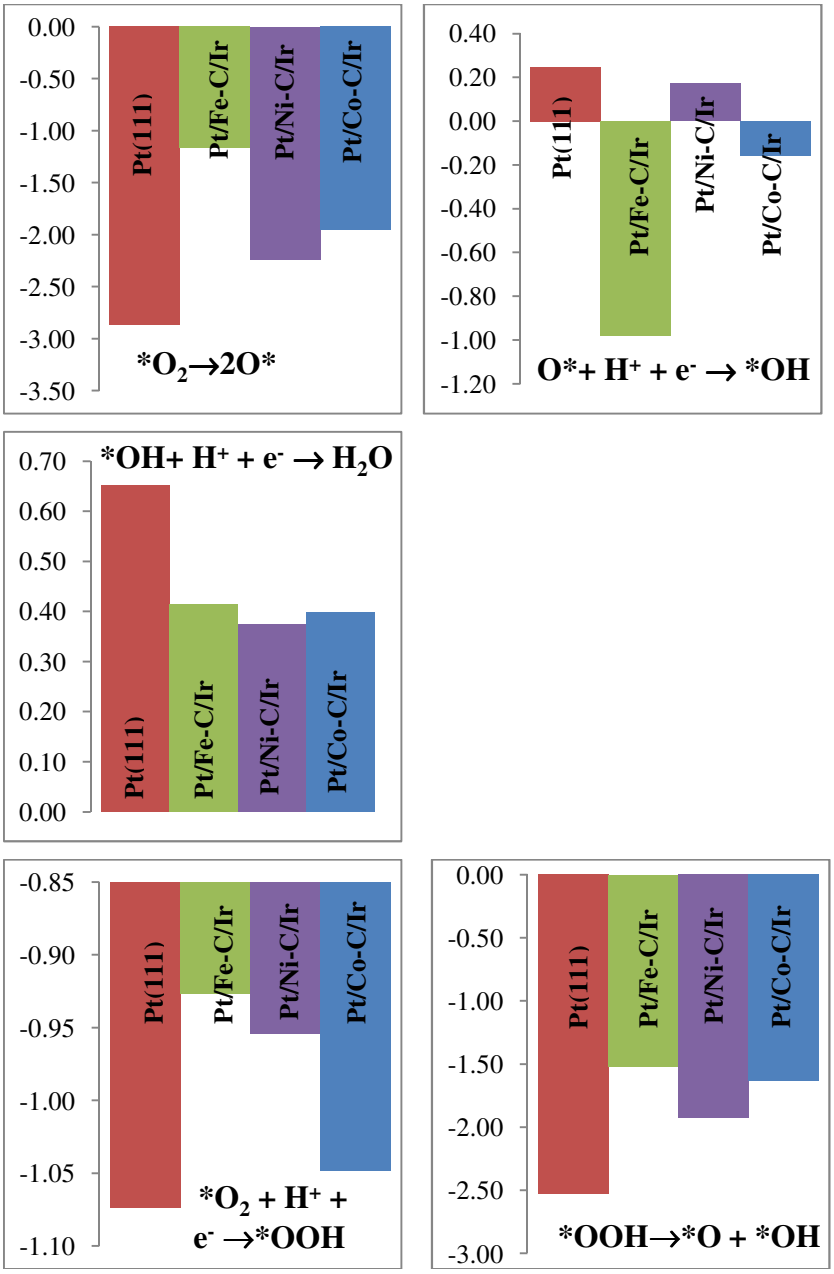

Fig.7.4. Reaction barrier free-energy of all reaction steps at 0.9 V, pH = 0 on Pt(111), Pt/Fe-C/Ir, Pt/Ni-C/Ir and Pt/Co-C/Ir.

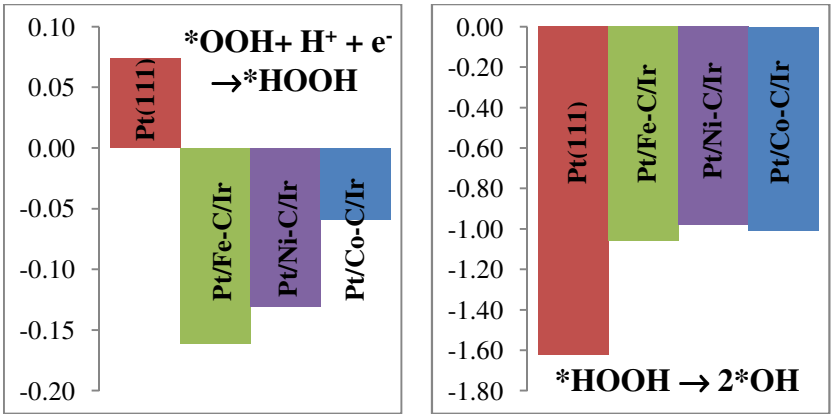

Fig.7.4. (cont'd)

The corresponding measured activity based on a microkinetic model (explained in Chapter VI section 6.4.4) are calculated and shown in Fig. 7.5. The DFT-based activities are calculated at 1 bar, 300 K, pH = 0, and 0.9 V. Fig. 7.5 illustrates the activity following the associative II mechanism. The activity trend is the same for dissociative and associative I mechanisms. The activity values in Fig. 7.5 arrange nicely following the OH adsorption trend; therefore, OH adsorption energy is an indicator of ORR activity of these surfaces. The shell-anchor-core structures present significantly higher activity than Pt(111) which results from weaker O and OH adsorption and lower O and OH coverage; however, they show a comparable activity among themselves. In summary, besides the anti-segregation and positive shift in Pt dissolution potential on Pt/Fe-C/Ir, Pt/Ni-C/Ir and Pt/Co-C/Ir [153], the results suggest that Pt/Fe-C/Ir, Pt/Ni-C/Ir and Pt/Co-C/Ir shows significant higher activity.

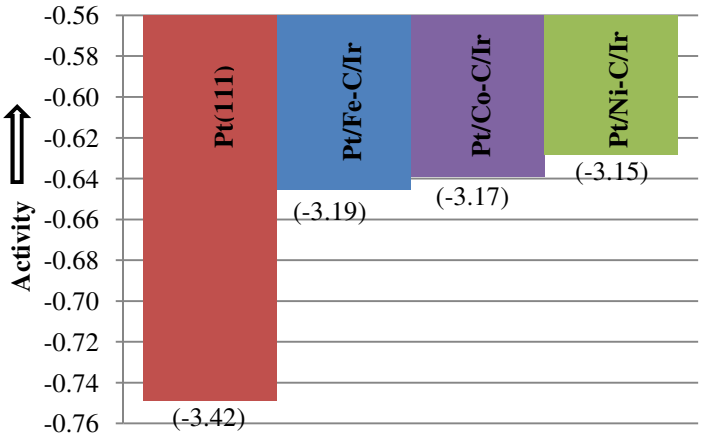

Fig. 7.5. Oxygen reduction activity following associative II mechanism at 0.9 V plotted in the order of strongest to weakest OH binding energy (with water), shown in parenthesis in eV.

7.4.3. Stability and activity investigation of shell-anchor-core structure with Pd_3Co, Ir_3Co, IrCo and IrNi core materials

Since Ir is a relatively expensive metal (although less expensive than Pt), the attempt to reduce catalyst cost lead to the investigation of other core materials which contain relatively cheaper metals (i.e. Co and Ni) and less load of expensive metal (i.e. Ir and Pd) while still show promising stability and activity toward ORR. As shown in Chapter VI, Ir_3Co and IrCo display good characteristics as a catalyst core for ORR. Also, Pd-Co was experimentally shown to be a good core material for ORR [41, 131] and Ni is relatively cheap metal and shows activity toward ORR [26]. In this section, how core materials i.e. Pd_3Co, Ir_3Co, IrCo and IrNi affect to catalyst stability and activity is discussed.

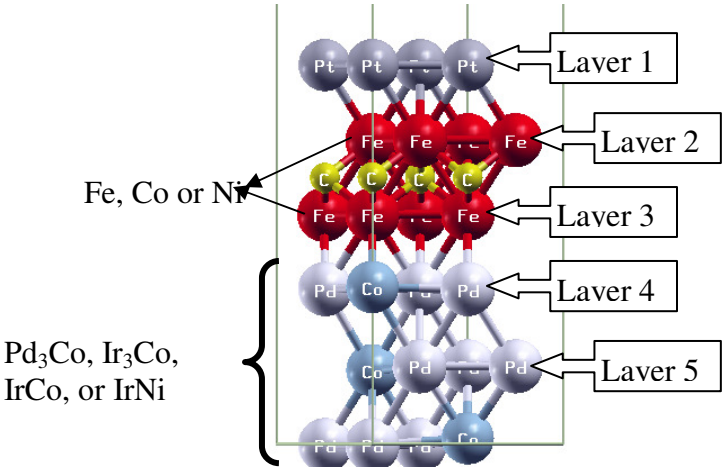

Fig. 7.6. Slab model for study of Pd_3Co, Ir_3Co, IrCo, and IrNi core materials.

Table 7.2
Segregation energies (eV) of Pt/Fe-C/**Pd_3Co**, Pt/Co-C/Pd_3Co and Pt/Ni-C/Pd_3Co structures in vacuum and under 0.25 ML of O adsorption.

	Vacuum			with O adsorption		
	Fe	Co	Ni	Fe	Co	Ni
Fe/Co/Ni segregate from atomic layer 2 to 1	1.97	1.79	1.52	1.49	1.69	0.52
Pd segregates from atomic layer 4 to 3	1.24	1.02	1.05	1.22	1.72	1.41
Co segregates from atomic layer 4 to 3	-0.19	-	-0.66	-0.20	-	-0.97
Pd segregates from atomic layer 5 to 4	-0.19	-0.85	-0.41	-0.18	-0.19	-0.67
Co segregates from atomic layer 5 to 4	0.15	0.14	0.96	0.83	0.83	0.66
Carbon segregates to interstitial site between atomic layer 1 and 2	1.44	1.24	-0.44	2.12	2.85	0.40
Carbon segregates to interstitial site between atomic layer 3 and 4 bonding with 3Pd on layer 3	0.93	1.09	-0.59	1.05	1.88	-0.83
Carbon segregates to interstitial site between atomic layer 3 and 4 bonding with 2Pd and 1Co on layer 3	0.45	-0.07	-0.46	0.59	0.70	-1.40

The segregation energies are calculated in which negative segregation energies (E_{seg}) indicate that segregation of the specified element is energetically favorable and the

opposite for positive E_{seg}. The slab model consists of 6 layers in which the bottom layer is fixed at its core alloy bulk lattice constant (Fig. 7.6). The segregation of elements in atomic layer 1-5 is investigated both in vacuum and under 0.25 ML oxygen adsorption. Atomic oxygen is located at the most stable fcc three-folded hollow site for all structures.

Table 7.2 shows segregation energies of the structures with Pd_3Co core. The segregation of Fe/Co/Ni atoms in subsurface to surface is thermodynamically unfavorable; thereby the Pt-skin surface is maintained. However, Co inside core tend to segregate to the anchor layer (layer 3) in which Fe and Ni presents and Pd inside core is also favorable to segregate and form rich-Pd layer inside core. Ni may not be a good choice with Pd_3Co core because carbon atoms are likely to move into interstitial positions above and below the anchor layer (above layer 2 and below layer 3) which may lead to segregation of Ni atoms in subsurface to surface and the structure would not achieve the main purpose to improve the stability of Pt-skin surface of this particular shell-anchor-core structure. Co and Fe are good alternatives for Pd_3Co core, although Pd and Co have tendency to segregate inside the core. Co may be a better choice because Fe may eventually stay inside core with Co segregate to the anchor layers bonding with interstitial carbon atoms.

The results of segregation energies with the core material Ir_3Co, are shown in Table 7.3. Similar to the Pd_3Co core, in the presence of Ni, carbon atoms are energetically favorable to move to other interstitial position above the subsurface and below layer 3. Also, Co inside core tends to segregate to the anchor layer (layer 3) and Ir is likely to segregate forming Ir-rich layer inside core. Like Pd_3Co core material, Pt/Co-C/Ir_3Co and Pt/Fe-C/Ir_3Co are good candidates with high durability for Ir_3Co core material.

Table 7.3
Segregation energies (eV) of Pt/Fe-C/**Ir_3Co**, Pt/Co-C/ Ir_3Co and Pt/Ni-C/ Ir_3Co structures in vacuum and under 0.25 ML of O adsorption.

	Vacuum			with O adsorption		
	Fe	Co	Ni	Fe	Co	Ni
Fe/Co/Ni segregate from atomic layer 2 to 1	1.93	2.08	1.53	1.76	1.93	0.82
Ir segregates from atomic layer 4 to 3	1.12	1.27	0.58	1.14	1.41	0.53
Co segregates from atomic layer 4 to 3	-0.01	-	-0.53	-0.02	-	-0.58
Ir segregates from atomic layer 5 to 4	-0.31	-0.31	-0.33	-0.31	-0.32	-0.33
Co segregates from atomic layer 5 to 4	0.27	0.29	0.26	0.26	0.31	0.26
Carbon segregates to interstitial site between atomic layer 1 and 2	1.48	1.41	-0.57	2.30	2.30	0.58
Carbon segregates to interstitial site between atomic layer 3 and 4 bonding with 3Ir on layer 3	0.30	0.82	-1.29	0.46	0.73	-1.43
Carbon segregates to interstitial site between atomic layer 3 and 4 bonding with 2Ir and 1Co on layer 3	0.34	0.71	-1.32	0.51	0.74	-1.32

Table 7.4
Segregation energies (eV) of Pt/Co-C/**IrCo** structure in vacuum and under 0.25 ML of O adsorption.

	Vacuum	with O adsorption
Co segregates from atomic layer 2 to 1	2.04	1.92
Ir segregates from atomic layer 4 to 3	1.22	1.26
Ir segregates from atomic layer 5 to 4	-0.24	-0.23
Co segregates from atomic layer 5 to 4	0.33	0.35
Carbon segregates to interstitial site between atomic layer 1 and 2	1.38	1.59
Carbon segregates to interstitial site between atomic layer 3 and 4 bonding with 1Co and 2Ir on layer 3	0.28	0.39
Carbon segregates to interstitial site between atomic layer 3 and 4 bonding with 2Ir and 1Co on layer 3	0.42	0.49

Table 7.5
Segregation energies (eV) of Pt/Fe-C/**IrNi**, Pt/Co-C/ IrNi, and Pt/Ni-C/ IrNi structures in vacuum and under 0.25 ML of O adsorption.

	Vacuum			with O adsorption		
	Fe	Co	Ni	Fe	Co	Ni
Fe/Co/Ni segregate from atomic layer 2 to 1	1.94	2.24	1.49	1.96	1.39	1.23
Ir segregates from atomic layer 4 to 3	1.03	1.25	0.00	1.05	1.24	0.00
Ni segregates from atomic layer 4 to 3	0.26	0.18	-	0.24	0.19	-
Ir segregates from atomic layer 5 to 4	0.08	0.00	0.21	0.09	-0.03	0.22
Ni segregates from atomic layer 5 to 4	0.37	0.25	0.15	0.37	0.26	0.16
Carbon segregates to interstitial site between atomic layer 1 and 2	1.35	1.41	-0.53	2.30	2.28	0.61
Carbon segregates to interstitial site between atomic layer 3 and 4 bonding with 1Ir and 2Ni on layer 3	0.18	0.45	-1.45	0.37	0.50	-1.43
Carbon segregates to interstitial site between atomic layer 3 and 4 bonding with 1Ni and 2Ir on layer 3	0.07	0.34	-1.49	0.24	0.37	-1.52

Since the study with Pd_3Co and Ir_3Co has shown the segregation trend of Co inside core to the 3rd atomic layer in which Fe or Ni atoms present, only the presence of Co in the 2nd and 3rd atomic layers (anchor layers) is considered with IrCo core and the results are shown in Table 7.4. As expected, only segregation of Ir inside core is favorable and other elements show thermodynamically favorable antisegregation trends.

Table 7.5 shows the results of structures with IrNi core material. Again, with the presence of Ni in the anchor layers, carbon atoms are likely to move to other interstitial positions above subsurface and below the 3rd atomic layer, thus Pt/Ni-C/IrNi may not serve as a good catalyst with improved stability. Interestingly, the segregation of Ir inside IrNi core is not favorable except with the presence of Co in anchor layers.

In summary, Pt/Co-C/Pd_3Co, Pt/Fe-C/Pd_3Co, Pt/Co-C/Ir_3Co, Pt/Fe-C/Ir_3Co, Pt/Co-C/IrCo, Pt/Co-C/IrNi, Pt/Fe-C/IrNi show good stability. With the presence of Co in core material, Co-C display better stability than Fe-C and Ni-C. With the presence of Ni in core material, both Co-C and Fe-C display better stability than Ni-C. Ni is not a good choice to serve as metal anchored by carbon atoms because carbon atoms tend to relocate to other interstitial sites inside core.

It has been shown in ref [154] that on the structure Pt/Fe-C/Ir, Pt/Co-C/Ir and Pt/Ni-C/Ir the charges of carbon atoms are -0.92, -0.75 and -0.7, respectively and the charge of Fe, Co and Ni are +0.7, +0.57 and +0.52, respectively. The Pt surface charge are similar in which they are -0.25, -0.2 and -0.2 for Fe-C, Co-C and Ni-C, respectively. Co shows moderate positive charge and negative charge of carbon while Fe show the highest positive and highest negative charge for carbon and Ni show the lowest polarization. As we have seen the trend of Co inside core to segregate to the anchor layers with Fe and Ni this may result from the preference of moderate degree of oxidation of Co and carbon reduction (moderate polarization) comparing to Fe-C and Ni-C which induce Co-C more favorable. Ni-C may show too small polarization leading to carbon to relocate inside core either Co or Ni presents. Also, Fe-C is favorable with Ni inside core may suggest X-C should have higher polarization when Ni is present inside the core.

Table 7.6
Calculated electrode potential shift, ΔU, in V, in vacuum and under 0.25 ML O.

Structure	In vacuum (V)	Under 0.25 ML O (V)
Pt/Co-C/Pd_3Co	-0.09	0.07
Pt/Co-C/Ir_3Co	0.26	0.07
Pt/Co-C/IrCo	0.25	0.07
Pt/Fe-C/IrNi	0.27	0.12
Pt/Co-C/IrNi	0.26	0.07

The electrode potential shift for the Pt dissolution reaction $Pt \rightarrow Pt^{2+} + 2e^-$ relative to that on Pt(111) (the calculation method is explained in Chapter VI section 6.3.1) is calculated as shown in Table 7.6. A positive shift indicates a delay on the dissolution of Pt surface atoms with respect to that occurring on a Pt(111) surface; the opposite holds for a negative shift. We considered only the structures with antisegregation trends of the metal and with stable interstitial carbon. All of them show positive shifts under O adsorption which indicate that Pt surface dissolution may occur at relatively higher potential than Pt(111) suggesting higher durability.

It has been shown that a good ORR catalyst should not bond with O and OH too strong in order to facilitate O-O breaking, and the O and OH adsorption strengths should not be too weak to facilitate further reduction of O and OH [109]. Also, the previous section shows that OH removal step forming water is the limiting step on Pt/Fe-C/Ir, Pt/Co-C/Ir and Pt/Ni-C/Ir, thus OH can be an activity descriptor for shell-anchor-core structures. Table 7.7 shows O and OH adsorption energies on the structures. They adsorb O and OH weaker than Pt(111), therefore, these shell-anchor-core structures facilitate O and OH removal step by lowering its barrier energy leading to favorable ORR activity. Pt-Pt surface distances (Table 7.8) simply demonstrate the geometric effect in which surface strain can induce weaker adsorption energy [43, 157]. All structures show compressed Pt-Pt distance comparing to Pt(111) (approximately 0.07 Å shorter), consequently weaker O and OH adsorption. Although the Pt-Pt distance on shell-anchor-core structures are all similar (~2.74 Å), their adsorption energies can differ more than 0.1 eV. This may arise from the electronic effect that the core material imparts to the carbide layer i.e. Fe-C/Co-C/Ni-C, consequently affecting the Pt-skin layer.

Table 7.7
O and OH adsorption energies (eV) at 0.25 ML coverage on Pt/anchor/core structures arranging in the order of strongest (top) to weakest (bottom) adsorption. Structures show good stability is in red.

Structure	O adsorption energy (eV)
Pt(111)	-4.48 [a]
Pt/Co-C/Pd_3Co	-4.35
Pt/Fe-C/Ir	-3.84 [b]
Pt/Co-C/Ir	-3.67 [c]
Pt/Ni-C/IrNi	-3.66
Pt/Co-C/IrCo	-3.66
Pt/Ni-C/Ir_3Co	-3.66
Pt/Fe-C/IrNi	-3.64
Pt/Co-C/Ir_3Co	-3.63
Pt/Ni-C/Ir	-3.63 [c]
Pt/Co-C/IrNi	-3.61
Pt/Fe-C/Ir_3Co	-3.47
Pt/Fe-C/Pd_3Co	-3.44
Pt/Ni-C/Pd_3Co	-3.38

Structure	OH adsorption energy (eV)
Pt(111)	-2.38
Pt/Fe-C/IrNi	-2.23
Pt/Co-C/Ir	-2.16
Pt/Fe-C/Ir	-2.14
Pt/Fe-C/Ir_3Co	-2.12
Pt/Co-C/Pd_3Co	-2.11
Pt/Fe-C/Pd_3Co	-2.11
Pt/Co-C/IrCo	-2.11
Pt/Co-C/IrNi	-2.10
Pt/Co-C/Ir_3Co	-2.10
Pt/Ni-C/Pd_3Co	-2.04
Pt/Ni-C/Ir	-2.04
Pt/Ni-C/Ir_3Co	-2.02
Pt/Ni-C/IrNi	-2.00

[a] from ref [126], [b] from ref [153], [c] from ref [154]

Table 7.8
Pt-Pt distance on shell-anchor-core structures.

	Pt-Pt distance (Å)
Pt	2.814
Pt/Co-C/Ir	2.744
Pt/Co-C/Ir_3Co	2.741-2.746
Pt/Co-C/IrCo	2.742-2.744
Pt/Co-C/IrNi	2.741-2.747
Pt/Co-C/Pd_3Co	2.743-2.744
Pt/Fe-C/Ir	2.744
Pt/Fe-C/Ir_3Co	2.743-2.744
Pt/Fe-C/IrNi	2.743-2.744
Pt/Fe-C/Pd_3Co	2.743-2.744
Pt/Ni-C/Ir	2.744
Pt/Ni-C/Ir_3Co	2.743-2.744
Pt/Ni-C/IrNi	2.740-2.747
Pt/Ni-C/Pd_3Co	2.743-2.744

7.5. Conclusion

DFT calculations employed to investigate activity and properties confirm the promising ORR characteristics of shell-anchor-core catalysts of Pt/Fe-C/Ir, Pt/Ni-C/Ir, Pt/Co-C/Ir and Pd/Fe-C/Ir. The structures were designed to improve stability of the structure due to the anti-segregation of core elements and higher potential of Pt surface dissolution compared to Pt(111), thus the Pt monolayer surface durability is improved better than other reported Pt-skin core-shell structures. The calculated surface Pourbaix diagrams demonstrate the delay of water oxidation onset on Pt/Fe-C/Ir while for the other systems water oxidation onset takes place at approximately the same potential (~0.7 V) as Pt(111). However, the surface O and OH coverages are lower and do not increase rapidly with potential as seen on the Pt(111) diagram. Also, the very low OH coverage on these structures can enhance the ORR activity. The Pd/Fe-C/Ir surface is not recommended due to Pd surface dissolution at a potential as low as 0.95 V. All proposed ORR mechanisms are possible showing the same limiting step OH removal to form water. The calculated activities of Pt/Fe-C/Ir, Pt/Ni-C/Ir, Pt/Co-C/Ir are comparable and they are significantly higher than those on Pt(111).

Stability and activity of the structures composed of other core materials i.e. Pd_3Co, Ir_3Co, IrCo and IrNi are examined. With the presence of Co inside core, the structure with Co-C shows good stability of the anchor layers and with IrNi core, both Fe-C and Co-C show good stability of the anchor layers. Segregation inside core possibly happens for Ir in Ir_3Co, IrCo and for Pd in Pd_3Co core materials. The Pt-skin shows high durability against surface segregation and dissolution. All shell-anchor-core structures may achieve higher ORR activity as a result of weaker O and OH adsorption than those on Pt(111). The study suggests that Pt/Co-C/Pd_3Co, Pt/Fe-C/Pd_3Co, Pt/Co-C/Ir_3Co, Pt/Fe-C/Ir_3Co, Pt/Co-C/IrCo, Pt/Co-C/IrNi, Pt/Fe-C/IrNi promisingly show both improved durability and high ORR activity.

CHAPTER VIII

CONCLUSIONS AND RECOMMENDATIONS

The PEM fuel cell has a good potential as a clean-energy resource for transportation purposes; however, some challenges must be overcome to achieve full commercialization. In this work, we focused on the challenges of the high cost of PEM fuel cell due to Pt loading in the cathode electrode-catalyst where ORR takes place, and on the catalyst durability. DFT calculations are the main methodology for this work, which have been shown to appropriately describe both geometric and electronic properties of transition-metal systems. This dissertation is aimed to develop an understanding of the factors that determine ORR activity together with stability against surface segregation and dissolution of Pt-based alloys catalysts using DFT calculations. The outcome of this analysis can provide useful guidelines for the design of ORR catalysts.

PtCo alloys atomic distribution, water and atomic oxygen adsorption on the structures and electric field effect were firstly investigated. Pt-skin surface with Co-rich subsurface is found to be the most favorable configuration. Co on the surface shows high affinity to oxygenated species which is explained by the density of states of surface d-bands revealing that as Co composition on the surface increases there is a larger contribution of the minority-spin states at the Fermi level and in the neighbor unoccupied states. Water adsorption energies become stronger with the increase of Co on the surface, and this analysis suggests that both the surface and the first sub-surface layer are the main factors determining water adsorption energies. Water adsorption on Pt-skin surfaces is found weaker than on pure Pt(111) and dependent on the Co concentration on the sub-surface. A depletion of the electron density along the O–Pt bond on the Pt-skin surface is attributed to charge transfer to the surroundings in order to minimize the Pauli repulsion between the p and d orbitals of water and the surface respectively. In contrast, the electron density along the O–Co on the PtCo surface increases because of less repulsion

due to smaller overlap between the water 3a1 and the d orbitals of Co compared to that found in Pt(111) and Pt-skin surfaces.

On Pt-skin structures, O binding energies are significantly weaker than on PtCo and Pt(111). Similar to water adsorption, the stronger O binding energy of Co-rich surface can be explained with the electronic structure (d band) and the Co-rich subsurface alternate the electronic structure of Pt-skin structure resulting in weaker O binding energy on Pt-skin than on Pt(111). O binding energy on Pt-skin structure is further reduced by water co-adsorption thus favoring the subsequent oxygen reduction on the surface. At higher O coverage, further surface reconstruction effect (buckling effect) where surface and subsurface atoms shift upward or downward with respect to the bare surface due to screening of O-O interactions are found. Buckling increases with the increase of O coverage, and at a given coverage, especially with the Co surface atoms. However, on Pt-skin surfaces, buckling effects are negligible compared to those found on Pt(111) surfaces at the same O coverage. This finding is another indication of the stabilization effect of the alloy subsurface on the Pt-skin atoms. On the other hand, at relatively low O coverage, co-adsorption of O with water induces surface atom displacements of a magnitude comparable to that found at higher O coverage in absence of water. However, buckling of subsurface atoms mainly is affected by O adsorption rather than by water adsorption. Within the entire applied electric field range (-0.51 to 0.51 V/Å), spontaneous water dissociation is not found on the ordered and segregated alloy surfaces. The electric fields induce very small effect in the binding energies and geometries of water adsorption for all the surfaces, but significant polarization of the surface and subsurface is found on the PtCo surface. Yet, the changes are more pronounced in cluster models, where the surface atoms have much lower coordination.

The presence of Co-rich on subsurface under the Pt-skin can modify the Pt-skin characteristics toward higher ORR activity and stability. Nevertheless, Co in the subsurface tends to segregate to the surface with the presence of oxygenated intermediates and is accompanied with a large dissolution of Co atoms in acid medium

which determines drastic changes in the catalytic composition. Thus we hypothesize that a good catalyst may be obtained by adding other elements to the core to stabilize Co and reduce the cost, while retaining the Pt-skin structure and its high activity and stability. Core-shell structures are alternative catalysts for these characteristics. Pt loading can be reduced even further with this type of structure, having Pt only present on Pt-skin (shell) and the core composed of non-Pt elements.

Therefore, we examine stability and activity of Pt-skin core-shell structure on IrCo and Ir_3Co core both with and without Pd interlayer between Pt-skin and core elements which have been experimentally shown to possess significantly enhanced stability and ORR activity over Pt(111) [158]. In presence of atomic oxygen adsorption, Co and Ir are likely to segregate to the surface which can be easily dissolve and oxidized under ORR environment. The Pd interlayer plays a considerable role to prevent the segregation of core elements to the surface and maintain the Pt-skin on the surface compared to the same systems without Pd interlayer. However, oxygen adsorption on the surface might draw the segregation of Pd to the surface weakening the long-term stability of the structure because Pd can be oxidized at lower potential than Pt consequently, changing surface composition, structure and eventually may lead to substantial reduction of ORR activity. The significant stability improvement in terms of Pt surface atom dissolution for the Pt-skin with Pd interlayer structures compared to Pt(111) is not found as the Pd interlayer is not found to reduce the oxidation degree on Pt-skin. Although, these Pt-skin structures do not show higher stability for Pt dissolution than Pt(111), they show higher potential for water dissociation compared to Pt(111), and the corresponding O/OH coverage do not rapidly increase when potential increases as occurs on Pt(111). The delayed onset of water oxidation leads to more surface free sites available. Consequently, the relative ORR activity increases on Pt/(Pd)/Ir-Co. When Pd segregates to the surface the onset of water oxidation potential is lower due to strong O adsorption.

In addition, the investigation of ORR mechanisms reveals that the step of water formation is determined to be the limiting one. The highest activity among the clean

surfaces at a potential of 0.9 V is observed for Pt/Pd/IrCo (w/Pd seg) surface, followed by Pt/Pd/Ir_3Co (w/Pd seg) surface and Pt/Pd/IrCo; Pt/Ir_3Co and Pt(111) both show much lower activity. OH adsorption energy is an indicator of ORR activity of these surfaces. The presence of Pd interlayer results in slightly higher activity. It should be noted that the segregation of Pd to the surface may be a crucial effect which leads to considerable changes of the surface composition and morphology caused by Pd dissolution.

In this work we also investigate the activity of a new structure proposed by Ramirez-Caballero and Balbuena [153] which is composed of a pure Pt-skin surface over transition metal i.e. Fe, Co and Ni atomic layers where extra carbon atoms are added to interstitial sites of the transition metal in order to stabilize them, and an Ir core (Pt/Fe-C/Ir, Pt/Ni-C/Ir and Pt/Co-C/Ir). The structures with Ir core have demonstrated enhanced durability which arises from the use of carbon in the interstitial sites of the subsurface that anchors the Fe/Ni/Co atomic layers in their positions, impeding their segregation to the surface while keeping their beneficial properties that favor ORR activity on the top platinum monolayer [153, 154]. The calculations demonstrated the delay of water oxidation onset only on Pt/Fe-C/Ir comparing to Pt(111). Also, the surface O and OH coverages on Pt/Fe-C/Ir, Pt/Ni-C/Ir and Pt/Co-C/Ir do not increase rapidly with potential even at high potential as seen on Pt(111). These lower O and OH coverages lead to their high activity toward ORR. The Pd/Fe-C/Ir surface in which Pt monolayer is replaced with Pd monolayer is not recommended due to Pd surface dissolution at as low potential as 0.95 V. The ORR limiting step on Pt/Fe-C/Ir, Pt/Ni-C/Ir, and Pt/Co-C/Ir is found to be the step of OH removal to form water. The calculated activity of Pt/Fe-C/Ir, Pt/Ni-C/Ir, and Pt/Co-C/Ir are comparable and they are significantly higher than Pt(111).

Additionally, stability and activity of Pt/Fe-C/core, Pt/Ni-C/core, and Pt/Co-C/core with several core materials of Pd_3Co, Ir_3Co, IrCo and IrNi are investigated. It is found that with the presence of Co inside core, the structure with Co-C show good stability of the carbide layer and with IrNi core, both Fe-C and Co-C show good stability of the carbide layer. Segregation inside the core possibly happens for Ir in Ir_3Co, IrCo and for Pd in

Pd_3Co core materials. The Pt-skin on the shell-anchor-core structures shows high durability against surface segregation and dissolution. Also, all the structures may achieve higher ORR activity as a result of weaker O and OH adsorption than those on Pt(111). The study suggests that Pt/Fe-C/Ir, Pt/Co-C/Ir, Pt/Ni-C/Ir, Pt/Co-C/Pd_3Co, Pt/Fe-C/Pd_3Co, Pt/Co-C/Ir_3Co, Pt/Fe-C/Ir_3Co, Pt/Co-C/IrCo, Pt/Co-C/IrNi, and Pt/Fe-C/IrNi promisingly show both improved durability and high ORR activity.

As mentioned above, metal dissolution can be caused by oxide formation and acid medium is crucial because it affects surface composition and morphology leading to activity deterioration. Dissolution especially tends to occur in speed-up and down cycles as well as in start-up and shout down cycles of a vehicle. In order to gain a better understanding of the system under operating condition, oxide formation on the surface and electrolyte species should be incorporated into a model. Also, surface defects caused by dissolution (rough surface, islands or vacancies) can be included in a model. Moreover, the experimental study on the shell-anchor-core structure will strongly give confidence on the advantages of the structures toward ORR and provide further insightful analysis on the particular structure.

REFERENCES

[1] http://www1.eere.energy.gov/hydrogenandfuelcells/fuelcell/ Energy Efficeiency & Renewable Energy, U.S. Department of Energy, information for general fuel cell technology, accessed Oct 01, 2009.

[2] D.P. Woodruff, Surface Structure, in: A. Nilsson, L.G.M. Pettersson, J. K. Nørskov (Eds.), Chemical Bonding at Surfaces and Interfaces, Elsevier, Oxford, 2008.

[3] V.R. Stamenkovic, N.M. Markovic, Electrochemistry at well-characterized bimetallic surfaces, in: M. T. M. Koper (Eds), Fuel Cell Catalysis: A Surface Science Approach, John Wiley & Sons, Inc, Hoboken, New Jersey, 2009.

[4] J.O.M. Bockris, S.U.M. Khan, Surface Electrochemistry: A Molecular Level Approach, Plenum Press, New York, 1993.

[5] N.M. Markovic, P.N. Ross, Surf. Sci. Rep. 45 (2002) 117-229.

[6] R.A. Olsen, G.J. Kroes, E.J. Baerends, J. Chem. Phys. 111 (1999) 11155-11163.

[7] J.L. Gland, B.A. Sexton, G.B. Fisher, Surf. Sci. 95 (1980) 587-602.

[8] C.T. Campbell, G. Ertl, H. Kuipers, J. Segner, Surf. Sci. 107 (1980) 220-236.

[9] K. Mortensen, C. Klink, F. Jensen, F. Besenbacher, I. Stensgaard, Surf. Sci. Lett. 220 (1989) L701-L708.

[10] K. Christmann, G. Ertl, Surf. Sci. 60 (1976) 365-384.

[11] G. Ertl, M. Neumann, K.M. Streit, Surf. Sci. 64 (1977) 393-410.

[12] F.T. Wagner, P.N. Ross, J. Electroanal. Chem. 250 (1988) 301-320.

[13] N.M. Markovic, T.J. Schmidt, B.N. Grgur, H.A. Gasteiger, R.J. Behm, P.N. Ross, J. Phy. Chem. B 103 (1999) 8568-8577.

[14] G. Jerkiewicz, Progress in Surf. Sci. 57 (1998) 137-186.

[15] N. Markovic, H. Gasteiger, P.N. Ross, J. Electrochem. Soc. 144 (1997) 1591-1597.

[16] A. Michaelides, P. Hu, J. Chem. Phys. 114 (2001) 513-519.

[17] N.M. Markovic, H.A. Gasteiger, P.N. Ross, J. Phy. Chem. 99 (1995) 3411-3415.

[18] N.M. Markovic, H.A. Gasteiger, P.N. Ross, J. Phy. Chem.100 (1996) 6715-6721.

[19] D.V. Tripkovic, D. Strmcnik, D.v.d. Vliet, V. Stamenkovic, N.M. Markovic, Faraday Discuss. 140 (2009) 25-40.

[20] T. Toda, H. Igarashi, H. Uchida, M. Watanabe, J. Electrochem. Soc. 146 (1999) 3750-3756.

[21] V. Stamenkovic, T.J. Schmidt, P.N. Ross, N.M. Markovic, J. Phys. Chem. B 106 (2002) 11970-11979.

[22] M. Wakisaka, H. Suzuki, S. Mitsui, H. Uchida, M. Watanabe, J. Phys. Chem. C 112 (2008) 2750-2755.

[23] S. Mukerjee, S. Srinivasan, J. Electroanal. Chem. 357 (1993) 201-224.

[24] C.A. Lucas, M. Cormack, M.E. Gallagher, A. Brownrigg, P. Thompson, B. Fowler, Y. Grunder, J. Roy, V. Stamenkovic, N.M. Markovic, Faraday Discuss. 140 (2009) 41-58.

[25] S. Chen, W. Sheng, N. Yabuuchi, P.J. Ferreira, L.F. Allard, Y. Shao-Horn, J. Phys. Chem. C 113 (2008) 1109-1125.

[26] V.R. Stamenkovic, B. Fowler, B.S. Mun, G. Wang, P.N. Ross, C.A. Lucas, N.M. Markovic, Science 315 (2007) 493-497.

[27] A. Nilekar, Y. Xu, J. Zhang, M. Vukmirovic, K. Sasaki, R. Adzic, M. Mavrikakis, Top. Catal. 46 (2007) 276-284.

[28] S. Koh, P. Strasser, J. Am. Chem. Soc. 129 (2007) 12624-12625.

[29] S. Koh, J. Leisch, M.F. Toney, P. Strasser, J. Phys. Chem. C 111 (2007) 3744-3752.

[30] H.T. Duong, M.A. Rigsby, W.P. Zhou, A. Wieckowski, J. Phys. Chem. C 111 (2007) 13460-13465.

[31] V.R. Stamenkovic, B.S. Mun, K.J.J. Mayrhofer, P.N. Ross, N.M. Markovic, J. Am. Chem. Soc. 128 (2006) 8813-8819.

[32] U.A. Paulus, A. Wokaun, G.G. Scherer, T.J. Schmidt, V. Stamenkovic, N.M. Markovic, P.N. Ross, Electrochim. Acta 47 (2002) 3787-3798.

[33] U.A. Paulus, A. Wokaun, G.G. Scherer, T.J. Schmidt, V. Stamenkovic, V. Radmilovic, N.M. Markovic, P.N. Ross, J. Phys. Chem. B 106 (2002) 4181-4191.

[34] L. Xiong, A. Manthiram, J. Mater. Chem. 14 (2004) 1454-1460.

[35] S. Mukerjee, S. Srinivasan, M.P. Soriaga, J. McBreen, J. Electrochem. Soc. 142 (1995) 1409-1422.

[36] T. Toda, H. Igarashi, M. Watanabe, J. Electroanal. Chem. 460 (1999) 258-262.

[37] L. Xiong, A. Manthiram, J. Electrochem. Soc. 152 (2005) A697-A703.

[38] M.B. Vukmirovic, J. Zhang, K. Sasaki, A.U. Nilekar, F. Uribe, M. Mavrikakis, R.R. Adzic, Electrochim. Acta 52 (2007) 2257-2263.

[39] J. Zhang, M.B. Vukmirovic, Y. Xu, M. Mavrikakis, R.R. Adzic, Angew. Chem. Int. Ed. 44 (2005) 2132-2135.

[40] W.-P. Zhou, X. Yang, M.B. Vukmirovic, B.E. Koel, J. Jiao, G. Peng, M. Mavrikakis, R.R. Adzic, J. Am. Chem. Soc. 131 (2009) 12755-12762.

[41] W.-P. Zhou, M. Vukmirovic, K. Sasaki, R. Adzic, ECS Trans. 13 (2008) 23-28.

[42] T. Bligaard, J.K. Nørskov, Heterogeneous catalysis, in: A. Nilsson, L.G.M. Pettersson, J. K. Nørskov (Eds.), Chemical Bonding at Surfaces and Interfaces, Elsevier, Oxford, 2008.

[43] B. Hammer, J.K. Nørskov, Theoretical Surface Science and Catalysis-Calculations and Concepts, Advances in Catalysis Vol.45, Academic Press, 2000.

[44] U. Starke, M.A. Van Hove, G.A. Somorjai, Prog. Surf. Sci. 46 (1994) 305-319.

[45] B. Hammer, J.K. Nørskov, Surf.Sci. 343 (1995) 211-220.

[46] B. Hammer, J.K. Nørskov, Surf. Sci. 359 (1996) 306-306.

[47] V. Pallassana, M. Neurock, J. Catal. 191 (2000) 301-317.

[48] B. Hammer, O.H. Nielsen, J.K. Nrskov, Catal. Lett. 46 (1997) 31-35.

[49] P. Kratzer, B. Hammer, J.K. Nørskov, Surf. Sci. 359 (1996) 45-53.

[50] S. Dahl, A. Logadottir, R.C. Egeberg, J.H. Larsen, I. Chorkendorff, E. Törnqvist, J.K. Nørskov, Phys. Rev. Lett. 83 (1999) 1814.

[51] B. Hammer, Phys. Rev.Lett. 83 (1999) 3681.

[52] V.R. Stamenkovic, B.S. Mun, M. Arenz, K.J.J. Mayrhofer, C.A. Lucas, G. Wang, P.N. Ross, N.M. Markovic, Nat. Mater. 6 (2007) 241-247.

[53] M. Weinert, R.E. Watson, Phys. Rev. B 51 (1995) 17168.

[54] D. Hennig, M.V. Ganduglia-Pirovano, M. Scheffler, Phy. Rev. B 53 (1996) 10344.

[55] M.V. Ganduglia-Pirovano, V. Natoli, M.H. Cohen, J. Kudrnovský, I. Turek, Phys. Rev. B 54 (1996) 8892.

[56] J.A. Rodriguez, D.W. Goodman, Science 257 (1992) 897-903.

[57] F. Jensen, Introduction to Computational Chemistry, John Wiley & Sons, New York, 1999.

[58] D.S. Sholl, J.A. Steckel, Density Functional Theory: A Practical Introduction, John Wiley & Sons, Inc., Hoboken, New Jersey, 2009.

[59] J.Greeley, J.K. Nørskov, Electrochim. Acta 52 (2007) 5829-5836.

[60] O. Wieckhorst, S. Müller, L. Hammer, K. Heinz, Phys. Rev. Lett. 92 (2004) 4.

[61] Y. Ma, P.B. Balbuena, Surf. Sci. 602 (2008) 107-113.

[62] V. Stamenkovic, B.S. Mun, K.J.J. Mayrhofer, P.N. Ross, N.M. Markovic, J. Rossmeisl, J. Greeley, J.K. Nørskov, Angew. Chem. Int. Ed. 45 (2006) 2897-2901.

[63] C.D. Taylor, M. Neurock, Curr. Opin. Solid State Mater. Sci. 9 (2005) 49-65.

[64] A. Michaelides, A. Alavi, D.A. King, J. Am. Chem. Soc. 125 (2003) 2746-2755.

[65] G. Materzanini, T. Gian Franco, J.D.L. Philip, S. Peter, Phys. Rev. B 71 (2005) 155414.

[66] A. Michaelides, V.A. Ranea, P.L.d. Andres, D.A. King, Phys. Rev. Lett. 90 (2003) 216102-216101-216104.

[67] P.J. Feibelman, Science 295 (2002) 99-102.

[68] G. Held, D. Menzel, Surf. Sci. 316 (1994) 92-102.

[69] P. Vassilev, R.A. Van Santen, M.T.M. Koper, J. Chem. Phys. 122 (2005) 054701.

[70] J. Ren, S. Meng, J. Am. Chem. Soc. 128 (2006) 9282-9283.

[71] R. Jun, M. Sheng, Phys. Rev. B (Condensed Matter and Materials Physics) 77 (2008) 054110.

[72] H. Ogasawara, B. Brena, D. Nordlund, M. Nyberg, A. Pelmenschikov, L.G.M. Pettersson, A. Nilsson, Phys. Rev. Lett. 89 (2002) 276102-276101-276104.

[73] M.A. Henderson, Surf. Sci. Rep. 46 (2002) 1-308.

[74] S. Meng, E.G. Wang, S. Gao, Phys. Rev. B 69 (2004) 195404-195417.

[75] L. Jibiao, Z. Shenglong, L. Ying, W. Fuhui, Phys. Rev. B (Condensed Matter and Materials Physics) 76 (2007) 235433.

[76] G.S. Karlberg, Phys. Rev. B (Condensed Matter and Materials Physics) 74 (2006) 153414.

[77] J.K. Norskov, J. Rossmeisl, A. Logadottir, L. Lindqvist, J.R. Kitchin, T. Bligaard, H. Jonsson, J. Phys. Chem. B 108 (2004) 17886-17892.

[78] P. Strasser, H. Ogasawara, Surface Electrochemistry, in: A. Nilsson, L.G.M. Pettersson, J. K. Nørskov (Eds.), Chemical Bonding at Surfaces and Interfaces, Elsevier, Oxford, 2008.

[79] R. Jerome, B.A. Alfred, J. Electrochem. Soc. 151 (2004) E340-E347.

[80] J. Roques, A.B. Anderson, Surf. Sci. 581 (2005) 105-117.

[81] G. Kresse, J. Furthmüller, Phys. Rev. B 54 (1996) 11169-11186.

[82] G. Kresse, J. Furthmüller, Comput. Mat. Sci. 6 (1996) 15-50.

[83] G. Kresse, J. Hafner, Phys. Rev. B 47 (1993) 558-561.

[84] G. Kresse, J. Hafner, Phys. Rev. B 49 (1994) 14251-14269.

[85] A. Kootte, C. Haas, R.A. De Groot, J. Phys.: Condens. Matter 3 (1991) 1133-1152.

[86] S. Ferrer, J. Alvarez, E. Lundgren, X. T**or**relles, P. Fajardo, F. Boscherini, Phys. Rev. B 56 (1997) 9848.

[87] J.P. Perdew, K. Burke, M. Ernzerhof, Phys. Rev. Lett. 77 (1996) 3865-3868.

[88] H.J. Monkhorst, J.D. Pack, Phys. Rev. B 13 (1976) 5188-5192.

[89] M. Methfessel, A.T. Paxton, Phys. Rev. B 40 (1989) 3616-3621.

[90] G. Henkelmana, A. Arnaldsson, H. Jónsson, Comput. Mater. Sci. 36 (2006) 354-360.

[91] E. Sanville, S.D. Kenny, R. Smith, G. Henkelman, J. Comput. Chem. 28 (2007) 899-908.

[92] A. Kokalj, Comput. Mater. Sci. 28 (2003) 155-168.

[93] Y. Ma, P.B. Balbuena, J. Phys. Chem. C 112 (2008) 14520-14528.

[94] R.K. John, R. Karsten, S. Matthias, Phys. Rev. B (Condensed Matter and Materials Physics) 77 (2008) 075437.

[95] T. Takako, I. Hiroshi, U. Hiroyuki, W. Masahiro, J. Electrochem. Soc. 146 (1999) 3750-3756.

[96] J. Roques, A.B. Anderson, V.S. Murthi, S. Mukerjee, J. Electrochem. Soc. 152 (2005) E193-E199.

[97] J. Roques, A.B. Anderson, Surf. Sci. 581 (2005) 105-117.

[98] S. Axnanda, D.K. Cummins, T. He, W.D. Goodman, and P.M. Soriaga, Chem. Phys. Chem. 11 (2010) 1468-1475.

[99] B. Hammer, J.K. Nørskov, Adv. Catal. 45 (2000) 71-129.

[100] K. Iwashita, T. Oguchi, T. Jo, Phys. Rev. B 54 (1996) 1159-1162.

[101] M. Shirai, H. Maeshima, N. Suzuki, J. Magn. Magn. Mater.140 (1995) 105-106.

[102] J.B. Hasted, Liquid Water: Dielectric Properties, in Water a Comprehensive Treatise, Plenum Press, New York, 1972.

[103] Z. Gu, P.B. Balbuena, J. Phys. Chem. C 111 (2007) 9877-9883.

[104] P. Hirunsit, P.B. Balbuena, Surf. Sci. 603 (2009) 911-919.

[105] Y. Xu, A.V. Ruban, M. Mavrikakis, J. Am. Chem. Soc. 126 (2004) 4717-4725.

[106] J. Lipkowski, P.N. Ross, Electrocatalysis, Wiley-VCH, New York, 1998.

[107] J.L. Fernandez, D.A. Walsh, A.J. Bard, J. Am Chem. Soc. 127 (2005) 357-365.

[108] Y. Wang, P.B. Balbuena, J. Phys. Chem. B 109 (2005) 18902-18906.

[109] J.K. Norskøv, J. Rossmeisl, A. Logadottir, L. Lindqvist, J.R. Kitchin, T. Bligaard, H. Jonsson, J. Phys. Chem. B 108 (2004) 17886-17892.

[110] A.B. Anderson, Electrochim. Acta 47 (2002) 3759-3763.

[111] G.B. Fisher, J.L. Gland, Surf. Sci. 94 (1980) 446-455.

[112] G.B. Fisher, B.A. Sexton, Phys. Rev. Lett. 44 (1980) 683-686.

[113] J. Roques, A.B. Anderson, J. Electrochem. Soc. 151 (2004) E340-E347.

[114] A. Panchenko, M.T.M. Koper, T.E. Shubina, S.J. Mitchell, E. Roduner, J. Electrochem. Soc. 151 (2004) A2016-A2027.

[115] H.J. Monkhorst, J.D. Pack, Phys. Rev. B 13 (1976) 5188-5192.

[116] M.P. Hyman, J.W. Medlin, J. Phys. Chem. B 109 (2005) 6304-6310.

[117] M.J. Frisch, G.W. Trucks, H.B. Schlegel, G.E. Scuseria, M.A. Robb, J.R. Cheeseman, J.A. Montgomery, T. Vreven, K.N. Kudin, J.C. Burant, J.M. Millam, S.S. Iyengar, J. Tomasi, V. Barone, B. Mennucci, M. Cossi, G. Scalmani, N. Rega, G.A. Petersson, H. Nakatsuji, M. Hada, M. Ehara, K. Toyota, R. Fukuda, J. Hasegawa, M. Ishida, T. Nakajima, Y. Honda, O. Kitao, H. Nakai, M. Klene, X. Li, J.E. Knox, H.P. Hratchian, J.B. Cross, V. Bakken, C. Adamo, J. Jaramillo, R. Gomperts, R.E. Stratmann, O. Yazyev, A.J. Austin, R. Cammi, C. Pomelli, J.W. Ochterski, P.Y. Ayala, K. Morokuma, G.A. Voth, P. Salvador, J.J. Dannenberg, V.G. Zakrzewski, S. Dapprich, A.D. Daniels, M.C. Strain, O. Farkas, D.K. Malick, A.D. Rabuck, K. Raghavachari, J.B. Foresman, J.V. Ortiz, Q. Cui, A.G. Baboul, S. Clifford, J. Cioslowski, B.B. Stefanov, G. Liu, A. Liashenko, P. Piskorz, I. Komaromi, R.L. Martin, D.J. Fox, T. Keith, M.A. Al-Laham, C.Y. Peng, A. Nanayakkara, M. Challacombe, P.M.W. Gill, B. Johnson, W. Chen, M.W. Wong, C. Gonzalez, J.A. Pople, Gaussian03, Revision C.02 ed., Gaussian, Inc., Wallingford, CT, 2004.

[118] M.P. Hyman, J.W. Medlin, J. Phys. Chem. C 111 (2007) 17052-17060.

[119] P.E.M. Siegbahn, M.R.A. Blomberg, M. Wirstam née Pavlov, R.H. Crabtree, J. Biol. Inorg. Chem. 6 (2001) 460-466.

[120] K. Morgenstern, K.-H. Rieder, J. Chem. Phys. 116 (2002) 5746-5752.

[121] K. Morgenstern, J. Nieminen, Phys. Rev. Lett. 88 (2002) 066102.

[122] T. Mitsui, M.K. Rose, E. Fomin, D.F. Ogletree, M. Salmeron, Science 297 (2002) 1850-1852.

[123] M. Otani, I. Hamada, O. Sugino, Y. Morikawa, Y. Okamoto, T. Ikeshoji, Phys. Chem. Chem. Phys. 10 (2008) 3609-3612.

[124] J.M. Hawkins, J.F. Weaver, A. Asthagiri, Phys. Rev. B (Condensed Matter and Materials Physics) 79 (2009) 125434.

[125] Z. Gu, P.B. Balbuena, J. Phys. Chem. C 112 (2008) 5057-5065.

[126] Y. Ma, P.B. Balbuena, J. Phys. Chem. C 112 (2008) 14520-14528.

[127] R. Adzic, J. Zhang, K. Sasaki, M. Vukmirovic, M. Shao, J. Wang, A. Nilekar, M. Mavrikakis, J. Valerio, F. Uribe, Top. Catal. 46 (2007) 249-262.

[128] A.U. Nilekar, M. Mavrikakis, Surf. Sci. 602 (2008) L89-L94.

[129] M.H. Shao, T. Huang, P. Liu, J. Zhang, K. Sasaki, M.B. Vukmirovic, R.R. Adzic, Langmuir 22 (2006) 10409-10415.

[130] M.-H. Shao, K. Sasaki, R.R. Adzic, J. Am. Chem. Soc. 128 (2006) 3526-3527.

[131] W.E. Mustain, K. Kepler, J. Prakash, Electrochim. Acta 52 (2007) 2102-2108.

[132] J.L. Fernandez, J.M. White, Y. Sun, W. Tang, G. Henkelman, A.J. Bard, Langmuir 22 (2006) 10426-10431.

[133] J.L. Fernandez, V. Raghuveer, A. Manthiram, A.J. Bard, J. Am. Chem. Soc. 127 (2005) 13100-13101.

[134] M. Shao, P. Liu, J. Zhang, R. Adzic, J. Phys. Chem. B 111 (2007) 6772-6775.

[135] B.C. Beard, J.P.N. Ross, J. Electrochem. Soc. 137 (1990) 3368-3374.

[136] D.A.J. Rand, R. Woods, J. Electroanal. Chem. 55 (1974) 375-381.

[137] K. Lee, L. Zhang, J. Zhang, J. Power Sources 170 (2007) 291-296.

[138] F.J. Vidal-Iglesias, J. Solla-Gullón, V. Montiel, J.M. Feliu, A. Aldaz, J. Power Sources 171 (2007) 448-456.

[139] K. Gong, W.-F. Chen, K. Sasaki, D. Su, M.B. Vukmirovic, W. Zhou, E.L. Izzo, C. Perez-Acosta, P. Hirunsit, P.B. Balbuena, R.R. Adzic, J. Electroanal. Chem. In press.

[140] E. Yeager, J. Electrochem. Soc. 128 (1981) 160C-171C.

[141] M.A. Genshaw, A. Damjanovic, J.O.M. Bockris, J. Phys. Chem. 71 (1967) 3722-3731.

[142] A. Damjanovic, M.A. Genshaw, J.O.M. Bockris, J. Phys. Chem. 71 (1966) 3722-3731.

[143] S.K. Desai, M. Neurock, Phys. Rev. B 68 (2003) 075420.

[144] P.W. Atkins, Physical Chemistry, sixth ed., Oxford University Press, Oxford, 1998.

[145] H. Ogasawara, B. Brena, D. Nordlund, M. Nyberg, A. Pelmenschikov, L.G.M. Pettersson, A. Nilsson, Phys. Rev. Lett. 89 (2002) 276102.

[146] K. Bedurftig, S. Volkening, Y. Wang, J. Wintterlin, K. Jacobi, G. Ertl, J. Chem. Phys. 111 (1999) 11147-11154.

[147] C. Clay, S. Haq, A. Hodgson, Phys. Rev. Lett. 92 (2004) 046102.

[148] G.S. Karlberg, F.E. Olsson, M. Persson, G. Wahnstrom, J. Chem. Phys. 119 (2003) 4865-4872.

[149] J. Rossmeisl, J.K. Norskov, C.D. Taylor, M.J. Janik, M. Neurock, J. Phys. Chem. B 110 (2006) 21833-21839.

[150] G.S. Karlberg, J. Rossmeisl, J.K. Norskov, Phys. Chem. Chem. Phys. 9 (2007) 5158-5161.

[151] H.A. Hansen, J. Rossmeisl, J.K. Norskov, Phys. Chem. Chem. Phys. 10 (2008) 3722-3730.

[152] J. Greeley, I.E.L. Stephens, A.S. Bondarenko, T.P. Johansson, H.A. Hansen, T.F. Jaramillo, RossmeislJ, ChorkendorffI, J.K. NÃ¸rskov, Nat. Chem. 1 (2009) 552-556.

[153] G.E. Ramirez-Caballero, P.B. Balbuena, J. Phys. Chem. Lett. 1 (2010) 724-728.

[154] G.E. Ramirez-Caballero, P. Hirunsit, P.B. Balbuena, submitted to J. Chem. Phys.

[155] S.C. Ball, S.L. Burton, J. Fisher, R. O'Malley, B.C. Tessier, B. Theobald, D. Thompsett, W.-P. Zhou, D. Su, Y. Zhu, R. Adzic, ECS Trans. 25 (2009) 1023-1036.

[156] E. Bucher, W.F. Brinkman, J.P. Maita, A.S. Cooper, Phys. Rev. B 1 (1970) 274.

[157] Y. Xu, A.V. Ruban, M. Mavrikakis, J. Am. Chem. Soc. 126 (2004) 4717-4725.

[158] K. Gong, W.-F. Chen, K. Sasaki, D. Su, M.B. Vukmirovic, W. Zhou, E.L. Izzo, C. Perez-Acosta, P. Hirunsit, P.B. Balbuena, R.R. Adzic, J. Electroanal. Chem. In press.

APPENDIX A

SUPPLEMENTAL DATA FOR EFFECTS OF WATER AND ELECTRIC FIELD ON ATOMIC OXYGEN ADSORPTION ON Pt-Co ALLOYS

A.1. Surface reconstruction at higher O coverage on Pt(111)

Table A1.
The differences in distances (in z direction) of water molecules co-adsorbed with different O coverage on Pt(111) from that without O adsorption. Positive value means the specified atom locate further away from the surface than that when without O adsorption and the opposite trend for negative value.

	O coverage								
	0.11 ML	0.22 ML	0.33 ML	0.44 ML	0.56 ML	0.67 ML	0.78 ML	0.89 ML	1.00 ML
O1 (O-Pt)[a]	0.00	-0.32	-0.38	-0.09	0.73	0.93	1.00	1.02	0.97
O2 (O-Pt)	0.55	0.92	1.17	1.12	1.03	1.05	1.05	1.01	0.96
O3 (O-Pt)	-0.02	0.86	0.82	0.79	0.72	0.70	0.68	0.86	0.96
O4 (H-Pt)[a]	0.02	0.36	0.44	0.49	0.58	0.64	0.64	0.67	0.67
O5 (H-Pt)	-0.02	0.05	0.06	0.37	0.62	0.65	0.64	0.67	0.67
O6 (H-Pt)	0.19	0.28	0.28	0.37	0.53	0.52	0.59	0.63	0.67
H1 (O1)[a]	0.09	-0.19	-0.23	0.02	0.69	0.79	0.93	0.94	0.88
H8 (O1)	-0.03	-0.28	-0.32	-0.04	0.70	0.85	0.86	0.89	0.86
H3 (O2)	0.35	0.61	0.78	0.96	0.91	0.93	0.94	0.90	0.87
H12 (O2)	0.37	0.64	0.93	0.91	0.87	0.91	0.91	0.88	0.85
H5 (O3)	0.00	0.77	0.67	0.70	0.70	0.69	0.68	0.82	0.88
H10 (O3)	0.06	0.68	0.65	0.68	0.65	0.64	0.60	0.74	0.85
H6 (O4)	-0.05	0.17	0.10	0.18	0.50	0.62	0.64	0.67	0.65
H7 (O4)	0.04	0.43	0.55	0.58	0.61	0.66	0.67	0.69	0.69
H4 (O5)	-0.06	0.21	0.21	0.46	0.55	0.55	0.55	0.64	0.67
H9 (O5)	0.00	0.09	0.13	0.50	0.65	0.69	0.67	0.69	0.69
H2 (O6)	0.26	0.45	0.55	0.58	0.64	0.64	0.67	0.68	0.66
H11 (O6)	0.20	0.36	0.39	0.44	0.54	0.54	0.63	0.66	0.69

[a](O-Pt) = H_2O corresponding to the oxygen atom bond with Pt(111) surface through oxygen atom
(H-Pt) = H_2O corresponding to the oxygen atom bond with Pt(111) surface through hydrogen atom
(O1) = the specified hydrogen atom belongs to oxygen atom 1.

A.2. Electric field effects

A.2.1. A water molecule adsorbed on Pt, PtCo, and Pt/Co/PtCo surfaces

Table A2.
Charges (in e) of subsurface atoms upon a water molecule adsorption on with Pt(111), PtCo(111) and Pt/Co/PtCo (111) surfaces using slab models.

	Pt(111)				PtCo				Pt/Co/PtCo			
Electric field (V/Å)	Pt5	Pt6	Pt7	Pt8	Pt3	Pt4	Co11	Co12	Co1	Co2	Co3	Co4
0.51	0.05	0.04	0.04	0.04	-0.40	-0.41	0.48	0.50	0.32	0.39	0.32	0.32
0.39	0.04	0.04	0.05	0.05	-0.40	-0.41	0.49	0.48	0.39	0.37	0.32	0.32
0.26	0.04	0.04	0.05	0.05	-0.40	-0.42	0.47	0.49	0.37	0.37	0.32	0.32
0.13	0.04	0.04	0.05	0.05	-0.41	-0.43	0.47	0.49	0.37	0.38	0.32	0.31
0	0.04	0.04	0.05	0.05	-0.41	-0.43	0.47	0.49	0.37	0.37	0.31	0.32
-0.13	0.04	0.04	0.05	0.05	-0.41	-0.43	0.47	0.49	0.29	0.39	0.32	0.32
-0.26	0.04	0.04	0.05	0.05	-0.41	-0.43	0.47	0.49	0.37	0.37	0.32	0.32
-0.39	0.04	0.04	0.04	0.05	-0.41	-0.43	0.47	0.49	0.38	0.37	0.32	0.32
-0.51	0.04	0.04	0.04	0.05	-0.42	-0.43	0.48	0.48	0.31	0.31	0.24	0.24

A.2.2. A water molecule adsorbed on Pt, PtCo, and Pt/Co/PtCo clusters

Table A3.
Water binding energy (eV), charges (in e) of oxygen, the total charge of a water molecule and Pt bonded with water on Pt cluster. Optimized distances (in Å) of Pt-O and Pt-H bonds of water molecule on Pt cluster.

E field (V/Å)	BE water	Charge on O	Charge on H_2O	Charge on Pt bonding with O	Charge on Pt bonding with H	Pt-O bond length	Pt-H bond length
0.51	-0.50	-0.47	0.48	0.04		2.05	
0.39	0.03	-0.45	0.33	0.01		2.03	
0.26	-0.10	-0.44	0.30	0.13		2.02	
0.13	-0.43	-0.45	0.20	0.12		2.02	
0.00	-0.72	-0.45	0.10	0.15		2.01	
-0.13	-0.39	-0.73	-0.18		0.14		2.99
-0.26	-0.05	-0.65	-0.27		0.16		2.69
-0.39	-0.50	-0.58	-0.36		0.17		2.71
-0.51	-0.29	-0.52	-0.45		0.20		2.67

(a)

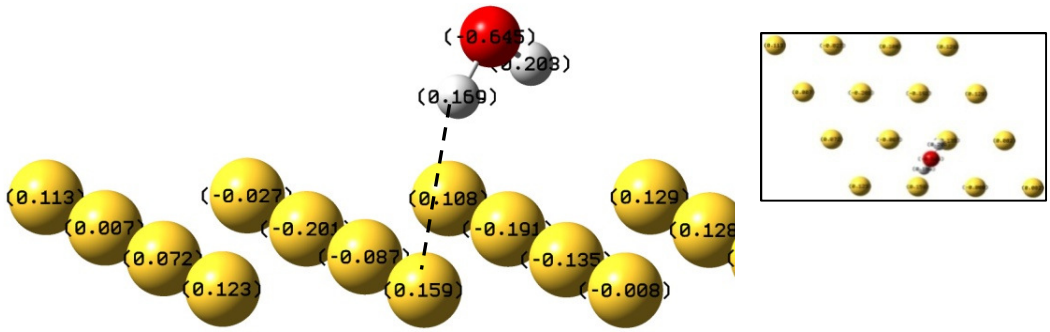

Fig. A1. Geometries and charge distribution of water adsorption on Pt cluster with applied electric field of (a) -0.26 V/Å (b) +0.26 V/Å. The insets show top views of each structure.

(b)

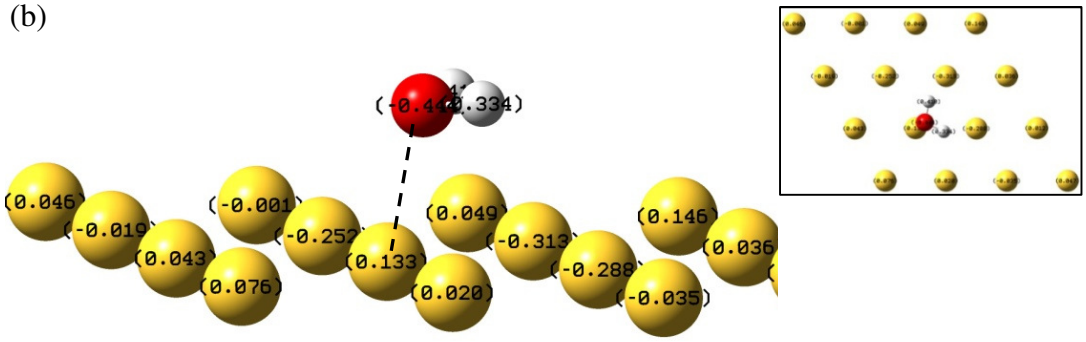

Fig. A1. (cont'd)

Table A4.
Water binding energy (eV), charges (in e) of water, Co atom bonding with water and lengths (in Å) of Co-O of water adsorbed on PtCo cluster.

E field (V/Å)	BE water	Charge on H_2O	Charge on Co bonding with O	Co-O bond length
0.51	-1.21	0.41	0.12	1.92
0.39	-1.65	0.41	0.12	1.92
0.26	-1.34	0.29	0.18	1.92
0.13	-1.13	0.18	0.29	1.92
0.00	-1.62	0.08	0.38	1.92
-0.13	-1.06	-0.07	0.35	1.92
-0.26	-1.63	-0.16	0.45	1.94
-0.39	-1.49	-0.29	0.45	1.96
-0.51	-1.03	-0.38	0.51	1.96

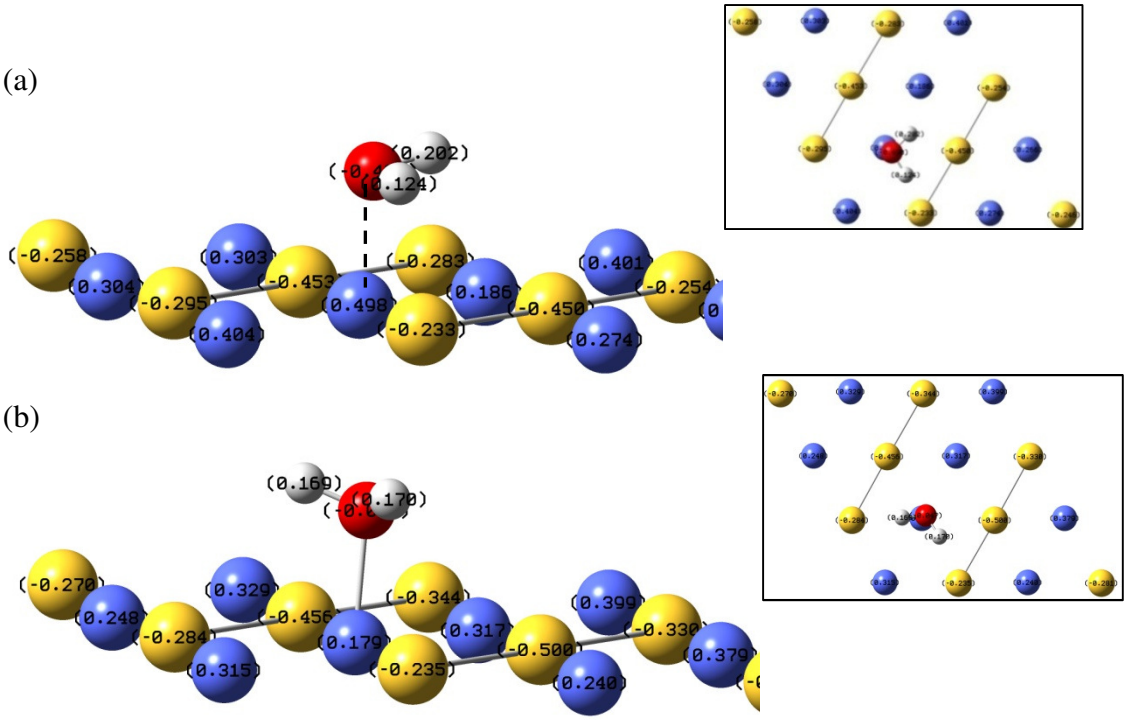

Fig. A2. Geometries and charge distribution of water adsorption on PtCo cluster with applied electric field of (a) -0.26 V/Å (b) +0.26 V/Å. The insets show top views of each structure. Pt: yellow, Co: blue.

A.2.3. Atomic oxygen adsorption on Pt, PtCo, and Pt/Co/PtCo surfaces in presence of a water molecule.

Table A5.
Charges (in e) of subsurface atoms upon a water molecule and O adsorption on Pt(111), PtCo(111) and Pt/Co/PtCo (111) surfaces using slab models.

	Pt(111)				PtCo				Pt/Co/PtCo			
E field (V/Å)	Pt5	Pt6	Pt7	Pt8	Pt3	Pt4	Co3	Co4	Co1	Co2	Co3	Co4
0.51					-0.43	-0.42	0.48	0.50	0.29	0.29	0.32	0.33
0.39	0.04	0.03	-0.02	0.04	-0.43	-0.40	0.47	0.49	0.29	0.37	0.31	0.32
0.26	0.03	0.03	-0.02	0.04	-0.44	-0.42	0.49	0.49	0.28	0.37	0.31	0.32
0.13	0.04	0.03	-0.02	0.04	-0.44	-0.42	0.49	0.50	0.28	0.37	0.31	0.32
0	0.04	0.04	-0.02	0.03	-0.44	-0.43	0.49	0.50	0.28	0.37	0.30	0.32
-0.13	0.04	0.04	-0.02	0.04	-0.44	-0.43	0.49	0.49	0.28	0.37	0.30	0.31
-0.26	0.04	0.04	-0.02	0.04	-0.44	-0.42	0.48	0.49	0.28	0.36	0.31	0.32
-0.39	0.03	0.04	-0.02	0.04	-0.44	-0.42	0.48	0.49	0.28	0.38	0.29	0.29
-0.51	0.03	0.04	-0.02	0.04					0.28	0.37	0.31	0.31

A.2.4. Atomic oxygen adsorption on Pt, PtCo, and Pt/Co/PtCo cluster in presence of a water molecule.

(a)

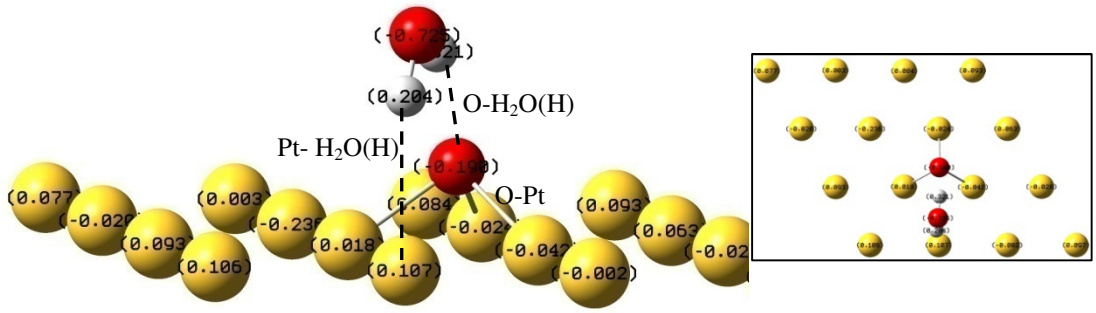

(b)

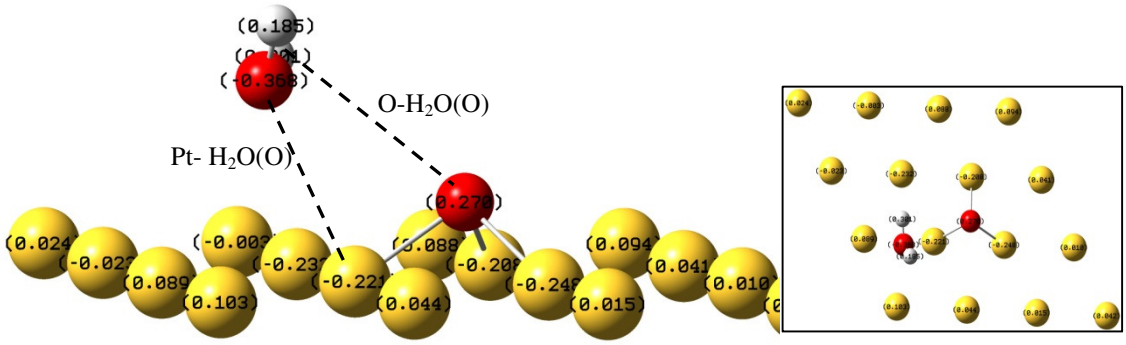

Fig. A3. Geometries and charge distribution of O and H_2O adsorption on the Pt cluster with applied electric fields of (a) -0.26 V/Å (b) +0.39 V/Å. The insets show top views of each structure.

Table A6.
Charges (in e) of O, H_2O, Pt bonded with atomic oxygen and optimized bonding distances of Pt-O, Pt-H_2O, and O-H_2O of a water molecule on the Pt cluster shown in Fig. A3.

E field (V/Å)	O charge	H_2O charge	Pt bonding with O charge[a]	Pt-O (Å)	Pt-H_2O (Å)[b]	O-H_2O (Å)[b]
0.51	0.37	0.16	-0.29	1.93	(O) 3.06	(O) 3.27
0.39	0.27	0.12	-0.25	1.93	(O) 3.13	(O) 3.36
0.26	0.20	0.05	-0.22	1.93	(H) 3.15	(H) 3.34
0.13	0.12	-0.05	-0.20	1.94	(H) 2.66	(H) 2.95
-0.13	-0.05	-0.18	-0.10	1.94	(H) 2.51	(H) 2.23
-0.26	-0.19	-0.20	-0.04	1.94	(H) 2.53	(H) 2.20
-0.39	-0.33	-0.22	0.15	1.95	(H) 2.55	(H) 2.18
-0.51	-0.48	-0.24	0.08	1.95	(H) 2.59	(H) 2.15

[a] Charge of the Pt atom in the Pt-O bond.
[b] In parenthesis the atom of H_2O (O or H) that is closest to adsorbed atomic oxygen.

Table A7.
Charges (in e) of O, H_2O, Pt bonded with O and optimized bonding distances (in Å) of Pt-O, Pt-H_2O, and O-H_2O on PtCo clusters shown in Fig. A4.

E field (V/Å)	O Charge	H_2O charge	Co bonding with O Charge [a]	Pt bonding with O Charge [a]	Co-O	Pt-O	Co-O_{H2O}	O-H_2O[b]
0.51	0.44	0.32	-0.11	-0.55	1.73	1.96	1.96	(O) 2.40
0.39	0.33	0.13	-0.05	-0.50	1.72	1.95	1.96	(O) 2.40
0.26	0.18	0.10	0.02	-0.46	1.72	1.95	1.96	(O) 2.41
0.13	0.02	0.07	0.09	-0.38	1.71	1.96	1.96	(O) 2.41
0.00	-0.10	0.03	0.18	-0.38	1.71	1.94	1.96	(O) 2.40
-0.13	-0.30	0.02	0.19	-0.28	1.73	1.96	1.96	(H) 1.96
-0.26	-0.51	-0.01	0.31	-0.23	1.72	1.98	1.99	(H) 1.93
-0.39	-0.66	-0.04	0.37	-0.18	1.72	1.97	2.00	(H) 1.85
-0.51	-0.84	-0.08	0.45	-0.12	1.72	1.98	2.00	(H) 1.86

[a] Charge of the Co or Pt atom at the Co-O and Pt-O bonds with atomic oxygen.
[b] In parenthesis the H_2O atom (O or H) corresponding to the bonding with atomic oxygen.

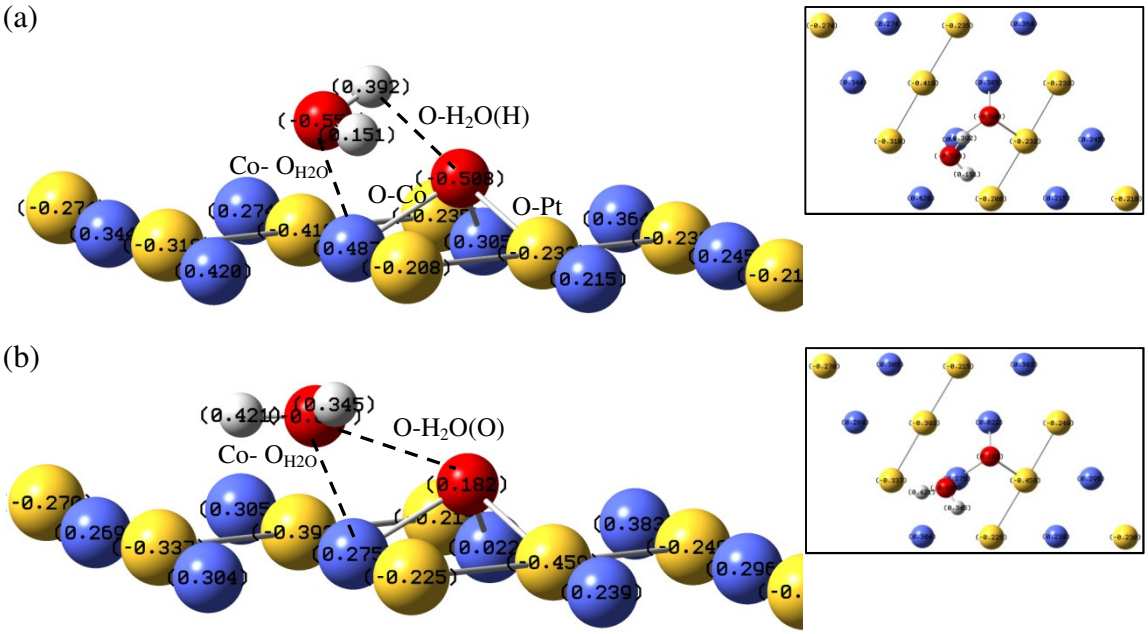

Fig. A4. Geometries and charge distribution of O and H_2O adsorbed on a PtCo cluster with applied electric fields of (a) -0.26 V/Å (b) +0.26 V/Å. The insets show top views of each structure. Pt: yellow, Co: blue.

APPENDIX B

SUPPLEMENT DATA FOR SURFACE POURBAIX DIAGRAMS, STABILITY, AND OXYGEN REDUCTION ACTIVITY OF Pt/Ir-Co AND Pt/Pd/Ir-Co

B.1. Structures of O* and *OH co-adsorption with water on Pt(111).

(a)

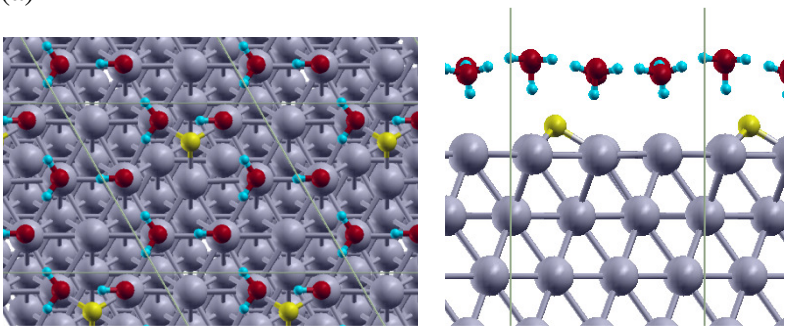

(b)

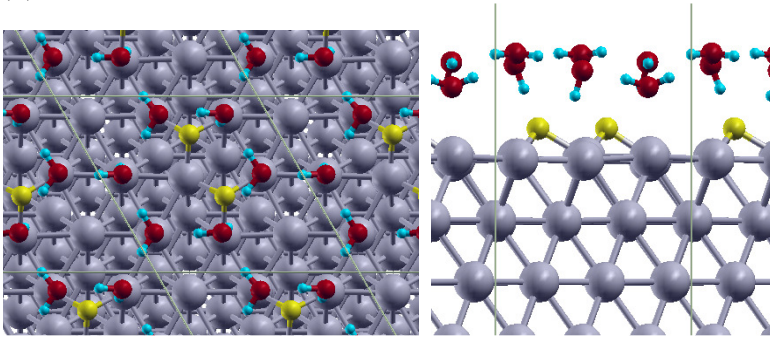

Fig. B1. Top view and side view of the Pt(111) structures with different coverage of O* co-adsorb with water. (a) 0.11 ML O* (b) 0.22 ML O* (c) 0.33 ML O* (d) 0.44 ML O* (e) 0.55 ML O*. Grey-Pt, Yellow-O, Red-O belonging to H_2O and Blue-H.

(c)

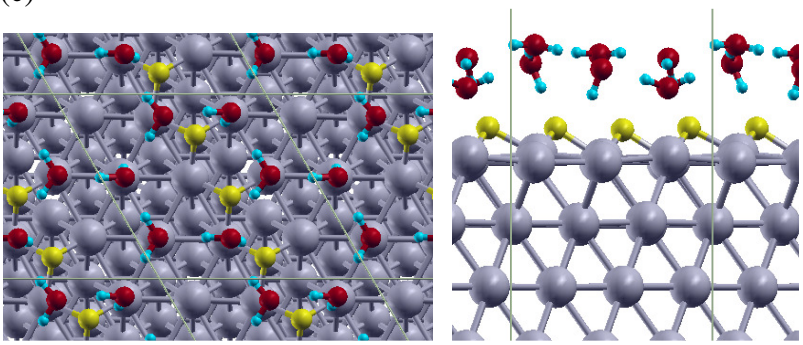

(d)

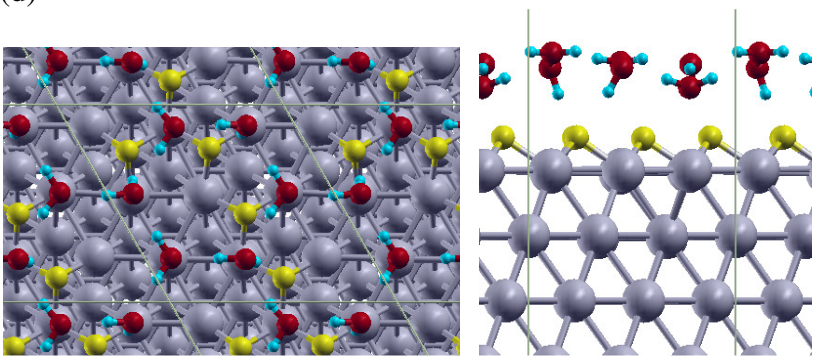

(e)

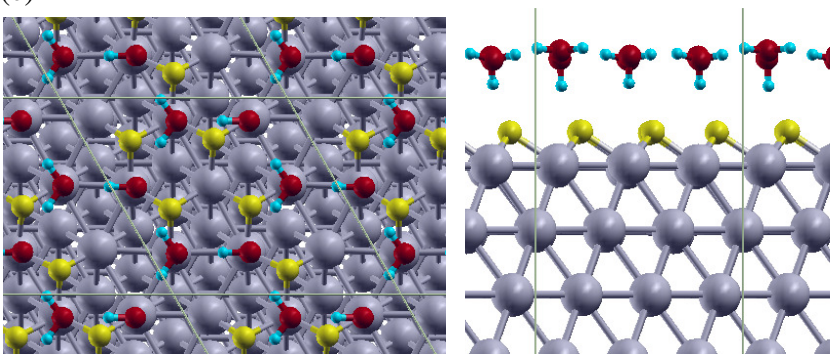

Fig. B1. (cont'd)

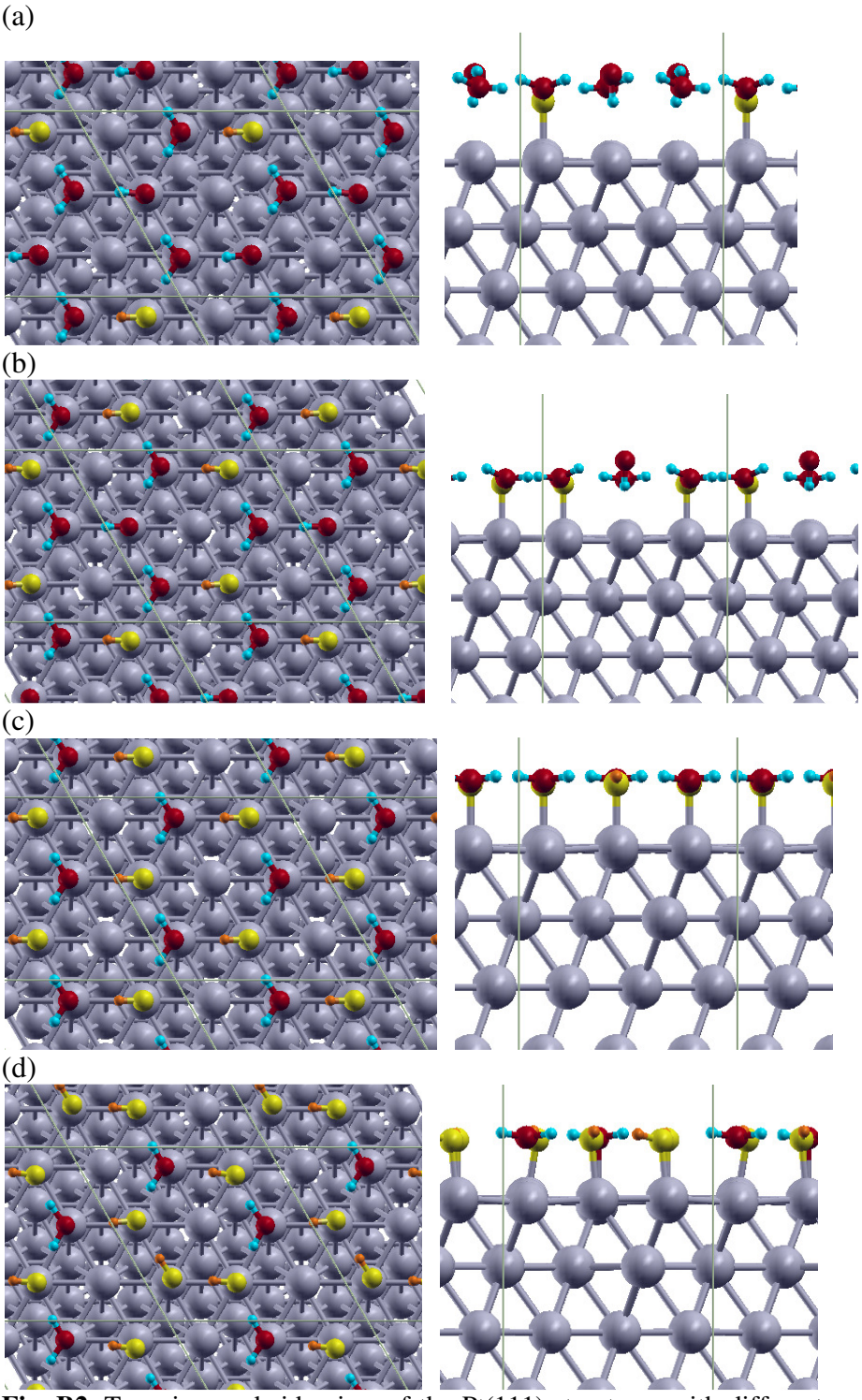

Fig. B2. Top view and side view of the Pt(111) structures with different coverage of HO* co-adsorb with water. (a) 0.11 ML OH* (b) 0.22 ML OH* (c) 0.33 ML OH* (d) 0.44 ML OH*. Grey-Pt, Yellow-O belonging to *OH, Orange-H belonging to *OH, Red-O belonging to H_2O and Blue-H belonging to H_2O.

B.2. Stability of O* and *OH on Pt/Ir-Co and Pt/Pd/Ir-Co at pH = 0 and surface Pourbaix diagrams

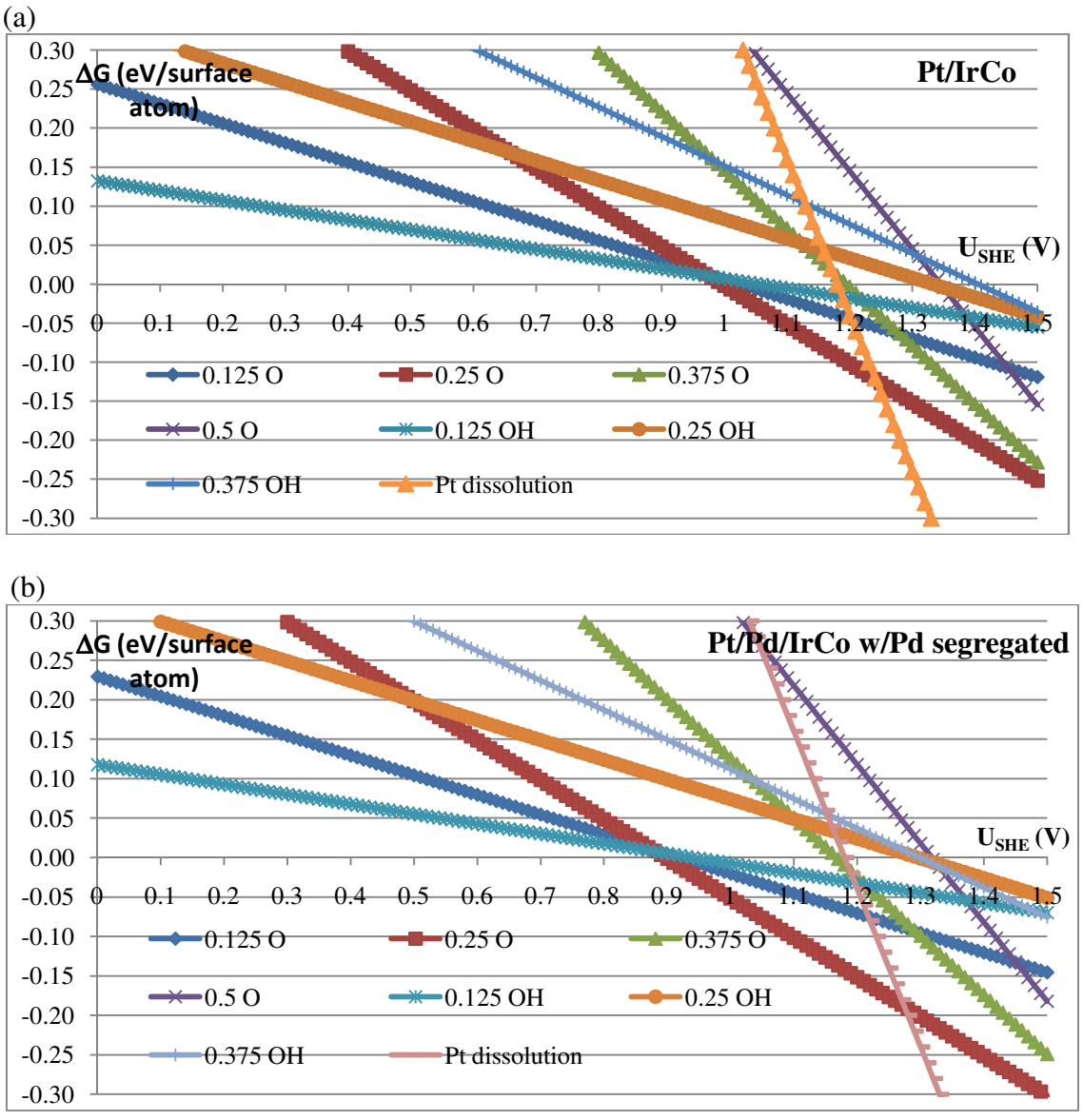

Fig. B3. Stability of O* and *OH on (a) Pt/IrCo, (b) Pt/Pd/IrCo with Pd segregate, (c) Pt/Ir_3Co, (d) Pt/Pd/Ir_3Co and (e) Pt/Pd/Ir_3Co with Pd segregate at pH = 0.

(c)

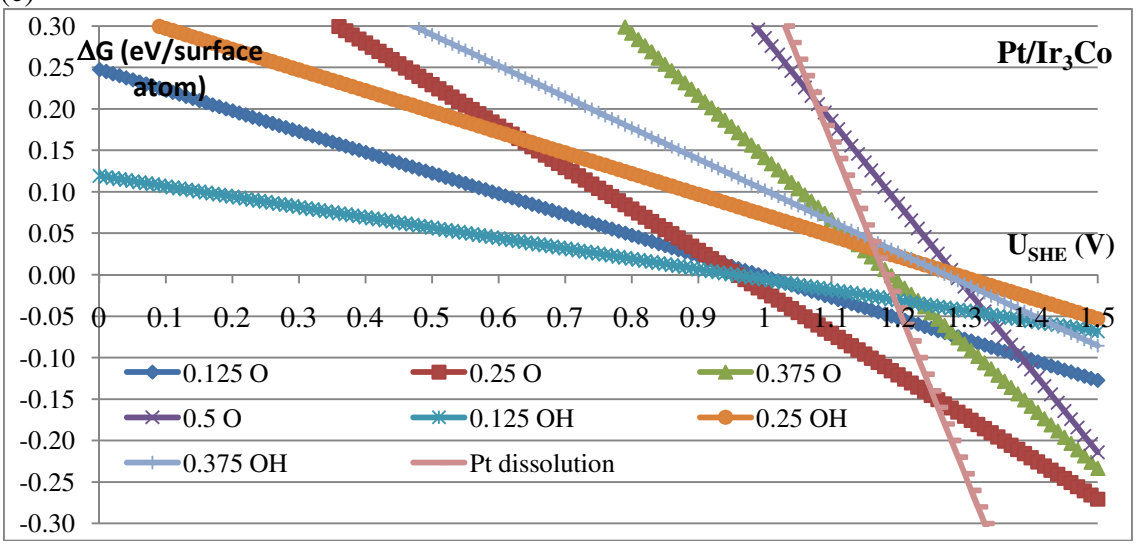

(d)

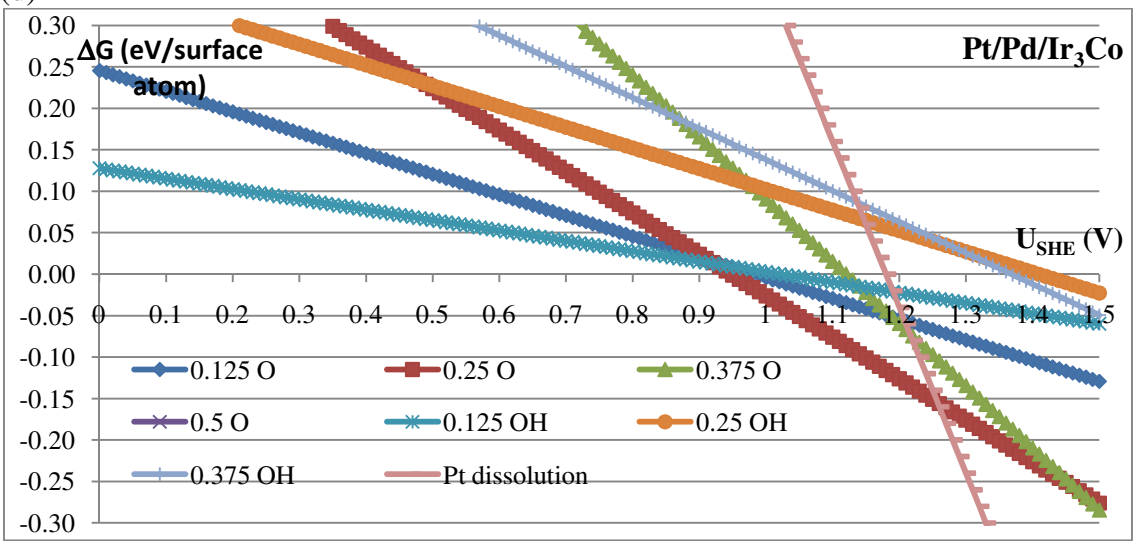

Fig. B3. (cont'd)

(e)

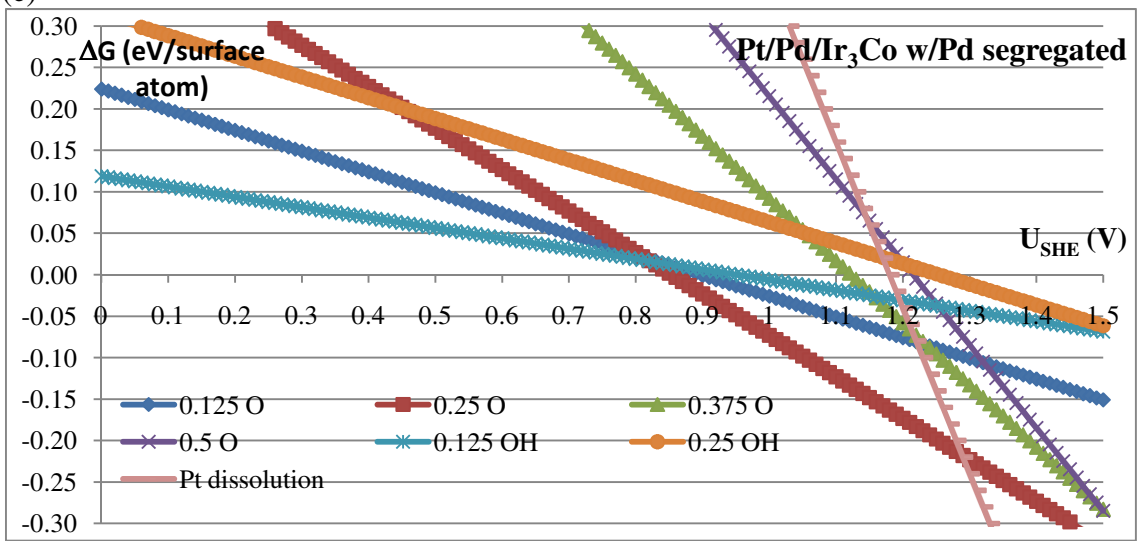

Fig. B3. (cont'd)

(a)

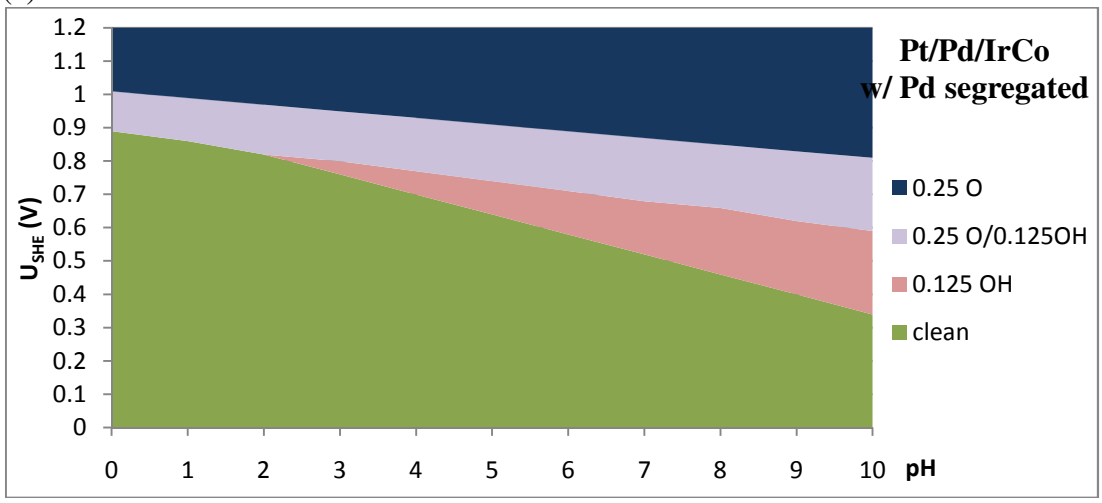

Fig. B4. Surface Pourbaix diagram of (a) Pt/Pd/IrCo with Pd segregate, (b) Pt/Ir_3Co, (c) Pt/Pd/Ir_3Co and (d) Pt/Pd/Ir_3Co with Pd segregate.

(b)

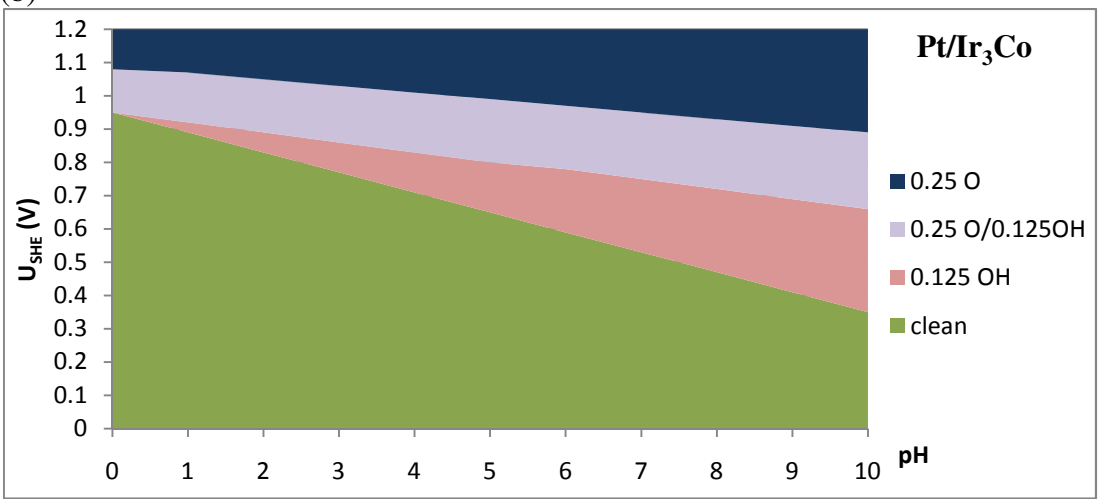

(c)

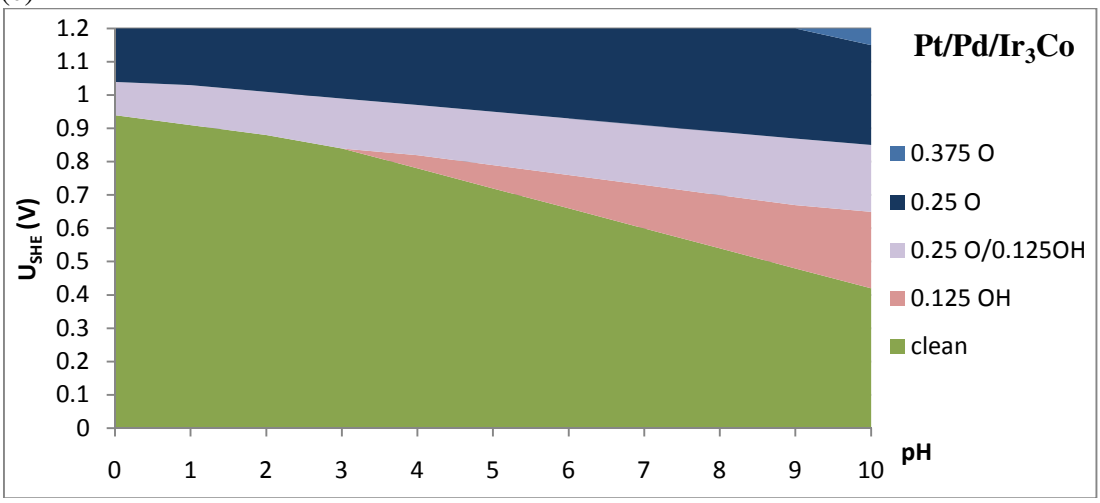

Fig. B4. (cont'd)

(d)

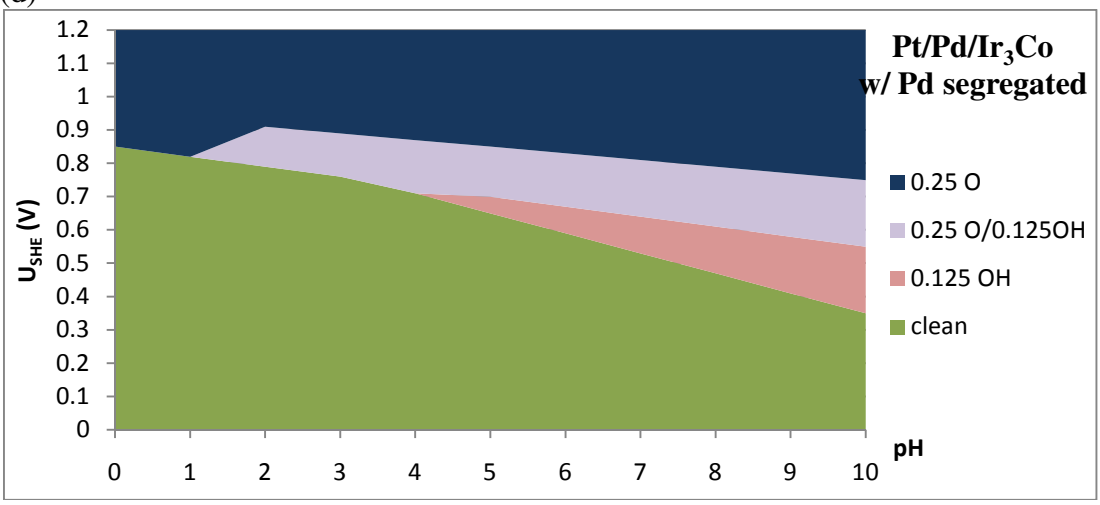

Fig. B4. (cont'd)

APPENDIX C

SUPPLEMENT DATA FOR STABILITY AND OXYGEN REDUCTION REACTION ACTIVITY OF SHELL-ANCHOR-CORE MATERIALS

C.1. Stability of O* and *OH on Pt/Fe-C/Ir, Pt/Co-C/Ir and Pt/Ni-C/Ir at pH = 0, 4 and 8.

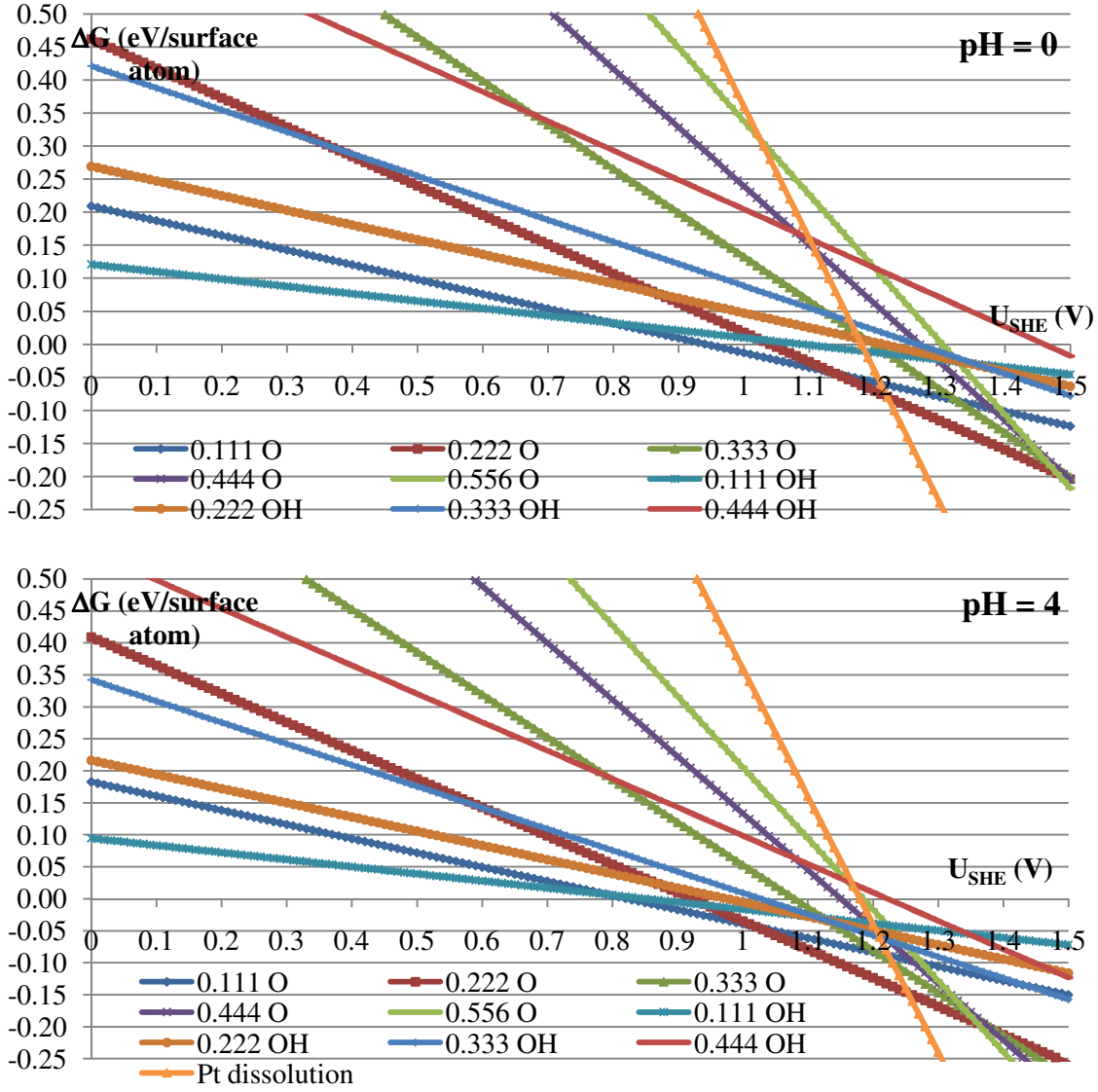

Fig. C1. Stability of O* and *OH on Pt/Fe-C/Ir at pH = 0, 4 and 8.

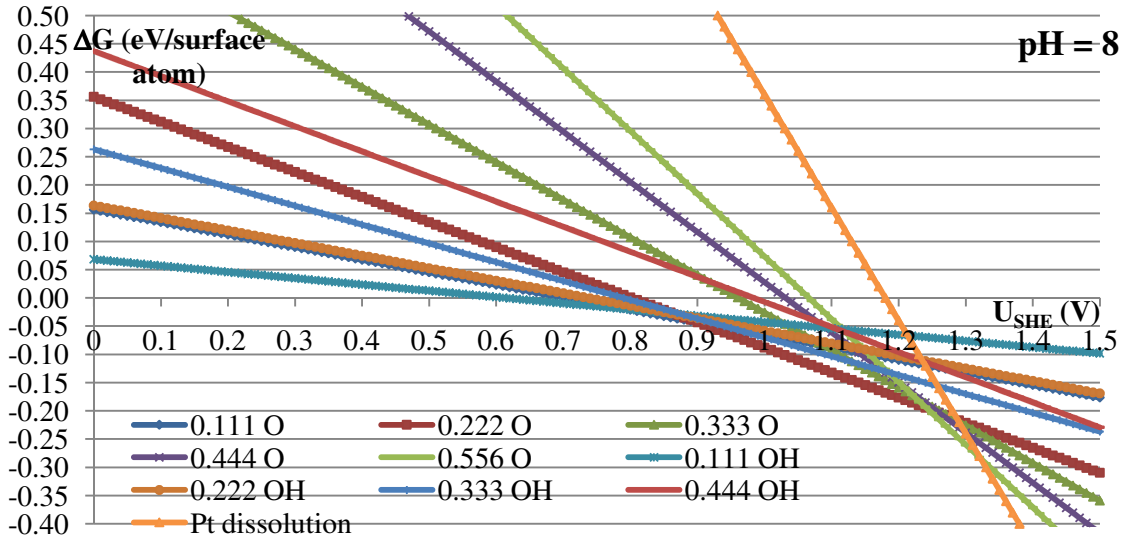

Fig. C1. (cont'd)

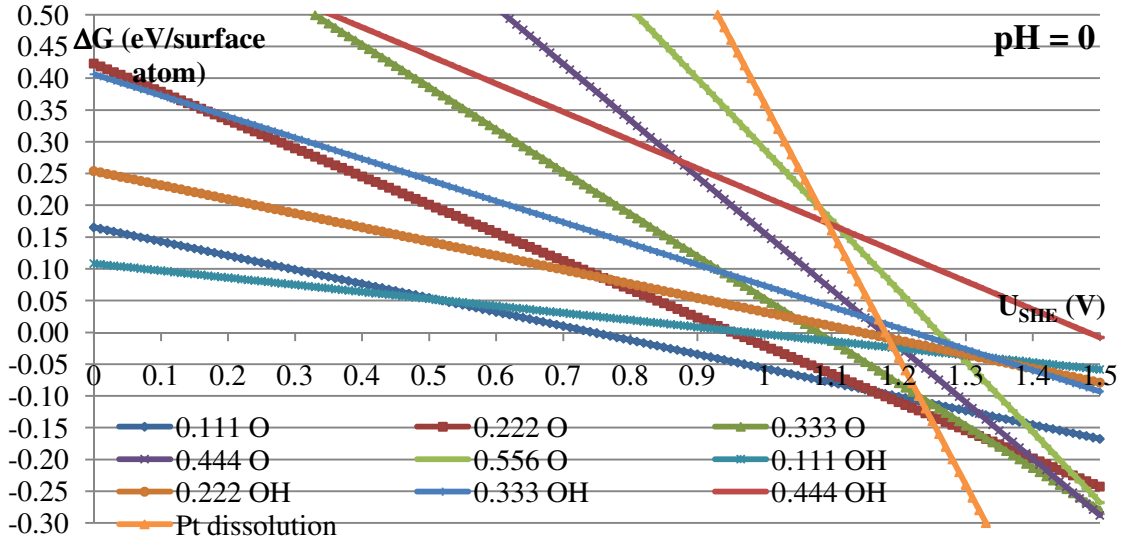

Fig. C2. Stability of O* and *OH on Pt/Co-C/Ir at pH = 0, 4 and 8.

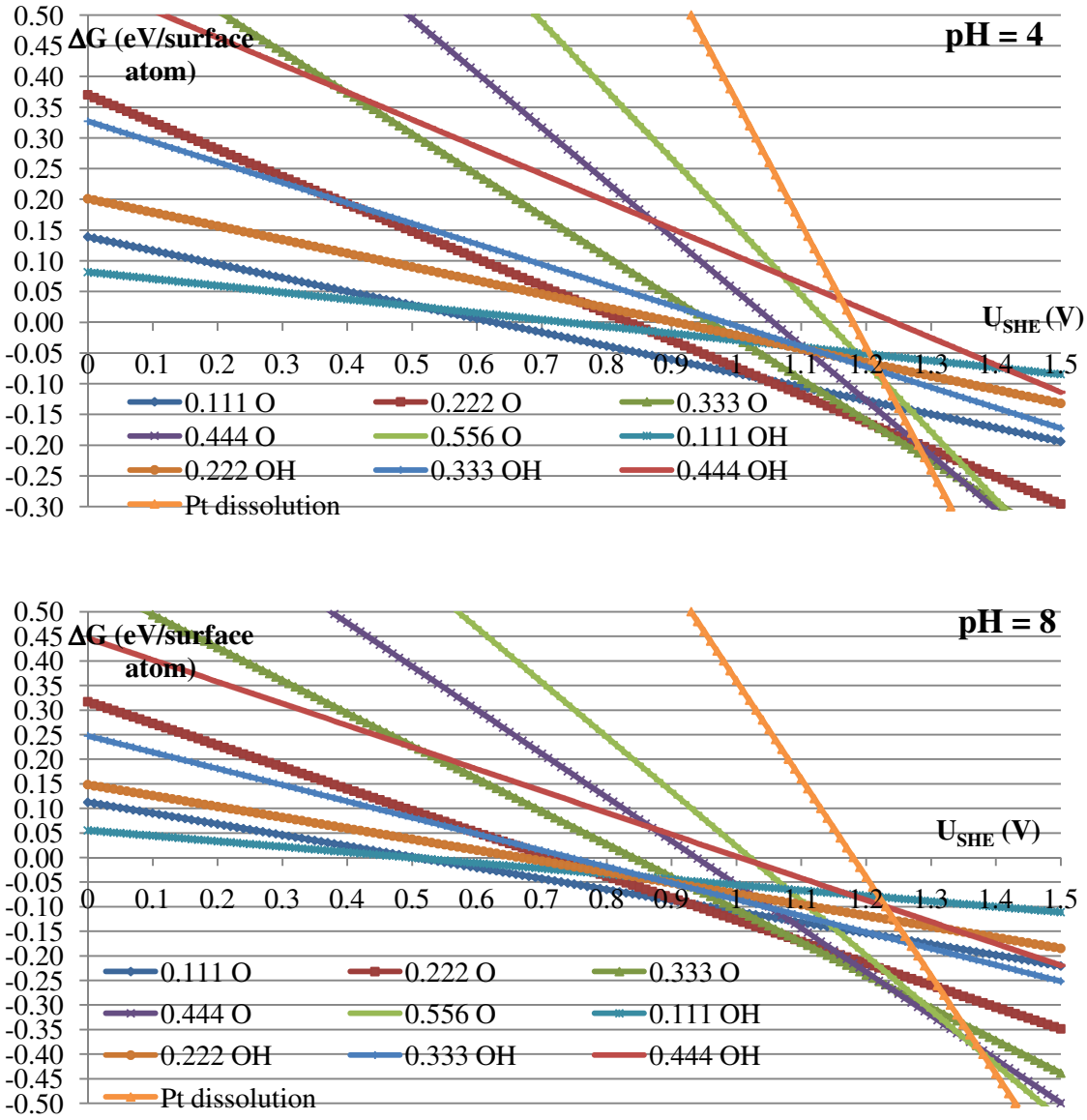
pH = 4
ΔG (eV/surface atom)
U_SHE (V)
0.111 O
0.222 O
0.333 O
0.444 O
0.556 O
0.111 OH
0.222 OH
0.333 OH
0.444 OH
Pt dissolution
pH = 8
ΔG (eV/surface atom)
U_SHE (V)
0.111 O
0.222 O
0.333 O
0.444 O
0.556 O
0.111 OH
0.222 OH
0.333 OH
0.444 OH
Pt dissolution

Fig. C2. (cont'd)

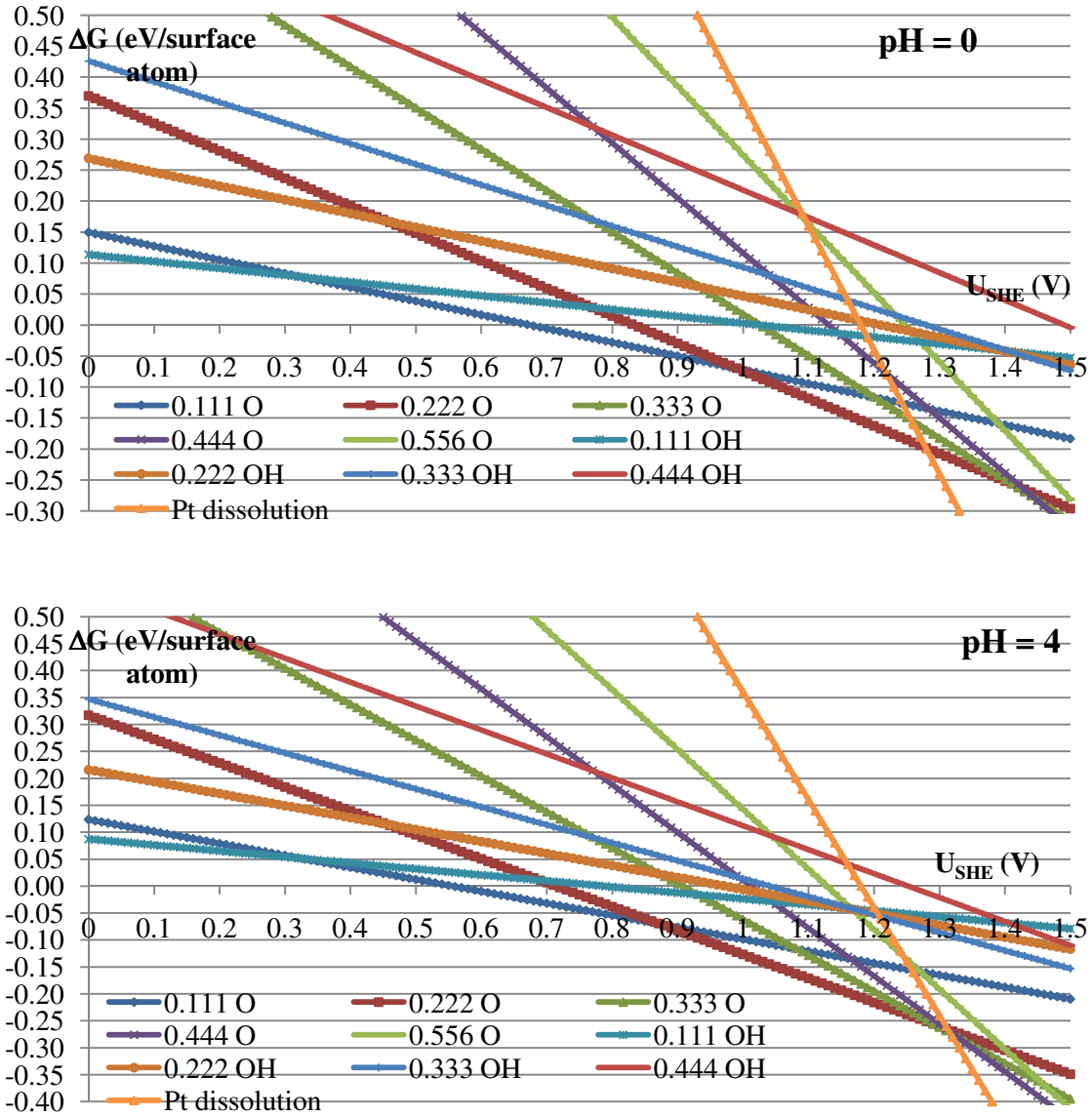

Fig. C3. Stability of O* and *OH on Pt/Ni-C/Ir at pH = 0, 4 and 8.

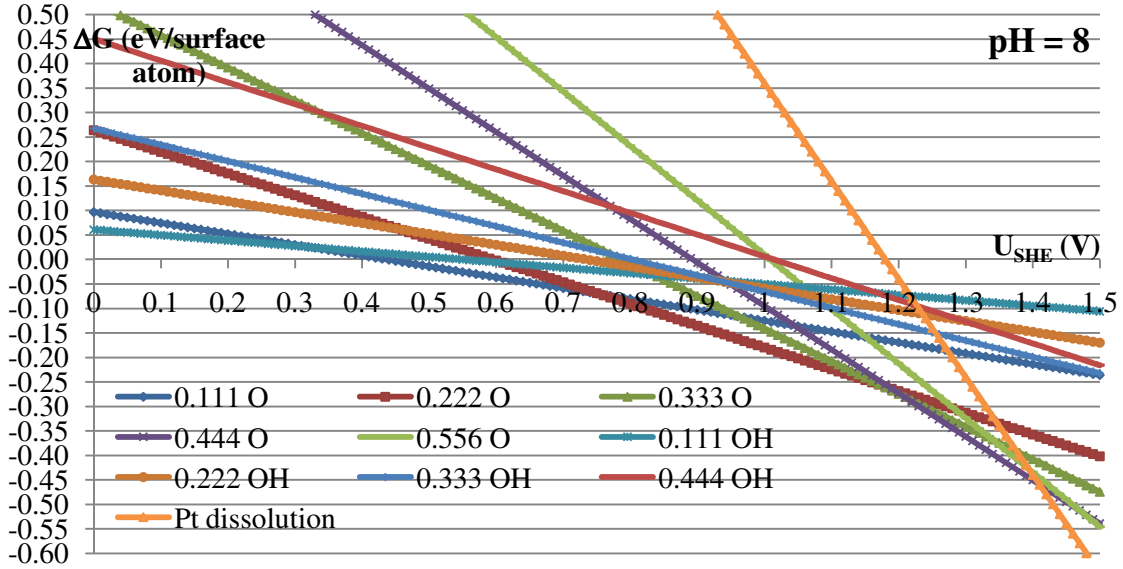
ΔG (eV/surface atom)
pH = 8
U_SHE (V)
0.50
0.45
0.40
0.35
0.30
0.25
0.20
0.15
0.10
0.05
0.00
-0.05
-0.10
-0.15
-0.20
-0.25
-0.30
-0.35
-0.40
-0.45
-0.50
-0.55
-0.60
0
0.1
0.2
0.3
0.4
0.5
0.6
0.7
0.8
0.9
1
1.1
1.2
1.3
1.4
1.5
0.111 O
0.222 O
0.333 O
0.444 O
0.556 O
0.111 OH
0.222 OH
0.333 OH
0.444 OH
Pt dissolution

Fig. C3. (cont'd)

VITA

Name: Pussana Hirunsit

Address: Department of Chemical Engineering, Dwight Look College of Engineering-Texas A&M University
200 Jack E. Brown Building
3122 TAMU, College Station, Texas 77843-3122

Email Address: pussana.hirunsit@chemail.tamu.edu

Education: B.Eng., Chemical Engineering, King Mongkut's Institute of Technology Ladkrabang, Bangkok, Thailand, 2000
M.Eng., Chemical Engineering, King Mongkut's University of Technology Thonburi, Bangkok, Thailand, 2002
M.S., Chemical Engineering, Texas A&M University, 2007
Ph.D., Chemical Engineering, Texas A&M University, 2010